# THE MECHANICS OF TRAUMATIC BRAIN INJURY: FROM BLUNT TO BLAST LOADING

By

Joseph Augustus Kerwin

A DISSERTATION

Submitted to
Michigan State University
in partial fulfillment of the requirements
for the degree of

Mechanical Engineering – Doctor of Philosophy

2021

## ABSTRACT

THE MECHANICS OF TRAUMATIC BRAIN INJURY:
FROM BLUNT TO BLAST LOADING

By

Joseph Augustus Kerwin

Traumatic brain injury (TBI) is an endemic problem in both civilian and military populations. In the United States, the incidence of civilian TBI is over a million cases annually, with some years (2014) reaching over 2.5 million TBI-related emergency department visits. In recent decades, a new category of TBI has emerged – primary blast loading or otherwise known as, blast-induced traumatic brain injuries (bTBI). bTBI has become the *"signature wound"* of the Iraq (Operation Iraqi Freedom [OIF]) and Afghanistan (Operation Enduring Freedom [OEF]) conflicts as it has accounted for nearly 70% of all of the injuries to military service members. Until recently, bTBI has been almost entirely isolated to conflict regions. In August 2020, a catastrophic detonation accidentally occurred in Beirut, Lebanon that instantly affected over 300,000 people.

The high prevalence of TBIs in both the civilian and military communities has led to a significant societal burden and is one of the leading public health problems we face today. The treatment and prevention of TBIs has become a major focus within the past decade for all of the United States military branches. The increased awareness of TBI / bTBI has brought about great understanding in both the medical and research fields of neurology; however, it has also shed light on just how little we previously understood about this injury. TBI is a multifaceted problem that encompasses multiple length scales, complex anatomical geometries, and nonlinear biological responses and has various time-scales depending on the severity of the injury.

The objective of this research is to investigate the potential injury-causing mechanisms present during the biomechanical loading of TBI events. More specifically, it focuses on the parallels between TBI and bTBI. The bTBI community is actively debating several potential damage-causing primary mechanisms: direct cranial transmission, skull flexure, skull orifices, and thoracic surge. To this end, a brain-tissue phantom was created to investigate its response to different biomechanical

loading scenarios. The phantom was fabricated into a three-dimensional extruded ellipsoid geometry made out of Polyacrylamide gelatin that incorporated gyri-sulci interaction. Additionally, the dominant length scales of the sulci, gyri, gray matter thickness, and overall brain dimensions were incorporated into the gelatin brain phantom. The phantom was assembled into a polylactic acid 3D-printed skull, surrounded with deionized water, and enclosed between two optical windows to create a human head surrogate.

In this work, the response of the human-head surrogate was evaluated under two biomechanical loading conditions: blunt-force impacts and blast loading. A custom-built drop-tower apparatus was used for the blunt-force impacts and a state-of-the-art blast chamber was employed to characterize the human-head surrogate under blast conditions. These two experimental apparatuses aided in the investigation into the potential damage-causing mechanisms associated with TBI/bTBI. A noninvasive high-speed imaging system was used to capture the surrogate-head response from each biomechanical loading condition. Finally, digital image processing techniques were used to evaluate the kinematic motion of the entire surrogate head, but more importantly the direct response of the gelatin-brain phantom itself.

## ACKNOWLEDGEMENTS

There are numerous people who have directly contributed to my academic success and life-long achievements. Before I explicitly mention the significance of several individuals, I would like to acknowledge all of the modest, mundane, and passive conversations that are countless in nature but nonetheless created support and guidance that have led me to where I am today. I am sincerely grateful for everyone who has contributed to these impactful moments in my life.

The first individual I would like to recognize and thank is my doctoral supervisor Prof. Ricardo Mejía-Alvarez. Dr. Mejía-Alvarez made my transition into graduate school an easy process and has continuously provided support, guidance, feedback, and insight at every step of my research. In addition to the invaluable academic advising, Dr. Mejía-Alvarez has been tactfully navigating both internally at Michigan State University and externally through numerous laboratories in creating collaborations that directly allowed my research to thrive. I am and will be forever grateful for the opportunity to work in his research group.

I cordially thank all my committee members: Dr. Adam M. Willis, Dr. Thomas Pence, and Dr. Sara Roccabianca. Dr. Willis (PhD, M.D., Maj USAF) has worked diligently from the conception of this work to the realization that it has become today. His experience, neurological insight, and patience has largely contributed to the success of my research. I appreciate Dr. Willis's direct contribution acting as the principal investigator of our team coordinating with the USAF for sponsoring my research (award numbers FA8650-18-2-6880 and FA865-17-2-6836). My sincere gratitude goes to Dr. Pence and Dr. Roccabianca, who both contributed to my passion for the sciences. Through their direct teaching I was able to grasp the formulations of my research. Additionally, both Dr. Pence and Dr. Roccabianca have provided invaluable suggestions to my research that have improved it greatly.

I would further cordially thank Dr. Michaelann Tartis. Dr. Tartis guided me through my undergraduate degree and gave me my first opportunity to work in a research setting. She provided continuous support and encouragement during my time at New Mexico Tech and convinced me

to pursue a graduate degree in the first place. She warmly welcomed and aided in the success of our research team's early collaborative visits to New Mexico. Her open and kind nature ensured a healthy and successful working environment that I greatly appreciated during my time under her mentoring.

Next, I would further like to thank colleagues who have assisted me throughout my doctoral tenure. First and foremost is Dr. Suhas Vidhate. His expertise, patience, creativity, generosity, and compassion have been insurmountable in my academic success. He openly welcomed me into our research group and has continuously provided me with close tutelage. I next want to thank Mr. Atacan Yücesoy. He has given countless hours to collaborate with my research. His computational expertise has expanded the understanding needed for one to grasp the complexity of my research and I will be forever grateful. My sincere gratitude also goes to Dr. Clément Roy. His passion for perfection, directly influenced my scrupulous attitude towards scientific understanding. Through his compassionate ridicule he is responsible for the success of my current research. I further owe my gratitude to Mr. Paul Sandherr. The success of my research is a direct result of his technical expertise. Through countless hours of discussion, early mornings, and design iterations his contributions have enabled me to conduct my research to high standards. I am fortunate to have benefited from his direct expertise. Next, I would like to thank Bianca Dávila-Montero. Her engagement, attentiveness, and enthusiasm elevated my research and for that I am grateful. Additionally, encouragement and guidance was provided by Ankit Gautam, Tushar Kailu, and Keith King through constructive conversations that helped me address numerous concerns with my research. I would like to thank each of them for the time they have contributed.

Last but not least, I would like to give my deepest thanks to my family. Their unconditional love and support in my academic journey has provided me with the strength to see myself through numerous struggles. They have provided guidance, laughter, encouragement, compassion, patience, and sacrifices that have directly contributed to my success. Without them the research presented herein would not have been possible. I am deeply grateful for each of you and thankful for all of the time we get to spend with one another.

## TABLE OF CONTENTS

## LIST OF TABLES

## LIST OF FIGURES

# CHAPTER 1

# INTRODUCTION

## 1.1 Motivation

Traumatic brain injury (TBI) is an endemic problem in both the civilian and military populations. TBI's are classified as a disruption in normal function of the brain caused by an external force; usually a bump, blow, or jolt to the head [22]. These types of TBI's are known as blunt-TBI's. A concussion is widely accepted as the most common form of TBI and is defined as the brain receiving trauma from an impact or a sudden momentum or movement change. In the United States, the annual incidence of civilian TBI is over a million cases [44, 115]. In 2014 alone, there were over 2.5 million TBI related emergency department visits here in the United States [22].

The vast majority of these TBI's were associated with accidental falls, motor vehicle crashes, or sporting events. TBI events affect thousands of individuals in every country of the world, every year. However, TBI events are not exclusive to the civilian population, they also indiscriminately affect the military community. Military service members are exposed to an entirely separate category of TBI – primary blast loading or otherwise known as, blast-induced traumatic brain injuries (bTBI). bTBI is one of the leading causes for military casualties and wounded service members [24, 36, 49]. Nearly 70% of all injuries are due to bTBI and has become widely accepted as the "signature wound" of the Iraq (Operation Iraqi Freedom [OIF]) and Afghanistan (Operation Enduring Freedom [OEF]) conflicts [35, 67]. The Department of Defense has identified over 413,000 military service members affected with a TBI ranging across severity levels from the first diagnosis in 2000 until the end of 2019 [34]. Until recently, bTBI has been almost entirely isolated to conflict regions. In August 2020, a catastrophic detonation accidentally occurred in Beirut, Lebanon. The blast killed more than 178 people, left more than 6,500 injured and 300,000 people homeless [9, 138]. This was one of the largest non-nuclear explosions in human history, with experts calculating the power on the order of 500 tons of TNT equivalent [4].

The high prevalence of TBI's in both the civilian and military communities has led to a significant societal burden and is one of the leading public health problems we face today. TBI's were on track to become the third leading cause of death in the world by the year 2020 (pre-Covid-19 pandemic predictions) [75, 82]. Additionally, Meaney et al. point out that the annual financial burden associated with civilian TBI is in the billions of dollars. The treatment and prevention of TBI's has become a major focus within the past decade for all of the United States military branches. Although, the attention has been mainly focused on combat-related TBI's, it is important to note that active military individuals face all of the same risks as a civilian: accidental falls, recreational sporting injuries, motor vehicle accidents, etc. The combination of risks present in everyday activities along with the exposure to blast waves associated with the requirements of military duty cause service members to be at an elevated risk for TBI.

The increase awareness of TBI/bTBI has brought about great understanding in both the medical and research fields of neurology. However, it has also shed light on just how little we previously understood about the injury even only two or three decades ago. Additionally, the increased understanding has pointed out areas that need to be studied further. TBI is a multifaceted problem that encompasses multiple length scales, complex anatomical geometries, and nonlinear biological responses and has various time-scales depending on the severity of injury. An aspect that makes studying TBI so difficult is that the biological variation present in each human makes every TBI case unique: from its mechanical loading conditions to the individual response of the system. Being able to create a universal approach, derived from entirely individual responses, is a daunting and difficult challenge that requires a multidisciplinary approach to solve.

Currently, research is being conducted in a variety of ways relating to TBI/bTBI: ex-vivo and in-vivo material characterization, experimental models (both animal and surrogate based), histological response, finite element models, clinical data analysis, and emotional/behavioral/cognitive responses just to name a few. Each of these areas of research are important and have contributed valuable insight to the current collective knowledge regarding TBI. However, TBI remains an elusive topic because it involves heterogeneous pathological processes. By further investigating each of these

areas, researchers hope one day to fully comprehend all of the contributing attributes of TBI as well as the biological responses.

### 1.1.1 Aims and Outline

The objective of this research is to investigate the potential injury causing mechanisms present during the biomechanical loading of TBI events. More specifically, it is focused on the parallels between TBI and bTBI. The bTBI community is actively debating several damage-causing, primary mechanisms: direct cranial transmission (DCT), skull flexure, skull orifices, and thoracic surge. There are additional mechanisms, acceleration, and cavitation present during a bTBI event. However, these are not stand-alone mechanisms; head acceleration is not a direct result of the static overpressure of a blast wave; and since cavitation requires the creation of negative pressure, it falls as a secondary mechanism that is initiated by one of the primary mechanisms [38].

Each mechanism has supporting evidence but also limiting aspects in regards to the physical, clinical, and physiological conditions associated with bTBI. In order to study the injury mechanisms, it is necessary to isolate as many mechanisms from one another as possible. This is necessary to reduce and ultimately eliminate the combining superposition that occurs when multiple mechanisms are present. The primary aims that are to be achieved are as follows:

- Identify the mechanisms directly associated with TBI.
- Design a noninvasive and ethically neutral replication of the human brain in order to study the mechanisms.
- Utilize optical approaches to experimental study the TBI mechanisms.
- Investigate the influence that is associated with each mechanism under a variety of loading conditions.
- Evaluate the potential effect that each mechanism plays in TBI.

By studying the underlying mechanics associated with the mechanisms of bTBI this research can increase the collective knowledge of both TBI and bTBI. This research can improve the validity of

numerous finite element models, reduce unnecessary animal testing, aid in the creation of protective equipment, improve medical professional's tools for diagnosis and treatment protocols, and help understand blast exposure thresholds for humans.

The remaining portion of chapter 1 gives a brief overview of the necessary information relating to this research. It discusses the anatomy of the brain, mechanical loading scenarios, and the potential injuries an individual may encounter and finally discusses the physics involved with a blast. Chapter 2 summarizes the current state of the literature: from general animal studies being performed experimentally, to the experimental techniques currently being utilize, the finite element models used to explore the phenomena computationally are also discussed, as well as the importance of the mechanical properties of brain tissue, and finally the effort to create accurate scaling laws to better predict damage outcomes. Chapter 2 gives great depth to the overall comprehension of this multifaceted problem. Chapter 3 then discusses the formulation and creation of the biofidelic test object used throughout this research. Understanding the relevance of the anatomical features discussed in §1.2 along with the limitations of current research covered in chapter 2 will aid the reader in understanding the importance of the creation and utilization of the brain phantom. The specific apparatuses used to impart experimental loading onto the test object will then be covered in chapter 4. The specific experiments performed, along with the targeted parameters of said experiments, are discussed in detail in chapter 5. The results of chapter 5 will then be discussed in chapter 6. Additionally, key experimental observations and findings will be discussed in this chapter. Finally, chapter 7 highlights the overall research discussed throughout this dissertation, the insights that have been learned, and how the results can be utilized across the TBI / bTBI community. The future direction of this research is briefly discussed in chapter 8.

## 1.2 Anatomy of the Brain

The human brain is the center of the nervous system and is the most complex organ in the human body. It comprises approximately only 2% a person's body weight, while requiring upwards of 20% of its oxygen and caloric intake [109]. The relative size, shape, functionality, and importance of the brain has been carefully documented. There are numerous published works on every aspect of the human brain – neural signaling, motor control, sensory processing, plasticity, early development, visual cortex, and the auditory system just to name a few. Every year thousands of researchers expand the understanding of the human brain and increase the collective understanding of how it works. This information detailing the human brain is so expansive that allocating only a section to its anatomy hardly seems justified. Any reader could go to a human anatomy text to obtain a general understanding of the anatomy of the brain.

However, for the same reason that the reader could seek to obtain the necessary information from one of the expansive collections available, is the exact necessity for having a brief description within this text. The average reader would have to sift through volumes of data, text books, and research articles without guided direction to obtain the relevant knowledge. There is an enormous amount of information about the human brain that can be easily obtained – yet, only a relative small portion (e.g., size, shape, anatomical features, regional importance, etc.) needs to be familiarized by the reader in order for them to have the minimum understanding required to grasp the remainder of this text.

The remainder of this chapter will be a brief description on the overview of the human brain. It begins with the broad description of the brain and then continues to describe with more and more detail down to the smallest length scale that is relevant to this work. Throughout this section, references will be provided so the curious reader may further explore any topic that may interest them. Furthermore, the information provided in this chapter is meant only to give the necessary information needed to understand the problem framework as well as to aid in the reader's understanding of the later chapters.

### 1.2.1 Overview

The human brain is the central component and main organ of the Central Nervous System (CNS). The brain is located inside of the human skull and is floating in a liquid called cerebrospinal fluid (CSF). Both the skull and the CSF surround the brain providing it protection. The skull is dense, made up of multiple layers of bone, providing protection from objects potentially striking the brain directly. The CSF surrounds both the brain and the spinal cord. The CSF flows through open channels located within the brain itself, called ventricles. The CSF acts as a shock-absorbing layer, which helps to mitigate any trauma that the brain may receive from an external injury. There are three other structures that also surround the brain: Dura mater, Arachnoid mater, and Pia mater, which are collectively called the meninges. These three structures will not be covered in this text in detail but will be briefly discussed in §1.4.2. Interested readers are invited to explore their anatomical role, cellular structure, and more by themselves. An important aspect to clarify before the detailed

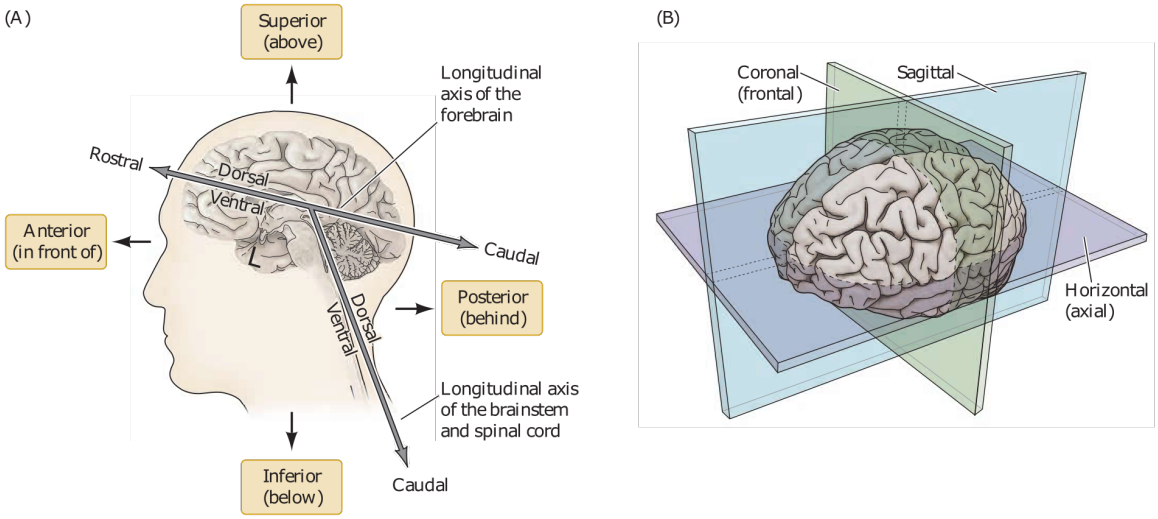


**Figure 1.1.** Axes of the human nervous system: (A) Anatomical terms used to describe locations in the CNS, (B) Major planes of interest for sectioning and imaging of the brain [107]

description of the brain is given is the standardized nomenclature used for the anatomical description of the human body and the brain. Figure 1.1 details the axes used in internal anatomy as well as the terms used for gross anatomical description. This description method allows for the unambiguous location to be understood independent of the observer's point-of-view.

There are three major planes of interest when studying the brain: Coronal, Sagittal, and Horizontal. Each of these planes lie along an axis of the body. The Coronal plane, also known as the frontal plane, corresponds to viewing the brain as if talking face-to-face with someone; this section extends from ear to ear and covers the superior to inferior directions. The Sagittal plan corresponds to the anterior to posterior directions (rostral to caudal) and is associated with the plane dividing the two hemispheres of the brain. The Horizontal plane, otherwise known as axial plane, also extends the anterior to posterior direction and comprises the entire brain from ear to ear. The axial plane is parallel to the ground if an individual is standing upright [107]. The human brain is comprised

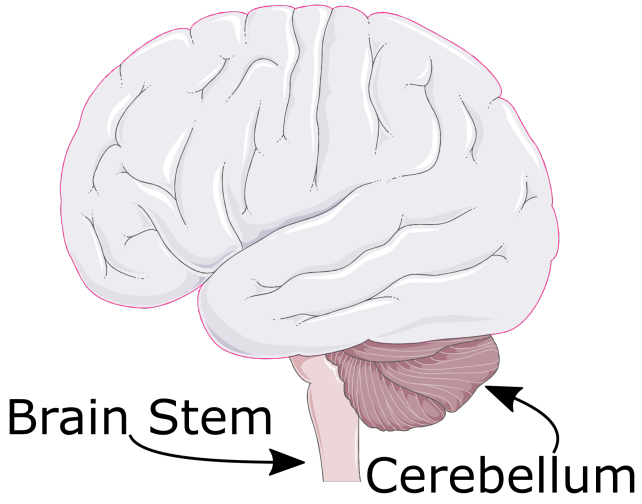


**Figure 1.2.** The main structures comprising the human brain. Adapted from [121].

of three separate but connected structures: cerebellum, brainstem, and the cerebrum, which can be seen in Figure 1.2. The brain stem and cerebellum are located inferior to the cerebrum, which is highlighted in pink in Figure 1.2. The brain stem connects the cerebrum and cerebellum to the spinal cord. The cerebellum is located between the brain stem and the inferior posterior portion of the cerebral cortex. The cerebellum plays a key role in the motor control of the body. The brainstem is comprised of three smaller additional structures: midbrain, pons, and medulla oblongata. Its primary role is to regulate cardiac and respiratory functions. The reader can explore the brainstem and cerebellum in detail if they so desire [93]. However, the remaining portion of this text will focus on the cerebrum.

### 1.2.2 The Cerebrum

The cerebrum is the largest portion of the human brain and rests in the superior most portion of the CNS. The cerebrum is divided into two symmetric hemispheres by the longitudinal fissure. Each of these hemispheres is further classified into four distinct, yet connected lobes: Frontal, Parietal, Temporal, and Occipital. Figure 1.3 illustrates the portion of the brain in each lobe. The four individual lobes are distinct by the major functions that they control for the human body with their names derived from the cranial bones that overlie them. However, with all of the lobes interconnected, they each play a role in every function for the human body. Brain tissue is further classified into two distinct sub-categories: white and gray matter. The outer most portion of each hemisphere is called the cerebral cortex, which is comprised of gray matter. The underlying region of the cerebral cortex, otherwise referred to as the subcortical region, is composed of white matter.

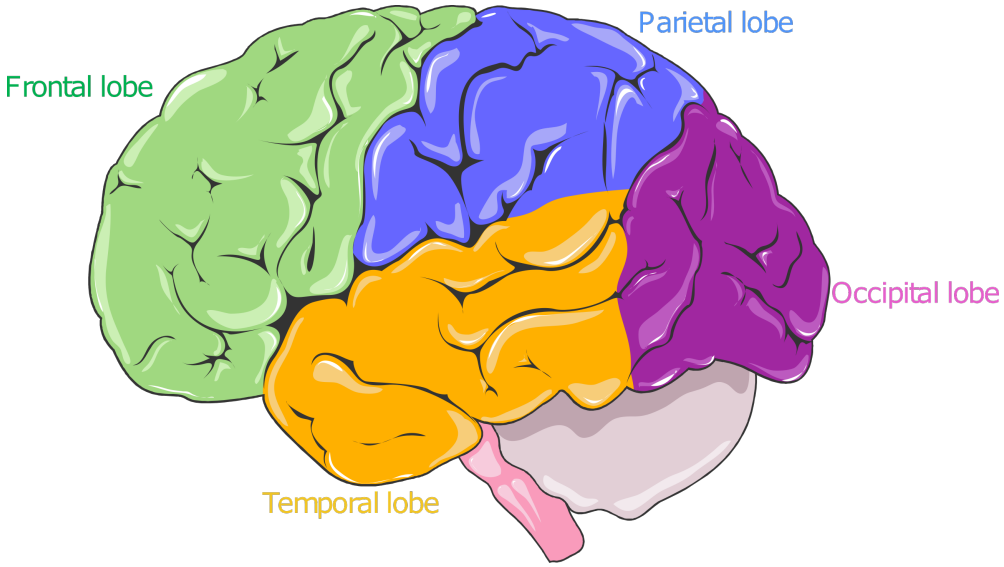


**Figure 1.3.** The four lobes of the Cerebral Hemispheres. Adapted from [121].

In addition to the four lobes of each hemisphere, there are internal subcortical structures located within the medial portion: diencephalon, ventricles, basal ganglia, limbic system, etc. The internal portions of the human brain are mentioned to demonstrate the high complexity of interconnecting regions within the brain. These regions, while important for the proper function of the body are outside the particular area of interest for this text. Thus, these portions of the human brain will not be discussed further and are left for the curious reader to explore [97, 107].

The cerebral cortex is the largest location of neural integration and plays a key role in nearly all functions of the human body and higher-level mental activity. The cerebral cortex is uniquely characterized by its highly folded or wrinkle like appearance. These highly folded structures are continuous in nature and are characterized by gyri and sulci, see Figures 1.4. Gyri (singular: gyrus) are the ridges of the folded tissue, whereas the sulci (singular: sulcus) are the grooves or valleys that separate the gyri from one another [71, 107]. The gyri/sulci surface features are created through a process called, gyrification. These surface convolutions allow for the largest surface area to be obtained in the confined amount of volume that is the human cranium. Having an optimized surface to volume ratio allows humans to have the largest gyrification index scores of all primates and one of the largest indexes for all mammals once it has been normalized by weight [31]. The gyrification of

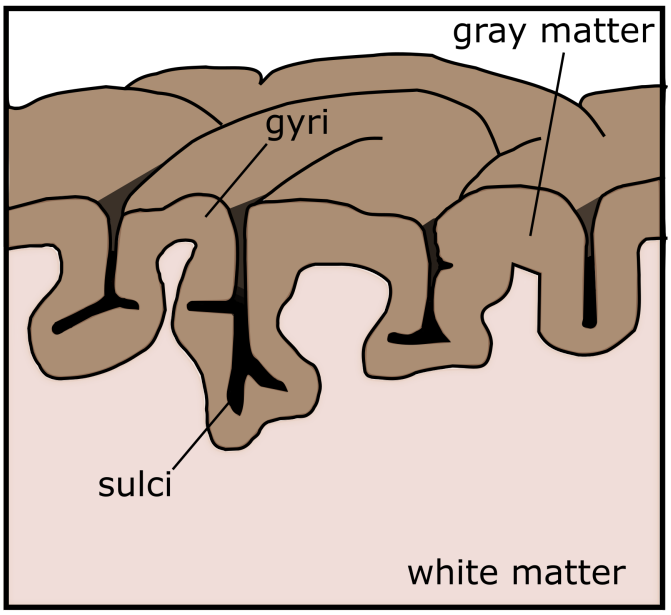


**Figure 1.4.** A visual representation of the gyri / sulci of a brain slice. Adapted from [71].

the human brain was brought about by the evolutionary necessity to be as efficient as possible. The gyrification allowed for greater cognitive functionality as well neural organization. All of which are significant advantages from an evolutionary standpoint. An unavoidable condition of gyrification is the increased complexity of the system. This increased complexity is advantageous in nature but does create certain difficulties for researchers. One of the main difficulties is the overall geometry of the brain itself. A significant portion of the brain's anatomical features are inaccessible and, thus,

difficult to study. The majority of the cerebral cortex is not visible externally but rather hidden in the sulci. The insular cortex, which is located medially from the temporal lobe deep inside of the lateral sulcus, is a perfect example. Only in the last several decades have technological advances (MRI, CT, EEG, PET, etc.) made significant progress, which makes studying internal regions of the brain possible without the need for postmortem subjects.

The overall size, shape, and weight of the human brain is the area of interest for this research. For this reason, detailed descriptions of the nervous system cells (neurons and glial cells) and how they operate will not be discussed. Although, it is necessary to understand the underlying cellular structures, their individual roles, and how they work together in order to grasp how the brain functions; this work aims at understanding how tissue is damaged as a result of mechanical loading on the entire organ.

An important aspect regarding neurons that is directly applicable to this research is the general orientation of the neurons within the brain. As seen in Figure 1.4 there are the cerebral cortex and the subcortical region. The cerebral cortex is composed of gray matter, which is the densely packed *cellular bodies* of the neurons. The subcortical region composed of white matter consists primarily of the axonal portion of each neuron [16, 92]. White matter draws its name from the myelin sheathing that insulates each neuron's axon, which is white in nature. The myelin sheathing plays an important role in the efficient signal transmission between neurons. The cellular bodies, or soma, of the neuron regulate the activities within the specific neuron and initiate the signal transmission from one neuron to the next.

The research discussed herein focuses on the loading parameters involved in an injury event. Depending on the specific location of damage within a neuron, signal transmission can be effected or eliminated altogether. Understanding the orientation of neurons, the overall geometry of the brain, and the mechanical loading conditions present during an injury can greatly improve the recovery of a patient through appropriate medical treatment. The subsequent sections of this chapter discusses the relevant mechanical loading involved in a TBI and the possible injuries resulting from such loading.

## 1.3 Modes of Mechanical Loading

The purpose of this section is to address the necessary information regarding the mechanical loading present during impulsive loading events of the brain. This section only highlights the aspects that will be required to understand later portions of this text and is only meant to operate in an introductory manner. Any curious reader who wishes further explanations on the sub-topics of this section is asked to investigate the cited references.

Brain injuries are classified into three distinct categories: skull fracture, focal injury, and diffuse brain injury [81]. To understand the premise of these injuries, the biomechanical loading involved in such events needs to be understood. These loading modes are demonstrated in figure 1.5. There are two fundamental biomechanical loading modes involved in head injuries: contact or inertial loading. Contact loading is when a force is applied to the head directly, whereas inertial loading involves the head being set into motion. An important aspect to note is that contact injuries are the sole consequence of the force applied to the head resulting from an impact. On the other hand, inertial injuries tend to be superimposed on top of contact injuries. This is due to the fact that the head requires an external applied force to be set into motion. This distinction, while modest, is important to clarify as it plays a role in the overall magnitude of an injurious event.

A third biomechanical mode of loading has become prevalent in the recent decades due to the military conflicts in both Iraq and Afghanistan: blast-overpressure (BOP). BOP, like contact and inertial loading, is a form of a dynamic loading event. Dynamic loading is classified as being rapidly applied, typically in durations less than 50ms [81]. However, BOP is quite unique compared to contact or inertial loading modes; it is ultra-dynamic (sub-millisecond loading duration) and is the direct result of explosively driven blast waves. In addition, the interaction of the shock wave is nearly unnoticeable as it interacts with the head, making it an entirely unique loading event compared to contact or inertial loading [81]. The loading event for the BOP mode involves extreme safety precautions to properly study the complex physical interactions present, which causes it to be the most difficult of the three to study, thus, making it the least understood of the three loading modes.

The damages resulting from all three loading modes are similar in nature. Specifically, the primary cause of tissue damage is the consequence of strain [81], which can be treated as the change of a tissue's shape (i.e., stretching, compressing, or shearing). If the change, or deformation, exceeds the natural limit of the particular tissue; then irreversible damage can occur. Understanding this process, along with the individual strain tolerances for different tissues, is paramount to understanding how brain injury might occur. To understand how a tissue may undergo deformation, each of the loading modes are further explained.

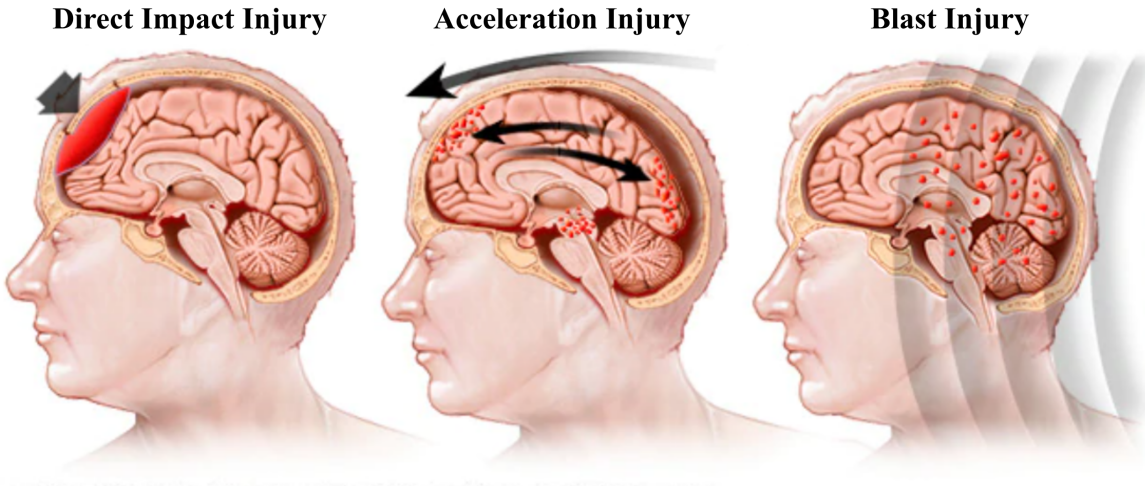


**Figure 1.5.** Examples of biomechanical loading modes. Adapted from [79]

### 1.3.1 Contact Loading

Contact loading occurs when a force is directly applied to the head. This is achieved when the head either impacts an object or is impacted by an object. The resulting injuries are dependent on the force and speed of impact. More generally, the contributing factors to the severity of injury relating to a contact loading event are the mass of impactor, area of impactor, velocity of impact, direction of impact, magnitude of impact, thickness of skull region, material strain tolerance, and the size of the impact area.

The resulting TBI associated with contact loading are generally divided into two sub-groups: local and remote. Local effects meaning damage near the impact site and remote effects are injuries

that occur distant from the impact site. Important to note is that contact loading produces focal injuries or skull fractures and not diffuse brain injury. Diffuse brain injuries are often referred to as diffuse axonal injury (DAI) due to the expansive damage to the supporting glial cells of the white matter and will be discussed below in section 1.3.2.

Local injuries are nearly always present during contact loading. The most common types of local contact injuries are linear skull fractures, depressed skull fractures, epidural hematomas, and coup contusions [81]. Remote injuries are often the effect of the stress wave propagation through the skull and intracranial contents. Skull distortions culminating at remote locations are often the cause of basilar skull fractures and contrecoup brain contusions [81]. Additionally, intracranial pressure (ICP) changes can occur from skull distortions themselves and from stress wave amplification due to complex three-dimensional (3D) wave interaction. Thus, impulsive pressure oscillations and stress amplification may alter cells, if exceeding tissue tolerance, can cause damage to intracranial contents [81]; however, it is important to note that the exact mechanisms / thresholds have not been well established.

Remote injuries are also a result of inertial loading that has been induced by a contact phenomena. These types of injuries are important to note as they are a direct result of contact loading; however, due to the nature of these injuries (mainly skull fractures) I shall not discuss them in-depth and leave interested readers to explore the phenomena individually.

### 1.3.2 Inertial Loading

Inertial loading, often called acceleration injuries, occurs when the head is set into motion. Inertial loading can happen indirectly as a result of another body region being set into motion (e.g., torso) or as a secondary result of contact loading. If the head in restrained, contact loading induces little to no movement upon the skull. However, if the head is free to move, as it is in nearly all clinical cases, then the head will be set into motion upon being struck by on object. The severity of inertial loading depends on the magnitude, rate, impulse duration, direction, type of acceleration, and force that is applied to the head.

Accelerating forces, much like contact loading, causes damage to brain tissue and surrounding vessels as a result of strain reaching damage tolerance of the tissue. A key aspect to distinguish is the type of acceleration involved during an injury: translational, rotational, or angular. Translational acceleration is when the head moves in a straight line without any rotation. Rotational acceleration occurs when the head rotates about a fixed point. Angular acceleration is the combination of both translational and rotational acceleration. Angular acceleration is the most common type of acceleration seen clinically, while also being the most damaging type of acceleration because it combines the injurious mechanisms of both translational and rotational movements [81]. The severity of damage is also a function of the magnitude and rate at which the acceleration is loaded and not just the specific type of loading itself. Inertial loading also exhibits similarities to contact loading, e.g., damage localized to the surface of the brain tissue and surrounding blood vessels.

Since acceleration injuries move the entire brain, the damage associated with this type of loading is often expansive and seen distributed throughout the different regions the brain. The distribution of injury is commonly identified as diffuse axonal injury (DAI). DAI is a direct result of the local deformations or alterations deep inside the brain due to the motion transmitted by inertial loading. This combination of mechanical forces and biological changes complicates the treatment approaches that are available to clinicians. In addition to DAI, inertial loading can lead to immediate life threatening issues such as hemorrhages or subdural hematomas.

### 1.3.3 Blast Over Pressure

As previously discussed in §1.3, BOP is the result of an explosive detonation. This loading mode has created a unique form of TBI, called blast-induced traumatic brain injury (bTBI). bTBI is characterized into four types of injuries: primary, secondary, tertiary, or quaternary. Primary bTBI is characterized when the incident pressure wave causes damage directly to the biological material (e.g., brain tissue) while propagating through the skull. Secondary bTBI involves damage as a result of focal impact by both penetrating and non-penetrating debris (e.g., shrapnel). Tertiary bTBI involves injuries resulting from a person being physically moved by the blast-wind of the shock

wave. Quaternary bTBI is the blanket category for all other injuries (e.g., burns, toxic gas, etc.). bTBI is classified even further as mild, moderate, or severe cases depending on the severity of resulting injuries. Secondary and tertiary bTBI can be directly associated with the two previously discussed loading modes (contact and inertial loading). Quaternary bTBI falls outside the scope of this text and will be left to the reader to investigate individually. The subsequent discussion aims to illuminate the complex nature of the primary injury type associated with bTBI.

Primary blast injury is unique due to the brain tissue's response directly from the BOP loading. Another exclusive aspect is that the pressure waves interact with the entire body, whereas contact and inertial loading for TBI events are almost always localized to the head itself. Additionally, BOP loading is an order of magnitude faster than contact or inertial loading; with strain-rates on the order of 2000 $s^{-1}$ (pronounced: inverse-seconds). This causes BOP to be classified as an ultra-high dynamic loading event. The exact profile of the pressure wave is dependent on the size, shape, type of explosive charge, and standoff distance. The characteristics of the pressure profile will be discussed further in §1.5.

Blast loading can cause a variety of injuries to the human body: ocular, aural, pulmonary, cardiovascular, musculoskeletal, and neurological. All of these can be life threatening depending upon the severity of injury. There are several competing theories as to the damage causing mechanism/s of primary bTBI: skull orifices (auditory, nasal, and orbits), direct cranial transmission (DCT), skull flexure, thoracic surge, and cavitation [38]. Each of these mechanisms will be discussed further in §2.1; but for brevity here, each mechanism leads to either focal and/or inertial injuries.

Due to the required knowledge to fully understand the evolution of injury (e.g., blast wave physics, neuroanatomy, impulse duration, etc.) BOP is the most complex of the three loading profiles discussed. Additionally, BOP has the greatest damage causing potential of the three loading modes. This is due to the result of the pressure wave interaction with the entire body – the pressure wave can directly cause damage but also can evoke secondary loading through the contact or inertial phenomena. BOP is nearly always coupled with one of the other loading modes in a clinical setting.

## 1.4 Brain Injuries

The relevant brain injuries that could be potentially sustained due to the mechanical loading previously discussed in §1.3 will be described below. The description of each injury will be brief in nature, offering the reader only the essential information needed to relate mechanical loading to the injuries seen clinically. As stated previously, there are three categories under which brain injuries are classified: skull fracture, focal injury, and diffuse brain injury. Each of these categories is further organized into more specific sub-groups. The grouping of these injuries is based on of the anatomical location, affected tissue/s, and severity. These groupings are a clinical standard, which aids in the quick dissemination of information that is imperative in emergency medicine. Understanding the key aspects of each injury type will assist in the comprehension of the overall injury event (i.e., mechanical loading $\rightarrow$ injury incidence $\rightarrow$ potential secondary loading $\rightarrow$ mechanical response of tissue $\rightarrow$ potential injuries $\rightarrow$ required medical treatment). Ultimately, defining injury mechanism/s allows for the anatomical localization, which then allows for quick understanding of the potential different pathophysiologies.

### 1.4.1 Skull Fractures

Fractures are medically defined as "...[the] process of breaking or the state of being broken" [87]. Clinically the term fracture is interchangeable between both solid and soft tissues (e.g., a kidney fracture). For the remainder of this text the term, fracture, will solely refer to the breaking of bone tissue and the term, rupture, will be used to refer to the breaking of soft tissue. Skull fractures are further characterized into three distinct groups: linear, depressed, and basilar fractures. Basilar fractures are also known as remote-vault fractures. The distinction between these fractures are relative to the location and severity of injury:

- Linear skull fractures are a break in the cranial bone resembling a thin line, without splintering, depression, or distortion of bone [61, 84].
- Depressed skull fractures are a break in a cranial bone with depression of the bone sunken in toward the brain and can be present with or without a cut in the scalp [61, 84] .

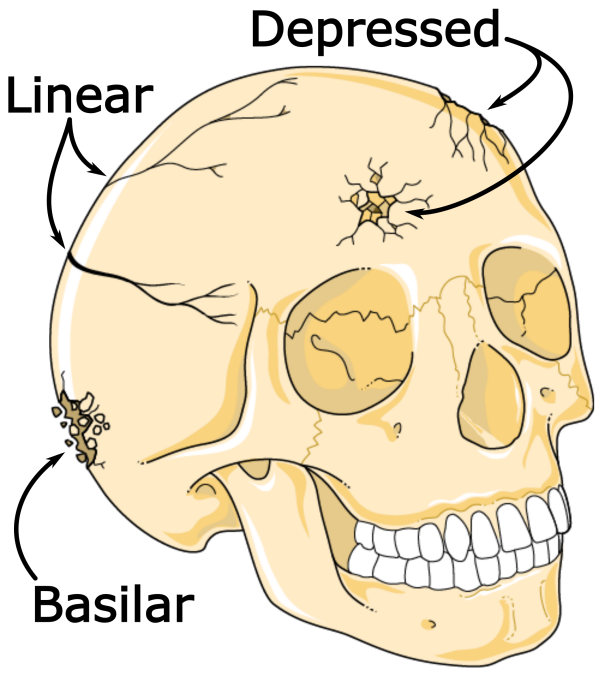


**Figure 1.6.** Examples of skull fractures. Adapted from [121]

- Basilar skull fracture involves a break in at least one of the bones that comprise the base of the skull [61]. They can represent both non-displaced (linear) and displaced (depressed) fractures [122].

Skull fractures, as seen in figure 1.6, are the result of contact loading previously discussed in §1.3.1. The formation of skull fractures depends on the individual parameters involved in the mechanical loading to the head. Contact loading involving objects larger than approximately 2 square inches will result in localized skull bending and the probability of linear skull fractures [81]. Small enough objects (approximately less than 2 square inches) produce concentrated areas of strain immediately beneath the impacting site – this concentration of energy increases the probability of penetration, perforation, and localized fracture pattern [81]. These injury patterns are directly associated with depressed skull fractures. Basilar skull fractures are most often caused by high-velocity blunt trauma directly to the basilar region of the skull [122]. However, basilar skull fractures can also result from stress wave propagation through the skull resulting from a remote impact [81]. The basilar portion of the skull is anatomically thinner than the other regions of the

skull – ultimately making it more susceptible to local skull deformations. Basilar skull fractures are clinically not common, but they are the most serious type of skull fracture due to the immediate life-threatening condition posed to the individual [61, 122].

Skull fractures are a common injury due to civilian activities (e.g. falls, bicycle/automobile accidents, sports, etc.), but are nearly always accompanied by another form of injury. The contact loading involved can lead to a secondary inertial loading of the head if the object is large enough or lead to immediate vascular damage due to perforation of the skull itself. The secondary injury increases the complexity of the overall injury and often complicates the necessary treatment protocols. If the secondary injury is more severe (i.e., life threatening), it takes precedence over the initial injury for the required medical treatment. Additionally, secondary injuries can evolve over time, further complicating the treatment protocol. The specifics of injury evolution are outside of the scope of this text and is left to the reader to explore further.

### 1.4.2 Focal Injury

Focal injuries are primarily the result of contact loading but have also been seen clinically due to inertial loading. Focal injuries are classified as damage to a limited area of the parenchyma (e.g., brain tissue, dura mater, etc.) near the site of mechanical loading [81]. Additionally, Meaney et al. point out that focal injuries account for nearly half of all patients with severe brain injuries and are responsible for approximately two thirds of brain injury related deaths. An aspect of focal injuries is that the damage is prominent and directly visible, whether be either to the naked eye or medical imaging techniques (e.g., MRI, CT, etc.). As seen with skull fractures in the previous section, focal injuries are further characterized into sub-groups pertaining to their physiological relevance. These categories are:

- Hematomas are defined as a collection of blood (clotted) in a tissue, organ, or body space outside of a blood vessel. [78]
- Contusions are defined as an injury to tissue without laceration. [86].
- Hemorrhages are defined as heavy discharge of blood from a damaged blood vessel [62, 86]

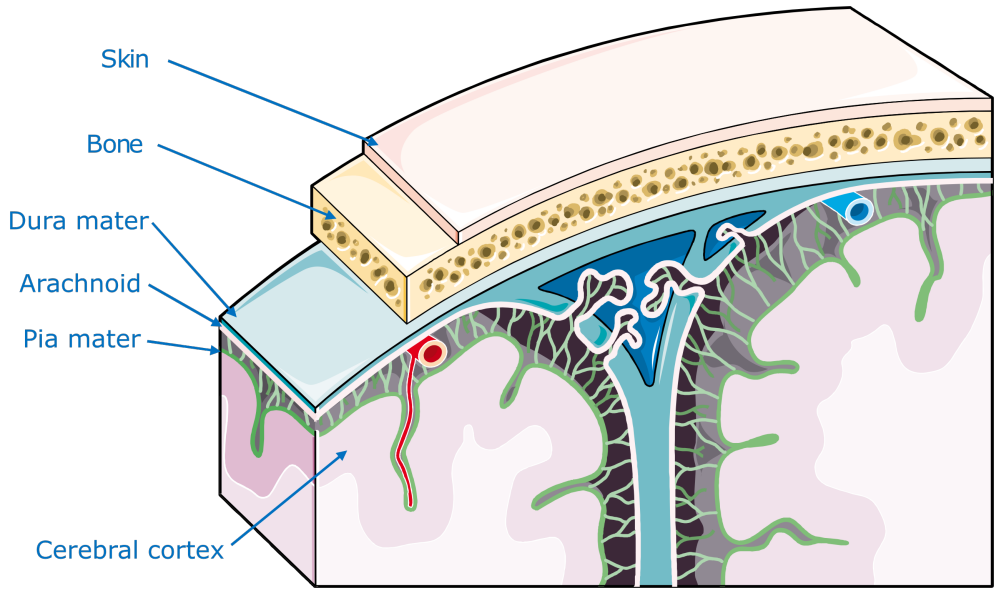


**Figure 1.7.** Isometric projection of skull brain interface. A description of the multiple layers that comprises the human head. Adapted from [121]

Hematomas are further categorized due to anatomical location of the injury: epidural hematoma, subdural hematoma, and intracerebral hematoma. These locations can be seen in figure 1.7, which illustrates the different layers that construct the human head. Epidural hematomas are located between the outer surface of the dura mater and the skull. Subdural hematomas occur between the dura mater and the brain itself. Intracerebral hematomas, as the name describes, are located within the brain tissue itself [78]. Epidural hematomas, due to the proximity to the skull, often result from skull fracture, but can also be present from skull bending. Epidural hematomas are the result of contact loading due to impacts with no inertial loading effects [81]. On the other hand, subdural hematomas are the result of forces induced by inertial loading. The acceleration of the head can lead to the parasagittal bridging veins to rupture due to concentrated shear strains between the brain and dura mater. Intracerebral hematomas can occur for a variety of reasons: trauma, aneurysms, high blood pressure, tumors, etc. Generally, the causes for intracerebral hematomas fall outside the scope of this research and will be left to the reader to explore independently. The formation of a hematoma is extremely dangerous. Not only is there localized blood loss, which can affect the surrounding cells; but the volume of blood can increase the ICP and put compression on the brain.

As stated above, a contusion is damage to tissue without laceration (tearing). This injury can be thought of as a bruise. Contusions are further described as being coup or contrecoup, which means directly underneath the impact site or on the contralateral side from the impact respectively. However, contrecoup contusions can happen anywhere on the brain, but typically they form on the contralateral side of impact. Coup contusions arise principally from the local bending or fracturing of the skull, whereas the predominant mechanism for contrecoup contusions are acceleration forces [81]. When a force is applied to the head, there is differential movement between the skull and the brain causing the brain to lag behind the skull due to inertial effects and the viscoelastic properties of the brain itself. Contrecoup contusions are prevalent if the brain strikes the cranial walls during this motion. Additionally, the brain is not required to impact the cranial walls at all in order for a contrecoup contusions to occur – vascular disruption and cortical damage can occur solely from acceleration effects exceeding local tissue tolerances [81].

Hemorrhages, like hematomas, are injuries involving blood vessels. However, hemorrhages refer to the active continuous bleeding taking place from a damaged blood vessel. Any amount of bleeding within the skull is an intracranial hemorrhage [62]. Active bleeding within the brain can have devastating effects on an individual: headache, seizures, nausea, loss of coordination, loss of consciousness, death, etc. Hemorrhages often involve multiple tissue tears to blood vessels and are a result of head motion caused by inertial loading [81]. Meaney et al. also point out that the acceleration forces coupled with the intricate intracranial geometry are contributing factors to the locations where hemorrhages are often seen. Additionally, the active bleeding of a hemorrhage can cause expansive dysfunction throughout the brain comparable to diffuse brain injury.

The presence of hematomas or hemorrhages are extremely dangerous and requires the immediate consideration of surgical intervention. Not only is there localized blood loss, which can affect the surrounding cells, but the volume of blood can increase the ICP and directly compressing the brain. Contusions that require medical observations are also of concern due to their potential of worsening. Contusions can evolve over the period of several days where initial small lesions can coalesce to form hematomas [5].

### 1.4.3 Diffuse Injury

As the name implies, diffuse injuries are not located in any specific region of the brain but rather cause wide-spread dysfunction due to effects seen throughout multiple regions of the brain. The dispersion of the diffuse injury is often hard to detect due to the microscopic nature of the injury, thus making it hard to define. Diffuse injury can be both the primary injury, a sudden or profound injury to the brain, or a secondary injury; changes that evolve over a period of hours to days following a primary injury [60]. The two prevalent forms of diffuse brain injury are cerebral concussion and diffuse axonal injury.

Concussions are widely known as, "traumatically induced transient disturbance of brain function" [37]. Concussions are a spectrum disorder that range from mild to severe, where the severity of a concussion is based on the Glasgow Comma Scale (GCS). The overall severity of injury is based on the mechanical loading involved with the injury. Both contact and inertial loading can lead to a concussion [37]. The severity of a concussion is often directly linked to the magnitude of forces present during the loading conditions. The neurological dysfunction associated with concussions is nearly always reversible – the strains present during injury are insufficient to cause structural damage but rather only a functional disturbances [81]. Additionally, secondary neurochemical disruptions can lead to further neurological dysfunction [37].

Diffuse axonal injury (DAI) primarily affects the white matter tracks (myelinated axons) in the brain [88]. DAI is the result of inertial loading – where the forces associated with acceleration exceeding the shear tolerance of the white matter tracts [81, 88]. These alternations to the white matter tracts directly affects brain connectivity due to their role in signal transmission. This reduction in connectivity can lead to wide-spread brain dysfunction.

Diffuse injuries are difficult to treat due to the qualitative nature of the prognosis. The diagnosis of diffuse injuries is based of clinical expertise and the relevant symptoms a patient may or may not be experiencing: emotional function (irritability or mood changes), cognitive function (confusion, amnesia, etc.), physical symptoms (headache, dizziness, loss of balance), and sleep (drowsiness) [37]. There is no laboratory test currently available to diagnose DAI, and a definitive diagnosis of

DAI can only be made in the postmortem pathological examination of brain tissue [88]. Physical examinations of the patient along with medical imaging techniques coupled with knowledge of the injury event can aid in prognosis of diffuse injuries; but again, the diagnosis of diffuse injuries are clinical in nature rather than being medically diagnosed by a laboratory test.

## 1.5 Blast Waves

As first discussed in §1.3.3 blast over pressure (BOP) is the third biomechanical loading mode involved in TBI. The prevalence of this injury mode has skyrocketed due to the expansive use of improvised explosive devices (IEDs) throughout conflicts around the world. The recent surge of BOP cases has created an unique classification known as, blast-induced traumatic brain injury (bTBI). Paramount to the understanding of this specific injury is understanding the source of the loading itself, blast waves.

Blast waves are a specific classification of shock waves – where shock waves are defined as, a sudden dissipation of energy resulting in a propagating disturbance moving faster than the local speed of sound [95]. Blast waves are the result of explosively driven detonations, whereas shock waves are a general term used when describing waves moving faster than the local speed of sound. This nuance between blast waves and shock waves, while technical in nature is important to note due to misrepresentation evident in the current literature. More on this specific classification will be discussed further in §2.4.

The physics of a blast wave are complex; they are compressible, time-variant, and multiphasic [38]. Additionally, the physics is further complicated depending on the environment in which a blast originates. Detonations in real-world environments are classified as either an open-field blast (otherwise referred to as, free-field blast) or confined blasts. Detonations within confined spaces (e.g., industrial facilities, naval vessels, buildings, etc.) fall outside of the scope of this research. Interested readers are welcome to explore this matter independently [117]. The open-field blast follows the characteristics of a Friedlander waveform, which is demonstrated in figure 1.8. A Friedlander waveform has four key components: peak pressure, positive phase, negative phase,

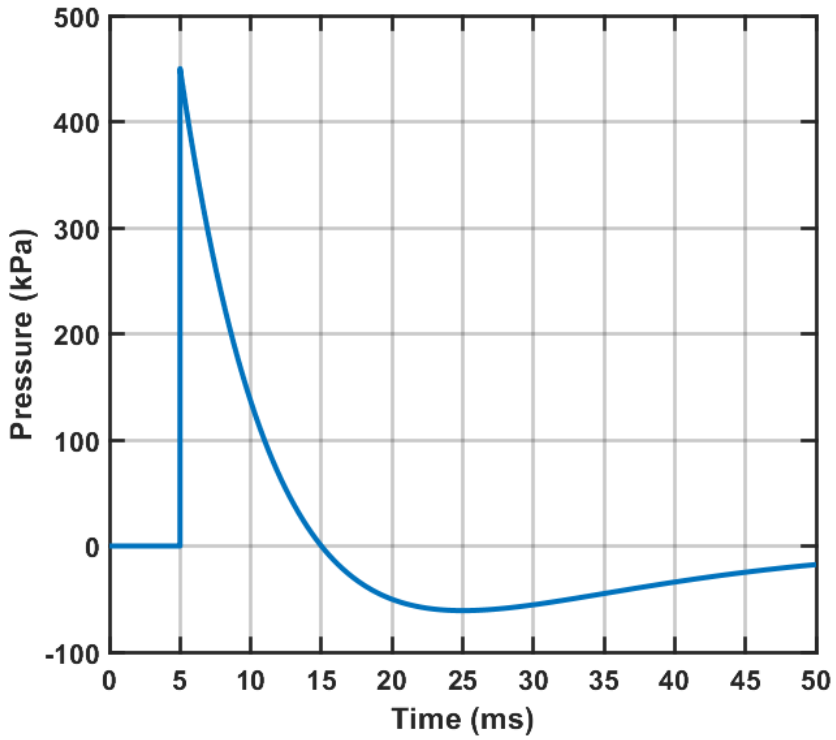


**Figure 1.8.** A representation of a Friedlander waveform: Peak Pressure 450 kPa, Positive Phase Duration 10 ms. Adapted from [130].

and impulse duration. The blast wave is characterized by a discontinuous rise at the shock front followed by an immediate exponential decay to a negative phase [95]. The positive phase of a blast wave is defined as the time between shock arrival (i.e., initial pressure jump) and the beginning of the negative phase – this is also referred to at the overpressure duration. The negative phase may asymptotically approach ambient pressure illustrated by figure 1.8. However, more commonly is a complex oscillatory behavior due to environmental interactions [95]. A blast wave weakens as it propagates outward from the detonation source and takes on the characteristics of a sound wave. Therefore, appropriate distance from the detonation source is the only sure protection against the potential damage from explosions [68]. Peak pressure is the maximum static pressure above ambient conditions. Impulse duration is also known as overpressure impulse and is calculated by integrating the overpressure as a function of time for blast physics. The impulse duration can often be associated with only the initial positive phase, because of how quickly ambient pressure

conditions are reestablished. However, such a practice should be explicitly stated to avoid confusion and improper reporting within a procedure.

There are several terms for pressure frequently used to describe blast waves: static, dynamic, stagnation, and reflected. Understanding the difference between each of these terms is important to reduce the potential confusion when comparing results from different experimental methods [129]. Static pressure is measured perpendicular to the flow direction and is defined as the pressure due to the thermodynamic state; for a free-field blast this is characterized by the equation-of-state for an ideal gas [68, 129]. Dynamic pressure is the specific kinetic energy of the fluid flow. Dynamic pressure cannot be measure, rather it is calculated from knowing the static and stagnation pressures. Stagnation pressure is also known as the total pressure, which is the combination of the static and dynamic pressure. These first three pressure terms are extensively used throughout classical fluid dynamics and any introductory text book will provide more information to an interested reader. Reflective pressure is the last descriptive term broadly used when describing the strength of a blast wave. It is defined as the peak pressure experienced at a non-responding surface exposed to the shock front [129]. Important to note, that reflective pressure is usually referred to a surface that is normal to the blast wave. However, an obstructive object does not have to be perfectly normal to a blast wave for the reflective pressure to be of importance. In saying this the research discussed herein focuses on far-field blasts, thus reflective pressure will be associated with the normal direction. Some researchers regard the peak reflective pressure to be the best parameter to define the loading conditions of a blast wave. This notion is simplistic and allows for quick comparison between different experimental studies, but it does not depict the entire physical phenomena present during blast loading. The overall loading by a blast wave is a function of the static, dynamic, and reflective pressures as well as the structure's geometry.

The geometry of an object plays a significant role in the interaction with a blast wave. As a blast wave propagates it will reflect off of, diffract around, or transmit a portion of its energy to the interacting object itself. Depending on the object's size and material properties any combination of these three actions will be present. The interaction between an object and a blast wave will vary

dramatically in both the spatial and temporal domain, which create areas of high and low pressures on the surface of the object. These pressure gradients can impart stress waves to develop within the object. The material properties of the object are critical to the development and the subsequent propagation of any stress waves generated. Further discussion on the generation and transmission of stress waves will covered in §2.1.2. The study of shock wave interaction is an entire field of its own and an in-depth analysis will not be covered within this text. Readers are advised to investigate [68] (chapter 5) and [95] (Chapter 13) for detailed discussions into shock wave interaction. Though to conclude, shock wave interactions are a dependent on the object's geometry and material properties, with the specific geometry having a profound affect on the overall blast loading. Therefore, in order to have an accurate description of the loading present during blast wave interaction not only does corresponding pressures (static, dynamic, and reflected) need to be reported, but also the relevant object's geometry needs to be described.

# CHAPTER 2

# CURRENT LITERATURE, LIMITATIONS, & WHAT-WE-KNOW

This chapter discusses and summarizes the current state of relevant peer-reviewed literature. The purpose is to address each facet of the multidisciplinary approaches that are currently being conducted in order to study phenomena of blast-induced traumatic brain injury. The importance of each section shall be addressed therein, but the global understanding of the phenomena is accumulated from the findings of individual research areas. The reader is not required to fully understand the intricacies of each of the following sections; however, anyone contemplating further commitment to this of study should take the time to develop comprehensive knowledge of all the applicable research areas. By understanding the intertwining of research areas, one will not only improve his/her own research but also be able to objectively evaluate the research being performed and published by others.

The order in which the following sections appear do not correspond to any particular hierarchy of importance, but rather, were ordered in a manner that conveniently propagates the foundation of knowledge. Each section intends to build on the information presented in the previous sections. The research areas discussed in each section are all individually critical, but it will be by furthering the knowledge from each and every one of these research areas that a more complete understanding of the phenomena will ensue.

## 2.1 Blast-induced Traumatic Brain Injury

Blast-induced traumatic brain injury (bTBI) has four distinct injury categories: primary, secondary, tertiary, and quaternary. Figure 2.1 illustrates each of these categories. Primary blast injury is classified as an injury that is the direct effect of blast wave propagating through tissue. Secondary blast injury refer to injuries sustained after being struck by an object; these objects can be blunt (e.g., rocks, surrounding debris, etc.) or penetrating (e.g., shrapnel). Tertiary injuries result from an individual being displaced by the force of the blast wind. An individual that is set into motion by a blast wave can sustain injuries resulting from the inertial (i.e., acceleration) loading mode

detailed in §1.3.2. Furthermore, the deceleration of an individual involved in a tertiary event often includes contact with rigid structures (e.g., cars, walls, trees, the ground, etc.), which can result in additional contact loading. Finally, quaternary injuries are comprised of all other potential injuries an individual may receive; these include burns (thermal and chemical), toxic gas inhalation, and asphyxia.

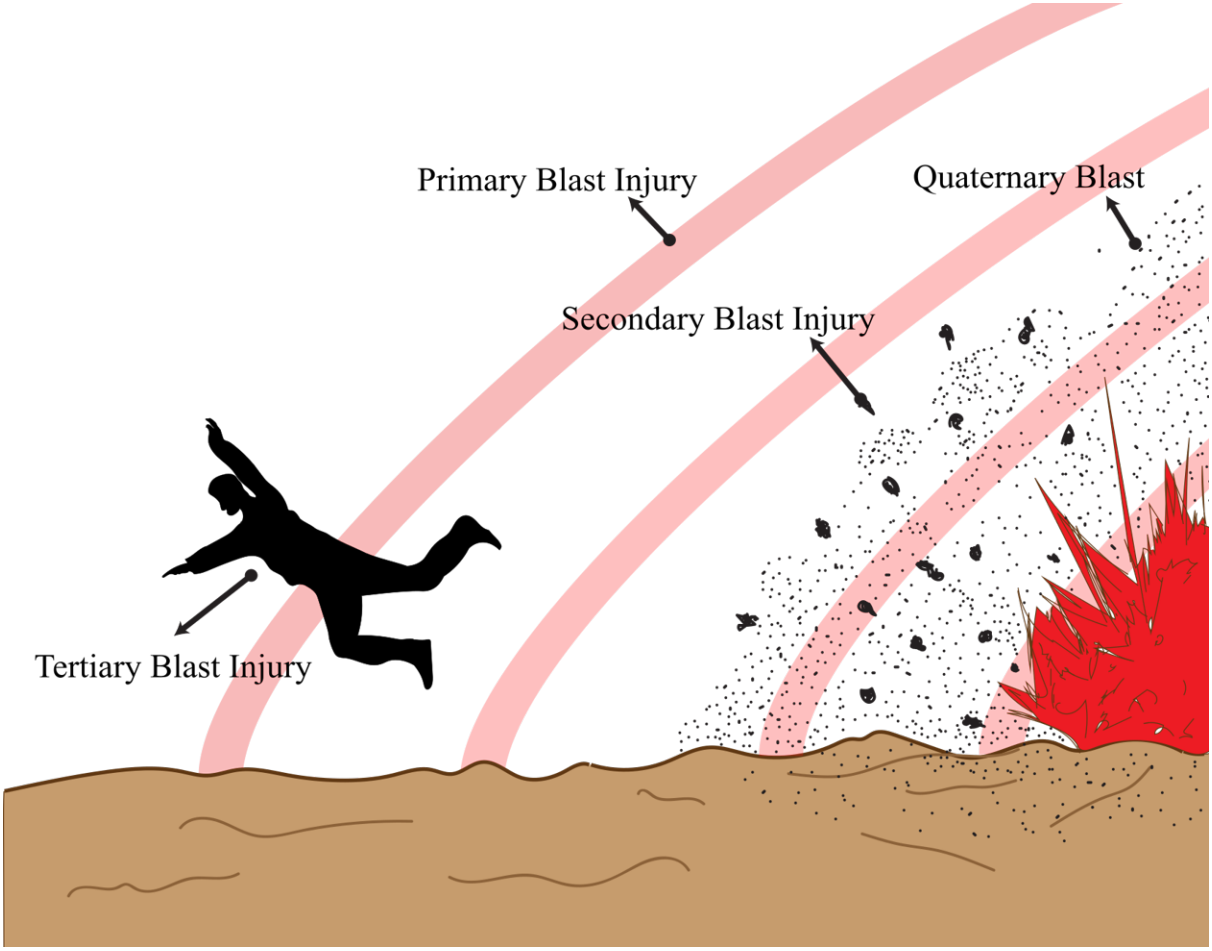


**Figure 2.1.** Visual representation of the bTBI injury categories. Primary injury: caused by the blast wave itself. Secondary injury: caused by impacting objects. Tertiary injury: caused by individual being set into motion. Quaternary injuries: are composed of all the other types of potential injuries [143].

Secondary and tertiary injuries involve the fundamental biomechanical loading modes, contact and inertial, which were detailed in §1.3.1 and §1.3.2, respectively. These injuries have been studied extensively as they parallel the injuries seen in civilian TBI. Quaternary injuries are also well understood clinically due to their prevalence in everyday life. Primary injuries are the least

understood of the four classification types. This stems from the injury mechanisms associated with primary bTBI being actively debated within the literature. The lack of consensus is not without merit though – each mechanism has both supporting and opposing evidence. The importance of understanding the basis of these mechanisms is paramount to understanding primary bTBI itself. The remaining portion of this section will be devoted to each of the debated mechanisms. Additionally, secondary mechanisms will also be briefly discussed.

### 2.1.1 Direct Cranial Transmission

The first potential damage causing mechanism to be discussed is the direct cranial transmission (DCT) theory. The premise of DCT is that the pressure transient is directly transmitted into the intracranial contents through the skull after exposure to a blast wave [38]. The resulting damage is subsequently caused by the pressure change interacting with the brain itself. The defining principle of the DCT mechanism follows the one-dimensional (1D) theory of acoustical impedance, where acoustical impedance is defined as the product of a materials density and the speed of sound within the said material [38, 94, 126]. Following the 1D theory of acoustical impedance, as a blast waves reaches the interfacial boundary of two materials a portion of the energy is reflected and another portion of the energy is transmitted. Additionally, energy from the propagating wave can be dissipated (i.e., absorbed) at the material interface itself [30]. The degree to which a wave is transmitted or reflected is governed by the impedance mismatch between the specific materials at the interface [38]. The governing equations for the 1D acoustic theory are as follows:

$$\Gamma_r = \frac{Z_2 - Z_1}{Z_2 + Z_1} \tag{2.1}$$

$$\Gamma_t = \frac{2Z_2}{Z_2 + Z_1} \tag{2.2}$$

where $\Gamma_r$ and $\Gamma_t$ are the reflective and transmission coefficients, $Z$ is the material impedance, and the subscript of 1 and 2 correspond to the material where the wave is originating from and the material the wave is transmitting to, respectively [38, 126]. As expected, perfect impedance matching

($Z_1 = Z_2$) would have no reflection wave present and only a transmission wave that perfectly matches the incident wave [130]. Now, depending on the order of impedance between the two materials (i.e., $Z_1 > Z_2$ or $Z_2 > Z_1$) will determine the compressive or tensile nature of the reflected wave.

Fundamental support of the DCT mechanism derives from the expansive use of ultrasound imaging. The effect of acoustic wave propagation is the basis for this medical imaging technique, where the noticeable impedance mismatch is exploited at the different tissue types of the body to create an image (sonogram). An additional compelling aspect in support of the DCT mechanism relies on the basic structure of the human head. The human head is comprised of a layer architecture: skin (scalp), skull, dura mater, arachnoid membrane, subarachnoid space, pia mater, and the brain [126]. Each layer has a different thickness and acoustical impedance. This layered architecture would generate a complex response upon interaction with a blast wave, specifically at the *sandwiched* layers within the head. Furthermore, if any energy dissipation at a material interface exceeded the local material tolerance of the tissue, then there is a potential to damage the tissue. Now, Fievisohn et al. point out that the impedance mismatch of the different layers comprising the head would reflect over 99% of a planar wave. This is directly contradictory to the 1D theory behind the DCT mechanism. However, it is important to note, that shock waves are non-linear, non-continuous, infinite amplitude pressure wave pulses that do not perfectly follow the theoretical behavior of linear acoustic waves [94]. This is to be expected, as a 1D theory inherently under represents the complexity of a 3D phenomena.

Now in contrast to the 1D theory, the experimental results reported within the literature often provide contradictory evidence to the DCT mechanism [38]. Some provide supporting evidence, while others report opposing evidence. However, published experimental results need to be carefully reviewed before accepting the reported findings. There are conflicting experimental reports about how the intracranial pressure (ICP) of animals responds to different blast loading scenarios. Fievisohn et al. discusses these discrepancies within the literature and it is recommended that any curious reader to further explore this reference in greater detail. One of the reasons for the inconsistency within experimental results may be the considerable complexity associated with blast related studies. Blast

injury experiments require careful planning, execution, and analysis in order for acceptable results to be obtained. Additionally, blast studies are expensive and require extensive safety precautions in order to operate correctly. These limitations will be discussed further in §2.4.

The DCT mechanism seems intuitive when considering wave propagation from a 1D perspective. However, the abundance of contradictory experimental results leads to the continuous debate of DCT as a potential damage causing mechanism for primary bTBI. A leading cause for this discrepancy, which elicits the need more specialized research, is the experimental challenge of ICP measurements. Additionally, isolation of DCT as an individual mechanism is difficult as both *skull flexure* and *skull orifices* share a similar damage causing origin.

### 2.1.2 Skull Flexure

The proposed skull flexure (SF) mechanism is directly contradictory to that of the DCT mechanism. The SF mechanism theory states that a force is applied by the blast wave, which directly imparts loading to the skull that leads to local deformation [38]. The basis of SF is due to the impedance mismatch between air and skull, which have a difference of four orders of magnitude. The energy resulting from the reflection of the blast wave on the surface of the skull leads to two different yet connected outcomes: traveling shear waves within the skull and the aforementioned local loading. The deformations of the skull are dynamic in nature, due to the distributive loading caused by the temporal interaction (propagation) of the blast wave, which creates localized regions of high and low pressure and large pressure gradients that sweep through the brain [91]. Additionally, the traveling shear waves also contribute to the high and low pressure regions leading the pressure gradients. The significance of the pressure gradients resides in the viscoelastic and nearly incompressible nature of the intracranial contents (e.g., brain tissue and CSF). The high bulk modulus of brain tissue and CSF ($\sim 2GPa$ [42]) result in extremely high pressure changes in response to relatively small volume changes [130].

The SF mechanism theory is supported by both experimental and computational studies. Bolander et al. demonstrated in a rat model that a shock wave was directly responsible for compressing the

skull's surface. Additionally, Bolander et al. showed that the magnitude of compression on the skull was linearly proportional to that of the incident shock wave. Moss et al. created a 3D model of the head / CSF / brain and demonstrated that skull flexures were present in a variety of different loading configurations and material properties. The agreement of computational and experimental investigations provides strong support for the SF mechanism. However, there are aspects from clinical data that do not fully support skull flexure as a stand alone mechanism. This leads to the opinion that mechanisms are coupled, which leads to the overall damage pathology seen clinically. There is an overall lack in the understanding how mechanisms are coupled to one another. This stems from the general unknown conditions involved in any specific blast loading scenario (e.g., proximity to explosion, magnitude of blast wave, orientation to blast wave, environmental features resulting in reflection etc.). More biomechanical testing investigating skull strain and ICP oscillations with respect to the blast wave metrics will help decipher this mechanism [38].

### 2.1.3 Skull Orifices

The next primary bTBI mechanisms to be discussed is the skull orifice (SO) theory. The SO mechanism theorizes that the potential damage is the result of ICP changes resulting from the blast wave traveling through air-filled cavities of the head [38]. The specific air-filled cavities of primary importance are the nasal cavity, auditory canal, and orbits. Additionally, the oral cavity and the sphenoid and frontal sinus can play a role in the SO mechanism. However, the significance of the oral cavity and sinuses (sphenoid / frontal) are difficult to quantify since they can be isolated (e.g., mouth entirely closed) from surrounding air during the propagation of a blast wave.

The majority of the supporting evidence for the SO mechanism stems from clinical injury data. In particular, clinical studies of blast injury on the auditory system have reported that approximately 60% of the patients evaluated had any type of hearing loss in addition to the tympanic membrane rupturing in about 32% of patients who were evaluated [27]. In spite of the general knowledge and prevalence of auditory injuries associated with blast waves there is little direct evidence that supports the claim that the auditory canal alters ICP [38]. It is important to note that the orientation

of the ear (facing blast vs. parallel to blast) does play a role in the overall damage seen from auditory canal patients [1]. This directionality factors suggests that the auditory canal is actually not a leading source of ICP changes [38].

The emphasis on the nasal cavity and orbits to the SO mechanism is directly reflected in the importance of how geometry contributes to the loading incurred on an object during interaction with a blast wave. Readers are recommended to review §1.5 to clarify the significance of an object's geometry. There is additional clinical evidence of a high prevalence of TBI that is coupled with combat ocular trauma [133] expressing a potential association between the two injuries. Now, there is also conflicting data among the literature; opposing evidence was demonstrated by how the use of eye protection has little effect on ICP after exposure to a blast [70]. On the other hand, Williams et al. illustrated how the quality of the eye protection (amount of ocular sealing present) used, in fact, does reduce the overall pressure exerted on the eye. A significant issue involving the coupling of SO injuries with TBI is that a TBI can lead to secondary injuries within the auditory / visual systems [38]. Thus, determining which was the primary and which was the secondary injury can be impossible without full knowledge of the history of the injurious event.

Much like the DCT and SF mechanisms the skull orifice theory needs additional experimental investigations to help clarify its role as a mechanism in primary bTBI. These future investigations need to take special consideration of the anatomy of the head as well as orientation with respect to the blast wave.

### 2.1.4 Thoracic Surge

The thoracic surge mechanism is unique compared to the other three mechanisms as it is the only one suggested to cause damage to the brain tissue without the blast wave directly interacting with the head. The premise of this mechanism is that exposure of the thorax and abdomen to a blast wave leads to rapid compression and creation of a shock wave that propagates through soft tissue and vasculature. The compression of great vessels is believed to lead to volumetric vascular surge that reaches the brain and injuries the more susceptible cerebrovasculature [38]. Additionally, Fievisohn

et al. indicate that the volumetric surge created by the increased thoracic pressure inhibits cerebral blood outflow, which ultimately leads to increased ICP and subsequent neuropathology.

The thoracic mechanism was not studied as part of the research discussed herein and therefore will not be discussed in great detail. The specific reasons for not exploring the thoracic mechanism will be discussed further in chapter 7. However, the importance of this mechanism, primarily due to prevalence and severity of thoraco-abdominal injuries caused by specific interaction of blast waves with the thorax should not be overlooked [38]. Additionally, there is a substantial amount of published literature with supporting evidence for this mechanism. Several review articles and the references cited within detail the relevant contributing attributes of the thoracic surge mechanism [25, 29, 38]. Though, for the sake of foundation, the highlights of these review articles will be briefly discussed.

The majority of supporting evidence for the thoracic mechanism was experimentally gathered using ballistic impacts rather than blast exposure. There have been though, a number of animal studies performed to investigate how the resulting blast effects change when chest protection is incorporated. Courtney and Courtney (2008) discuss how the expansive use of armor protected vests have reduced mortality rates in conflict theaters. However, the use of such vests do not eliminate all potential risks – non-penetrating impact can still lead to behind armor injuries of both local and remote tissues. Chen and Huang point out how blood flow in the carotid artery and aorta can be drastically increased by a lower extremity ballistic wound. Additionally, Chen and Huang discuss how the pressure waves are oscillatory in nature, which could create multiple blood flow disturbances in a short period of time. Fievisohn et al. take a more fundamental anatomical approach – detailing the physiological property of autoregulation in the cerebrovasculature. Vascular pathology can compromise the autoregulation process, which could lead to prolonged vascular contraction. Vascular contraction directly increases the resistance of flow within the vessel ultimately leading to increased ICP. All three articles discuss how interaction with the thorax can lead to changes in the ICP.

The thoracic mechanism is hard to quantify due to the difficulty of isolating it from the other

mechanisms during blast loading events. Additionally, secondary effects (e.g., ICP changes) are common among all of the mechanisms. Thus, determining the specific mechanism initiating the ICP changes is impossible without first isolating the mechanisms from one another. Further experimental investigations are needed to be performed in order to better quantify the thoracic mechanism.

### 2.1.5 Secondary Mechanisms

All four of the proposed mechanisms (direct cranial transmission, skull flexure, skull orifices, and thoracic surge) differ in how they interact with the body / head; but they share a similarity in regards to their effect on the head, specifically alternating the ICP. There are two additional mechanisms that are often discussed within the literature that are also relevant to this research: acceleration and cavitation.

The reason these two mechanism were not discussed earlier is because they are not stand-alone mechanisms, rather they are the result of one of the previously discussed mechanisms. Additionally, the acceleration mechanism falls outside of the guidelines for a primary injury; by definition it would be classified as a tertiary mechanism. The effects of acceleration were previously discussed in detail in §1.3.2 and should be referenced therein.

Cavitation is a phenomenon observed in liquid environments when the hydrostatic pressure falls below a critically low threshold resulting in the nucleation and expansion of vapor bubbles. The phenomenon has been investigated for over a century [113] and is found in dynamic fluid flows [15] or impulsive loading upon fluid filled containers [47] when local pressures fall near vapor pressure (for water / CSF this is below -100 kPa at STP) [50]. Cavitation can lead to damage from several unique mechanisms. For example, following bubble nucleation and expansion, these bubbles can collapse and produce very high pressures and temperatures which could effect adjacent structures [15]. Furthermore, if a bubble collapses occurs near a surface, a high speed microjet is formed and directed towards the surface [11, 142], leading to surface damage. It has been shown that microjetting can cause significant damage to propellers and other machinery [6, 65, 102] and thus if occurring during head trauma, could be a hypothesized mechanisms by which cavitation causes

brain damage. More specifically, if cavitation were to occur near a soft material such as human biological tissue, the production of high local strain from material displacement to accommodate an adjacent bubble expansion may be also lead tissue damage [51].

Cavitation as a mechanism intuitively explained the contrecoup injury found in the frontotemporal regions following occipital impacts [2, 47]. However, cavitation remains controversial as an injury mechanism in bTBI. The controversy of fluid cavitation relating to TBI extends from the lack of direct evidence present for cavitation within intracranial contents. To note, there is supporting evidence for cavitation as a mechanism of injury in blast related TBI being demonstrated by computational analysis [41, 94, 101, 132]. Although, the onset of cavitation has been predicted by computer models, the interaction of cavitation bubbles with brain tissues still remains unresolved (computationally) as does the expected and the anatomic distribution of cavitation bubbles. Thus, a clear association of cavitation with specific human neuropathology is still lacking.

Cavitation is an interesting phenomena and will be discussed again in §6. However, as stated previously, cavitation is the result of ICP changes that were initiated by one of the other mechanisms discussed (direct cranial transmission, skull flexure, skull orifices, and thoracic surge). This is an important aspect for the reader to retain in the coming sections / chapters.

## 2.2 Understanding Brain Tissue Properties

The mechanical properties of brain tissue are paramount to the understanding of TBI research. The injuries previously detailed in §1.4 share the common root of injury, specifically strain tolerances within a tissue. Strain is considered the proximal cause of tissue damage [81] and is simply defined as a change in an objects length compared to its original length

$$Strain = \varepsilon = \frac{\Delta L}{L} = \frac{Change\ in\ Length}{Original\ Length}$$

where the Greek letter $\varepsilon$ is the standard abbreviation denoting strain. Strain is classified into three categories depending on the applied force: compression, tension, and shear. Compression corresponds to reduction in length, tension corresponds to an elongation, and shear strain corresponds to a change in length parallel to the applied force. Further details on these categories can be explored through any introductory mechanics textbook and are now left to the reader [10].

Knowing these three mechanical properties of brain tissue can illuminate the behavioral response that brain tissue will undergo as a result of a loading event. To this end, numerous researchers have embarked to investigate the mechanical properties of brain tissue. The previously published literature as well the current literature have demonstrated the unique nature and properties of brain tissue. The ever increasing knowledge of brain tissue properties is improving computational models that will be discussed below in §2.3, improving the ability for predicting injury sites, and understanding of the plethora of secondary sequela present during TBI. This section details the general approaches used by researchers, the importance of protocol parameters, the conflicting results present in the literature, and the general consensus regarding brain tissue as a whole. The subsequent discussion is intended as an overview rather than a comprehensive review. The references cited herein give further details into testing procedures used by specific researchers. Furthermore, several review articles will be noted, which provide a great deal of information over various aspects of this section.

### 2.2.1 Mechanical Testing Apparatus

Brain tissue has been well established as being very soft, nonlinear, nearly incompressible, viscoelastic, strain-rate sensitive, anisotropic, and regionally independent. Furthermore, biological variations have also been documented in regards to brain tissue: age, sex, post-mortem time, and regional differences within brain tissue itself. In order to investigate such a complex material a variety of methods and protocols have been used over the years. Firstly, there are the classical engineering traction tests for compression, tension, and linear shear [18, 59, 69, 110–112]. These method includes obtaining tissue samples from post-mortem specimens and mechanically loading said samples, while tracking the applied load and specimen deformation. The specific mechanical loading can be applied in a uniaxial manner [59, 110–112], where any of the modes (tension, compression, or shear) can be investigated depending on the direction of the force applied. Mechanical loading can also be applied in a biaxial manner [69] to investigate the anisotropic nature of brain tissue. Interestingly, Budday et al. (2017) utilized a triaxial machine to investigate protocols where multiple loading directions were superimposed onto one another in a consecutive manner.

Another, testing method is micro or nano-indention. The premise of indentation methods relates the stiffness of a material to its elastic modulus through measuring the displacement caused by a known applied force [17, 43, 73, 74, 134, 135]. The direct advantage of indentation approaches is the ability for *in-situ* experimental testing rather than only *ex-vivo* testing [43]. With this being said, the vast majority of the reported literature for indentation protocols are still performed in an *ex-vivo* environment. Indentation methods remain advantageous over traction testing because they reduce the complexity involved in testing tissue samples: shorter handling time, no chemical bonding required (i.e., gluing), larger parameter variability, minimized boundary conditions, and greater repeatability [17].

The next method that has been used to determine the mechanical properties of brain tissue is magnetic resonance elastography (MRE). MRE has been rapidly advancing as an non-invasive in-vivo method for determining material properties of human brain tissue [28, 48, 136]. The principle of MRE is to introduce mechanical shear waves into the body then track the propagation

of said waves using magnetic resonance imaging (MRI) and ultimately determining the mechanical properties of the tissue based off the MRI displacement data [76]. One of MRE greatest advantage over the other testing methods is that it is the only method that allows *in-vivo* testing to be performed. This particular aspect will be discussed further in §2.2.2, but key to interpreting a methods result is understanding the testing procedures of the specific method.

The last two methods utilized to investigate the material properties of brain tissue are dynamic compression and rotational shear. Dynamic compression is performed on a Split-Hopkinson Pressure Bar (SHPB), whereas rotational shear is performed using a rheometer. The SHPB method will be discussed in more detail below in §2.4.1. Rheometers historically have been used to determine the mechanical properties of fluids and slurry's, but with the advancement of digitally control devices in the 1980s [89] their integration quickly began to expand other fields. The working principle of a rheometer is to induce rotation into a specimen on one side and measure the correspond torque and normal force generated. There are three common rotational shear tests performed: oscillatory shear testing, constant strain rate testing, and stress-relaxation tests. Oscillatory testing is performed to investigate the storage and loss moduli and how these moduli change with loading frequency; constant strain rate testing is performed to investigate the stress-strain relationship; and finally, stress-relaxation tests are performed to investigate the relaxation time of a material [26].

The overall number of peer-reviewed published data involving dynamic testing of brain tissue is quite limited (for SHPB: [103, 104, 106, 128], for rotational shear: [12, 26, 40, 52, 53]). In addition to the overall minuscule amount of published data for brain tissue measured using a SHPB, the general usable data are even further reduced; specifically, both Prabhu et al. and Trexler et al. reported procedures that lacked acceptable specimen preparation procedures and thus, said data should be carefully reviewed for comparison, if compared to at all. Discrepancies among published data are not exclusive to the SHPB technique, and rather, present in each of the mechanical testing methods. Further discussion on both the discrepancies between testing methods as well as the inconsistencies within the same testing approach will be detailed in §2.2.2.

### 2.2.2 Mechanical Testing Protocols

The five testing methods introduced in the previous section (traction tests, indentation, magnetic resonance elastography, split-Hopkinson pressure bar, and rotational shear) have brought immense clarity regarding the mechanical properties of brain tissue. Each one of the experimental techniques have been employed to investigate different parameters of a brain tissue's mechanical properties. While there are similarities across the testing methods, each one is unique in its ability to explore specific attributes of brain tissue that the others cannot. To have a better understanding of the unique capabilities of each testing method, one must first understand the limitations present during testing.

The limitations of each testing method depend on the multitude of conditions present during the testing of brain tissue. The upmost care needs to be taken from tissue harvesting all the way to loading parameters used in the experimental testing of biological tissue in order for the obtained results to be reliable, acceptable, and conclusive. Table 2.1 details individual testing conditions as well as their importance to reliable experimental testing. There are two distinct categories depicted in table 2.1, specimen preparation and testing protocol. Both are equally important for their individual reasons.

Proper specimen preparation ensures that the tissue being mechanically loaded is in a condition known to the researcher, which is critical to the understanding of the obtained results and their incorporation into finite element models. The specific testing protocols used in mechanical testing enable researchers to investigate specific mechanical properties (e.g., strain-rate sensitivity, regional differences, anisotropy, etc.), which is directly applicable to the global understanding of brain tissue and the incorporation of material properties into finite element models. It is important to note that the parameters discussed in table 2.1 correspond heavily to *ex-vivo* testing. MRE is an *in-vivo* testing method, thus requires no specimen preparation. The testing method of MRE still requires loading protocols, but the reader is left to the previously mentioned references for clarity of the specific loading protocol.

The specific testing protocols utilized by researchers are comprised of the individual parameters listed in table 2.1. Throughout the published literature there are a variety of testing protocols that

**Table 2.1.** Experimental parameters involved in mechanical testing of biological tissues

| **Specimen Preparation:** | | |
|---|---|---|
| **Parameter** | **Testing Relevance** | **Significance to Results** |
| Post-mortem time | Potential tissue degradation | Obtained results are higher than fresh tissue |
| Sample harvesting | Damage to brain tissue | Obtained results can be erroneous |
| Specimen size | Testing method limitations | Boundary condition effects |
| Specimen hydration | Reducing tissue degradation | Replicates *in-vivo* environment |
| Temperature | Preserving tissue quality | Temperature fluctuations can affect tissue quality |
| **Testing Protocol:** | | |
| **Parameter** | **Testing Relevance** | **Significance to Results** |
| Specimen mounting | Potential damage to specimen | Boundary condition effects |
| Preconditioning | Specific testing procedure | Improved reproducibility, Replicates *in-vivo* environment |
| Loading Rate | Specific testing procedure | Comparability for specific injuries, Comparability to other reported data |
| Loading magnitude | Specific testing procedure | Comparability to other reported data |
| Loading profile | Specific testing procedure | Comparability to other reported data |
| Temperature | Maintaining tissue quality | Replicates *in-vivo* environment |

are currently being used. While there are general similarities among the protocols being used for the same testing method, there are still significant differences present in nearly all comparable results between different research groups. The abundance of different testing protocols is directly reflected in the broad range of mechanical properties being reported for brain tissue. There is a general lack of agreement between different research groups published data on the mechanical properties of brain tissue.

### 2.2.3 Limitations of Reported Brain Tissue Properties

The mechanical properties of brain tissue have been studied for over 50 years [40]; however, there is still no universally accepted data set for the mechanical properties of brain tissue. This lack of exact material properties is one of the largest limitations within the current literature. The broad range of reported values are not only due to both the experimental testing method but also the exact testing protocol used to evaluate brain tissue. These two aspects have been previously discussed in §2.2.1 and §2.2.2, respectively. The disagreement is not solely due to the systematic differences employed by different research groups but also due to biological variations. Throughout the literature numerous animal species have been used to investigate brain tissue properties: pig, cow, sheep, monkey, and of course human. Both the inter-species variations as well as the inter-specimen deviations directly affect the ability to cross compared published results.

The biological variations among inter-species is inherent. Thus, the systematic differences between the testing protocols and experimental methods used across research laboratories will be the principal avenue to reduce the current spectrum of reported mechanical properties for brain tissue. Budday et al. (2019) have written the most comprehensive review of the mechanical behavior of brain tissue to date. The authors not only mention the testing parameters detailed in table 2.1 but discusses the significance of each parameter and how they affect the underlying microstructure. Additionally, Budday et al. (2019) discuss how the multiple testing time-scales affect the collected experimental results. This review encapsulates the complexity of testing brain tissue and should be read by all within this field of study. There are two additional noteworthy review articles that provide insight into the vastness of reported mechanical properties of brain tissue [26, 40]. These three articles will give any curious reader the foundation necessary to grasp the considerable complexity that is the undertaking of determining brain tissue's mechanical properties.

The greatest limitation within the current literature relating to this work involves the specific loading rate (i.e., strain-rate) used during the characterization of brain tissue. Traumatic brain injury (TBI) is classified as a dynamic event (less than 50 ms) and blast-induced TBI is an even faster event (sub-millisecond loading duration). Nearly all of the reported mechanical properties (with several

exceptions [74, 103, 104]) were tested under quasi-static loading conditions (0.01 to $1s^{-1}$), which are order of magnitudes slower than the loading rate associated with dynamic events (10 to $100s^{-1}$ for TBI and $1000s^{-1}$ for bTBI). The use of quasi-static results for dynamic loading conditions should be avoided, if at all possible. This is especially important for brain tissue mechanical properties. One of the only universal observations present across studies, laboratories, and testing methods is that brain tissue's mechanical properties are dependent on strain-rate – specifically, brain tissue stiffens with increasing strain-rate. Therefore, the use of any individually reported mechanical property is coupled to the loading regime used to obtain said results. These results should then only be used to simulate phenomena that exist at similar loading rates. While this practice may seem intuitive, it is not generally followed. The aspect of applying mechanical properties will be discussed further below in §2.3.

In conclusion, the limitations within the current literature are heavily application specific. The mechanical properties of the brain are not isolated just to TBI. Rather TBI comprises only a small percentage of the total research areas being investigated involving the brain (e.g., progression of neurodegenerative diseases, neonatal brain development, and pre-surgical planning, etc.). Each one of these categories is further investigated in [19]. By understanding the relevant length and time scales of a phenomena the applicable material properties of brain tissue can be applied. The reported mechanical properties of brain tissue up until 2008 have been consolidated in a review [26]. Cheng et al. provides these summaries in both detailed tabulated and graphical forms. A researcher is responsibility to be well familiarized with the physical parameters involved with a specific phenomena and be able to apply the appropriate conditions necessary to properly investigate it further. The mechanical properties of brain tissue will be addressed again in §3.3.

## 2.3 Finite Element Models

The finite element method (FEM) has become a fundamental approach to investigate engineering related problems. There have been expansive uses of finite element (FE) models to study biological phenomena and TBI is no exception. This approach is inexpensive, highly adaptable, and can be easily integrated within many different research settings. Readers should familiarize themselves with FEM if they have not already done so [57]. The direct integration of an FE model was not the intention of this research. However, understanding the fundamentals of FEM is crucial to modern day research for several reasons. Firstly, the number of applications and published literature relating to FEM is countless – FE models are present in every facet of engineering research. A tremendous amount of knowledge of a phenomena can be gleaned through reading the current FEM literature on a specific topic. Secondly, FE models require experimental validation in order to prove that the specific FE model is achieving desirable results. This aspect is important to consider during the developmental stages of an experiment; being able to replicate the boundary conditions associated with an experiment directly into an FE model reduces the error propagation present during FE calculations. Third, FE models allow for considerably more complex analysis to be performed. As long as a FE model has been properly validated, the integration of complex geometries or complex physical phenomena is only limited by the available computational power. Lastly, constructing an experiment with FEM in mind offers substantial insight into the desired question/s being investigated. An experienced experimentalist will account for as many aspects and potential irregularities as possible before conducting an experiment. Through scrupulous critique any experiment and/or FE model will increase the likelihood of providing accurate results.

### 2.3.1 Limitations of FE Models

Similarly to the reported brain tissue mechanical properties of the previous section the vast majority of the limitations within the published literature regarding FE models is application specific. However, the most common limitation present throughout FE models is the degree of simplification

incorporated during the generation process. Simplifications are a common practice and are made in some aspects of the material modeling in order to cope with computational constraints [75]. Simplifications are also integrated to reduce the complexity of the overall model depending on the application of interest being investigated. In order to understand the simplifications often applied to FE models, one must first understand the underlying frame work used in the modeling itself. There are several noteworthy review articles that provide the necessary foundation for FE modeling of brain tissue and TBI [33, 75].

Another major limiting aspect of FE models is the requirement for every model to be validated against experimental data in order to ascertain its usefulness and its potential for accurate predictions. In comparing FE results to the experimental data it is imperative that the proper boundary conditions are applied. Voyiadjis and Samadi-Dooki demonstrated that neglecting to account for the no-slip boundary effect for compression and tension can lead to errors up to 1500%. Other significant boundary conditions commonly present are the skull-brain interface or the elastic versus inelastic behavior of different loading conditions. In addition to the boundary conditions, the proper constitutive relations need to be applied correctly for the modeling. There are multitudes of aspects relevant for brain tissue modeling but are heavily application specific: time-dependent versus independent, multiphase versus monophase, linear elastic, hyperelastic, viscoelastic, isotropic versus anisotropic, compressible versus incompressible, etc. de Rooij and Kuhl (and the references they cite) go into great discussion about the appropriate applications of commonly used constitutive models. Budday et al. (2019) further expands on the specific application considerations that researchers should be accounting for during numerical analysis.

The last limitation I would like to discuss is the incorporation of material properties. As detailed in the previous section §2.2 the reported material properties of brain tissue depend heavily on the loading rate. Pervin and Chen (2011) show that brain tissue's compressive modulus for 30% strain ranged from 1 to 100 kPa for 0.01 and $2000s^{-1}$, respectively. The range of values reported within the literature leads to potentially incorporating inappropriate material properties within a specific FE model. Therefore, it is crucial to only be incorporating material properties within a

FE model that are valid for specific time-scale of interest (i.e., material properties gathered under quasi-static loading for the investigation of hydrocephalus, or investigating rotational effects of the brain using mechanical properties gathering from dynamic oscillatory rheometry tests). The practice of using only relevant material properties is not universally implemented across different research laboratories. Until recently, the importance of the loading rate associated with the phenomena of interest was underscored by the magnitude of the shear modulus. Budday et al. (2019) details the relevance of the contradictory results found in the literature and the importance of proper incorporation of material properties within FE models.

The limitations discussed in this section (simplification, appropriate constitutive incorporation, and accurate material properties) are general in nature and are not by any means the only aspects that can affect the results of a FE model. A comprehensive knowledge of the finite element method is truly needed to understand all the intricacies of the relevant limiting factors associated with FE modeling and their respective results. However, a mastery understanding of FE modeling is not necessary to draw meaningful insights from the literature. The vast majority of researchers detail the basic aspects of their respective FE models to aid in the dissemination of information. Before diving deep within the FEM literature it is crucial to keep in mind that appropriate mechanical modeling should be as complex as necessary but as simple as possible for the reader to understand [19].

## 2.4 Experimental Techniques for bTBI

In order to study blast-induced traumatic brain injury (bTBI) and its associated effects on the human body researchers need to be able to replicate the real-world scenario in which the original event transpired. Thus, researchers need to replicate the pressure profile associated with blast waves. Specifics on blast waves (the general pressure profile, overall behavior, commonly used descriptive terms, significant contributing factors, etc.) were previously discussed in §1.5. There are three common experimental techniques employed by researchers to replicate the pressure profiles of a blast wave: shock-tubes [23, 63, 70, 100, 123, 129], blast-tubes [3, 7, 32], and the Split-Hopkinson Pressure Bar [20, 103, 104, 119]. Additionally, researchers have investigated bTBI by performing open-field tests.

Each one of these techniques will be further discussed in detail below. An important aspect to keep in mind when comparing these techniques to one another, is the application of interest. This reoccurring theme of application specific significance, first mentioned in §2.2, is an inherent characteristic of bTBI. The individual testing apparatus chosen to investigate bTBI is no exception to this specific application restriction; thus, while one experimental technique may be ideal for one application, its general use may not be adaptable for another application.

### 2.4.1 Split-Hopkinson Pressure Bar

The Split-Hopkinson pressure bar (SHPB), also known as the Kolsky bar, is one of the most versatile methods for determining the dynamic mechanical properties at high strain rates in the range of $1 \times 10^2 \rightarrow 1 \times 10^5 \frac{1}{s}$ [124]. The SHPB does not replicate blast waves, rather it investigates the propagation of stress waves through a specific material at loading rates similar to that seen with blast waves. This technique has been extensively used and is well documented within the literature. The working principle is to sandwich a specimen between two cylindrical bars of known properties, which is illustrated in figure 2.2. A longitudinal stress wave is initiated when a striker hits the *incident* bar. The wave propagates towards the specimen; due to impedance mismatches a portion of

the propagating wave is transferred to the specimen itself and part of the wave is reflect back into the incident bar, the propagation of the stress wave continues from the specimen to the *transmission* bar. By measuring the wave propagation in both the incident bar and the transmission bar the material properties of the specimen can be calculated.

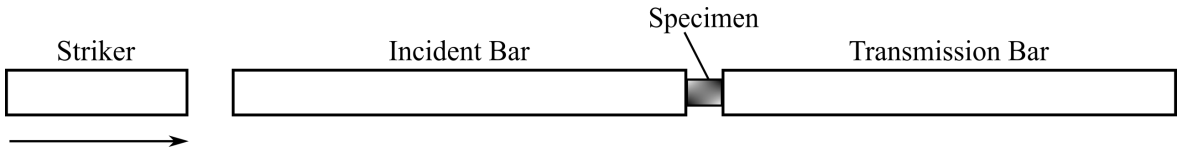


**Figure 2.2.** Schematic diagram of the basic components of a Split-Hopkinson pressure bar

The SHPB configuration illustrated in figure 2.2 is demonstrative and not representative of a true experimental set-up as it lacks the necessary instrumentation. Additionally, it only displays the fundamental components behind the theory of this technique. Detailed experimental set-ups are reported within the appropriate literature [103, 104, 119]. The SHPB technique is almost exclusively utilized for investigating stiff materials; however, as previously discussed in 2.2.1, appropriate modifications allow the investigation of material properties of soft materials, such as brain tissue. Investigating soft materials using a SHPB imposes many challenges for researchers; and generally this practice is not carried out by researchers, but few exceptions are present within the literature and they have been previously cited.

### 2.4.2 Shock Tubes

Gas-driven shock tubes are the primary experimental apparatus employed to explore bTBI due to their ease of use and repeatability [129]. A shock tube consists of a high pressure chamber and a low pressure chamber separated by a frangible membrane [23, 129]. The high pressure chamber is often referred to as the *driver* section, while the low pressure chamber is referred to as the *driven* section. The driver section is filled with gas and as the pressure in the driver section reaches the material limit of the membrane it ruptures releasing the high pressure which generates a shock wave that propagates through the low pressure chamber. Figure 2.3 illustrates the time evolution of a constant-area shock tube of a potential experiment.

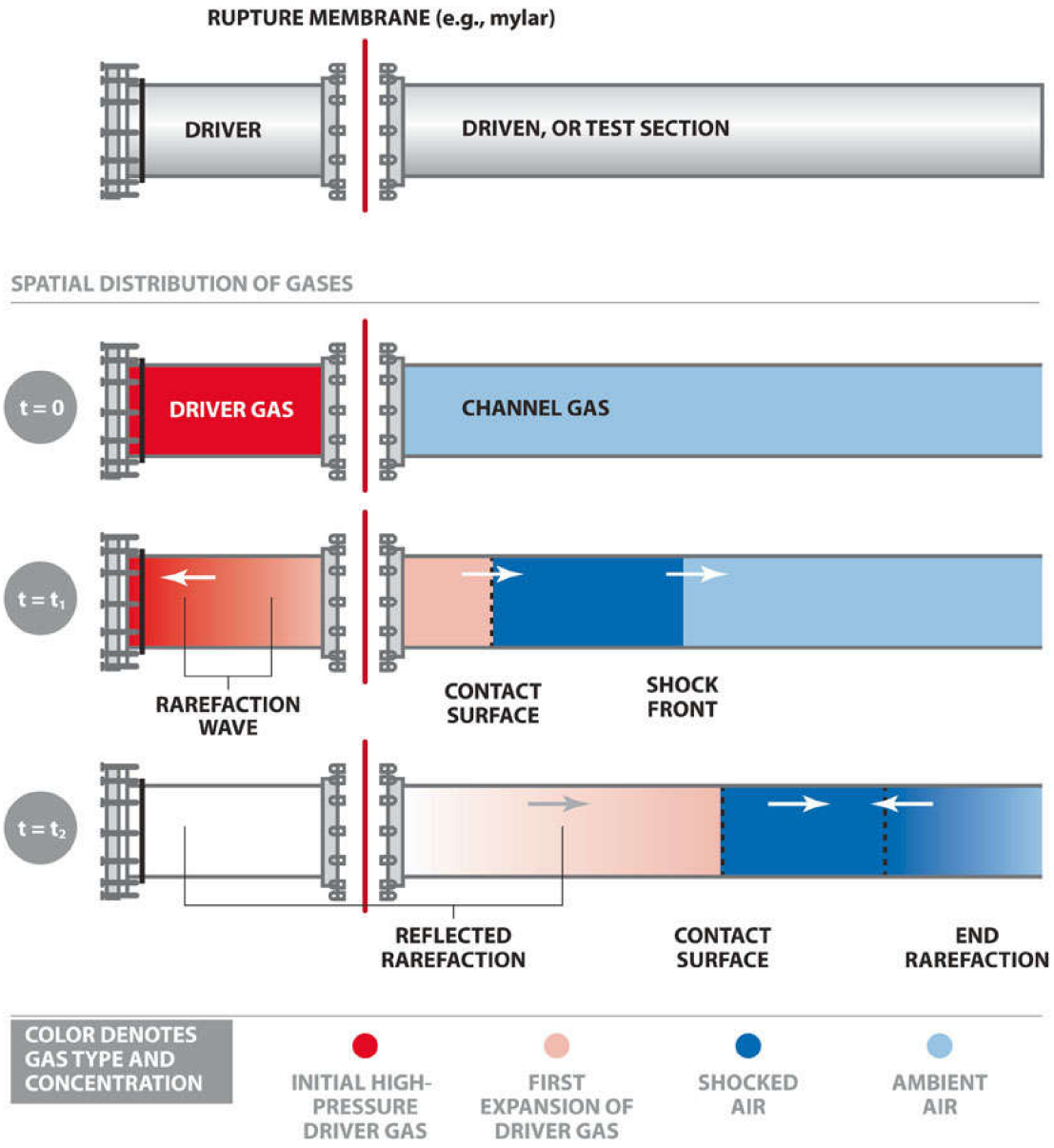


**Figure 2.3.** Schematic depiction of the development of the gas dynamic flow conditions within a constant-area shock tube. The spatial distribution of gases are represented by color. At time, $t = 0$, the driver is filled with high pressure gas which is separated from the driven section filled with ambient air by a frangible membrane. Once the membrane ruptures ($t_1$), the high-pressure gas expands into the driven section creating the shock front. In addition, the high-pressure gas reflects off the rear wall of the shock tube and creates a rarefaction wave. [129]

Shock tubes are often custom built for specific applications with both circular and square cross sectional areas being employed by different research organizations. Additionally, a range of sizes are reported within the literature: 3-inch diameter [100], 9x9 square inches [63], 12-inch diameter [70],

12x12 square inches [129], 0.71x0.71 square meters (~28x28 square inches) [123], just to name a few. There is a wide use of shock tubes to explore multiple aspects relating to bTBI; everything from investigating changes in cell cultures and animal models to analyzing ICP changes in cadaver heads. The use of shock tubes brings the ability to study blast related conditions within the laboratory setting. There are limitations associated with using shock tubes, which will be discussed in detail in §2.4.5, but the relative ease of incorporating shock tubes within a laboratory setting has greatly improved the collective knowledge towards bTBI and blast trauma in general.

### 2.4.3 Blast Tubes

Blast tubes are similar to shock tubes in design and functionality; however, they are different due to the principle driving mechanism. Instead of using compressed gas as the driving mechanism to generate a shock wave, blast tubes use controlled explosive detonations to produce a blast wave rather than just a shock wave. As described in §1.5 free-field blast waves follow the characteristic of a Friedlander waveform. Thus, replicating a Friedlander waveform as much as possible is imperative for comparing generated results to real-world scenarios. Employing blast tubes is effortless in this regard as the physics associated with detonations naturally produce a Friedlander waveform.

The general construction of a blast tube is often simpler than its shock tube counter parts; only a single continuous chamber is commonly used for blast tubes compared to the double chamber of the standard shock tube. The simpler design coupled with the immense internal energy of explosives allows for significantly larger cross-sectional tubes to be employed in the field – Bauman et al. performed experiments on a 71-inch diameter blast tube and Mejía-Alvarez et al. utilizes a 80x80 square inch blast tube. This is important for the proper investigation of bTBI in large animal models (e.g., porcine, bovine, ovine, etc.) because large cross-sectional areas are necessary to maintain the relative low blockage percentage required for proper experimental procedure.

Additionally, the use of explosives also allows for smaller cross-sectional tubing to be utilized in order to investigate bTBI. This is because a blast tube requires significantly smaller quantities of explosives in order to produce free-field target peak pressures associated with real-world scenarios,

compared to the traditional open-field testing [7]. This fact enables the implementation of smaller cross-sectional area tubes without compromising the ability to produce significant pressures representative of those seen on the battle field [3]. The use of explosives reasonable broadens the range of cross-sectional areas available for blast tubes. However, due to the elevated safety hazards associated with operation and the extensive governmental regulations for explosives the use of blast tubes are quite limited compared to shock tube counterparts.

### 2.4.4 Open Field Testing

As the name implies open-field tests are conducted outside by detonating explosive charges. Open field testing is often seen as the closest representation of an operational blast scenario; however loading conditions are not guaranteed to be reproducible. Open-field testing is only mentioned to acknowledge its presence but will not be discussed in depth. As previously stated, there are extensive governmental regulations regarding the use and implementation of explosives. The severe hazards associated with open-field testing coupled with the imposed restrictions nearly always limits open-field testing to the military sector. Now, there are few exceptions, but the safety concerns and excessive price of open-field testing make it generally impractical for most academic researchers.

### 2.4.5 Limitations of Experimental Techniques

Each of the experimental techniques discussed in this section has helped broaden the understanding of bTBI from a variety of areas: material characterization at high strain rate, pathophysiology, wave propagation through complex materials, exploring both small and large scale animal models, etc. However, each one of these experimental techniques is not without limitations. While each has their own specific limitations, these three experimental instruments have several common limitations among them. The first is the significant laboratory space required to house these instruments. None of these experimental techniques can be used without the proper facilities to house all the necessary equipment. The second mutual limitation is the technical expertise required to employ each of these experimental instruments. While the exact expertise varies depending on each instrument

itself, all three of them employ advance engineering principles that need to be properly accounted for in order to obtain accurate results. Failure to properly operate these instruments will certainly lead to erroneous or misinterpreted results but also could lead to serious personal injuries. Finally, the expensive nature of these three experimental techniques cannot be overlooked. Each one of these instruments require both substantial overhead as well as continual operating costs for them to properly function. The implementation of any of these instruments is an investment that needs to be carefully considered.

In addition to the shared limitations, shock tubes and the SHPB both have application specific limitations. The SHPB technique is only suitable for small specimen testing as the specimen is required to be sandwiched between the *incident* and *transmission* bars. Furthermore, the conventional SHPB is still challenging to use on specimens with low strength, stiffness, or impedance, such as biological tissues, foams, gels, and polymers [130]. Few researchers have been able to investigate biological tissues using a modified SHPB, readers are referred to §2.2.1, but these are the exceptions that prove the general rule. The SHPB is ideal for material characterization, but applications for dynamic loading on biological specimens are narrow as they are required to fall within the small specimen size restrictions.

The specific limitations associated with shock tubes do not directly inhibit blast-related studies; rather, each experimental aspect needs to be carefully considered in order to properly execute investigations involving shock tubes. Common experimental conditions to account for are: blockage within the tube, specimen mounting, specimen location within the shock tube, failure to allow "wrap-around" loading, open-end rarefaction, proper measuring of static and dynamic pressures, and the choice of driving gas [96, 129]. Failure to account for each of these aforementioned aspects will result in flawed or misinterpreted results. The primary reason for erroneous results is the fact that a conventional shock tube does not intrinsically generate a "blast-like" shock wave [96]. Rather, only the positive phase of a Friedlander waveform is experienced within a shock tube. Furthermore, a specimen only experiences the representative positive phase if and only if it is positioned in the proper location within the tube itself – the specific location being unique to every shock tube and

requiring detailed characterization to determine this appropriate region. The specimen location dilemma is an attribute that with advance technical experience can be all together eliminated for a specific research group. However, each and every shock tube investigation should highlight the calibration performed to determine the appropriate region of interest in order to aid in the replication of said experiments as well as the comparison to other shock tube experiments.

The difficultly of obtaining representative "blast-like" pressure profiles within a shock tube has been detailed indepth in the published literature [96, 129]. However, VandeVord et al. have addressed these concerns and proposed a solution by modifying conventional shock tubes with an end wave eliminator (EWE). The EWE neutralizes open-end rarefaction waves from traveling back up the shock tube and allows the shock tube to produce more accurate representations of a Friedlander waveform [129]. Interested readers are encouraged to investigate the specifics of the EWE independently. The remaining experimental conditions that vastly influence the loading present during an experiment are heavily coupled to one another: specimen mounting, blockage, and the "wrap-around" loading effect. Specimen mounting is crucial because it allows for specific positioning of the specimen for the investigation of interest (e.g., head-on impact, side-on impact, etc.). Specimen mounting is also linked to the appropriate specimen location discussed previously. The mounting structure used for specimen mounting needs to be strong enough to securely house the specimen but also needs to be as small as possible reduce blockage; where blockage is defined as the ratio of the total "presented area" of the obstruction relative to the cross-section of the tube [96]. Specimen mounting can also affect or entirely eliminate the "wrap-around" loading that is a characteristic of free-field blast loading. Warp-around loading arises from the rejoining of the propagating shock front traversing around the specimen itself. At this re-joining point there is constructive wave interaction leading to an area of higher loading, which is critical to the imparted global displacements and stresses on the specimen [96]. Thus, the specific specimen mounting utilized in an experiment should interfere with the potential "wrap-around" loading as little as possible because it is nearly always present in operational blast scenarios.

For all things considered, blast tubes may be the best choice for investigating blast studies. However, blast tubes, while being able to easily generate a Friedlander waveform, bring sizeable safety concerns anytime they are employed; these safety concerns are arguably the greatest limitation when considering the use of blast tubes. The dangers associated with using explosives imposed to personnel, infrastructure, and equipment is daunting, which often discourages researchers from employing blast tubes as the primary experimental instrument of choice. Moreover, governmental regulations restrict the personnel able to directly handle explosives. These established regulations are necessary due to the elevated safety risks, but they do impose further complications in the employment of blast tubes. Additionally, blast tubes are quite similar to shock tubes as they share all of the same limiting aspects regarding implementation: blockage within the tube, specimen mounting, specimen location within the shock tube, failure to allow "wrap-around" loading, open-end rarefaction, as well as properly measuring of static and dynamic pressures. These experimental aspects are nearly always secondary to the elevated safety concerns and imposed governmental regulations when considering the limitations of blast tubes.

The choice of the experimental technique employed to investigate blast studies is heavily application specific (e.g., small animal versus large animal models) as well as researcher specific. The implementation of the discussed instruments usually is influenced by the researcher's preferential bias. Each method has its merits and limitations. Careful consideration of each method should be taken when evaluating the potential usage for involvement in blast-related studies. The attention of researchers should specifically address specimen size, time-scale, length-scale, experimental costs, and technical expertise for incorporation into their experimental design.

## 2.5 Scaling Laws

Scaling laws have been an effective tool to researchers working in the field of explosives for decades. They were first utilized to understand how the weight of an explosive charge affects the relative peak pressure experienced at different standoff distances. There are now a variety of different scaling laws implemented across the explosive field. Scaling laws are defined as describing the functional relationship between two physical quantities that scale with each other over a significant interval. This is technical in nature and allows the term to be applied to a variety of different disciplines. The term, scaling law, has been adapted to have a more unique interpretation relating to the explosive and bTBI communities. Specifically, a scaling law for the purpose of this research is a relationship that is empirically derived from either one or multiple sets of experiments in a manner that allows extrapolation from one system to a system that may not be easily evaluated directly (e.g., blast studies on human subjects).

Some of the most commonly used scaling laws are based on the work performed in the 1960s to investigate the influence that explosive blasts had on different mammals thoraxes and are commonly referred to as the Bowen Curves for lung injury threshold [14, 116]. The use of scaling laws have become widely used and sought after for their general ease of implementation as well as their predictive capabilities used for experiment planning. Another desirable quality of scaling laws is the ability for inexperienced individuals to comprehend otherwise complicated engineering principles. This common trait of scaling laws increases the potential collaborative effort between research disciplines as well as the dissemination of reported experimental results. The implementation of scaling laws have the ability to greatly improve the collective understanding towards a specific problem and the Bowen curves are a perfect example.

While the use of scaling laws can be extremely beneficial to the research communities, the incorporation of any new scaling laws needs to be carefully validated before they are widely implemented within the research community. The validation process is a matter of debate due the variety of characteristics that can be compared to one another. The particular scaling law of interest that is currently being debated regards the formulation of an injury threshold for evaluating

animal-to-human risk assessment. The reason for this is because there is still no widely accepted injury criteria for human brains exposed to blasts [58, 140]. The only currently accepted indicator for primary blast brain injury uses pulmonary primary blast injury curves as a lower boundary, given that previous research suggested that the tolerance for pulmonary primary blast injury is less than that for brain primary blast injury [108]. Additionally, due to the restrictive and highly unethical nature of human experimentation, any direct observations cannot be performed. Thus, there is no controlled data available for determining human brain injury tolerances. There are isolated cases relating to human data from military conflicts; however, the incidence of injury is often unknown due to multiple mechanisms present and unknown blast loading conditions [108].

The available alternative is to utilize animal models. Animal models have been and currently still are extensively used to investigate blast related studies from histological assays to behavior observations to gross examinations from post-mortem dissections. The abundance of animal investigations over the last 60 years have allowed for rigorous investigation of the biomechanical thresholds and pathophysiological mechanisms of TBI using controlled and highly efficient protocols [140]. However, during that same time period a general scaling law has not been created that accurately predicts the relative damage seen in humans after blast exposure. A primary reason is the over simplified mass scale assumption often employed by researchers [108, 146]. The mass scaling approach equates either the respective animal's body mass or brain mass to that of a human and applies a power-law weighting function to predict the approximate damage threshold based off of the loading input parameters of the animal model [108, 140, 146]. The mass scaling law approach does not account for the anatomical and morphological complexity present between interspecies. Additionally, the mass scaling method assumes the mechanical responses of the brain to be elastic, homogeneous, isotropic, even though it is well known that the mechanical response of brain tissue is non-linear, viscoelastic, heterogeneous, and anisotropic [140].

Considering the lack of predictive capabilities and anatomical accuracy of the mass scaling approach several researchers have branched out and proposed alternative scaling laws. The first notable independent approach accounts for the protective tissues surrounding the brain and their

relative acoustic impedance [58]. The second unique and noteworthy approach is based on a frequency-scaling method [140]. Wu et al. describes how the frequency-scaling approach considers directional-dependence as well as indicating that a brain with higher natural frequency (e.g., smaller brains) will require higher angular velocity and acceleration than a brain with a lower natural frequency (e.g., larger brains) for the equivalent biomechanical responses. This is important to note because it is much more representative of the clinically observed human brain behavior. An additional aspect for all scaling laws that needs to be further addressed is the regionally specific responses from animals to humans. A recent study has clearly depicted that there are significantly different injuries in pigs and humans, which were exposed to equivalent blasts [120]. This study highlights the importance to separate the regional and global predictive capabilities of a scaling law. Both regional and global injuries affect the overall accuracy and effectiveness of a scaling law. However, knowing more about the regional aspects plays a greater role in aiding clinicians in their diagnosis and applied treatment regiments.

The search for highly accurate and predictable scaling laws is an active area of research within both the bTBI and TBI communities. Currently, there is not a widely accepted scaling law or injury criteria for human brains. The recent advancements in testing capabilities as well as the material properties of brain tissue has brought significant understanding about the effectiveness and use of the current scaling laws. By incorporating additional characteristic that are relevant to the human brain (e.g., morphological features, nonlinear response, viscoelastic behavior, etc.) scaling laws will be able to increase their overall accuracy that will enable one day the careful development of risk assessments and human injury criteria based off of animal studies.

# CHAPTER 3

# BIOFIDELIC BRAIN PHANTOM

As explained up until this point, traumatic brain injury (TBI) and blast-induced traumatic brain injury (bTBI) are complicated topics; topics that are nearly impossible to cover from a single point-of-view. The reason for this is the complex coupling of the biological and mechanical features involved in such events. The complexity arises from the both anatomical nature of the human brain as well as the mechanical loading that leads to the injurious event.

In order to investigate such a complex coupled phenomena the individual components of the overall injurious event need to be isolated as much as possible to allow rigorous analysis to be performed. The importance of analyzing individual aspects of an overall event allows for the potential observation and subsequent isolation of unique characteristics present during particular loading conditions. This approach, while simple in essence, is generally more difficult to apply when replicating real-world loading scenarios. Additionally, the isolation of components is nearly altogether impossible in animal based studies; the leading cause for this is the biological variations present in both inter-species and inter-animals that have been previously discussed in §2.2.1 and §2.2.3. These limitations along with the others addressed in §2.5 exemplify the need for an alternative experimental approach.

The devised alternative approach was to create biofidelic test objects utilizing cranial tissue simulants. These test objects allow for a reproducible investigation into the potential injury causing mechanisms that were previously discussed in §2.1.1 – 2.1.4. The remainder of this chapter details each of the important components of the biofidelic test objects: conception, the materials / processes used for its fabrication, the multi-step fabrications process itself, and the material used as the brain tissue simulant. Important to note is that aspects of the fabrication process for the biofidelic test object and its incorporation into FE analysis have been previously published [90, 137]. The individual significance of the previously published data will be highlighted in their respective sections to follow.

## 3.1 Conception of the Test Object

The biofidelic test objects (henceforth, just test object or (TO)) arouse from the need for highly controllable and reproducible experimentation. By creating the TOs within the laboratory the need for biological specimens collected from animals has altogether been eliminated. This is advantageous for several reasons: first, it removes the specimen variation present in animal studies, second it eliminates the ethical burden associated with animal based studies, third it reduces the overall cost of experimentation, and finally it allows for the tunability of said test objects. Having a TO that is adaptable creates the ability for its integration into a variety of different experimental set-ups, which is crucial when studying phenomena as complicated as the ones associated with TBI/bTBI.

The adaptability parameter was paramount during the test object's conception. To this end, the additive manufacturing approach of three-dimensional (3D) printing was chosen as the principle technology for creating the required materials for the test object fabrication. 3D printing, also referred as rapid-prototyping, allows for the generation of engineering designs within a matter of hours. Compared to traditional machining, 3D printing is capable of reducing both the time and cost of fabrication by orders of magnitude. The specific methods employed in regards to 3D printing for the TO will be discussed further in §3.2.

With the technological approach settled the remaining limiting factors for the TO fabrication needed to be established in order to properly confine the viable experimental procedures. The relevant limiting factors regarding the TO fabrication are related to the anatomical accuracy needed to investigate the potential injury mechanisms associated with TBI/bTBI. Having high anatomical accurate TOs allows for quick comparison to a real human brain; however, a model needs to be as complex as necessary, while remaining as simple as possible [19]. Additionally, Budday et al. (2019) point out that the multitudes of overly complex FE models currently being employed by researchers across different disciplines often times over estimate potential damage or inaccurately predicts deformation compared to experimental results. While FE models are different from test objects, the principles pertaining to their implementation are similar and thus should not be overlooked. This

topic has been previously discussed in detail in §2.3 and should be referred to for clarity on this matter.

The implementation of the TO needs to maintain anatomical significance, while simultaneously being able to isolate important features during experimental procedures. This coupling of biofidelity with current experimental acquisition limitations stresses the need for a simplistic model that allows for the capturing of quantifiable data. To this end, the TO's conception has emphasized the need to balance the requirements from both the clinical and mechanical understanding relating to the injurious events associated with TBI/bTBI.

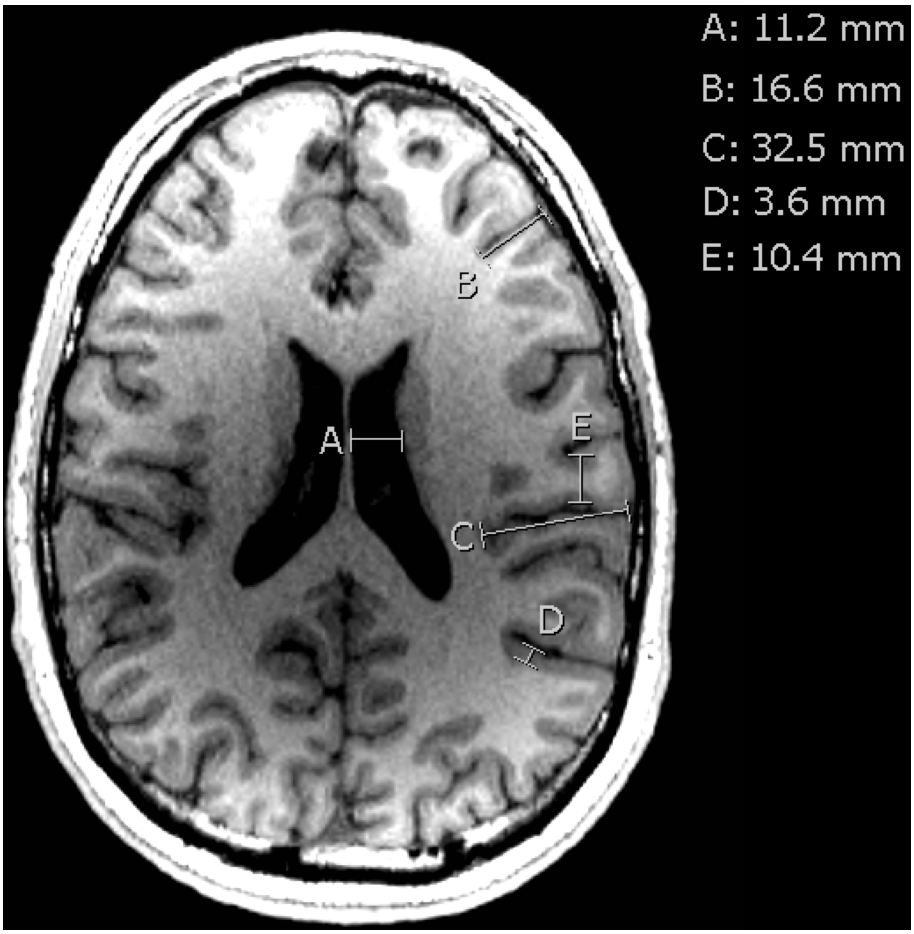


**Figure 3.1.** The axial MRI image used for the construction of the biofidelic test object. Embedded lettering corresponds to dimensions of significant anatomical features: **A**: gap for ventricle space, **B**: depth of shorter sulcus, **C**: depth of larger sulcus, **D**: thickness of gray matter, **E**: thickness of gyrus including both gray / white matter.

The biofidelic test object is based on an axial slice of a healthy 35-year-old-male, which can be seen in figure 3.1. The TO was constructed via computer aided drafting (CAD) software (SOLIDWORKS, 2018). A 3D geometric representation was developed based on the dominant length scales of the sulci, gyri, gray matter thickness, and overall brain dimensions. As seen in figure 3.1 the dimensions embedded on the MRI image represent the different regions of interest. The values for the MRI dimensions were used as a reference in the creation of the TOs geometric representation and not as a direct transfer of dimensions. Figure 3.2 illustrates this rough transfer of the dominant length scales of interest; specifically, the dimensions for *B* and *E* can be clearly seen in the letter call-outs in figure 3.2.

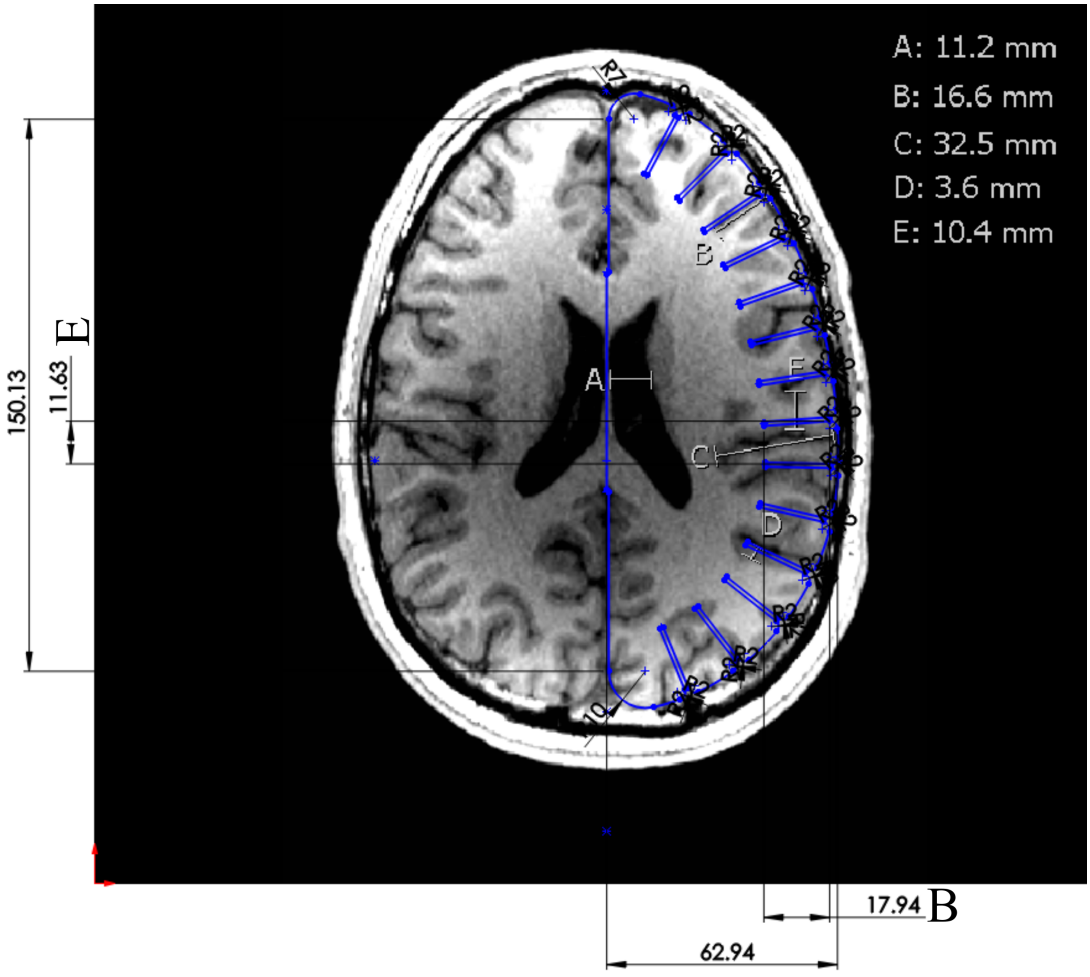


**Figure 3.2.** The axial MRI image with the dimensions used to create the 3D geometric representation. Dimensions **B** (17.94 mm) and **E** (11.63 mm) have call-outs to illustrate proximity to the corresponding MRI reference values. Adapted from [90].

The difference between the reference MRI values and the generated values for dimensions *B* and *E* are 1.34 and 1.23 mm, respectively. The idealized 2D overlay present in figure 3.2 demonstrates the simplicity previously discussed, while the values for dimensions *B* and *E* clearly emphasis the preserving of biofidelity within the model. The simplified 2D representation included the following dimensions: width (medial-to-distal), length (rostral-to-caudal), sulcal depth to gyral width, sulcal width, gray / white matter thickness, and CSF layer thickness. The overall geometry was reviewed and verified by a board-certified neurologist who confirmed the relative size and shape of the human head was maintained in the brain phantoms while maintaining the dominant length scales of the gyri/sulci.

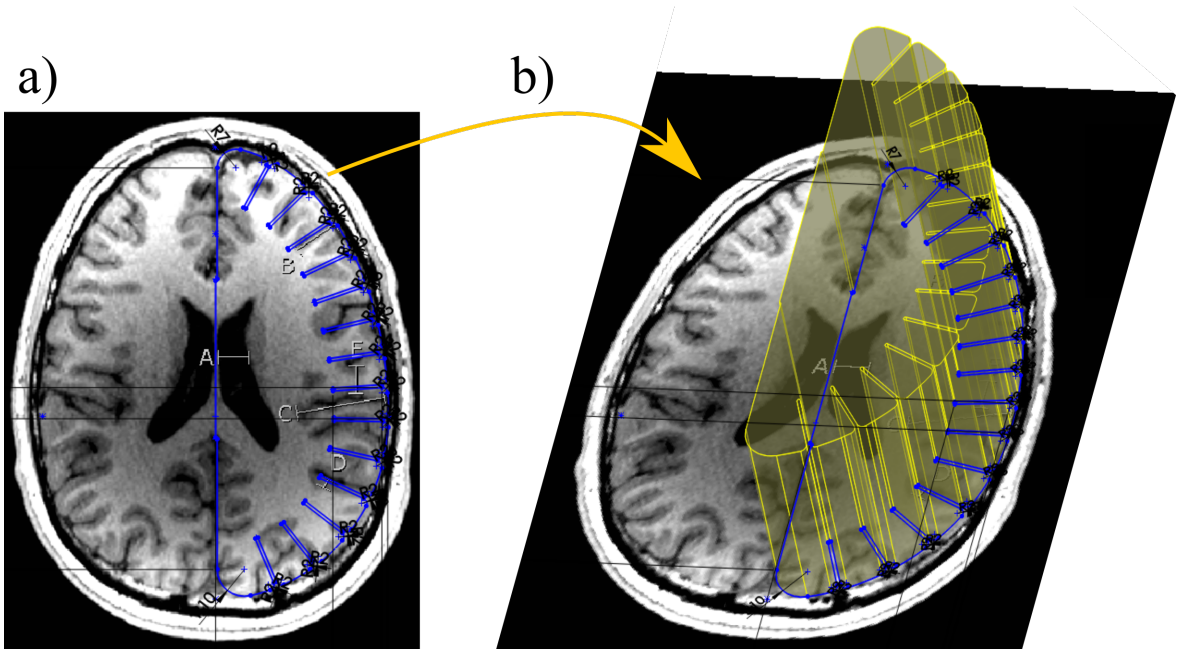


**Figure 3.3.** Visual representation of 3D ellipsoid extruded from 2D overlay. **a)** corresponds to the 2D sketch overlay first presented in figure 3.2. **b)** illustrates a CAD extrusion to match the relevant height of a human brain. Adapted from [90].

The 2D CAD representation was extruded to the approximate height (inferior-to-superior) of a human brain, which is illustrated in figure 3.3. The extrusion displayed in figure 3.3 is only meant to demonstrate the general procedure for the TO creation and not the final representation that was used during experimentation. Additionally, only one half of the brain representation has been displayed in figures 3.2 and 3.3 – this is due to utilizing the relative anatomical symmetry that is present along

the longitudinal fissure, which is the deep groove that divides the left and right hemispheres of the cerebrum. The overall representation of the TO utilized in these studies can be seen in figure 3.4. Figure 3.4 is a CAD representation that has both a two-material (left) exploded view of the TO as well as a fully collapsed representation of the TO (right). The gray matter (GM) and white matter (WM) representations are both symmetric as previously stated and were designed to be interconnected at the material interface boundary. Interfacial boundary conditions will be explained further in 3.3. The fully collapsed portion (right side of figure 3.4) presents how the GM / WM TO sits inside of a 3D printed skull. Additionally, you can see that there are two optical windows; these optical windows allow the direct visual observation of the intracranial content's response to mechanical loading, which is paramount to the isolation of critical phenomena during an potential injurious event. The remaining sections of this chapter will further explain the necessary steps involved in the creation of the biofidelic test object.

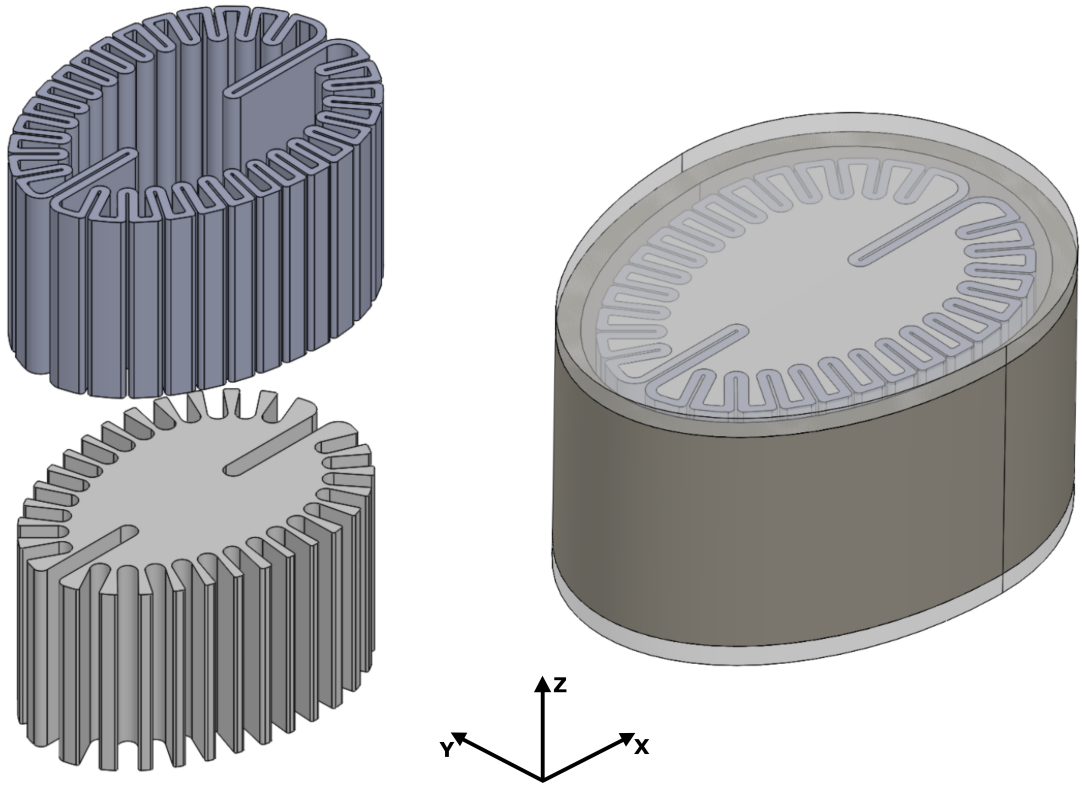


**Figure 3.4.** 3D Representation of the Biofidelic Brain Phantom: (Left) Exploded view of Geometry [Top: GM, Bottom: WM], (Right) Collapsed Fully Assembled Test Object

## 3.2 3D Printing

As explained in the previous section, 3D printing was chosen as the principle technology in the creation of the biofidelic test objects. The expansive use of 3D printers has not only brought about their knowledge into the public realm but also their use across a multitude of industries; aerospace, medical, academic, automotive, construction, etc. The applications involving 3D printing have grown to be countless in number. One of the main reasons for this is the various printing technologies currently being used as well as the specific materials being employed in the different 3D printing processes. All of the 3D printing technologies allow for design iterations, and often times more than a single technology can achieve a desired result for a specific application [114]. Redwood et al. give a great overview of all of the 3D printing technologies and the vast number of combinations currently available on the market. This is a great resource to all 3D printing users, whether a novice or an expert.

The intention of this section is not to be an extensive discussion over all of the 3D printing technologies but rather an introduction to the processes used for this research. With this being said, understanding the different 3D printing technologies can aid the reader in selection process of the individual technology used. Furthermore, the incorporation of different 3D printing technologies can improve the overall adaptability of the TO. The former takes precedent here; however, the later is an key attribute to the TO and thus important to keep in mind. A brief overview of the 3D printing technologies will address any concern to the individual process selected for the creation of the TOs. Afterwards, the details pertaining to the creation of this 3D printed skull along with the molds used to fabricate the TO will be discussed.

### 3.2.1 3D Printing Materials & Technologies

3D printing can be categorized by two main components: printing technology (process) and printing material. While the printing material is often times limited to a specific printing process, there are numerous printing materials available for each printing process. This is important to note for

the application purposes; a single printing technology can achieve a range of desirable results (functionality [high-temperature, strength, flexible], aesthetics [transparent, textured, smoothness], etc.) for different applications by often times only changing the printing material. Figures 3.5 and 3.6 are flowcharts that explain the classifications for the 3D printing technologies and materials, respectfully. Additionally, table 3.1 gives a brief explanation of the each processes and the relevant acronyms associated with the different 3D printing technologies. The individual 3D processes increase in both complexity and cost moving from left to right as seen in figure 3.5. However, both the complexity and cost are reducing across of the different 3D printing processes with the increasing widespread use of 3D printing. This is important to note due to the potential for highly complex, multi-material, fabrication approaches soon to be available in the near future to researchers. There are several additional 3D printing technologies, but they completely fall outside the scope of this text and will not be expanded on. Furthermore, each of the processes mentioned in figure 3.5 are explained in detail in the cited reference and any curious readers are advised to review said reference.

In addition to the 3D printing technologies, individual readers are encouraged to review the cited reference to investigate the different 3D printing material groups. The specific chemistry behind each applicable material falls outside the scope of this research. Understanding the benefits and limitations of each material (and technology for that matter) will aid in the consideration of different manufacturing techniques for different applications. Applications are altogether unlimited when considering the use of all of the 3D printing technologies. However, access to the individual 3D printing technologies is still limiting within the research setting. For this reason (among others), only a single 3D printing technology will be expanded upon in detail within this text, specifically, fused deposition modeling (FDM).

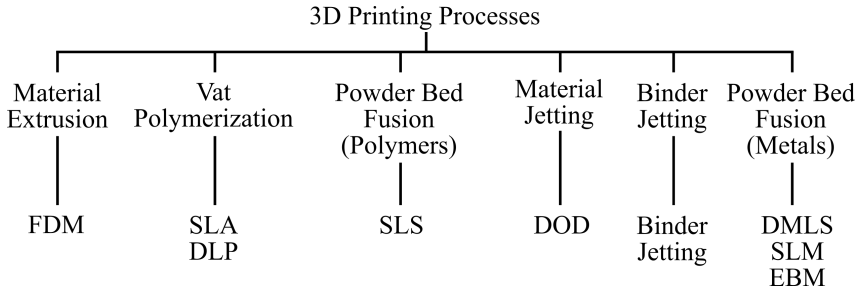


**Figure 3.5.** Classification of 3D Printing Technologies. Adapted from [114]

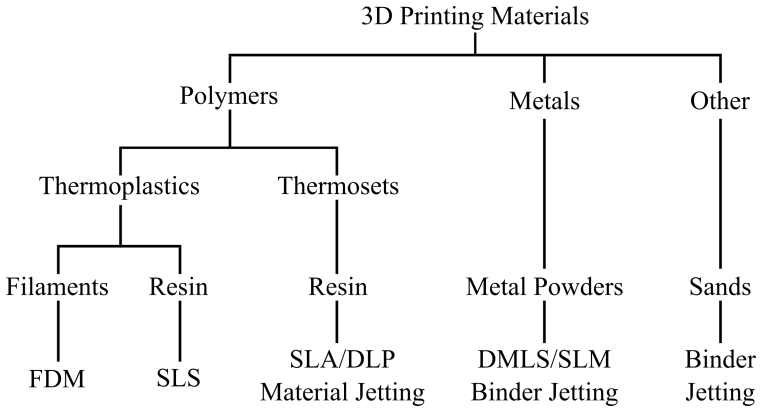


**Figure 3.6.** Classification of 3D Printing Materials. Adapted from [114]

**Table 3.1.** Description of 3D Printing Technologies. Adapted from [114]

| **Process** | **Description** | **Technologies** |
|---|---|---|
| Material Extrusion | Material is selectively dispensed through a nozzle. | Fused Deposition Modeling (FDM)<br>Fused Filament Fabrication (FFF) |
| Vat Polymerization | Liquid polymer is selectively cured by light-activated polymerization | Stereolithography (SLA)<br>Direct Light Processing (DLP) |
| Powder Bed Fusion | Thermal energy selectively fuses regions of a powder bed. | Selective Laser Sintering (SLS)<br>Direct Metal Laser Sintering (DLMS)<br>Selective Laser Melting (SLM)<br>Electron Beam Melting (EBM) |
| Material Jetting | Droplets of a material are selectively deposited and cured on a build platform. | Material Jetting (MJ)<br>Drop on Demand (DOD) |
| Binder Jetting | Liquid bonding agent selectively binds regions of a powder bed. | Binder Jetting (BJ) |

### 3.2.2 Selected 3D Technology

Fused deposition modeling (FDM), also referred as fused filament fabrication (FFF), was the 3D printing technology utilized in the creation of the components for the biofidelic test objects. As seen in figures 3.5 and 3.6, FDM is an *material extrusion* method that uses a polymer based *thermoplastic* as its printing material. The working principle of FDM (*material extrusion*) is to heat a *thermoplastic* (filament) beyond its melting point and extrude it through a nozzle that deposits the material on a build platform in a predetermined path [114]. FDM is the most widely used 3D printing technology available to consumers today. This is the primary reason for its selection as the 3D printing technology used for the creation of the necessary components required for the TO fabrication. Due to its prevalence in the market, FDM is capable of producing exceptionally low-cost parts at fast speeds. Additionally, FDM has a relatively low learning curve, which allowed for its quick integration into the manufacturing process of the necessary parts.

The filament (*thermoplastic*) of choice in the creation of the necessary TO components was polylactic acid (PLA). PLA is the most widely used filament in the FDM process across the world. PLA has both good thermal and mechanical properties for 3D printed parts. Additionally, PLA requires the lowest heat-bed / nozzle temperature of the non-specialized common FDM filaments available on the market. This is important because printing temperature is one of the key parameters that affect the overall quality of a 3D printed part through the FDM method. In addition, the lower the nozzle / heat-bed temperatures can be during printing reduces the overall potential of unwanted printing defects (e.g., warping, poor layer adhesion, shrinkage, etc.) or print failures entirely. In general, thermoplastics with better engineering properties are required to be heated to higher temperatures, and therefore causing the material to be harder to print [114]. There are a multitude of different thermoplastics available on the market (e.g., PLA, ABS, PP, PE, PC, PETG, etc.) all exhibiting different material properties that can be beneficial or restrictive depending on the application of interest. The decision of utilizing PLA as the filament of choice along with FDM makes the components discussed herein the most reproducible of all of the available combinations of 3D printing technologies and printing materials.

#### 3.2.2.1 Printed Components for Test object

As previously discussed in §3.1, the biofidelic test object was based on an MRI image of a healthy 35-year-old-male. The CAD representations of the gray matter (GM) previously discussed was directly transformed into 3D printed mold. As previously seen in figure 3.4 the GM representation perfectly fits around the white matter (WM) representation. Thus, the negative space on the inside of the GM representation creates the formation of the WM space. This idea of positive / negative space is fundamental to all mold making techniques and is repeatedly utilized in the formation of the TOs. In order to achieve both the GM and WM space of the TO, a tissue simulant was used that had similar material properties of brain tissue [137]. More information of the specific tissue simulant will be discussed in §3.4 and §3.3.

To help clarify the use of positive / negative space figure 3.7 illustrates the individual components of the TO in a 2D CAD representation. As stated before, the WM component (yellow in fig. 3.7) can be created by utilizing the negative space bounded by the GM component. The GM component (gray in fig. 3.7) can then subsequently be created from the difference of the WM and CSF space. Now, the GM component is created by using a mold that corresponds to the CSF space. This is because during the fabrication process of the GM component, the GM component is directly created around the previously formed WM component; more to come on this later in §3.4. The specific molds used to create the WM and GM components can be seen in figures 3.8 and 3.9, which have top-views of the CAD files (left-side) used to create their respective molds (right-side). As seen in figure 3.9, the GM mold corresponds to the CSF space present in figure 3.7.

The final 3D printed component of the TOs was the skull itself. As seen in figure 3.7 the skull is an ellipsoid shell that fully encompasses the outside perimeter of the WM / GM representations. Additionally, the size of the skull was created to be large enough to allow the CSF space to entirely surround the WM / GM representations. This was important to maintain the anatomical relevance of the TO to that of a human – for a human brain is surrounded by CSF, which acts as a shock absorbing protecting layer. Lastly, the skull was 3D printed with a 50% rectilinear in-fill pattern. This in-fill pattern served to mimic the natural sandwiching of trabecula bone between two layers of

dense cortical bone that is present within the human skull. Figures 3.10 and 3.11 demonstrate this comparison between the nature of the flat bones that comprise the human skull and how the 3D printing method resembles that of the anatomical structure present within the human skull. Now it is important to note that the material (PLA) used for the fabrication of the skull does not exactly mimic the overall density of human skull; however, the density of PLA ($1.25\, g/cm^3$) is on the same order of magnitude as the density of human skull ($\sim 1.7 - 1.9\, g/cm^3$) [92, 105].

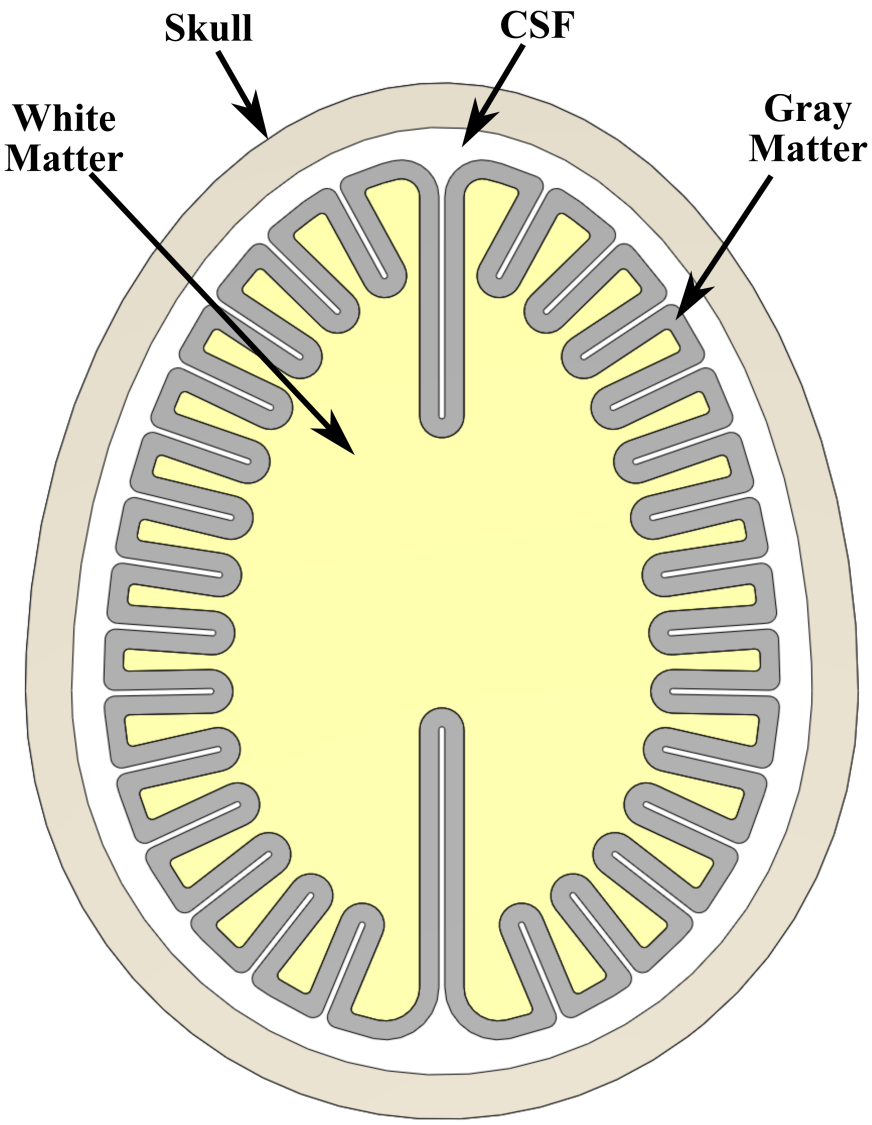


**Figure 3.7.** Two Dimensional Top Down View of Test Object. Component Coloring: yellow is white matter, gray is gray matter, white is cerebral spinal fluid, and tan is the skull.

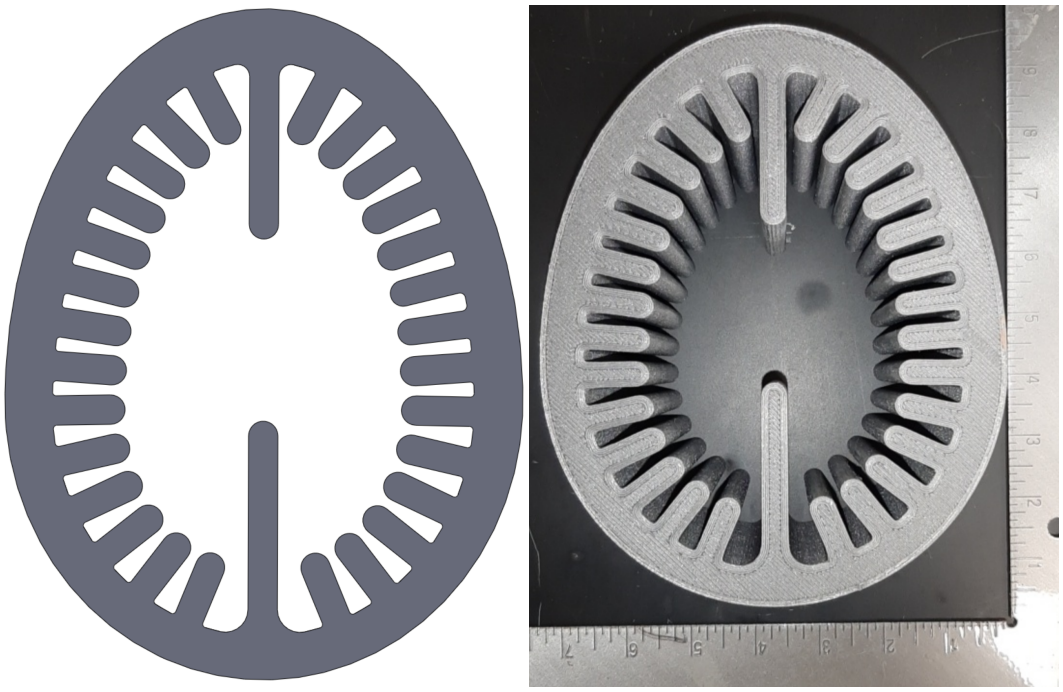

**Figure 3.8.** Design of the White Matter Mold (Top Down View). The inner space of the mold corresponds to the resulting representation that will be the white matter simulant. Left-side: 2D CAD representation. Right-side: physical 3D printed mold.

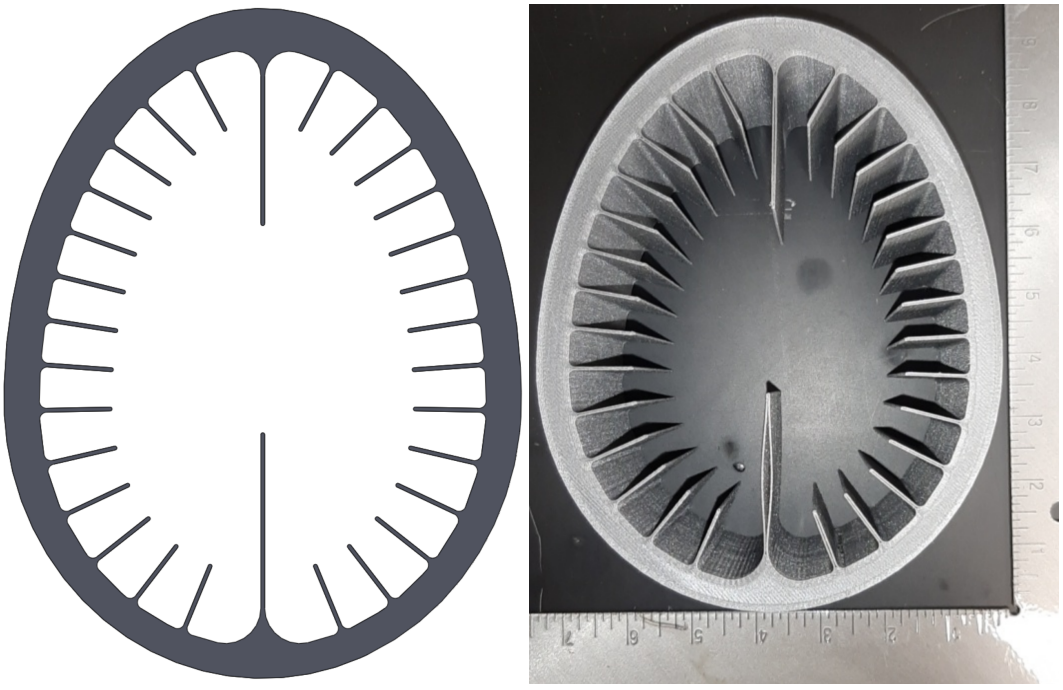

**Figure 3.9.** Design of the Gray Matter Mold (Top Down View). Left-side: 2D CAD representation. Right-side: physical 3D printed mold.

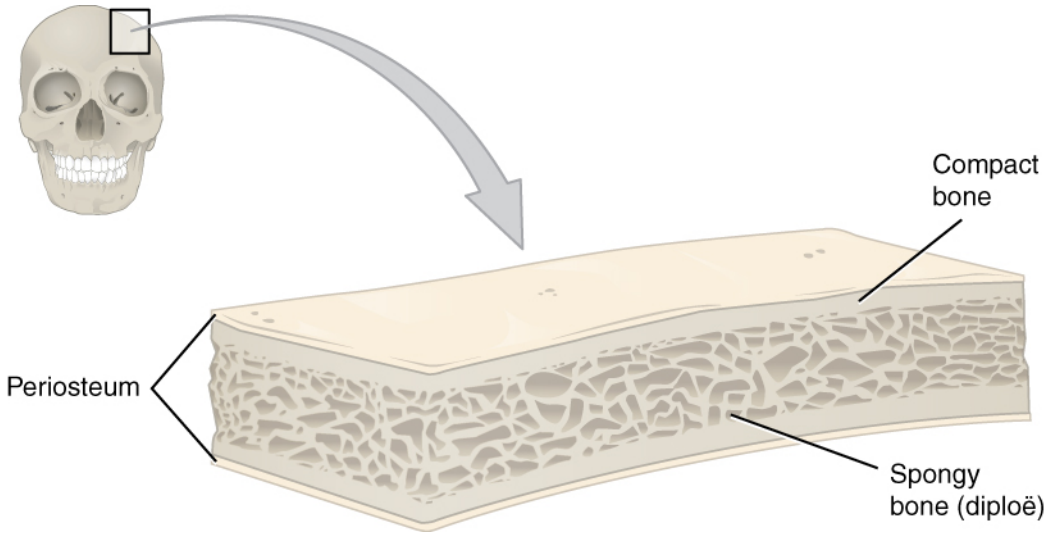


**Figure 3.10.** Example of the composition of a flat bone that comprise the human skull. The bone itself if a composite of three individual layers: outer cortical bone, middle "spongy bone" (known as diploë / trabecular / cancelleous), and inner cortical bone. [46]

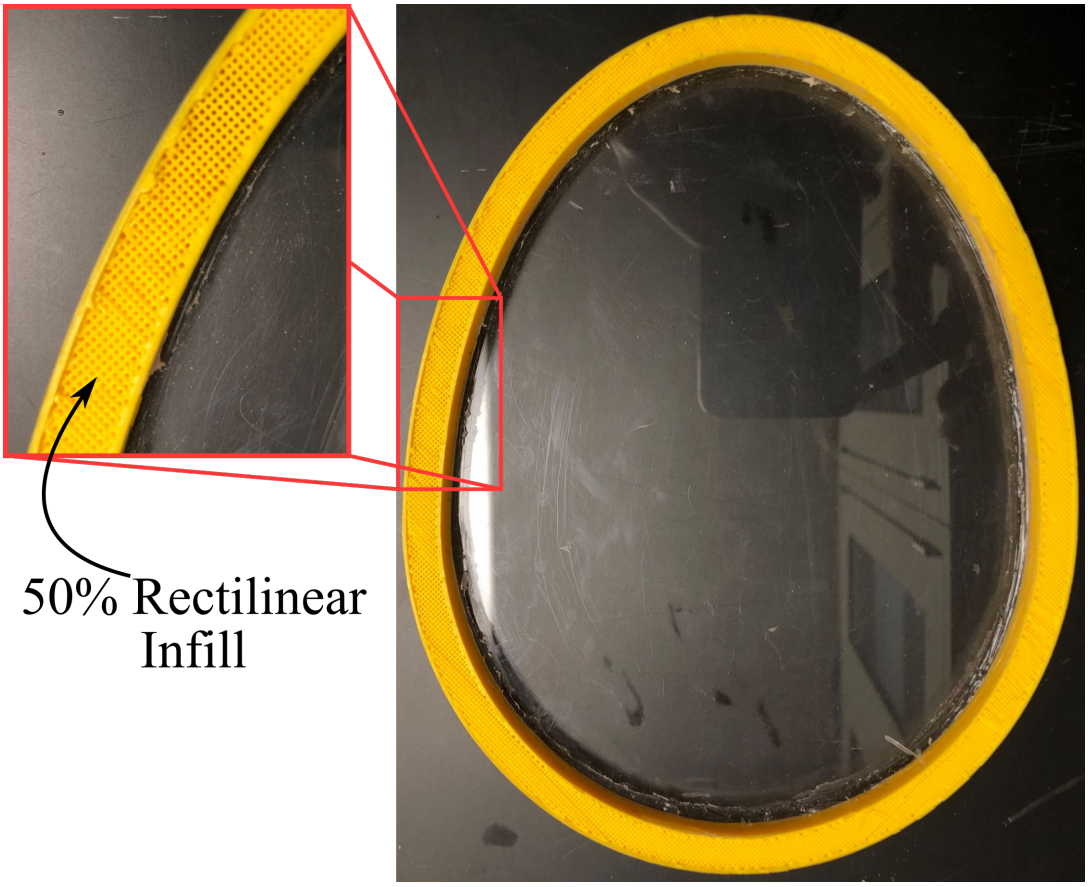


**Figure 3.11.** Example of the 50% rectilinear infill pattern present within the 3D printed skulls.

## 3.3 Brain Tissue Simulant

The 3D printed molds were employed to form a tissue simulant into the aforementioned geometry discussed in §3.1 and §3.2.2.1. The specific tissue simulant utilized throughout this research in the creation of the biofidelic test objects was Polyacrylamide (PAA) gelatin. PAA was chosen because it is an ideal material for a brain tissue simulate due to its easily tunable material properties, room temperature fabrication, and high level of transparency for optical access. Additionally, PAA has a relatively short assembly time and low energy requirements making it a superior choice over other common inorganic gelatin. The conclusion to utilize PAA was based on the work by Wermer et al., who performed engineering traction measurements on a series of gelatin materials in the pursuit of determining the optimal synthetic gelatin for human brain surrogates. The information henceforth on the tissue simulant has been broadly established by Wermer et al.; but due to its significance, key aspects will be summarized for the readers convenience.

PAA results from the cross-linking of two monomers, Acrylamide (ACR) and Methylene-bis-Acrylamide (MBA). Ammonium Persulfate (APS) induces these two monomers to cross-link, and the process is catalyzed with N,N,N',N'- tetramethylethylenediamine (TEMED). PAA has a wide variety of uses across different disciplines: gel electrophoresis, food industry, pharmaceuticals, drug delivery, agriculture, etc. [127, 141]. Additionally, the use of PAA as a tissue phantom has become quite prominent over the last decade: having tissue applications for the prostate [21], general ablation therapy [125], and breast tissue [144] just to name a few. A major advantage of PAA is its ability to finely tune its material properties by varying the composition (monomers and cross-linker ratio) [137], which makes it suitable for different tissue phantom applications. Furthermore, the cross-linking within the polymeric network of PAA allows for adjacent layers to chemically bond to one another. This approach, using different weight percent concentrations (weight/volume) of PAA, was how the GM and WM representations were created for the biofidelic brain phantom. The proportion of the components was tailored to approximate the bulk mechanical properties of WM and GM that have been previously reported [137].

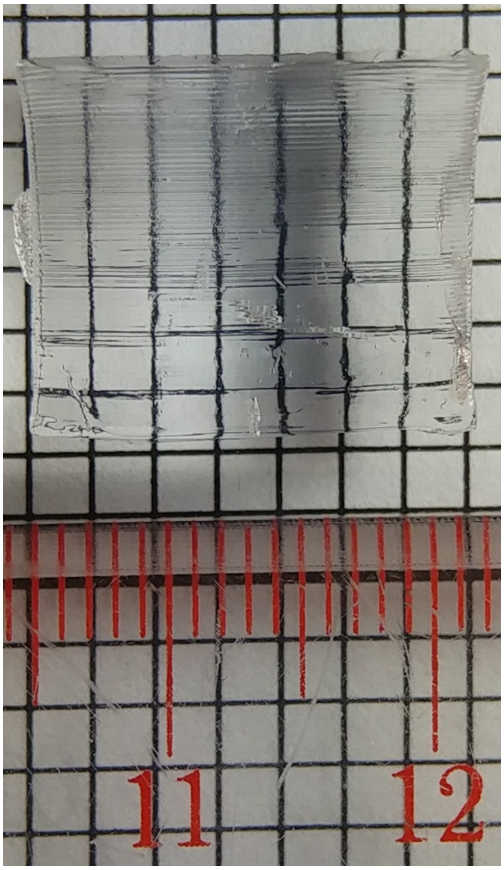


**Figure 3.12.** Demonstration of PAA's transparency as seen over graph paper.
(Ruler graduation marks are cm.)

This ability for PAA to chemically cross-link to itself at adjacent layers allows for special focus on observing phenomena occurring at the interfaces of adjacent tissue simulant types or material-fluid boundaries. The locations of these material interfaces are extremely important to the overall understanding of the direct cranial transmission (DCT) mechanism of bTBI, which was first discussed in §2.1.1. Moreover, the transparency of PAA, as seen in figure 3.12, allows for these material interfaces to be investigated at a variety of different depths within the cranial phantom itself.

This transparent characteristic of PAA was key to the implementation of the biofidelic test objects in experimental settings because it directly allowed for the observation and, thus, the investigation of the intracranial gelatin response after a biomechanical loading event. The direct observation, compared to *in-situ* analysis, allows for the isolation of any phenomena that may be present with the definitive understanding of said phenomena's specific location within the test object.

The use of PAA was not without its draw backs. While PAA itself is safe to handle, the preparation of PAA requires elevated safety precautions during the fabrication process due to the carcinogenic and neurotoxic effects of the monomer, acrylamide [137, 144]. These safety concerns are genuine and should not be overlooked. However, the natural advantages in using PAA as a tissue simulant for phantom fabrication greatly outweighs the safety concerns present during its preparation; especially, if the proper protective equipment is worn and basic chemical safety is applied.

## 3.4 Fabrication

The fabrication process begins with selecting the weight concentrations (weight / volume, [w / v]) to be used for the WM and GM representations. As stated previously, the formulation of PAA allows for different material properties to be generated by merely changing the weight / volume ratio of the acrylamide monomer. Additionally, Wermer et al. investigated how modifying the cross-linker to monomer ratio can also influence the material properties, while retaining the approximate weight percentages for a desired PAA formulation; interested readers should explore that reference for further details.

An example of the specific chemical concentrations used in the fabrication process of two frequently used volumes can be seen in table 3.2. The acronyms within table 3.2 correspond to the following chemicals: Acrylamide (ACR), Methylene-bis-Acrylamide (MBA), Ammonium Persulfate (APS), N,N,N',N'- tetramethylethylenediamine (TEMED). The two volumes presented in table 3.2,

**Table 3.2.** Chemical concentrations for PAA gelatin formulation at a 30:1 monomer ratio.

| Water [ml] | w / v | ACR [g] | MBA [g] | APS [g] | TEMED [ml] |
|---|---|---|---|---|---|
| 100 | 0.20 | 20 | 0.667 | 0.1739 | 0.1 |
| 100 | 0.10 | 10 | 0.333 | 0.0870 | 0.1 |
| 100 | 0.05 | 5 | 0.167 | 0.0435 | 0.1 |
| 1000 | 0.20 | 200 | 6.667 | 1.739 | 1.0 |
| 1000 | 0.10 | 100 | 3.333 | 0.8696 | 1.0 |
| 1000 | 0.05 | 50 | 0.167 | 0.4348 | 1.0 |

100 ml and 1000 ml, were chosen for demonstrative purposes as their individual values allow for easy mathematical calculations. The initial volumes (100 ml and 1000 ml) each have three different (w / v) formulations that are an integer value of the following formulation.

The second column in table 3.2 corresponds to the desired weight percent (e.g., 20%, 10%, or 5%) of the resulting PAA gelatin. The desired (w / v) concentration is multiplied by the total volume of water required for the specific fabrication batch to obtain the necessary mass of acrylamide.

$$(Column\,1) * (Column\,2) = Column\,3 \quad or \quad (100\,ml) * (0.20\,g/ml) = 20\,g$$

As indicated in table 3.2 the monomer to monomer ratio used during the PAA fabrication was 30:1. Therefore, the desired mass of MBA is $1/30^{th}$ of the mass of ACR used in any formulation process. The 30:1 (ACR:MBA) multiplication factor was used for all of the PAA gelatin formulations throughout this research. To note, this specific ratio can be modified to achieve different material properties of the PAA gelatin; this topic will be addressed again in §8; however, this falls outside of the scope of this particular study.

The fourth and fifth columns of table 3.2 can also be determined from multiplication factors based on either the mass of the ACR or volume of water. The mass of APS is calculated based on the total mass of ACR within the specific PAA formulation; the multiplication factor for APS is $1/115$. The desired volume of TEMED is based on the total volume of water used and has a multiplication factor of 0.001. The particular multiplication factors for APS and TEMED are arbitrary in nature but were selected base off of preliminary experimentation and the previously cited work [137, 144].

Now, the previous information relating the biofidelic brain phantom's conception, the specific 3D printing technology used to create the necessary molds, and the material information regarding PAA itself all come together for producing the required procedure necessary to fabricate a test object. The following are the explicit set of steps employed in fabricating the test objects.

First, the WM gelatin representation needs to be created. To generate the WM simulant, 83 g of Acrylamide (purity $\geq$ 98%, gas chromatography, Sigma-Aldrich, USA) was dissolved in 830 ml of deionized (DI) water, resulting in a 10% (w / v) solution. The Acrylamide was allowed to fully dissolved. Next, 2.77 g of *N,N'*-methylene-bis-Acrylamide (MBA, purity 99%, Sigma-Aldrich) was

slowly added to the solution while stirring in order to avoid aggregation of the fine powder. The MBA was allowed to homogenize. Then, 0.72 g of Ammonium Persulfate (APS, purity ≥ 98.0%, Sigma-Aldrich) was added, which initiates the cross linking of the two monomers of acrylamide. Again, the APS is allowed to dissolve into the solution.

To expedite the curing process, 0.83 ml of *N,N,N',N'*-tetramethylethylenediamine (TEMED, ReagentPlus, 99%, Sigma-Aldrich), which serves as a catalyst, was added. Following the addition of TEMED, the solution was immediately poured into the 3D printed mold shown in figure 3.8. With the purpose of creating a mid-layer of micron-sized particles in the phantom, the solution was initially poured until it filled half the volume of the mold. After this initial section cured, micron-sized particles were sprinkled on the free surface of the gelatin to form a randomized speckle pattern in the mid-plane of the phantom. The particle layer can be seen in figures 3.13c and 3.14. Subsequently, the second half of the solution was poured on top of the tracer layer to complete the WM simulant.

Once the WM simulant cured, it was removed from its 3D printed mold. This WM gelatin representation was given a quick rinse with DI water and then visually inspected for any defects that would affect experimental results. If visible defects were detected, then the WM gelatin

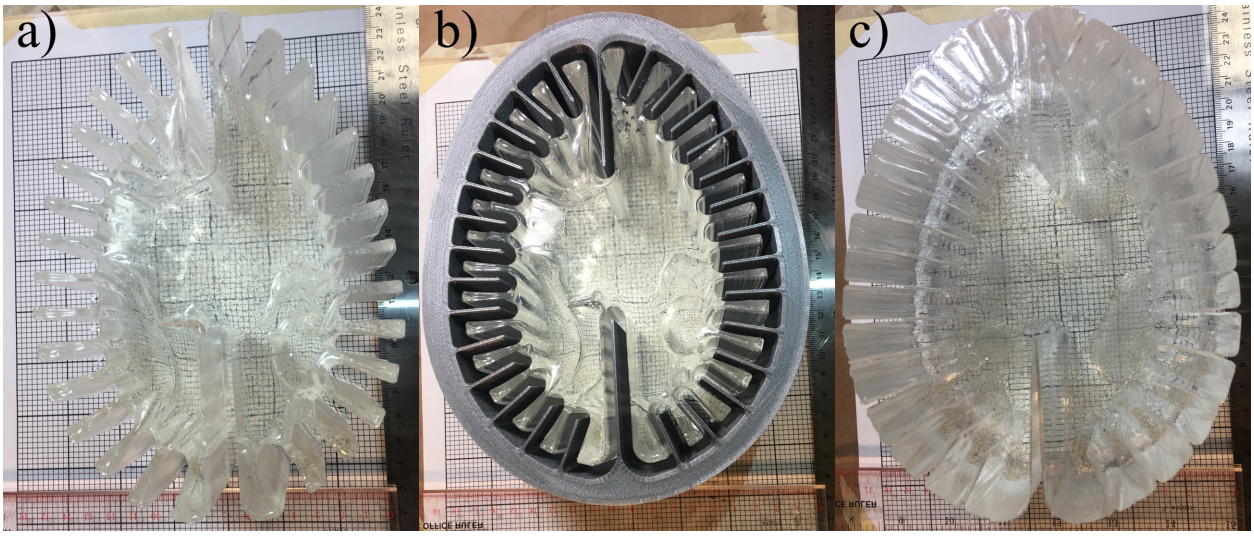


**Figure 3.13.** Fabrication steps of the Biofidelic Brain Phantom; a) Fabricated white mater simulant; b) white mater simulant in gray mater mold. c) fabricated two-material brain phantom.

representation would be discarded and the previous steps would be repeated until an acceptable WM representation was created. An example of the WM gelatin simulant can be seen in figure 3.13a.

The development of the GM simulant was achieved by using a 12% (w / v) solution of Acrylamide in 500 ml of DI water. This slight modification in the formulation was enough to approximate the mechanical properties of GM [137], but otherwise the procedure was unchanged from that of WM formulation. As shown in figure 3.13b, the previously synthesized WM simulant was set in the middle of the GM 3D-printed mold. Then, the 12% PAA solution was poured into the gap between the WM representation and the GM mold immediately after TEMED was added. After the GM was fully cured, the gelatin brain phantom was removed from the molds, obtaining a two-material phantom as shown in figure 3.13c.

After removal of the two-material gelatin phantom from the 3D printed mold it was washed with DI water to remove any surface impurities. A second visual inspection was performed in order to ensure the high quality of all of the gelatin phantoms that were created. Upon passing the visual inspection the gelatin was then submerged into a water bath at room temperature for 24-hours allowing it to swell. This *pre-swelling* step is crucial to maintain the overall anatomical

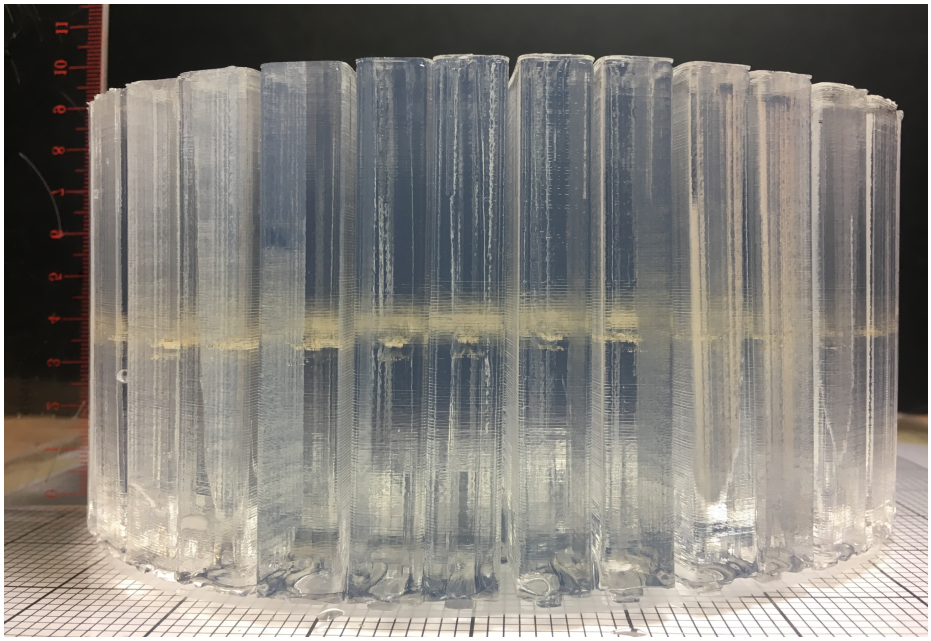

**Figure 3.14.** Side view of two-material gelatin phantom with particle layer located at the mid-plane.

accuracy of the test object because hydrogels are hygroscopic materials they tend to swell in aqueous environments. Without the *pre-swelling* step, the gelatin phantom would subsequently swell within the enclosed test object due to the presence of the artificial CSF. The *pre-swelling* of the gelatin allows for the size and shape of the two-material phantom to remain constant upon final completion of the test object and throughout its use in experimentation.

Upon completion of the 24-hour swelling period, the *swollen* gelatin phantom is then transferred to the 3D printed skull previously discussed in §3.2.2.1. DI water was located within the 3D printed skull, which acts as an artificial cerebrospinal fluid (CSF). Water has been widely accepted as a CSF substitute within the literature for previously performed phantom-based studies [45, 66, 72, 80, 118]. Finally, the gelatin phantom was sealed inside of the 3D printed skull by attaching (using cyanoacrylate glue) acrylic side panels to either side of the skull. In addition to sealing the intracranial contents of the test object these acrylic windows served as optical access points allowing the use of high-speed imaging during experimentation.

There are two additional items regarding the fabrication of the gelatin phantoms that have not been discussed: incorporation of a pressure transducer within the 3D printed skull and embedding of fiducial markers within the gelatin. These two components are important for the test object's incorporation into experimentation; however, they are both standalone factors that do not inhibit the previously described fabrication procedure. For this reason, the pressure transducer incorporation and fiducial markers will not be described in this section. Both of these items will be discussed in detail in §5 and §6. The fabrication procedure detailed in this section is the fundamental basis for the creation of the test object. Any additional item / alteration / modification can be understood as derivations of the original test object. Detail regarding the final dimensions of both the gelatin phantom and the final fully assembled test object are detailed in Appendix B.

As explained at the beginning of this chapter, utilization of a test object required the preserving of important anatomical features in order to understand and relate the mechanical response of the system to real-world loading scenarios. Additionally, an emphasis on adaptability was paramount to the successful implementation of the test object and was stressed at each stage of the test object's

fabrication: conception, design, 3D printing, gelatin formation, and final assembly. To this end, the layout of this chapter presented the necessary foundation to grasp the incorporation of a test object and how care was taken to balance the requirements of both clinical significance and mechanical understanding required to fully comprehend the complex coupled phenomena present when studying TBI / bTBI.

# CHAPTER 4

# EXPERIMENTAL APPARATUSES

There were two different experimental apparatuses used in the investigation into the mechanisms of TBI / bTBI: a drop-tower and a blast chamber. These two apparatuses allowed for the investigation of the test objects' (TO) mechanical response from blunt and blast loading, respectively. The drop tower and the blast chamber were both custom built for their incorporation into studying the effects associated with TBI / bTBI for this research.

The biomechanical loading, as discussed in §1.3, is paramount to understanding the resulting injuries that may occur during an injurious event. The specific aspects relevant for blunt loading (§1.3.1) and blast loading (§1.3.3) were taken into account during the conception and fabrication of the two apparatuses. Additionally, the noninvasive data acquisition requirements were integrated into each apparatus so that there was no interaction or altering of the loading events.

To note, the initial investigation of the TO's mechanical response was intended to be solely for blast loading. The primary reason as detailed in §1.3.3 was due to blast loading being the least understood of the biomechanical loading modes. However, information gathered from preliminary experiments as well as understanding the overall response of the TO emphasized the need for the additional characterization under blunt loading conditions. In addition, understanding how the TOs responds to blunt loading is beneficial for multiple reasons. First, it allows for the direct comparison to the vast clinical data associated with civilian head traumas (e.g., sport injuries, accidental falls, automobile accidents, etc.). Moreover, being able to compare blunt and blast loading for the same TO directly allows for the extraction of either similar mechanisms, different mechanisms, TOs mechanical response, or any other useful mechanical related comparisons.

The next two sections detail the specific drop tower and blast chamber utilized throughout this study. Key features of each apparatus will be discussed therein; specifically, how the noninvasive data acquisition requirements were directly incorporated into the fabrication of each apparatus. To clarify for the reader, the premise of *noninvasive data acquisition* was to utilize an approach that did

not require embedding sensors within the TOs intracranial contents. To this end, an optical approach (i.e., high-speed imaging) was used to capture the TO's response associated with a loading event. Additionally, outlines of the procedures employed for both the drop tower and the blast chamber will be discussed to highlight the care taken to properly conduct experiments and to avoid the limitations associated with blast testing discussed in §2.4.5. It is important to note that despite the beneficial aspects each apparatus does have limitations associated with its use. The individual draw backs will also be briefly discussed in their respective sections.

## 4.1 Drop Tower

A custom-built drop tower was assembled out of 80/20 T-slotted railing (80/20 Inc.) as can be seen in figure 4.1. The height of the drop tower was 1.829 m (6 ft.); however, the base was installed at 0.305 m (1 ft.). The height of the base plate allowed for appropriate placement of the ultra-high-speed cameras, LED lighting, and pressure sensor, which were all used as part of the noninvasive data acquisition technique. The TO was placed directly in the center of the drop tower and was secured in place with a custom frame created out of clear acrylic. This acrylic frame did not inhibit visual acquisition of data, while maintaining the biofidelic test object in the appropriate position.

The TO was loaded using a custom-built impact striker that was 3D printed out of PLA that can be seen on the top of figure 4.1. The striker was designed to be an empty container that was guided down the drop tower using low-friction linear bearings on guide rails. The container portion of the striker was designed for the addition of incremental weights to the striker assembly, which allows for the adjustment of experimental parameters (i.e., different height and weight combinations). Copper balls, with an individual weight of 0.34 g, were selected as the material of choice to achieve incremental weight change for experiments. Copper balls (i.e., Copper BB's) come in a variety of sizes, are readily available, and have high quality manufacturing specifications making them an ideal candidate to use as the drop weight. The individual drop weights used in the experiments will be discussed later in §6. It is important to note that the striker assembly, without any copper balls, has a mass of 1.058 kg.


**Figure 4.1.** 3D CAD Representation of the Drop Tower with Impactor and Biofidelic Test Object. External dimensions: $X$- 61 cm (24 in), $Y$- 46 cm (18in), $Z$- 183 cm (6ft).

The bottom surface of the striker was designed with the same curvature as the frontal region of the skull in order to distribute the load evenly upon impact. This design eliminates localized loading that could lead to perforation of the 3D printed skull. The guiding of the striker, via the linear bearings, ensures proper alignment upon contact with the TO. The alignment between the

impact striker and the TO is evident in figures 4.2 and 4.3. In addition to the alignment feature, there are other key experimental aspects depicted in these two figures. The first item is the clear acrylic frame that maintains the TO's positions within the drop tower; the frame is rectangular and can be seen at the base of the TO.

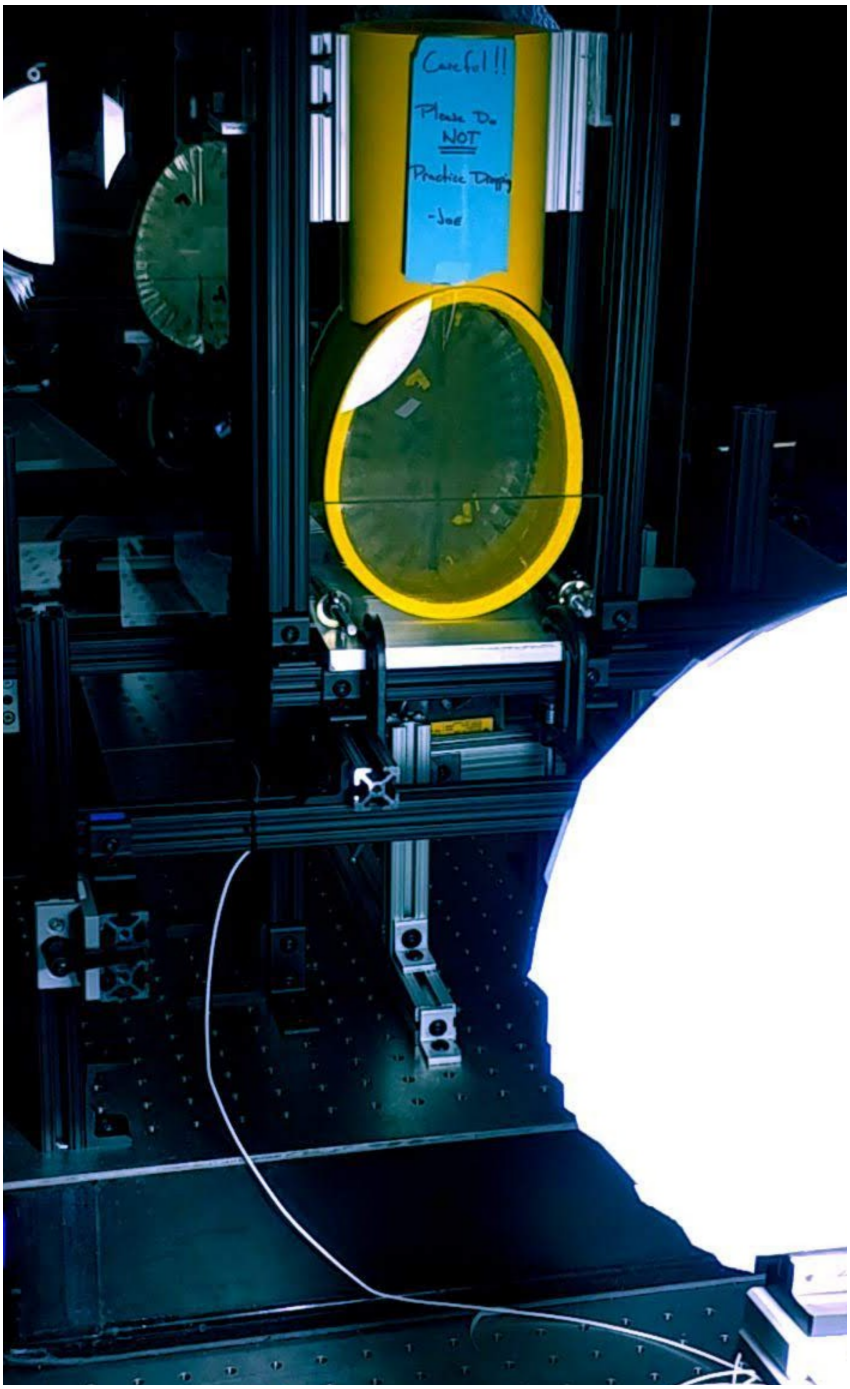


**Figure 4.2.** Example of the Experimental Drop Tower with Test Object, Impact Striker, and LEDs.

The second key feature depicted in figures 4.2 and 4.3 is the LED lighting. The LEDs are located in the foreground of figure 4.2, which corresponds to a backwards illumination set-up (i.e., cameras are located out of view behind the TO). Backwards illumination was used for the entirety of the experiments performed with the drop tower. The orientation of all the experimental components (LEDs, test object, and cameras) is demonstrated in figure 4.3. The backwards illumination set-up was utilized for its overall convenience, but it is important to note that it also provides higher intensity of available light. The significance of this is relevant to the fundamental need of illumination for high-speed imaging. The employment of backwards illumination achieved desirable imaging results for all experimental trials.

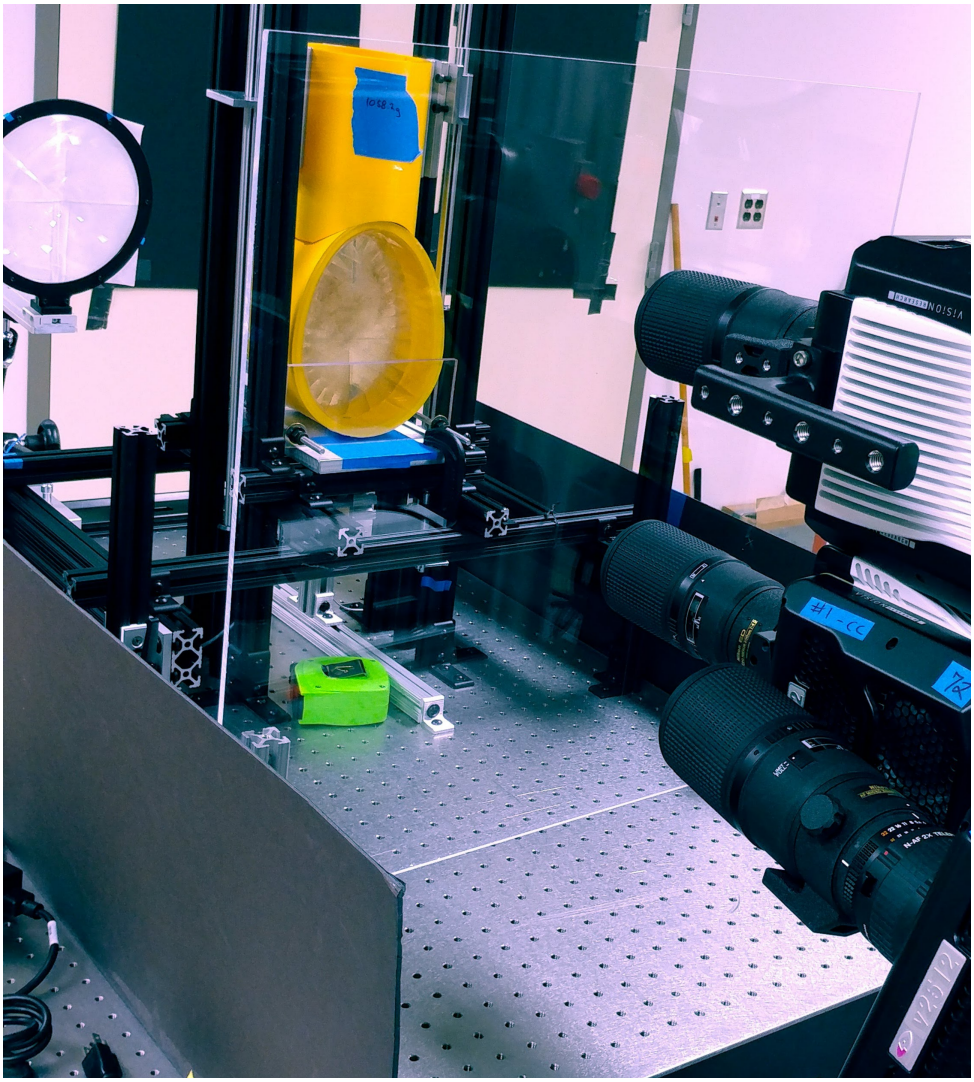

**Figure 4.3.** Example of Backwards Illumination as employed in the Drop Tower Experiments.

### 4.1.1 Data Acquisition & Imaging

Data acquisition was performed through a custom-built LabVIEW Virtual Instrument (VI) program (NI Austin, TX). The VI synchronized the ultra-high-speed cameras (Phantom V2512 Series) with pressure sensor data. The pressure sensor (PCB Piezotronics Inc., Model-113B27) tracked the intracranial pressure at 100k samples per second, while the Phantom cameras recorded images at 25k frames per second at full resolution ($1280 \times 800$ pixels), with a shutter exposure of $20\,\mu$s per frame. The field of view was 75 mm wide by 47 mm high, which was a magnified region of interest within the TO giving an overall spatial resolution of 0.059 mm/pixel. The implementation of the high-intensity LEDs illuminated the mid-layer of particles, as first described in §3.4, which effectively produced a speckle pattern of shadows in the captured images.

### 4.1.2 Experimental Procedure

The general procedure for the drop tower experiments was as follows: obtained a fully assembled biofidelic test object (as described in §3), center the TO within the drop tower and secure its position using the clear acrylic frame; set-up the imaging system (LEDs and camera/s); take time to calibrate and focus camera/s on specific region of interest; establish the experimental parameters (i.e., height of drop, drop weight, etc.); prepare data acquisition system; initiate data acquisition system; and execute experimental trial for specific height / weight combination. Upon completion of the drop, one needs to visually examine the TO for any structural failures to both the 3D printed skull and acrylic optical windows.

The examination of the TO is critical to an understanding of the obtain experimental results. Any damage incurred by the 3D printed skull or at the optical window interface alters the boundary conditions present for the intracranial contents, thus, changing the overall response of the gelatin phantom to the blunt loading. Assuming that the TO was not physically damaged after a drop test, the next drop test combination can be performed. Two experimental drops were performed for each corresponding drop test combination to establish a level of repeatability. The specifics of the experimental test combinations performed will be discussed in detailed in §6.

### 4.1.3 Drop Tower Limitations

The major limiting factor of the drop tower described herein is in regards to the specifications of its fabrication. The drop tower itself was created around the dimensions of the current test object. Thus, the drop tower is the perfect instrument for the blunt related loading of the test object. However, for the exact same reason, the overall dimensions of the current drop tower are limiting with respect to its usefulness for impact loading of different geometries. Furthermore, the incorporation of the current drop tower for different blunt force trauma studies (i.e., animal models) can be difficult, if not altogether impossible, due to the limiting space between the guide rails.

In addition to the limiting space between the guide rails, the overall height of the drop tower is restrictive as it is only 1.83 m (6 ft.) tall. Again, the current height of the drop tower was designed for loading of the biofidelic test object. Therefore, the height is not a concern for the experiments performed for this study. However, if the influence of momentum is to be investigated, the current height would establish the upper bounds available for such a study.

The limitations describe, while being inhibitory in nature, do not affect the experiments conducted for this research. Additionally, due to the overall design and implementation of the current drop tower, modifications can easily be added in order to accommodate any future blunt force trauma studies. Specifically, the use of 80/20 T-slotted railing as the construction material provided an adaptability parameter to the drop tower. Equally important, as seen in figures 4.2 and 4.3, the drop tower was installed on top of an optical table, which allows for alterations to the current dimensions and / or the overall design if necessary.

## 4.2 Advanced Blast Chamber

The specific blast chamber utilized during this research study was custom built at Michigan State University (MSU) and will be referred to as the Advanced Blast Chamber (ABC). The majority of the information presented in this section about the ABC has been previously reported and published within the literature [85]. Mejía-Alvarez et al. [85] details the entirety of the ABC from accounting for known experimental limitations during its conception to the experimental characterization of the facility itself. The purpose of this section is not to repeat all of the information initially presented by Mejía-Alvarez et al. but rather highlight the significance of the ABC's novelty as well as its overall incorporation into studying the mechanisms associated with bTBI. Interested readers who wish to fully understand every facet behind the ABC are encouraged to read the cited reference. The information presented henceforth, covers the general features of the ABC and how they were employed for this research.

The ABC is a large cross-section explosively-driven blast chamber. The cross-section of the facility is 2.03 m × 2.03 m (80 in × 80 in) and the length of its tunnel is 5.5 m (18 ft). The conception of the ABC as pointed out by Mejía-Alvarez et al., was the need to study full-size human models interacting with blast loading scenarios. In order to respect the *blockage* limitation, discussed in §2.4.5, the minimum cross-sectional area required for such studies would be 3.33 $m^2$ (based on the projected area of a human adult being around 0.764 $m^2$ – 0.825 $m^2$). To this end the cross section of the ABC is 4.12 $m^2$, which establishes a blockage of 18.5% – 20.0% for a full-size human mannequin or around 4.24% to a human head phantom including the neck.

In addition to the ABC's large cross-sectional area another attribute of the ABC that makes it unique is the design of its driver section. The production of flat shock fronts is an operational hindrance for all shock-tubes and blast-tubes alike. However, obtaining a flat shock front within a blast chamber is required for the realistic comparison to open-field blast scenarios; details on the specifics of blast waves can be found in §1.5. To this end, the ABC employs a driver section in the shape of a logarithmic spiral, based on shock-focusing theory, to produce low-curvature blast fronts. An example of the logarithmic spiral geometry is illustrated by figure 4.4. Now, the logarithmic

spiral in the ABC generates relatively flat blast fronts, from what is an initially cylindrical wave, by directed reflections of its walls due to the overall geometry. It is important to note that the initial premise of the logarithmic spiral design was to focus a travelling shock wave rather than use it to generate flat shock fronts. The information provided by Mejía-Alvarez et al. demonstrates how the logarithmic spiral geometry is capable of producing a reversible process (i.e., both focusing a shock wave to a line / single point and producing a flat shock wave from said line / single point).

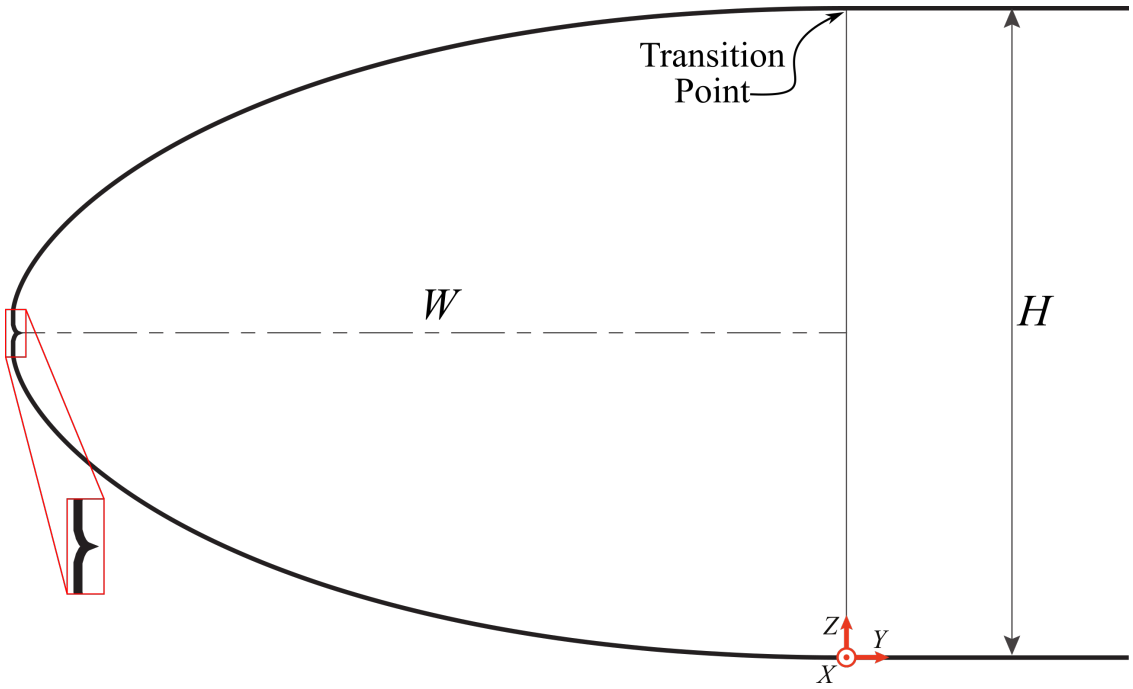


**Figure 4.4.** Example of the Logarithmic Spiral Profile of the ABC. The logarithmic spiral is symmetric (top / bottom) and initiates at a mutual focus point (red box). The driver and driven sections of the blast chamber meet at the Transition Point, where the length of the driver section is $W = 2.41m$ and the height of the driven section is $H = 2.032m$. Adapted from [85]

A significant benefit of utilizing the logarithmic spiral geometry can be seen in the reduction in the overall required length of the blast chamber. The total length of the ABC including both the driver and driven section is 7.9 m (26 ft). This is less than 6.5% the required length associated with a traditional shock tube (122 m) that would have an equal cross-sectional area. This is because the logarithmic spiral reduces the distance necessary for a shock wave to develop into a flat profile; thus, making the ABC a relatively compact experimental instrument for its overall size.

Information pertaining to the full design and construction of the ABC can be found within the previously published work [85]. To note, the blast chamber is entirely enclosed during operational use and exits into a dissipation chamber. This *dissipation chamber* allows for the safe and controlled release of pressure caused by the explosively driven blast wave. The *dissipation chamber* vents to the surrounding environment and reestablishes atmospheric pressure within the chamber post blast.

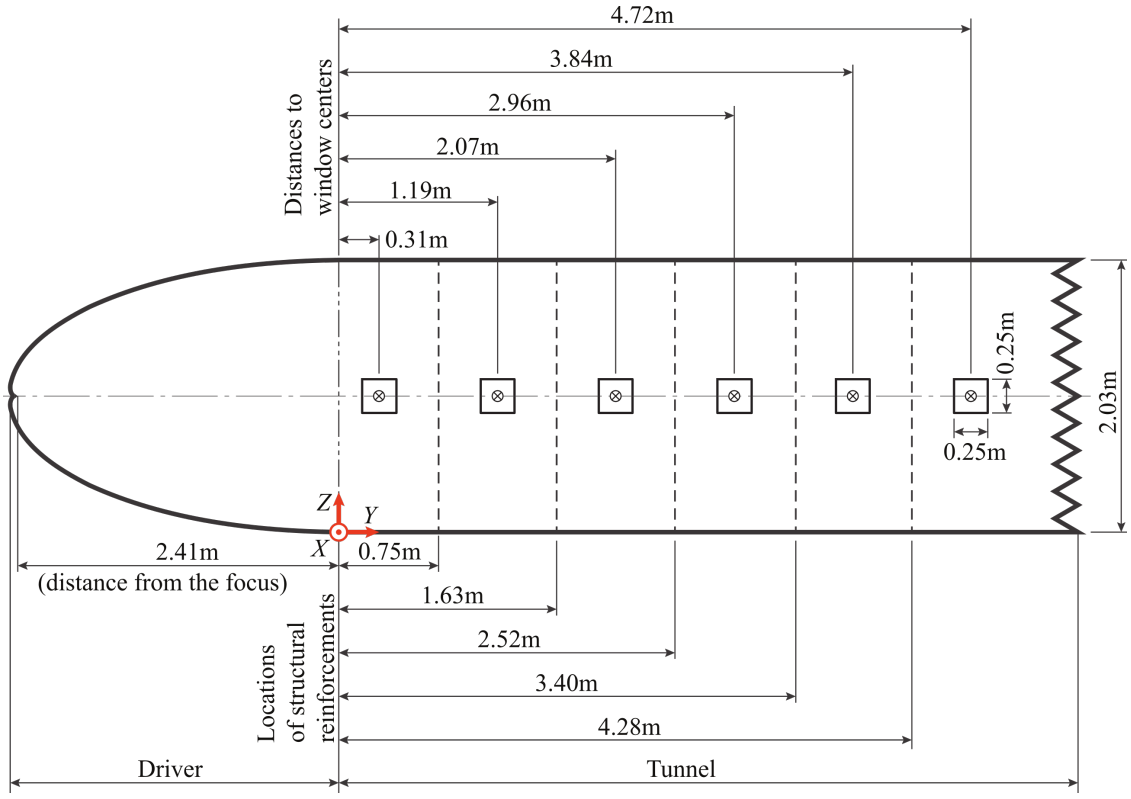


**Figure 4.5.** Side View Schematic of the ABC. Window Standoff Distances and Structural Reinforcement Locations identified. ⊗: window-mounted pressure transducer. Adapted from [85]

A fundamental attribute of the ABC's design is the incorporation of access windows along the length of the chamber walls, as seen in figure 4.5 and 4.6. These access points directly allow the use of a noninvasive imaging system to be employed much like that of the drop tower. As seen in figure 4.5 and 4.6, there are six individual windows corresponding to different standoff distances from where the explosive charge is placed (focus point). Additionally, figure 4.5 illustrates the locations of structural reinforcements located along the chamber's wall and are demarcated by the vertical dashed lines. The structural reinforcements are U-channels and play a key role in the experimental characterization of the chamber discussed below.

In addition to the imaging system, the access windows provide areas where other measurements can be taken (e.g., pressure measurements). Having pressure measures at known standoff distances is integral to understanding how pressure propagates down the length of the tunnel as well as the overall characterization of the ABC; more on this specific topic in §4.2.2. The individual access windows can be set to different configurations depending on the specific experimental interest: optical access, pressure access, or no access (completely enclosed tunnel). Figure 4.6 demonstrates different window configurations.


**Figure 4.6.** Isometric Side View of the ABC detailing Driver and Tunnel sections. Called-out Structural Reinforcements correspond to the vertical demarcated line in figure 4.5. Individual access windows are numerically labeled. Access point for the mounting and detonation of the explosive charges is identified (black circle, left side of figure). Adapted from [85]

The optical access configuration allows for the imaging system to be employed (window *4* in figure 4.6). Upon close inspection one can see that window *4* is transparent and the material selected for the optical windows was polycarbonate. The pressure configurations allows for wall

mounted pressure sensors to be employed. The pressure configuration can be seen in windows *1, 2, 3,* and *5* in figure 4.6, where pressure sensors are mounted in solid 3.8 cm (1.5 in) thick high-density polyethylene (HDPE) blocks. Lastly, the *no access* configuration (not visible in figure 4.6) merely seals the access window while creating a flush surface on the inside of the chamber as to not inhibit the flow of the shock wave during experiments. Any combination of the three configurations can be employed for the entirety of the chamber; however, each individual access window can only be set into a single configuration at any given time (i.e., different mounting windows provide different configurations).

**Figure 4.7.** Example of how Det-cord is mounted along the focus point of the logarithmic spiral of the driver section. Adapted from [85]

Figure 4.6 also demonstrates the access location for the mounting and detonating of the explosive charge. The energetic material of choice for the ABC is Pentaerythritol tetranitrate (PETN). The

advantage of using PETN is due to its use in commercially available detonating cord (det-cord). Det-cord is a thin, flexible plastic tube that has PETN loaded into its core. Additionally, due to the geometry of the driver section, det-cord is advantageous because it can easily be placed and secured at the desired focus point of the logarithmic spiral, as demonstrated by figure 4.7. Properly mounting the energetic material to the focus point is fundamental to obtaining a flat shock front upon detonation. This point will be discussed further in §4.2.2. Figure 4.7 only shows a single strand of det-cord, but additional strands can be attached to this primary strand in order to increase the mass of the explosive charge, which ultimately increases the overpressure of the blast wave.

### 4.2.1 Data Acquisition & Imaging

The data acquisition and imaging system utilized for experiments at the ABC was the exact same as the drop tower experiments, first detailed in §4.1.1. Pressure measurements were acquired at a sampling rate of 100kHz. High-speed imaging was captured at 25k frames per second. To note, the magnification factor is different for the captured images from the ABC experiments in comparison to the drop tower due to the larger focusing distance required for operational safety. Backwards illumination was employed by using high-intensity LEDs for all experiments performed with the ABC.

An additional aspect required for the ABC is to have the data acquisition started remotely (i.e., cameras and pressure sensors are triggered from a safe and secluded location). This stems from the risks associated with the proximity to a detonation source. The data acquisition is initiated by the Control Point Officer prior to the detonation of the energetic material.

### 4.2.2 Experimental Procedure

The experimental procedure for the ABC generally follows that of the drop tower. However, due to the elevated safety concerns associated with the use of energetic material, there are additional steps to the overall procedure in order to perform experiments with the ABC. Prior to any experimentation a visual inspection of the ABC is performed by operational personnel to ensure the integrity of

the chamber has not been compromised. Any and all safety concerns are appropriately assessed and corrected before continuing with the planning / preparation / execution of energetic related experiments.

The first step in the experimental procedure when utilizing the ABC is to determine the desired overpressure to which the tests materials are to be exposed. To note, the term *test materials* is used as a general term because the conception of the ABC is intended for a variety of materials /geometries to be tested (e.g., fabricated test objects, human mannequins, large animals, composite structures, etc.). The desired overpressure directly dictates operational variables required for an experiment – the mass of the explosive charge and the standoff distance. The combination of the explosive charge weight / standoff distance is capable of achieving a range of overpressures within the chamber. Specifically, closer standoff distances for the same mass of explosives will achieve higher overpressure. Conversely, farther standoff distances will reduce the total overpressure experienced by the test materials. Once the selection of the desired overpressure has been established, the other experimental parameters can be set.

The overpressure selection allows for the explosive charge weight and standoff distance to be determined. The determination of the explosive charge weight and standoff distance is based on preliminary experiments performed to characterize the pressure attenuation within the ABC. Details pertaining to the ABC's characterization will be discussed in detail in the next section, §4.2.3. Once the standoff distance is established, the data acquisition systems can be installed at their appropriate locations. As seen in figure 4.6, the access windows have physical locations along the length of the chamber. These are the ideal locations for experimental setup as they directly allow visual observation during the blast loading event.

After the installment of the data acquisitions system the mounting of the specific test materials can be conducted. To achieve mounting within the blast chamber itself, two custom-built tension rods were fabricated. These tension rods were designed to withstand the exerted force of a blast wave, while also being movable within the chamber as so desired. To clarify, the tension rods can be positioned at any desirable location within the ABC (i.e., different standoff distances). Once

in position, the tension rods are bolted against the inside chamber walls resulting in them being held in place by friction. The test materials are mounted on the tension rod/s at a desired location and fixed into position. Upon the completion of mounting the test material a final check of the data acquisition system is performed. The successful triggering of the data acquisition system allows the final step of the experimental procedure to proceed.

The final step performed for the ABC is the mounting of the energetic material. For safety reasons, setting the explosive load must be the last operation that takes place in the ABC before an experimental run. Prior to the handling of any explosive material all unnecessary personnel are removed from the ABC's facility. The energetic material is only handled by approved personnel that have been properly trained. After successful mounting of the explosive charge the driver section's access points are secured and the remaining personnel are relocated to a safe operational distance before performing the experiment run.

As stated in §4.2.1, each experimental run is initiated by the Control Point Officer located at a safe operational distance. The control point officer triggers the data acquisition system in sequence with detonating the energetic material. Visual inspection of the ABC's facility is performed remotely using security cameras after the detonation to ensure a safe environment before re-entering the facility. The individual experimental run is completed only after the Lead Chamber Officer clears the shot and communicates to the remaining personnel of safe operating conditions.

Before conducting any additional experimental runs, the ABC and the experimental components are visually inspected. The ABC is inspected again to ensure that its integrity has not been compromised. Test materials and mounting structure (i.e., tensions rod/s) are inspected to ensure no physical damage has been incurred or movement has happened within the blast chamber itself. Lastly, the collected data is saved for later analysis.

### 4.2.3 Characterization of ABC

There were two sets of experiments performed in order to characterize the pressure profiles present in the ABC. Full details of the experimental characterization have already been presented by

Mejía-Alvarez et al. [85]. Excerpts of these experiments are presented herein to emphasize their importance and to explain how the said experimental characterization is utilized for experimental planning.

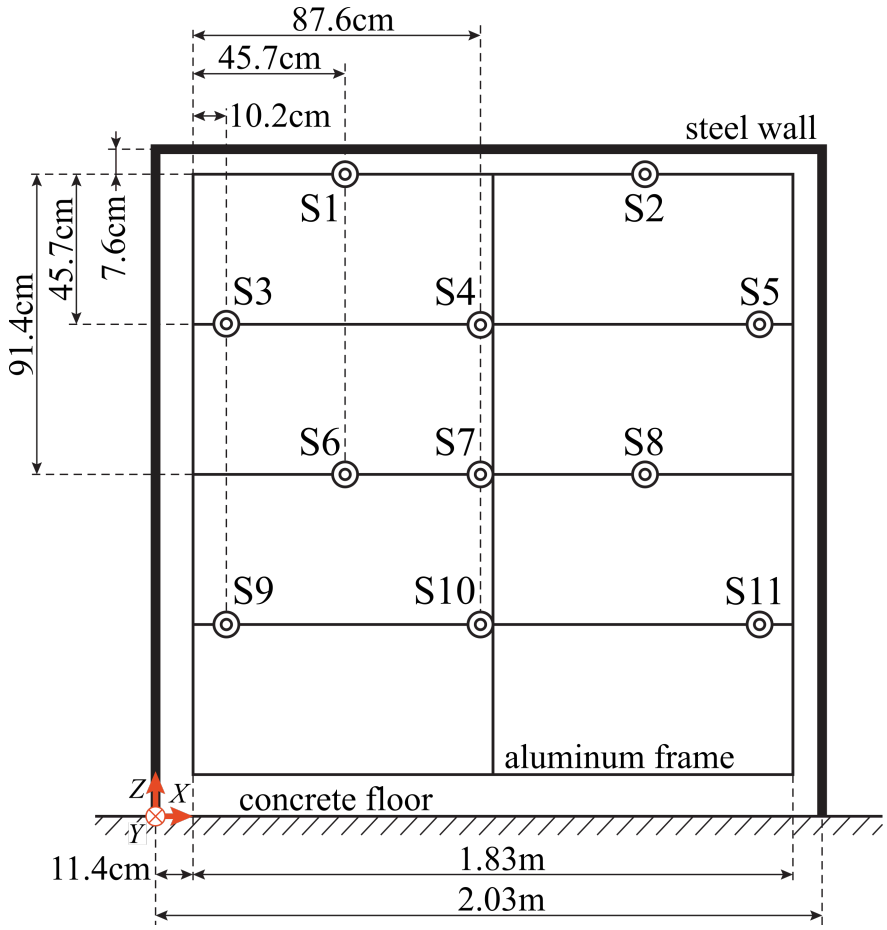


**Figure 4.8.** Pressure transducer array used to obtain pressure profiles at fixes streamwise locations. ◎: pressure transducer locations. [85]

The two characterization experiments performed have brought clarity to the overall behavior of the blast waves within the ABC. The first experiment's objective was regarding the *flatness* profile of the blast front. The *flatness* of a blast front directly communicates as to how well-developed the blast may be. This is imperative information for experimental planning as it expresses just how close to the inlet of the tunnel a test object can be mounted. To investigate the flatness profile of the blast waves within the ABC, a custom-built symmetric frame was instrumented with pressure transducers (PCB Piezotronics Inc., Model-113B27). The pressure transducer layout on the frame can be seen in figure

4.8. As illustrated in figure 4.8, the specific locations of the pressure transducers have been identified with the terminology *S1, S2, S3,* etc. and the symbol ◎. Additionally, the overall dimensions of the frame as well as the mounting location within the tunnel (w.r.t the $xz$–plane) of the ABC are presented in figure 4.8. The pressure array was mounted on the previously discussed tension rods, which were located at either the second (1.63 m) or third 2.52 m) structural reinforcement location as presented in figure 4.5.

The mounting of the pressure array at the second (1.63 m) or third (2.52 m) structural reinforcement locations correspond to standoff distances of 4.04 m and 4.93 m, respectively. The investigation of the *flatness* profile for blast waves was evaluated at each of these two locations as well as compared to one another. The results obtained from the pressure array experiments indicate a low degree of tilt and curvature (i.e., high *flatness*) is present in the blast waves generated in the ABC. For the exact results of the pressure array experiments refer to the previously published work [85].

The second set of experiments were conducted to investigate how blast waves evolve as they propagate down the length of the ABC's tunnel; specifically, how pressure attenuation is affected by changes in the weight of the explosive charge. Understanding the pressure attenuation within the ABC is crucial to experimental planning. Therefore, by understanding the blast characteristics (such as overpressure) as a function of the explosive charge weight and standoff distance directly allows for this information to be applied to other blast-studies. As stated previously, the selection of the desired overpressure experienced on a test object is the first step in experimental planning; thus, making overpressure characterization of the ABC essential.

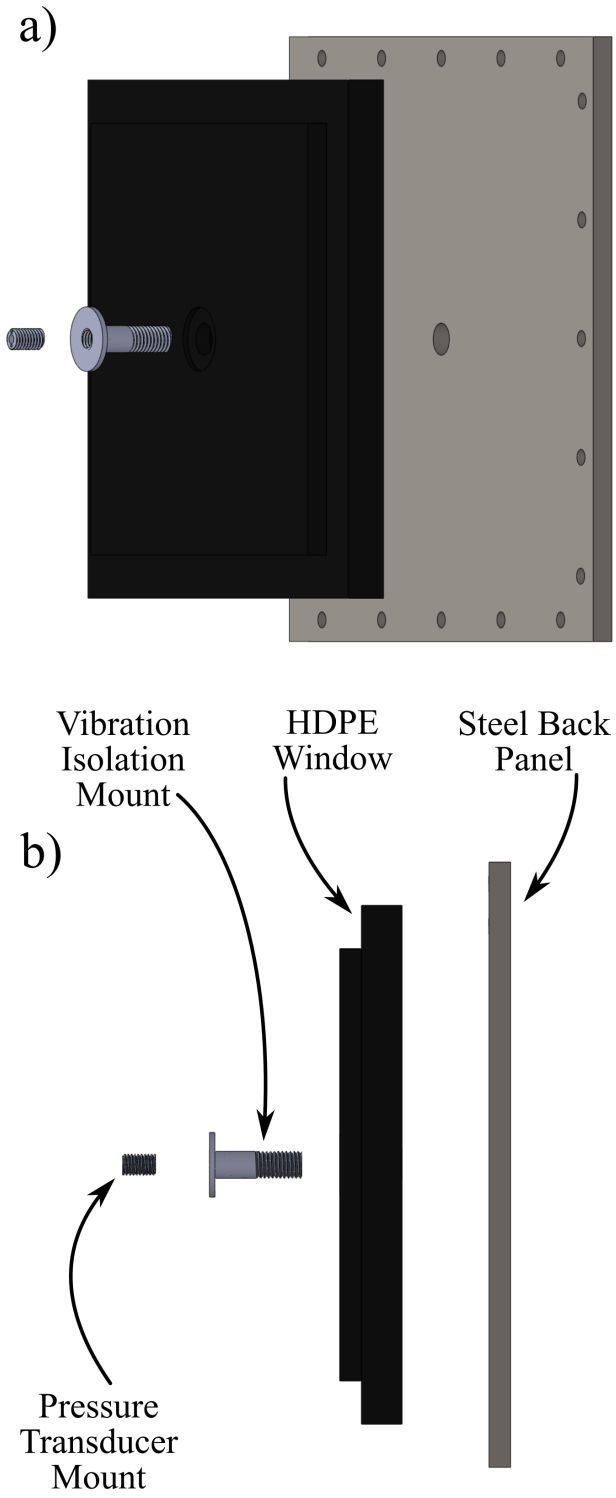


**Figure 4.9.** Representation of the wall-mounted pressure sensor assembly used during pressure attenuation characterization of the ABC. a) Exploded isometric-view, b) Exploded side-view with labels of the individual components.

In order to investigate the evolution of pressure down the length of the tunnel a series of wall-mounted pressure sensors were employed. As previously described in §4.2 and seen in figure 4.5 there are six access windows located on either side of ABC.The pressure sensors themselves were embedded into 3D printed vibration isolation mounts and secured into the high-density polyethylene (HDPE) windows. These HDPE windows were positioned in each access point along the chamber walls of the ABC and are marked by the symbol ⊗ in figure 4.5. Subsequently, all of the HDPE windows were secured into place by back-supported 6.35 mm (1/4 in) thick steel frames. The wall-mounted pressure sensor assembly is demonstrated in figure 4.9. An exploded isometric view of the wall-mount assembly is presented in figure 4.9a, which illustrates how the individual components of the assembly fit together. Figure 4.9b is a side-view of the same assembly demonstrating the profile shape of each component. Aspects not clear in figure 4.9 are the tolerances within the vibration isolation mount itself. To reduce the overall vibration the pressure sensors experienced during experiments, the 3D printed mount's flange was isolated from the HDPE window using a rubber washer. Additionally, the shaft of the 3D printed mount was entirely isolated from both the HDPE window and steel back-support by an air gap. These two features increased the signal-to-noise ratio for the pressure sensors, allowing clear detection of the rising edge and peak overpressure duration present for each of the experiments conducted.

The results gathered from the pressure attenuation characterization have been integral to the subsequent experiments performed using the ABC. Specifically, the information provided from the experimental results were generalized into equations that described the operational conditions necessary to obtain a desired peak overpressure. These equations describing peak overpressure are functions of the mass of the explosive charge (i.e., number of det-cord strands ($N_s$) used) and the standoff distance from the focus point of the logarithmic spiral. The equations themselves can be found in [85].

Five explosive charges of different weights were detonated and the subsequent static pressure profiles were recorded at each access window. The results for the pressure attenuation experiments can be seen in figure 4.10. Note, the $Y$ distance values in figure 4.10 correspond to window standoff

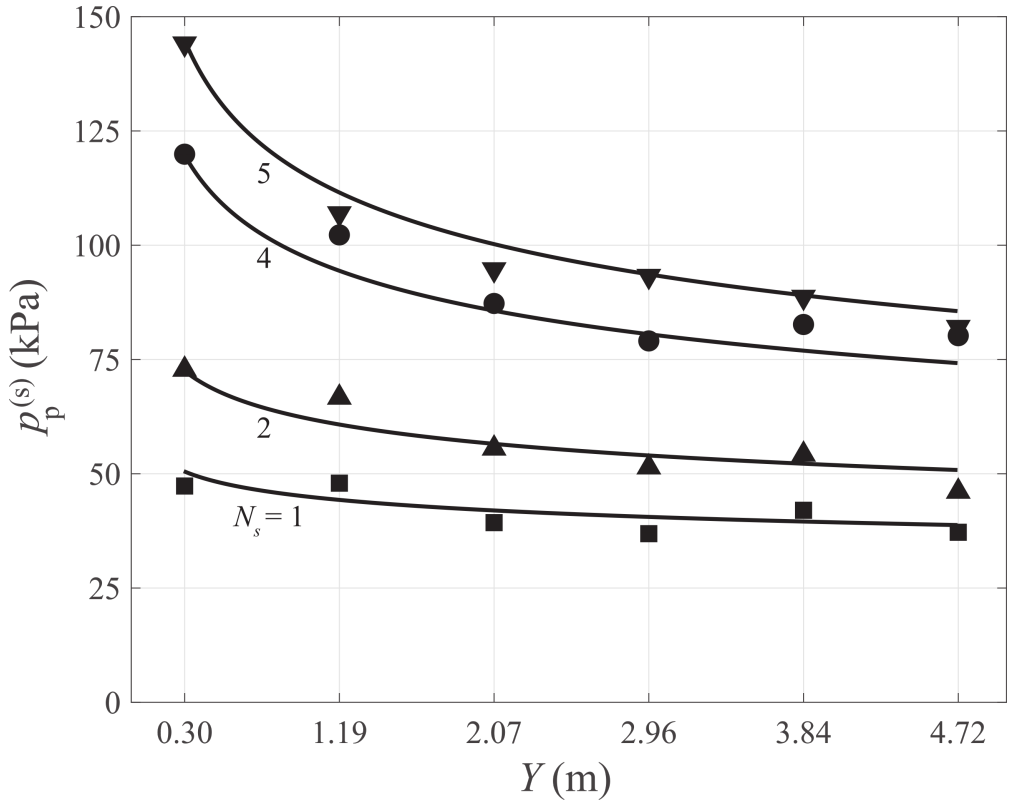


**Figure 4.10.** Peak overpressure, $p_p^{(s)}$, as it decays along the ABC tunnel for $N_s = 1$ (■), $N_s = 2$ (▲), $N_s = 4$ (●), and $N_s = 5$ (▼). (–): estimates the peak overpressure curves based off individual data points. Error bars: not shown because they are fully contained within symbols. Adapted from [85]

distances in figure 4.5. Additionally, note that the data for $N_s = 3$ is not presented in figure 4.10. This is not an accident as there was an error in the data acquisition system ultimately causing the data to be lost for the $N_s = 3$ experimental trial. Information regarding the blast speed decay and overpressure duration were also analyzed from the gathered experimental results. Both of these additional characteristic can be used to aid in experimental planning but will not be detailed herein. Readers may refer to [85] for specifics.

The observations of the overpressure and blast speed decay (i.e., Mach number) demonstrate a power-law decay behavior for the blast waves generated in the ABC. Furthermore, the results from wall-mounted pressure attenuation experiment give a nominal overpressure duration value of $\approx 1.3$ ms. This is significant because 1.3 ms is a quick overpressure duration for an experimental environment but quite representative of those experienced in real-world blast loading scenarios.

The findings from the pressure array and pressure attenuation experiments demonstrated that the ABC is capable of producing low-curvature blast waves in a relatively short distance that also have extremely small overpressure durations. These are significant findings that not only validate the use of the ABC, but also established criteria that can aid in designing future experiments using the ABC.

### 4.2.4 ABC Limitations

Despite its successful execution and positive experimental results, the ABC is not without its own limitations. These limitations are primarily the same as first detailed in §2.4.5: physical space, technical expertise, proper experimental set-up and data acquisition, governmental regulations, and the elevated operational risk associated with explosive handling, etc. In addition to these limitations, the ABC has two extra aspects that need to be accounted for in order to perform experiments. First is the required operational personnel and logistical planning; the ABC requires a team of personnel to successfully execute experimental operations, which includes scheduling, chamber preparation, proper safety communication, and operational redundancies. The second unique attribute of the ABC is in regards to the power-law decay behavior it exhibited during the characterization experiments. This behavior establishes an upper limit to the overpressure that can be achieved with the ABC under the same experimental parameters (i.e., explosive source (PETN)). This power-law behavior is not explicitly a operational limitation – rather, it was an experimental observation highlighted for its importance concerning future experimental planning. Any future study employing the ABC will need to take this behavior into account. With this being said, the power-law behavior does not inhibit the use of the ABC for bTBI related experiments. This is directly reflected in the overall positive results obtained from the two characterization experiments.

# CHAPTER 5

# EXPERIMENTAL METHODS

The following experiments were performed to assess the mechanical response of the biofidelic test object (TO) as well as to investigate the potential mechanisms associated with bTBI, as previously discussed in §2.1. The experiments were performed using the drop tower and the ABC following their respective procedures detailed in §4. Any deviation from the previous discussed procedures will be highlighted herein along with the experimental parameters for each performed test.

## 5.1 Drop Tower

A total of six (n=6) drop tower trials were performed. The drop height for all experiments was 1.016 m (40 in), while three individual drop weights used were: 1 kg, 2 kg, 3 kg. The drop weight values are rounded to their closest integer value to streamline discussion; however, the exact experimental parameters of each test can be seen in table 5.1. As seen in table 5.1, there were two experimental drops performed for each corresponding weight. Additionally, the theoretical energy present during impact is also presented, which is based on the conservation of energy for the corresponding input parameters. A preliminary set of experiments demonstrated the limited reliability of repeated drops on a single TO – it was determined from these preliminary experiments that the safe operating range for a single TO was not to exceed six drops. Thus, only six-drop tower experiments were performed.

**Table 5.1.** Experimental parameters for the individual drop tower experiments.
*Denotes calculated value from theory.

| Test no. | Weight [kg] | Height [m] | Energy [J] |
|---|---|---|---|
| 1 | 1.058 | 1.016 | 10.50* |
| 2 | 1.058 | 1.016 | 10.50* |
| 3 | 2.018 | 1.016 | 20.12* |
| 4 | 2.018 | 1.016 | 20.12* |
| 5 | 3.0 | 1.016 | 29.90* |
| 6 | 3.0 | 1.016 | 29.90* |

Important to note, that both aerodynamic resistance (i.e., drag) on the striker and the presence of mechanical friction within the striker assembly are negligible. The presence of friction is unnoticeable due to the high-efficiency linear bearings. Similarly, the drag imposed for the experimental drop height, table 5.1, would only be 0.08%. These observations allow the striker's speed to be calculated from the non-dissipating equation for free-fall.

Three ultra-high-speed cameras (Phantom V2512 Series) were employed for these drop tower experiments. The cameras were focused on three separate regions-of-interests (ROI): coup, contrecoup, and an individual sulcus. These three regions were chosen due to their relevance associated with damage seen clinically. All cameras were set to record at 25k frames per second and were synchronized allowing for comparison of the ROIs to one another within the time domain. The coup and contrecoup ROI were both framed around the central gyrus with two additional gyri on either side. The individual sulcus ROI was located at the first distal position off the central gyrus on the contrecoup side.

A pressure transducer (PCB Piezotronics Inc., Model-113B27) was embedded into the 3D printed skull in order to track the intracranial pressure (ICP) during blunt loading and can be seen in figure 5.1. The incorporation of a pressure transducer is an extension of the TO originally described in §3.4. The importance of understanding the ICP evolution during a mechanical loading event has been discussed extensively in §2.1; hence, the incorporation of a pressure transducer into the final design of the 3D printed skull. Figure 5.1a demonstrates how the pressure transducer was threaded in from the outside of the 3D printed skull, resulting in a water tight seal. Figure 5.1b illustrates the total surface area of the pressure transducer exposed to the intracranial contents. The pressure transducer was designed to be located directly in the midplane (z-direction) of the 3D printed skull on the contrecoup side. This location, much like the ROI chosen for each camera, was selected for its relevance based on clinical data. The pressure measurements were sampled at 100kHz. This provided four data points of pressure for every captured image from the high-speed cameras. Additionally, a laser-based displacement sensor (Model LK-G5001P, Keyence Corporation) was positioned to track the downward displacement present at the contrecoup region of the skull.

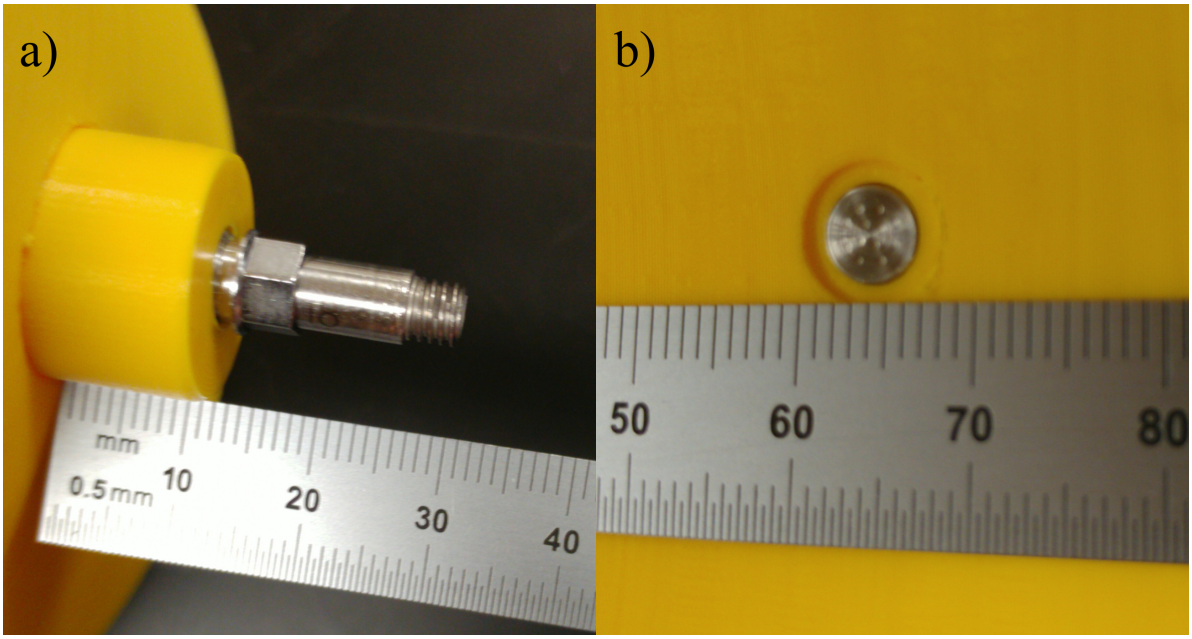


**Figure 5.1.** Embedded pressure transducer in the 3D printed skull.
a) illustrates the pressure transducer threaded into the pressure cap from the outside of the skull,
b) illustrates the exposed surface area present on the inside of the skull.

The last experimental parameter involved in the drop tower trails was the material selection for the base plate. The drop tower was designed with the ability to remove the base plate in order to change it as an additional experimental variable. The premise for this was, if desired, a parametric study could be performed in order to investigate the influence of boundary conditions. With this being said, all six trials discussed herein were performed using a 152.4 x 177.8 x 12.7 mm (6 x 7x 0.5 in) slab of 6061 aluminum. The material selection choice of the base plate will be discussed further in §8.

## 5.2 Advanced Blast Chamber

There were a total of six (m=6) trials performed using the ABC to investigate blast loading on the TO. The six trials were divided into two explosive charge weight categories: 86.4 g and 172.8 g. These two categories will be referred to as *lower exposure* and *higher exposure* from this point on. The explosive weights were selected to achieve overpressures that would correspond to mild and moderate blast exposure, respectively. bTBI is classified into four distinct categories as discussed in

§2.1; however, bTBI can further be classified by the range of its severity: mild, moderate, and severe. Now, the exact pressure thresholds for each category have yet to be definitely established. Therefore, the desired overpressure for the ABC experiments were chosen based on the data from the pressure attenuation characterization of the ABC described in §4.2.3. Specifically, the characterization equations developed by Mejía-Alvarez et al. were used to calculate the explosive weights that would correspond to overpressures around 12 psi (83 kPa) for mild bTBI and 20 psi (138 kPa) for moderate bTBI, resulting in the previously mentioned 86.4 g and 172.8 g. To note, these overpressures correspond to the standoff distance associated with the fourth access window as seen in figure 4.5.

**Table 5.2.** Experimental parameters relating the length of 50 grain/ft detonation cord (10.8 g/m) to its explosive mass of PETN and its TNT Equivalence

| $N_S$ | **Det-cord Length** | **Weight of PETN** | | **TNT Equiv.** | |
|---|---|---|---|---|---|
| | [m] | [g] | [lb] | [g] | [lb] |
| 1 | 2.03 | 21.60 | 0.0476 | 23.205 | 0.051 |
| 2 | 4.06 | 43.20 | 0.0952 | 46.410 | 0.102 |
| 3 | 6.10 | 64.80 | 0.1429 | 69.615 | 0.153 |
| 4 | 8.13 | 86.40 | 0.1905 | 92.820 | 0.205 |
| 5 | 10.16 | 108.00 | 0.2381 | 116.025 | 0.256 |
| 6 | 12.19 | 129.60 | 0.2857 | 139.230 | 0.307 |
| 7 | 14.22 | 151.20 | 0.3333 | 162.435 | 0.358 |
| 8 | 16.26 | 172.80 | 0.3810 | 185.640 | 0.409 |
| 9 | 18.29 | 194.40 | 0.4286 | 208.845 | 0.460 |
| 10 | 20.32 | 216.00 | 0.4762 | 232.050 | 0.512 |

The ABC was designed with the implementation of Detonation cord (det-cord) as its energetic material of choice. Det-cord is a flexible plastic tubing with PETN loaded within its core. The specific det-cord used in all experiments was 50 grain/ft (10.8g/m). Thus, to achieve the desired explosive weights aforementioned, only the total length of det-cord needed to be changed. Furthermore, the implementation of the det-cord within the ABC has been design to correspond to integer values of the chamber's width (e.g., a single strand ($N_s = 1$) is 2.03 m and 21.6 g, double strand ($N_S = 2$) is 4.06 m and 43.2 g, etc.). This is explained further in table 5.2. Table 5.2 demonstrates the explosive weights up to 10 strands ($N_s$) of det-cord. The specific number of strands of det-cord that correspond to explosive weights of interest for these experiments are $N_S = 4$ and $N_S = 8$.

As stated previously, the weight for the explosive charges were established to achieve the desired overpressures at the downstream distance of 3.84 m within the tunnel. The data acquisition system was set-up and arranged accordingly in order to capture the high-speed images and pressure data. Before the final step of mounting the TO within the chamber can be discussed, incorporated modifications to the TO assembly need to be explained.

In order to increase the anatomical accuracy of the TO assembly a Hybrid-III $50^{th}$ Male neck (Humanetics Innovative Solutions Inc.) was incorporated. The Hybrid-III $50^{th}$ Male neck (H3N) is part of the overall Hybrid-III $50^{th}$ Male anthropomorphic test device (ATD). The Hybrid-III $50^{th}$ Male ATD is the most widely used crash test dummy in the world for the evaluation of automotive safety restraint systems in frontal crash testing and was developed in conjunction with the National Highway Transport and Safety Administration (NHTSA). The H3N has been designed to match the angle-torque response data in forward (flexion) and rearward (extension) directions for humans seated in automotive posture [54]. Thus, the incorporation of the H3N allows for investigations into the angular component associated with the mechanical response of the TO.

Incorporating the H3N into the TO assembly required the fabrication of several custom mounts. The H3N was originally designed to be attached to the overall Hybrid-III $50^{th}$ Male ATD in a vertical position. Therefore, in order to integrate the H3N within the TO assembly the custom mounts were required to be robust and resilient in order to withstand the blast loading. Additionally, the mounts needed to be attached to the TO and H3N in a manner that would not change the natural response of the neck itself. These design restrictions along with their engineered solutions will be highlighted in the next section.

### 5.2.1 Head-Neck Assembly

The incorporation of the H3N required a solution that could withstand the force applied during blast loading that simultaneously did not inhibit the natural response of the system. Restricting the H3N response would ultimately affect the anatomical relevance of the mechanical response. To this end, the solution was to create three individual custom in-house fabricated mounts that connected the TO

to the H3N and allowed them to be mounted together. The three custom fabricated mounts are H3N bottom mount, the H3N-to-skull mount, and the test object alignment mount. These mounts along with an example of the full head-neck assembly is demonstrated in figure 5.2.

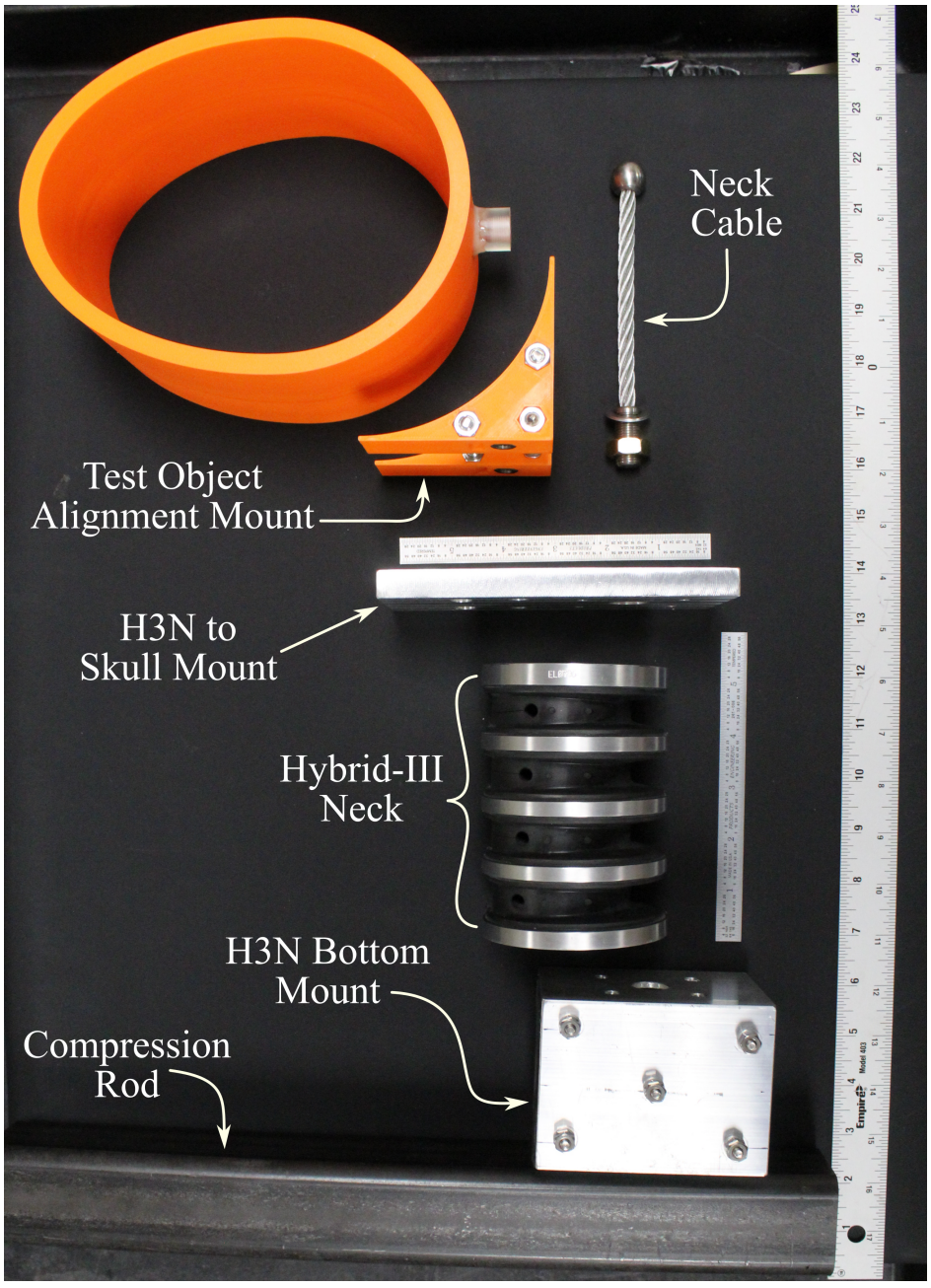


**Figure 5.2.** Exploded view of the head-neck assembly with individual component callouts.

Each of the custom fabricated mounts serve their own unique purpose. The H3N bottom mount is a U-channel of 0.125-inch wall-thickness that is mechanically fixed to the H3N using screws. This mount is then able to attach to the compression rod in a tight friction fit due to the incorporation of a zero-inch tolerance gap created by two layers of 0.375 in neoprene rubber, which can be seen in figure 5.3. The H3N bottom mount is then clamped to the compression rod, which compresses the neoprene rubber creating a tight rigid connection. The U-channel design allows for the full TO assembly to be finely adjusted within the ABC as needed to focus the high-speed cameras, while simultaneously being able to be clamped down securely.

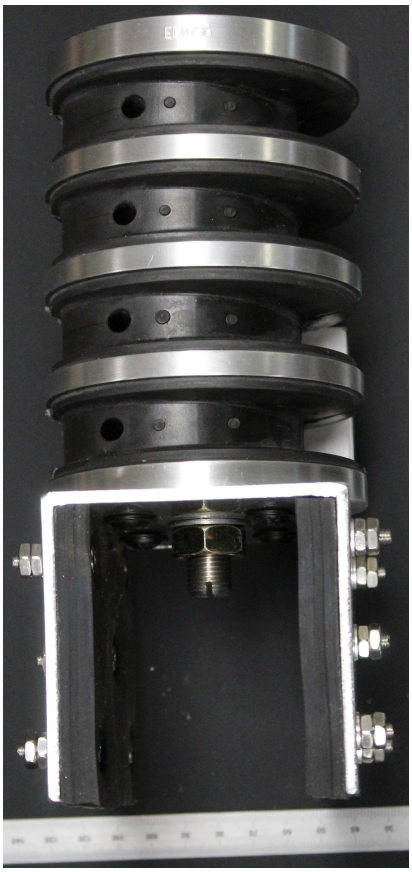

**Figure 5.3.** Hybrid-III Neck attached to its Bottom Mount.

The next mount to be discussed in the H3N-to-Skull mount. This mount was fabricated out of 0.5-inch thick 6061 aluminum stock and can be seen in figure 5.4. The purpose of this mount was to utilize the pre-existing mounting holes on the H3N in order to connect the TO to the H3N. This was achieved by machining the aluminum stock to a predetermined size with several different mounting

holes. There were three different sets of mounting holes incorporated into the H3N-to-Skull mount. The first set connects the mount directly to the H3N itself. The second set connects to the TO-Alignment mount through the opposite side of the H3N-to-Skull mount. Finally, two channeled through-holes were added to allow the TO to be securely attached to the neck assembly. Clarity as to how each set of mounting holes for the H3N-to-Skull mount is used can be seen later in figure 5.6.

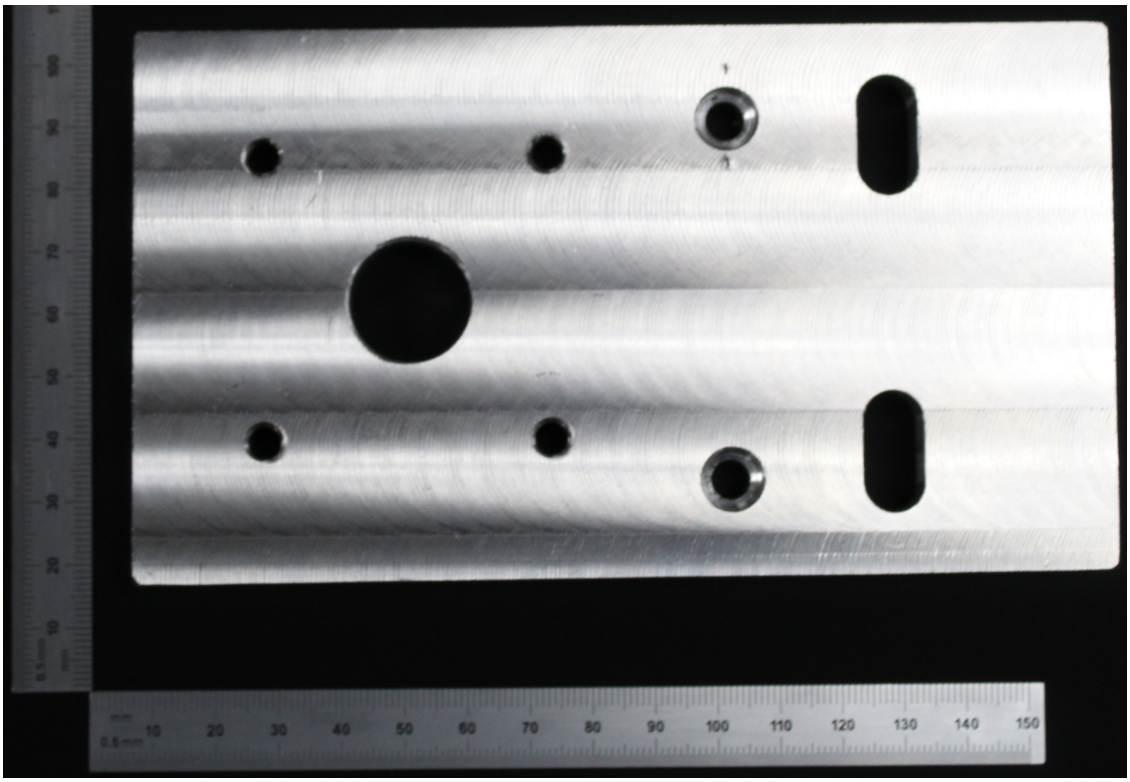


**Figure 5.4.** The H3N-to-Skull mounting bracket. (from left to right): H3N mounting holes (2), neck cable through hole, another set of H3N mounting holes (2), counter sunk test object alignment mount holes, channeled through-holes (2).

The last custom fabricated mount was created to be able to properly align the TO during the experiments. The significance of this was to maintain the proper configuration for the TO (e.g., head-on versus side-on); head-on configuration was of interest during these ABC experiments. To achieve the desired alignment, the external curvature of the contrecoup portion of the skull was incorporated into the geometry of the TO-Alignment mount. The TO-Alignment mount itself was created by 3D printing two identical components and rigidly connecting the components using

mechanical fasteners. Figure 5.5 demonstrates each of the different components involved in the full TO-Alignment mount. As seen in figure 5.5a, the individual 3D printed parts were designed with recesses intended to embed the mechanical fasteners flush with its surfaces. The individual fasteners were comprised of 1/4"-20 threaded rod and zinc-coated steel nuts, which are detailed in 5.5b. The assembled TO-Alignment mount can be seen in figure 5.5c. Additionally, figure 5.5d also demonstrates the fully assembled TO-Alignment mount. Figure 5.5d illustrates the isometric-bottom-view of the TO-Alignment mount, where the left-side corresponds to the bottom of the mount and the right-side corresponds to the back of the mount.

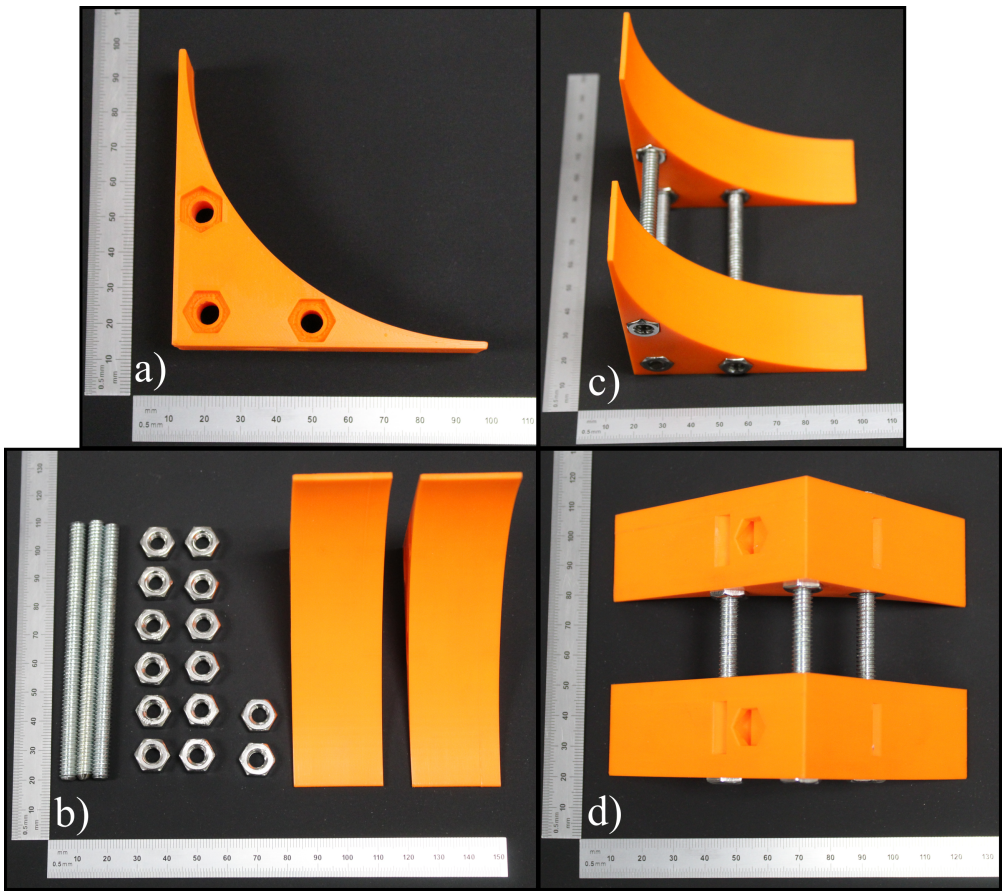


**Figure 5.5.** Multiple views of the Test Object Alignment mount. a) Side-view of an individual 3D printed component, b) Image of the individual components, c) Isometric-Top-View of the full assembled mount, d) Isometric-Bottom-view presenting additional mounting aspects.

The bottom of the TO-Alignment mount (left-side of figure 5.5d) has two extra features to highlight: additional recesses designed for mechanical connectors and through channels. The

recesses on the bottom of the 3D printed components have the same intention as the others; however, rather than connecting the individual components together, these recesses are to be used to connect the TO-Alignment mount to the H3N-to-Skull mount. Once the TO-Alignment mount is connected to the H3N-to-Skull mount, the through channels seen in figure 5.5d will align with the channeled through holes seen in figure 5.4.

The assembly and alignment of all of the custom fabricated mounts with the hybrid-III neck and test object itself can be seen in figure 5.6. The information provided in figures 5.2 and 5.6 are complimentary to one another, but both have unique aspects that help to fully understand the implementation of the hybrid-III neck. For instance, figure 5.6 demonstrates how the H3N-to-Skull mount attaches to the TO-Alignment mount from the bottom. Additionally, figure 5.6 illustrates the alignment of the channeled through holes in the H3N-to-Skull mount with the through channels in the 3D printed components of the TO-Alignment mount. This is clearly evident by how the hose clamps are seen to be looped through the two mounts in figure 5.6. Without perfect alignment between the two mounts there would be a discontinuity that would inhibit the hose clamps from fully encircling the TO. The hose clamps are the final component of the head-neck assembly. The compression applied by tightening the hose clamps secures the TO in place against the alignment mount. Additionally, the hose clamps provides a downward compression from the TO to the H3N-to-Skull mount, which creates a redundancy in case the mounting screws between the H3N-to-Skull mount and TO-Alignment mount would fail during the blast loading.

The final aspect regarding the methods for the experiments performed with the ABC is the specific mounting of the head-neck assembly. As initially discussed in §4.2.2, tension rods were used to mount the head-neck assembly at the appropriate location within the chamber. Figure 5.7 demonstrates the mounting of the head-neck assembly for this experimental set-up. The two sub-figures 5.7a and 5.7b illustrate how the head-neck assembly is mounted onto one of the compression rods. Additionally, the mounting of pressure transducers can also be seen in the sub-figures 5.7a and 5.7b. Notice how figure 5.7a was captured from the illumination side as evident by the high-speed camera being visible in the background. Conversely, figure 5.7b shows the

experimental set-up from the cameras point-of-view. The experimental set-up is fully encapsulated in figure 5.7c, which has been captured from a point-of-view behind the test object looking in the direction of the denotation source.

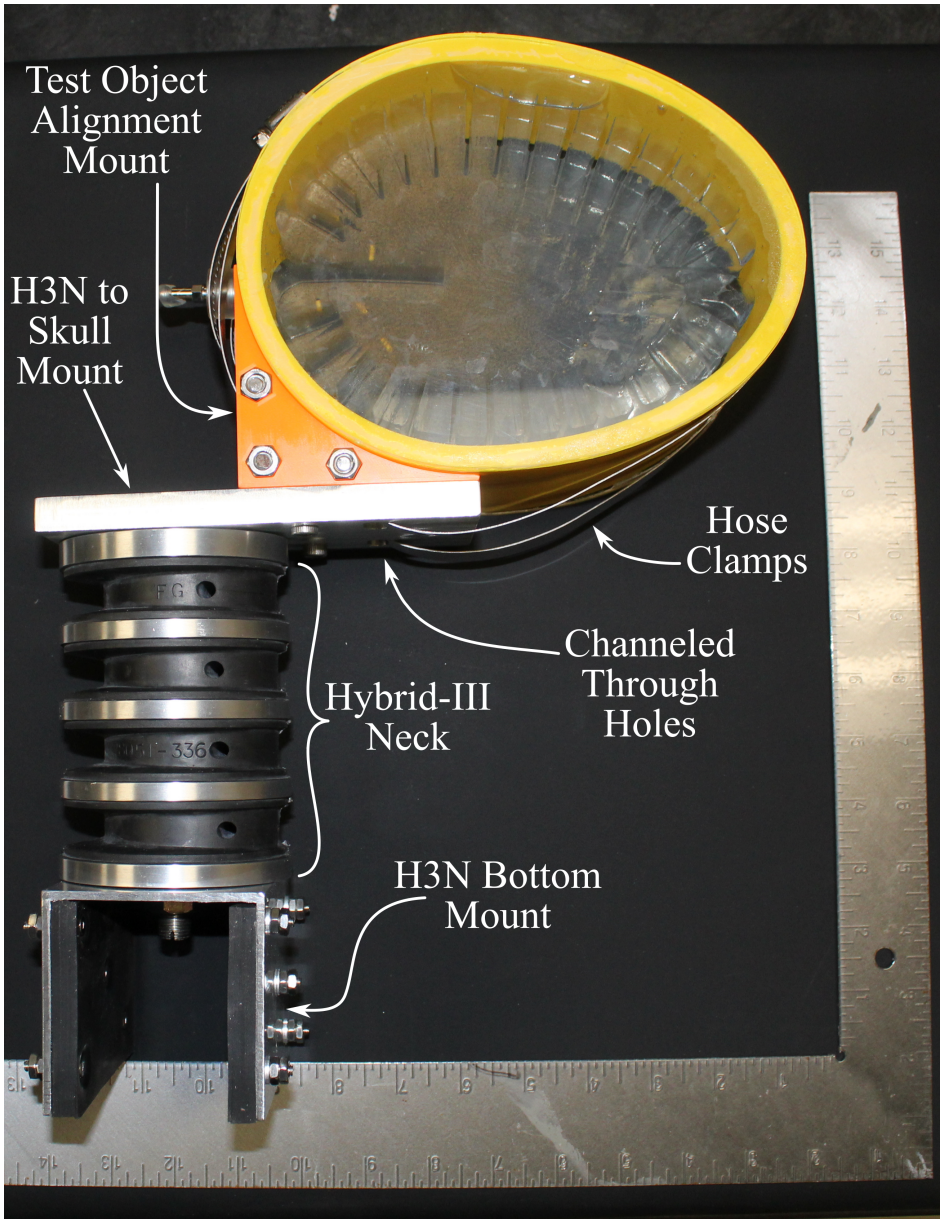


**Figure 5.6.** Collapse view of the head-neck assembly with individual component callouts.

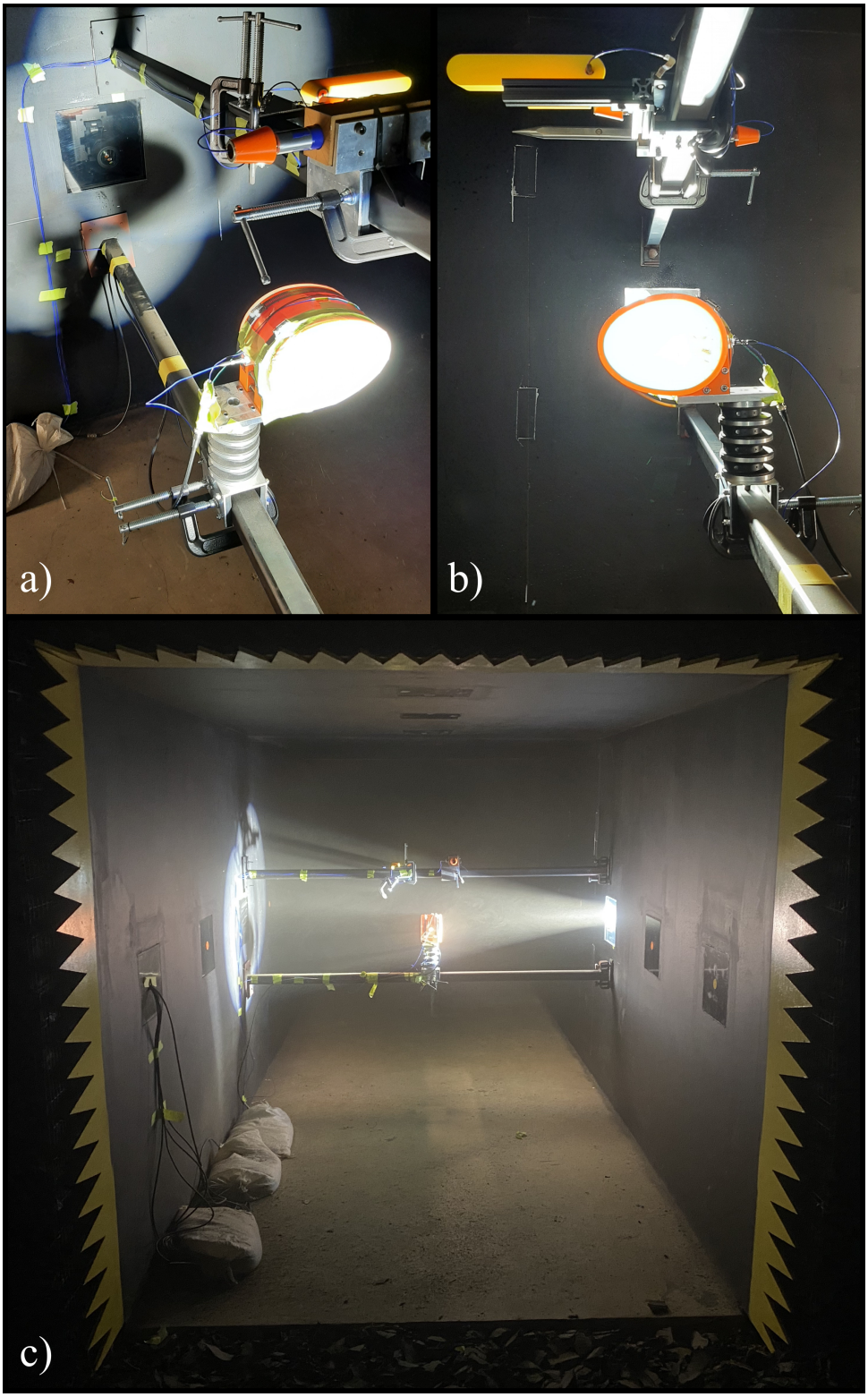


**Figure 5.7.** Experimental mounting of the head-neck assembly for the ABC experiments. a) Isometric-Top-View detailing test object mounting from illumination side, b) Experimental mounting from the camera's point-of-View, c) Full field-of-view for experimental set-up

# CHAPTER 6

# RESULTS & DISCUSSION

The results for the drop tower and the ABC experiments will be presented individually, where the significant independent findings relating to the mechanical response of the test object will be discussed. Then, experimental observations that were similar between the different experimental methods will be discussed. Finally, comparisons between the two methods will be highlighted along with their individual relevance to the data seen clinically.

## 6.1 Drop Tower Results

### 6.1.1 Pressure Response of the Test Object

The evolution of intracranial pressure (ICP) within the test object was tracked by the embedded pressure transducer located at the contrecoup region of the skull for all of the drop tower tests. The maximum negative pressure for all of the individual drops fell below the theoretical vapor pressure threshold ($-98.15 kPa$) for water at $25^{\circ}C$. The maximum negative pressure experienced for each of the drop tower experiments can be seen in table 6.1. A quick examination of table 6.1 shows that ICP ranged from -113 to -146 kPa, with the average of all six trials being -135.1 kPa. Additionally, with the exception of Test #1 and Test #3, the measured minimum pressure was -140 kPa or more. The behavior of the ICP for Test #1 and Test #3, while not directly reflected from the maximum negative pressure, were quite similar to the rest of the trials and will be discussed further below.

**Table 6.1.** Experimental parameters and resulting maximum negative pressures experienced for the individual drop tower experiments. *Denotes calculated value from theory.

| Test no. | Weight [kg] | Height [m] | Energy [J] | Max Neg. Pressure [kPa] |
|---|---|---|---|---|
| 1 | 1.058 | 1.016 | 10.50* | -113.06 |
| 2 | 1.058 | 1.016 | 10.50* | -140.26 |
| 3 | 2.018 | 1.016 | 20.12* | -123.49 |
| 4 | 2.018 | 1.016 | 20.12* | -142.52 |
| 5 | 3.0 | 1.016 | 29.90* | -146.68 |
| 6 | 3.0 | 1.016 | 29.90* | -144.68 |

The evolution of ICP for all of the six trials behaved quite similarly to one another and figure 6.1 illustrates the ICP behavior for Test #1 and Test #2. The ICP for each trial exhibited an initial decrease in pressure followed by a short period ($\sim 1\,ms$) of small pressure oscillations; then there was a sudden increase in the ICP (ranging from 1-3.4 times larger in magnitude compared to the initial depression in pressure experienced in the contrecoup region). Finally, after this period of positive pressure there was an instantaneous shift back towards the negative region. These oscillations between positive and negative pressure regions continue for several milliseconds after an initial impulse but before atmospheric pressure was returned within the test objects.

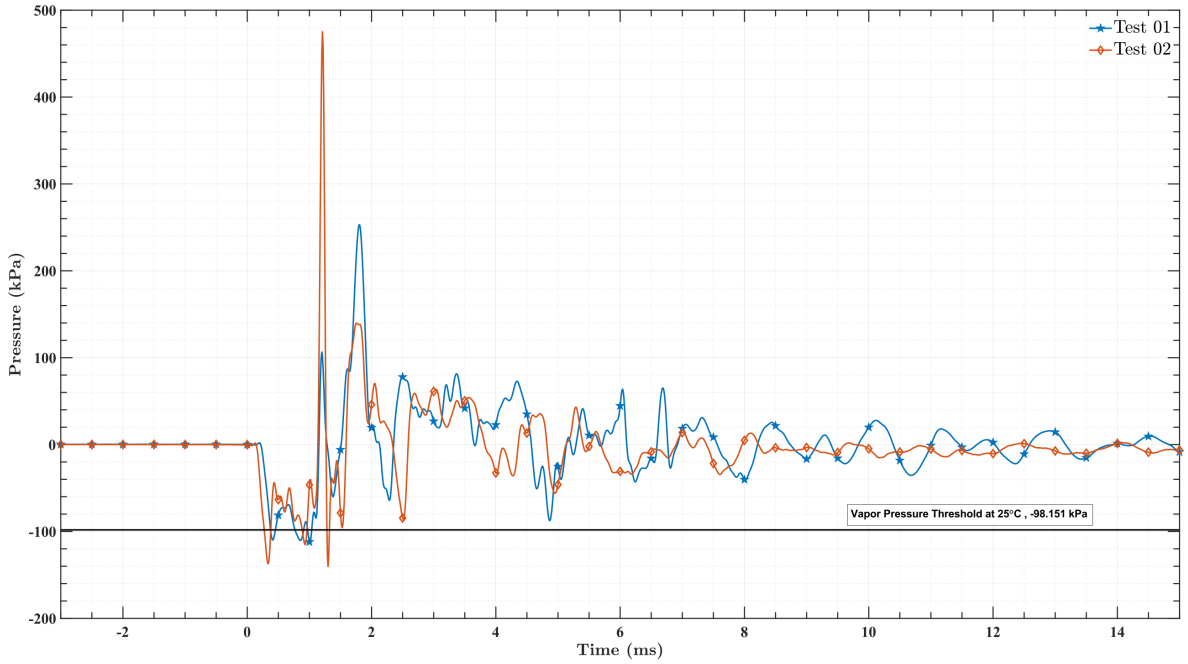


**Figure 6.1.** Evolution of Intracranial Pressure for Test #1 and Test #2. 1 kg drop weight.

This description for the evolution of ICP can further be seen in figure 6.2. All of the pressure profiles from the individual drop tower tests have been overlaid on to one another. The pressure profiles have been registered so that the moment of impact corresponds to $t = 0\,ms$. Additionally, the original pressure profiles signals were noisy; therefore, each signal was processed using a low-pass filter with a cutoff frequency of 5kHz. The pressure profiles seen in figures 6.1 and 6.2 are the results after the signal smoothing was performed. Figure 6.2 is crowded due to the overlaying of all the pressure profiles; however, it demonstrates several interesting observations for the drop tower

experiments. The first observation is that the striker was not perfectly symmetric during impact. This is evident by the slight time difference for the onset of the negative pressure phase that can be seen in the enlarged callout of time 0-1.1 ms. The asymmetric impact was confirmed for each of the experimental drop tests from the captured high-speed images.

The next observation present in figure 6.2 is the general agreement between all of the pressure profiles. The overall behavior of each pressure profile follows the previously described trend, but the characteristic pressure peaks / troughs are unmistakable when comparing all of the pressure profiles to one another. Now, there are high-frequency perturbations present within each pressure profile; but to reiterate, the overall behaviors (initial negative phase $\rightarrow$ positive pressure spike $\rightarrow$ oscillations between positive and negative regions) of the pressure profiles are quite similar to one another. The last prominent observation from figure 6.2 to be highlighted corresponds to $t = 3\,ms$. Specifically, none of the pressure profiles fall below the *vapor pressure threshold* beyond $t = 3\,ms$. Additionally, the pressure oscillations present after the $t = 3\,ms$ position are only a fraction of the positive or negative pressure magnitudes resulting in the initial response from the impact ($t < 3\,ms$).

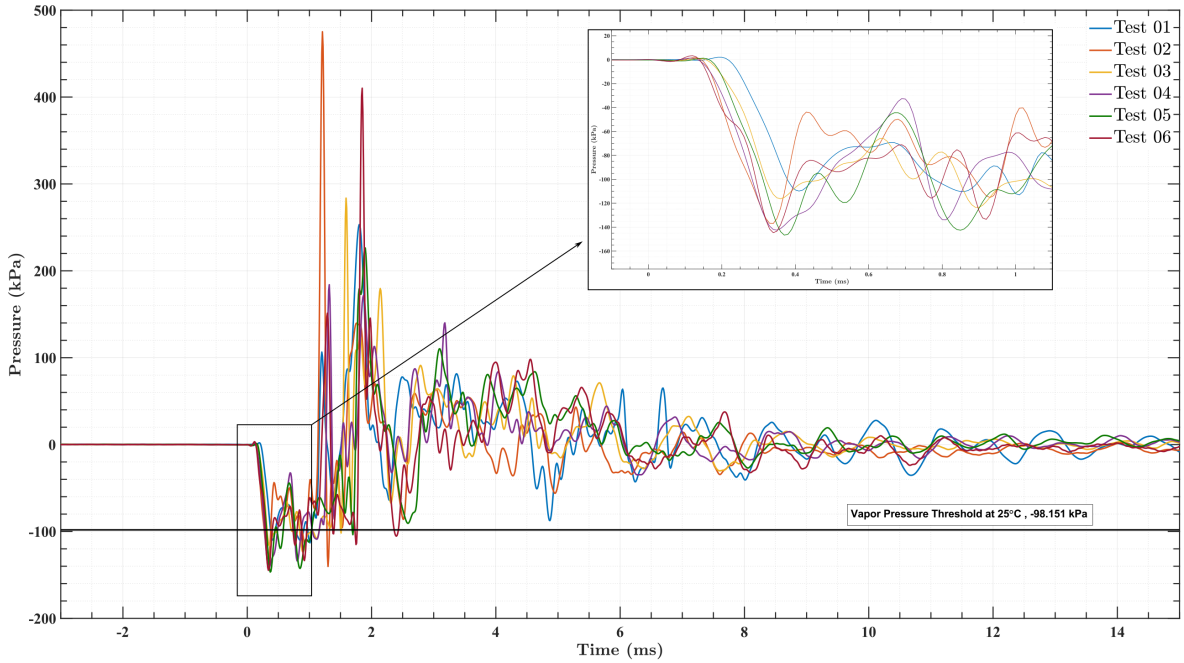


**Figure 6.2.** Evolution of Intracranial Pressure for all Drop Tower tests with a data callout superimposed for $0 < t < 1.1\,ms$.

The remaining information presented in this section will be confined to the 1 kg tests. The rational for focusing on the 1 kg experiments will be discussed below. With this is mind, the individual pressure profiles corresponding to the different drop weights (1 kg, 2 kg, and 3 kg) can be found in Appendix C. The ICP profiles are grouped by drop weight with each profile being distinguished by a different data point marker. The selected color schemes along with the different data point markers for each pressure profile were chosen in guidance with the Color Universal Design (CUD) criteria. The CUD is a set of principles developed to aid in the transfer of information of colored images [77]; specifically, the CUD was developed to resolve major issues for individuals experiencing colorblindness. Additionally, for the ease the of reader the order of figures C.1, C.2, C.3 allows for the direct comparison of the ICP profiles for different drop weights. To follow the CUD criteria figure, C.4 is an extension of figure 6.2 illustrating the data markers for each pressure profiles. The data markers were initially omitted from figure 6.2 to not overcrowd the figure and obscure the overall behavior. The data markers in all the figures are placed at every 50th data point; again, this was intentional as to prevent overcrowding on the figures themselves.

As highlighted by figure 6.2, the reader can see that the ICP for all of the drop tower experiments fell below the theoretical vapor pressure threshold for water at $25°C$, $-98.15kPa$. Thus as expected, all six experimental tests exhibited cavitation as a result of the blunt force impact. Readers are encouraged to review §2.1.5 if they are unfamiliar with the phenomena of cavitation. Figure 6.3 is an example of the cavitation resulting from the blunt force impact – it details the evolution of cavitation for a 1 kg weight drop experiment. The 1 kg drop weight was selected to emphasize the formation of cavitation from the lowest energy level of the experiments. Additionally, the resulting cavitation from the 2 kg and 3 kg drop weight experiments behaves quite similar to the 1 kg experiments. Thus, the 1 kg drop weight results are a suitable representation of the cavitation phenomena for all of the experiments. The cavitation was first observed in the contrecoup region in the bulk fluid of the CSF, on the CSF-skull interface, and then along the gelatin-CSF interface. The cavitation observed in the coup region followed shortly after the onset at the contrecoup region following the theory of wave propagation. The difference in onset times for the coup and contrecoup can be seen in figure 6.3.

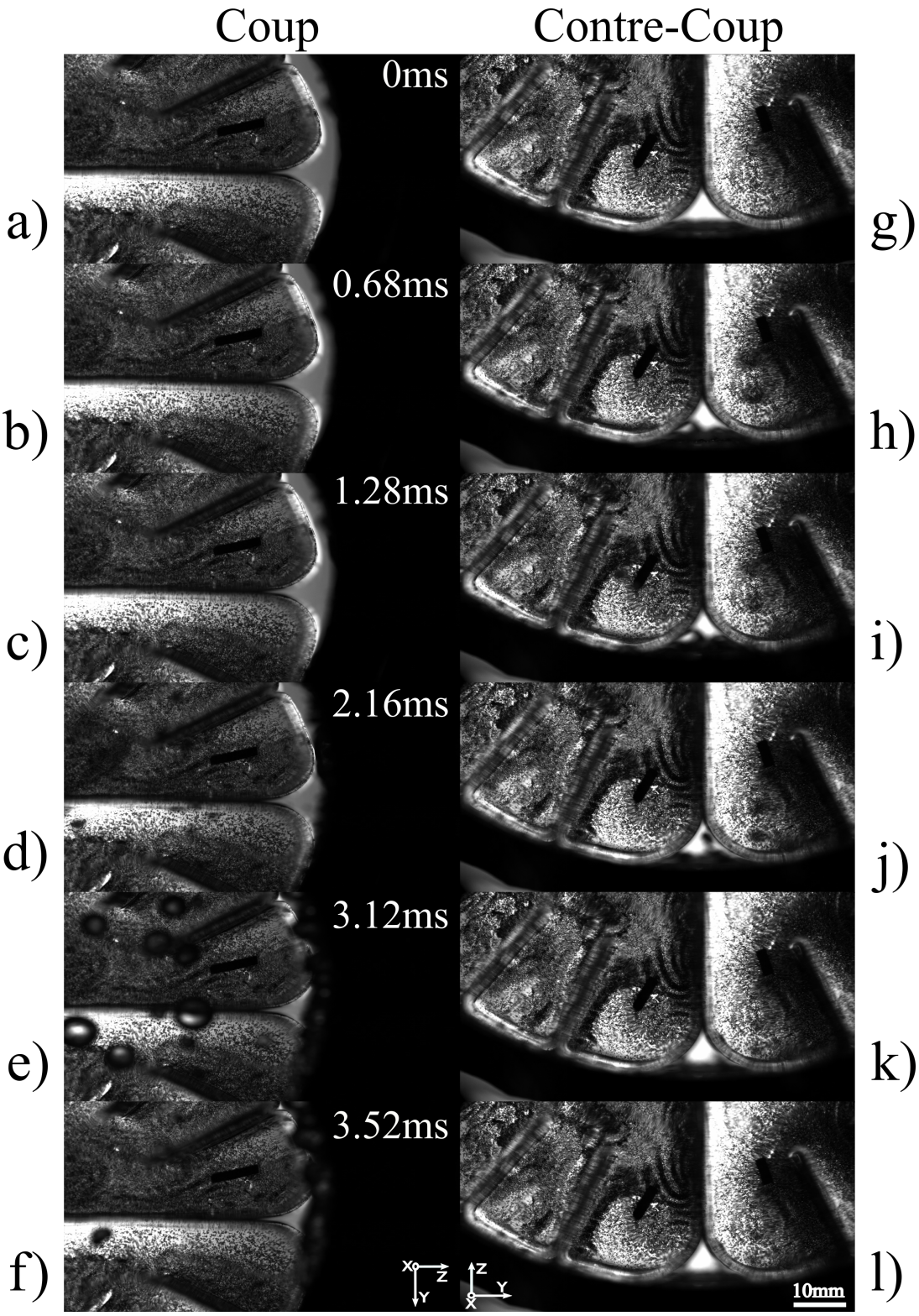


**Figure 6.3.** The Evolution of Cavitation: Comparing Coup and Contrecoup Regions for Test #1, 1kg weight drop. Note the image configuration corresponding to the impactor: *a-f)* has the impact direction from right to left, while *g-l)* has the impact direction top to bottom

Before gross examination of the cavitation phenomena in figure 6.3 is undertaken, it is important to understand the overall layout of the figure. Figure 6.3 is divided into two columns corresponding to a time-lapse series of the coup and contrecoup region of the biofidelic test object. The coup region corresponds to the sub-images *a-f*, while the contrecoup region corresponds to sub-images *g-l*. The individual rows of figure 6.3 correspond to the same physical time stamp at the respective regions. Sub-images *a)* and *g)* correspond to the moment the impactor struck the test object. An important aspect to point out about figure 6.3 is the orientation of the two columns. The coup images have been rotated by 90°. The coup images have been rotated by 90° to allow figure 6.3 to be symmetric along its width. Additionally, in order to have the largest field-of-view capturing the coup region during the experiments the entire camera was rotated. This rotation is evident by the axes present in figure 6.3.

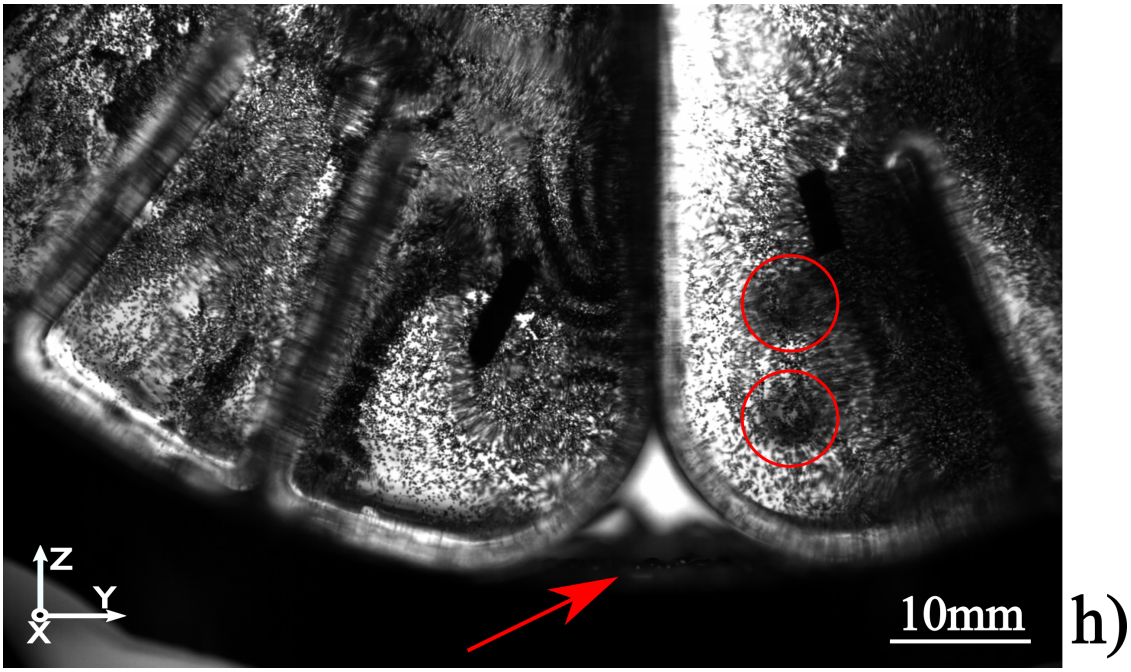


**Figure 6.4.** Enlargement of sub-image *h)* from figure 6.3. Red identifiers indicates cavitation within the CSF; circles indicate cavitation in the bulk fluid, arrow indicates cavitation on the surface of the skull.

The cavitation was first observed in the contrecoup region; specifically, it was initiated in the bulk of the artificial CSF. This can be seen in sub-image *h)* of figure 6.3 but will require zooming in to ~ 500% to see the finer details. To aid the reader and any printed versions of this text, the

sub-image *h)* has been enlarged to show the cavitation. Figure 6.4 is the enlargement of sub-image *h)* that clarifies the specific location where the initial cavitation is observed; the arrow points to a collection of cavitation bubbles that are located on the skull at the focusing plane, whereas the two red circles identify large cavitation on the far side of the gelatin outside of the focusing plane within the bulk of the CSF. The subsequent images within figure 6.3 demonstrate the full evolution of cavitation (inception → expansion → collapse) at the coup and contrecoup regions. Though it is important to acknowledge that for the coup region, sub-image *f)* still has remnants of cavitation; however, the overall presence of cavitation has been substantially reduced compared to its previous time-stamp of 3.12 ms.

The corresponding pressure profile for Test #1 can be seen in figure 6.5. To aid with understanding the evolution of cavitation that is presented in figure 6.3 there are individual data callouts in figure 6.5; these callouts are associated with the individual time stamps in figure 6.3. One can see that the inception of cavitation happens during the initial negative phase. Conversely, the full collapse of the cavitation bubbles within the test object does not immediately happen when the ICP re-enters the positive pressure region. This is evident by sub-image *e)* and its respective data callout in figure 6.5.

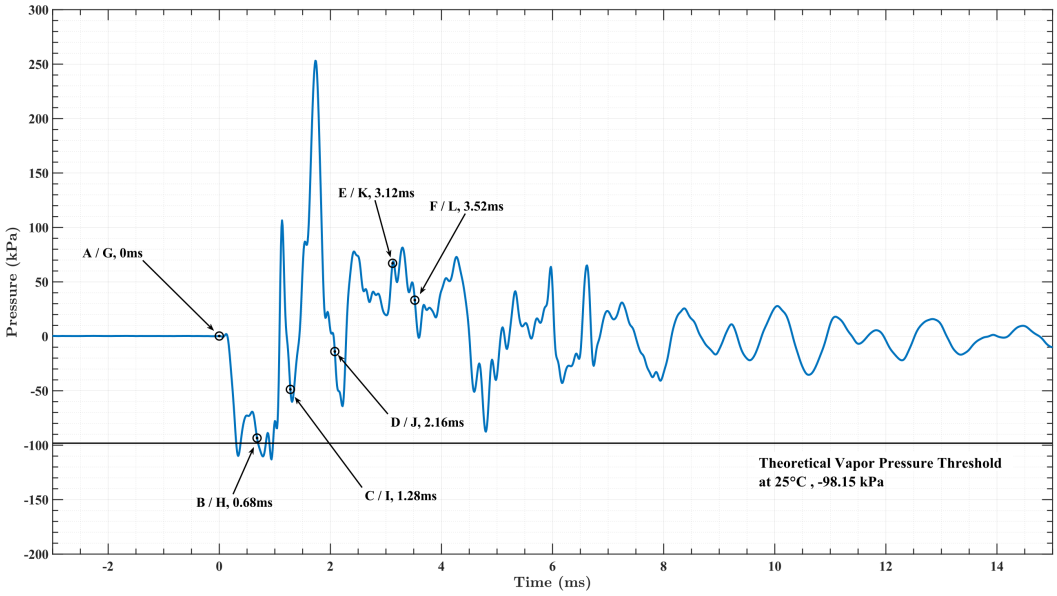


**Figure 6.5.** Evolution of Intracranial pressure for Test #1 with 1 kg drop weight. The individual data call outs correspond to the time stamps of the sub-images in figure 6.3.

Sub-image *e)* of figure 6.3 corresponds to the time stamp where the cavitation in the coup region is at its maximum bubble diameter. This demonstrates that there are cavitation bubbles in the expansion phase, while there is a positive pressure within the intracranial contents. Now, the reader is reminded that the location of the pressure transducer is directly in the mid-plane of the contrecoup side. This suggests that the pressure profiles recorded for the individual experiments may not fully describe the pressure experienced in the coup region. This is inherently intuitive since the location of the sensor itself is physically separated from the coup region. Additionally, only a single pressure transducer was utilized in all of the experiments; therefore, the pressure profiles presented herein are intended to represent the average pressure experienced at the contrecoup location. In contrast, the exact pressure profile experienced for the coup region is unknown; however, since the test object is a closed system, the pressure experienced in the coup region can be assumed to be similar to that of the contrecoup region. More on this specific topic given later in §7.

The entire evolution of cavitation (inception → expansion → collapse) ranged from 3.4-4.1 ms for each of the experimental trials. The cavitation event located specifically within the contrecoup region ranged from 1.12-1.76 ms. The current time span for cavitation is in good agreement with previously reported data [99]. Cavitation was seen both in the bulk fluid as well as on the surface of the skull; this trait was common in both the coup and contrecoup regions of interest. The negative pressure associated with the cavitation ranges from -113 to -146 kPa, as seen in Table 6.1; however, the onset of cavitation began at approximately 0.2 ms in the contrecoup region after the blunt impact for all of the six experiments. The high-speed images captured confirmed this and it was consistent for all the experimental trials. Additionally, there is no discernible difference between the observed cavitation from Test #1 and Test #3 on the contrecoup side, where the maximum negative pressures differed from the overall average of the rest of the experiments. All the experiments had the same onset time for the cavitation, and had relatively the same duration for the cavitation, and all trials had cavitation seen in the same general locations as one another.

To continue, the quantity of cavitation at the coup region is generally less than that of the contrecoup region without any noticeable pattern associated with the increase in drop weight.

An exception to this is Test #1, where there was a quantifiable difference between the amount of cavitation in the coup region and that of the contrecoup region. This was not the case for Test #2, the other 1 kg test, or any of the other experimental tests. Furthermore, the cavitation located at the coup region generally covers a larger area on the test object's skull; however, the cavitation seen on the contrecoup side is more uniform in size, shape, duration, and general location for the six experiments.

Although there are significant similarities in both the pressure data and the high-speed images collected for the six trials, each trial exhibited uniqueness. The majority of the distinctive aspects present throughout the drop tower experiments stems from the behavior of the cavitation bubbles themselves, specifically how the cavitation bubbles interacted with the gelatin of the brain phantom. The observed interactions were two fold – first, bubble expansion was observed to take place within the sulci (Tests #3, #4, and #6) and second the formation of micro-jetting resulted from bubble collapse on a free surface (Tests #3-6). To note, the micro-jetting phenomena was observed on both the coup and contrecoup sides; however, only Tests #3 and #4 displayed jetting on the coup side, while jetting was observed in the contrecoup region for Tests #3-6.

An example of the jetting phenomena is presented in figure 6.6. Figure 6.6 illustrates the evolution of a micro-jetting event: a bubble's maximum diameter, its complete collapse, and the resulting micro-jetting phenomena itself. The time stamps on figure 6.6 correspond to the time after the impactor first makes contact with the test object. Figure 6.6a calls out the specific cavitation bubble that eventually exhibits micro-jetting at its maximum diameter (0.69 mm). The subsequent sub-images, *b)* and *c)*, correspond to the complete collapse of the bubble in question and the resulting jetting stream, respectively. Notice the uniform time difference, 0.12 ms, between the sub-images of figure 6.6. This behavior of uniform time for a free surface collapsing bubble and the resulting jetting happens to be a coincidence. Further examination of the other jetting occurrences does not display such steady behavior; rather, each occurrence is quite unique and the resulting jetting is the only consistent behavior associated with each incident.

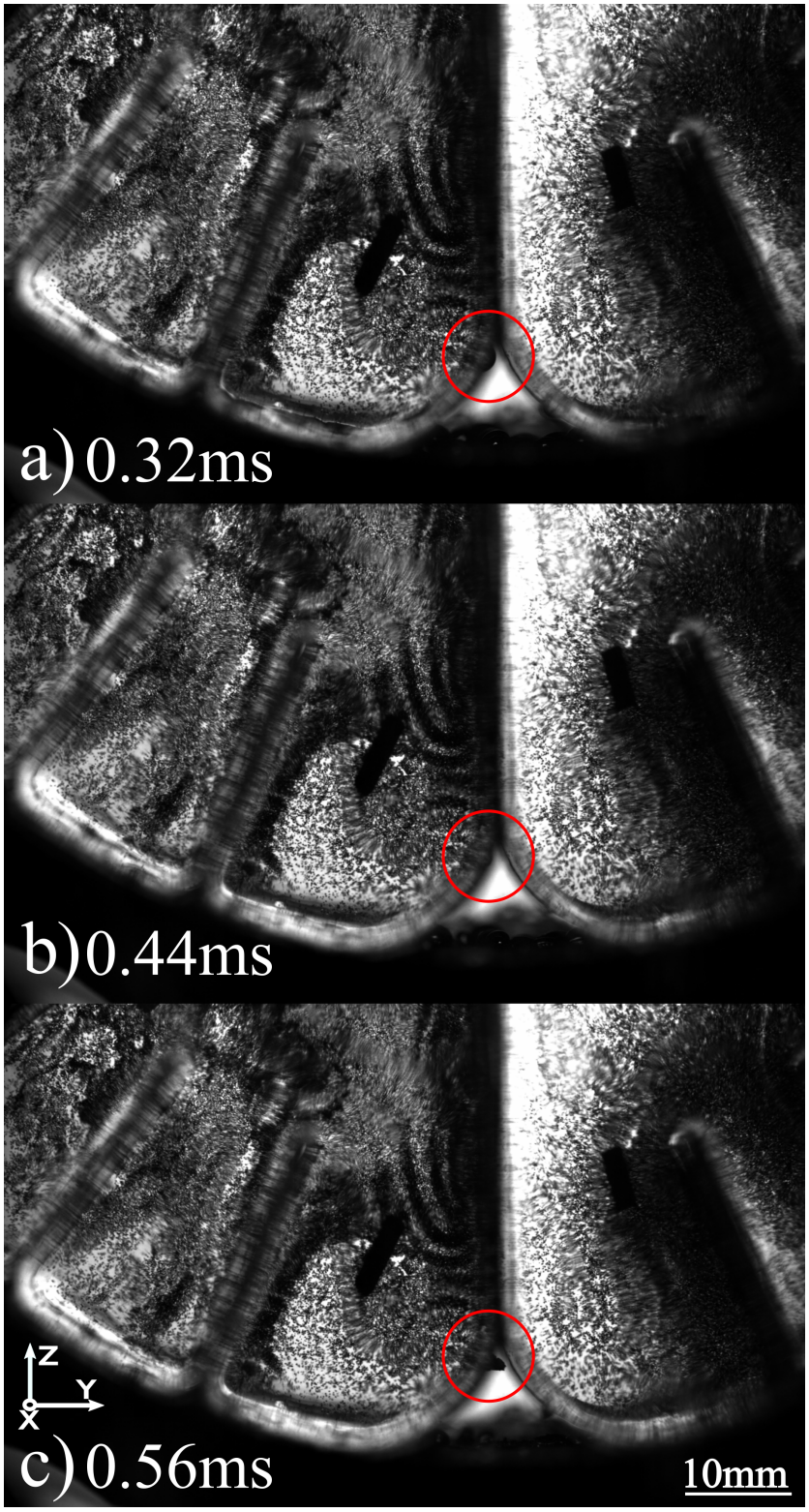


**Figure 6.6.** Evolution of jetting phenomenon in the Contrecoup Region for Test #4:
*a)* Maximum bubble diameter - 0.69mm, *b)* Complete bubble collapse, *c)* Visible micro-jetting

There are two additional interesting observations from the experimental results. First is the presence of high-frequency longitudinal waves propagating along the surface of the gelatin, which result from the collapse of the cavitation bubbles. Cavitation bubbles generate high-pressure shock waves if they experience a symmetric collapse. Additionally, as discussed previously, micro-jetting can result from the asymmetric collapse of a semi-confined cavitation bubble (e.g., bubble on a free-surface), see figure 6.6. Both the high-pressure shock waves and the impinging micro-jet interact with the surface of the gelatin phantom resulting in the formation of the stress waves. The observed shock waves and micro-jetting present in all of the experimental tests are in good agreement with the well established phenomena in the literature [55, 98].

The last observation regarding cavitation pertains to the specific locations where it was observed during the experiments. As previously mentioned, the cavitation was first observed in the contrecoup region located within the bulk fluid of the CSF, then on the CSF-skull interface, and finally along the gelatin-CSF interface. These consecutive locations were identical for all of the six experimental tests. In addition to these general locations, one test in particular (Test #6) presented cavitation bubbles that generated within the gelatin itself. This was the first and only event of this nature captured for all of the experiments.

Now, as detailed in §3.4 the gelatin is a hydrogel comprising mainly of water, so the notion of cavitation generating within the substrate is not without merit. With that being said, the internal confinement due to the molecular cross-linking greatly restricts the possibility of said cavitation generation. Nonetheless, there is evidence from the captured high-speed images of this specific event. Since there is only a single case within the current set of experiments, it is difficult to draw any definitive conclusions. The observation of cavitation within the brain tissue simulant is still significant as it demonstrates the potential presence of cavitation throughout the intracranial contents. Coupling the knowledge of cavitation in the bulk fluid of the coup / contrecoup regions now with the potential of dispersed cavitation in brain tissue itself provides an additional damage causing mechanism for diffuse axonal injury (DAI). Readers may refer to §1.4.3 for details on DAI. This topic will be addressed again later.

### 6.1.2 Displacement of Test Object

The downward motion of the test object was tracked using a laser-based displacement sensor (Model LK-G5001P, Keyence Corporation), which was positioned to focus on the contrecoup region of the skull near the pressure transducer. The test object's maximum displacement was proportional to the drop weight for a specific experiment test. The maximum displacement results as well as the calculated velocity and acceleration are gathered in table 6.2. To note, the experimental data for Test #5 is not presented in table 6.2. There was an error with the displacement sensor during data acquisition for this particular experimental run. Therefore, the maximum displacement of the test object was not obtain. Any partial collected data were omitted for the sake of clarity and to not confound any comparisons based off the displacement data.

**Table 6.2.** Maximum displacement, velocity, and acceleration experienced on the test object for the individual drop tower experiments.

| Test no. | Weight [kg] | Max. Disp. [mm] | Max. Vel. [m/s] | Max Acc. [g] |
|---|---|---|---|---|
| 1 | 1.058 | 0.90 | 1.16 | 978.8 |
| 2 | 1.058 | 1.24 | 1.56 | 1237.4 |
| 3 | 2.018 | 2.29 | 1.36 | 855.7 |
| 4 | 2.018 | 2.15 | 1.54 | 1303.4 |
| 5 | 3.0 | - | - | - |
| 6 | 3.0 | 3.08 | 1.15 | 1259.4 |

The displacement values presented in table 6.2 are to be expected based off the experimental set-up. The reader is reminded that the test object was place on top of a 1/2-inch aluminum slab for the experiments as detailed in §5.1. The combination between the density of aluminum ($2.7 g/cm^3$) and the thickness of the slab established the base to be rigid compared to that of the 3D printed skull (i.e., the skull will deform not the aluminum base). With this being said, there is no such thing as a perfectly rigid system. Thus, the test object will ultimately move upon the blunt force impact.

To this end, the design of the drop tower assembly and the incorporation of the rigid aluminum slab as its base was intended to restrict the test object's motion as much as possible. The purpose for this was to only allow translational acceleration to be present after the blunt force impact. The

reason for this is that previously reported data [8, 81] have demonstrated how head acceleration, primarily rotational / angular acceleration, leads to differential movement between the skull and the brain ultimately producing regions of low pressure. These areas of low pressure, as seen in the previous section, can lead to the formation of cavitation if the ICP drops below the theoretical vapor-pressure threshold of the fluid. On the contrary, translation is the simplest form of acceleration and is highly uncommon to be the sole generator of intracranial motion; the physiological nature of the head, neck, and spine nearly always incorporates either rotational and / or angular acceleration during a dynamic loading event. With this in mind, the drop tower apparatus aims at understanding and fundamentally isolating the translation acceleration mechanisms present during impact loading events from that of its counterparts: rotational / angular acceleration. The isolation of translational acceleration will aid in the overall understanding of TBI; specifically, it will aid in understanding how rotational / angular accelerations are superimposed on to that of translational acceleration.

The general displacement behavior of the test object was quite similar for each of the experimental drop tests. Each test had an initial delay, approximately $0.8\,ms$, between when the striker impacted the test object and the onset of downward motion. The downward motion continued for several milliseconds followed by a rebound of the test object back towards its starting position. The rebound (i.e., upward motion) was more gradual in nature compared to that of the initial downward displacement for all of the experimental tests.

The displacement of the test object for each trail can be seen in figure 6.7. Important to note, the same color schemes and data markers used to identify the pressure profiles have been incorporated into the displacement figures. The displacement profiles have also been registered so that the moment of impact corresponds to $t = 0\,ms$. Additionally, note the sign convention in figure 6.7 – the initial downwards motion corresponds to the positive displacement. Conversely, the second half of the displacement profiles, with the negative slopes, correspond to the upward movement of the test object during the rebound phase. The reason for this was due to the internal configuration within the laser-based displacement sensor itself (e.g., positive displacement is approaching the sensor and negative displacement is moving away from the sensor).

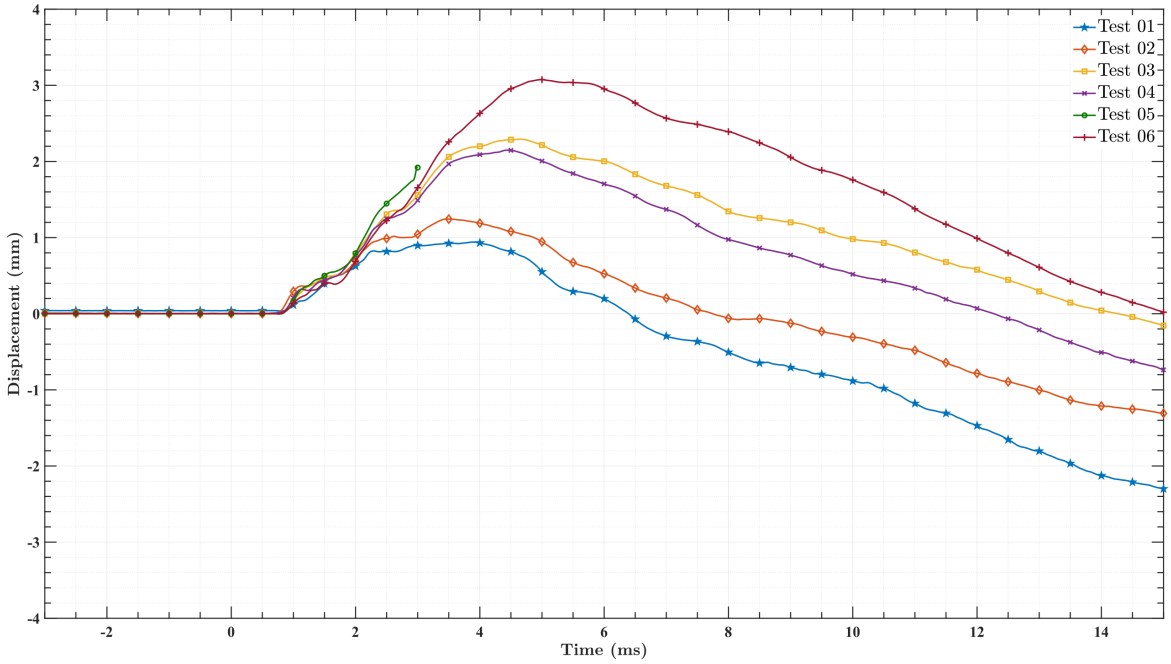


**Figure 6.7.** Displacement profiles for the Test Object during all of the Drop Tower Experiments. 1 kg: Test #1 and Test #2, 2 kg: Test #3 and Test #4, 3 kg: Test #5 and Test #6.

Another aspect to note from figure 6.7 is the abbreviated Test #5 displacement data. As previously stated, there was an error during the data acquisition and the full displacement profile was not obtained. The partial profile presented for Test # 5 in figure 6.7 highly agrees with Test #6, its 3 kg drop weight counterpart, for the same displayed time period. Due to the data acquisition error the full agreement between Tests #5 and #6 displacement profiles will never be known; however, due to the near identical behavior of the ICP profile, figure C.3, for Tests #5 and #6 as well as the general agreement observed from the high-speed imaging it is safe to assume that the omitted portion of Test #5 displacement profile would follow nicely to that of Test #6 displacement profile.

A closer comparison of Tests #5 and #6 displacement profiles can be found in figure D.3. Additionally, all of the displacement data for the individual drop weights (1 kg, 2 kg, 3 kg) can be found in Appendix D. The order within Appendix D allows for easy comparisons to be made between the two tests performed for each drop weight along with comparing the different drop weight experiments to one another. Furthermore, the displacement data in Appendix D can be easily compared to its respective intracranial pressure data found in Appendix C.

There are two additionally interesting observations from the displacement data and both can be seen in figure 6.7. First, is how the overall downward displacement increases with the increasing drop weight. The maximum displacement for each tests can be found in table 6.2. A quick examination of table 6.2 shows a proportional relationship between the drop weight and the maximum displacement; specifically, that the test object's downward displacement is approximately $1\,mm$ per $kg$. The required time associated with reaching the maximum displacement also increases for the larger drop weights. This behavior follows an anticipated trend associated with increase drop weights; namely, that increase weight increases potential energy, which ultimately increases the momentum associated with impact.

The last observation regarding the displacement of the test object is the oscillatory behavior that is superimposed onto the overall displacement data. Now, this specific behavior can be seen in figure 6.7, but it is easier to visualize in the individual displacement profiles seen in figures D.1, D.2, D.3. Each individual test, including the abbreviated data of Test #5, demonstrates several periods of *step-like* behavior on the rising edge of its displacement data. There are differing degrees of similarity between the two displacement profiles for each drop weight (e.g., Tests #3 and #4 agree more with one another than Tests #1 and #2). Nonetheless, the general *step-like* behavior is present in each of the data sets. Additionally, this same behavior can also be seen on the tail end of the displacement data, which corresponds to the rebound phase of the test object. Much like the total displacement profile, the *step-like* behavior is more gradual in nature compared to the initial downward displacement phase.

The observation of the oscillatory behavior present within the displacement data provides experimental evidence that supports the skull flexure theory as a possible damage-causing mechanism relating to TBI. The *step-like* behavior demonstrates that there is differential movement present within the skull from that of the total test object. Additionally, the presence of this behavior in both the downward displacement / rebound phase further suggests that this differential movement is confined within the skull, rather than being caused by any outside interaction (e.g., a reaction force due to the rigid bottom plate). To continue, the presence of vibrations within the skull can lead to

localized regions of high or low pressure, which could be directly influencing the ICP leading to the complex and dynamic pressure profiles seen throughout these experiments (figures C.1, C.2, C.3). This notion of local skull deformations contributing to the complexity of the ICP profiles have been previous documented within the literature [13, 38, 91]. The results discussed here only further support the previously reported findings. This particular topic will be discussed further below.

## 6.2 Advanced Blast Chamber

### 6.2.1 Pressure Response of the Test Object

The intracranial pressure (ICP) of the test objects was measured at the same location as the drop tower experiments for all of the tests using the ABC. Two additional pressure transducers were also used and were mounted within the tunnel section in order to track the behavior of the pressure profile within the chamber itself. The two additional pressure transducers were mounted in-front of and above the test object, see figure 5.7. Figure 5.7a and 5.7b demonstrate how the additional pressure transducers were mounted above the top of the test object. The alignments of the pressure transducers themselves are difficult to quantify in figure 5.7, but they were positioned so that they would align with the front edge of the test object. The alignment with the front edge of the test object was crucial to fully understand the evolution of the ICP. Therefore, great care was taken during the initial set-up of the pressure transducers to achieve proper alignment. Additionally, the alignment of the pressure transducers were checked after each experiment to ensure that the force from the blast wave did not alter the experimental set-up between trials.

In addition to the overall placement of the pressure transducers within the chamber, the two additional pressure transducers were positioned to be perpendicular compared one another; one pressure transducer was normal to the on coming shock front and the other was rotated 90°. The normal facing pressure transducer collected the *reflective pressure* profile, whereas the pressure transducer orientated to be perpendicular to the on-coming blast wave collected the *static pressure* profile. Again, the center of the two additional pressure transducers were positioned to be aligned horizontally with the outer-front edge of the test object. Positioning of the pressure transducers at the

outer-front portion of the test object allows for significant events to be extracted from the pressure data: arrival of shock wave, reflective and static pressure experienced during loading, initial ICP wave propagation, and the pressure evolution experienced within the tunnel.

The maximum and minimum values for the ICP of the test object along with the *reflective pressure* and *static pressure* from within the chamber can be found in table 6.3 for all of the experiments. Table 6.3 is laid out corresponding to the *lower exposure* and *high exposure* set of experiments. As described in §5.2, the *lower exposure* and *higher exposure* refer to the total explosive charge weight of PETN used during the experiments. The results from the *lower exposure* and *higher exposure* experiments differ in total magnitude, but the general response of the system and pressure behavior is similar between the two exposures. Due to the high degree of similarity between the *lower exposure* and *higher exposure* sets of experiments, the majority of the discussion will be limited to the *higher exposure* results. Key observations regarding the *lower exposure* set of experiments will be discussed as they are relevant. There were a total of four tests performed for the *higher exposure* experiment; however, there was a data acquisition error with the high-speed imaging for the first test, so only Tests #2-4 will be discussed herein.

**Table 6.3.** Experimental parameters and resulting pressure extrema experience for the individual ABC experiments. The units for pressure are kilopascals (kPa).

| **Test** | **Expl.** | **Intracranial Press.** | | **Reflective Press.** | | **Static Press.** | |
|---|---|---|---|---|---|---|---|
| **no.** | **Weight [g]** | Max. | Min. | Max. | Min | Max. | Min. |
| 1 | 86.40 | 185.23 | -111.5 | 200.31 | -9.93 | 99.10 | -17.60 |
| 2 | 86.40 | 214.65 | -124.26 | 199.89 | -57.28 | 102.20 | -60.30 |
| 3 | 86.40 | 189.94 | -108.68 | 190.54 | -10.84 | 101.95 | -17.64 |
| 2 | 172.80 | 254.33 | -176.95 | 322.42 | -46.14 | 186.50 | -32.66 |
| 3 | 172.80 | 262.88 | -173.16 | 315.12 | -13.22 | 177.93 | -19.13 |
| 4 | 172.80 | 272.20 | -183.61 | 309.24 | -14.81 | 183.47 | -23.56 |

A quick examination of table 6.3 will show that the *reflective pressure* experiences the highest pressure out of the three measurements. This is as expected as it follows the theory of wave propagation, specifically the nature of interaction of a wave reflecting off of a surface. There is one exception to this in the data, Test #2 of the *lower exposure* experiments. An additional trend that can

be observed from table 6.3, is that the negative pressure experienced within the tunnel itself is quite uniform. This is clear when comparing the *reflective pressure* and the *static pressure* maximum and minimum values – they are quite similar to one another and on the same order of magnitude for all the experiments. Additionally, the evolution of pressure from the *reflective pressure* transducer and *static pressure* transducer are nearly identical to one another; this similarity can be seen in figure 6.8. The agreement between the *reflective* and *static* pressure profiles can be further examined by evaluating the profiles from the individual experiments, which can be found in Appendix E. Additionally, there is great similarity between the *reflective pressure* and *static pressure* profiles between all of the *higher exposure* tests. The *reflective pressure* profiles are nearly perfectly identical to one another and there is good agreement between the *static pressure* profiles; these trends can be seen in figures E.4 and E.5, respectively.

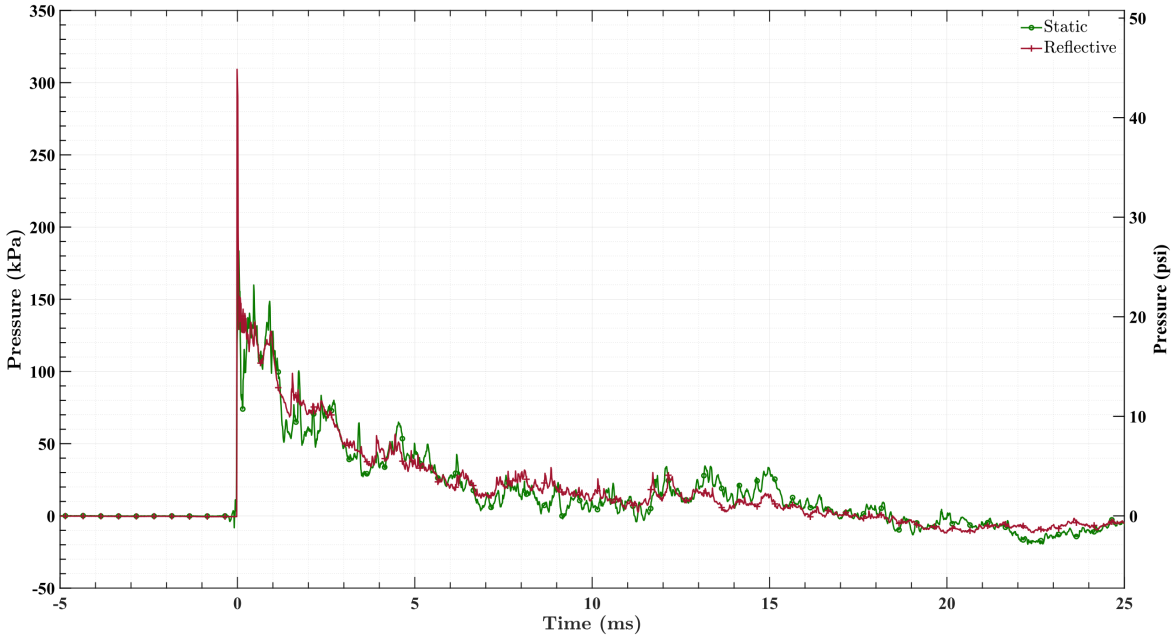


**Figure 6.8.** Example of static and reflective pressure profile's similarity for the *higher exposure* Test #4: maximum reflective pressure 309.24 kPa, maximum static pressure 183.47 kPa.

It is important to note that the pressure profiles have been registered, so at $t = 0\,ms$ corresponds to when the shock-wave first interacts with the outer-front portion of the test object. The evolution of the ICP for the test object was quite similar throughout all of the experiments performed using the ABC. There was an initial delay, 0.12 ms, between when the shock-wave first interacts with the

test object and when the pressure transducer located within the contrecoup region of the skull first registers an alteration in the pressure. Then there is a period of high-frequency oscillations that lasts for approximately 0.4 ms, which tends to be nearly isolated to the negative phase. Following this initial negative phase, the ICP shifts towards the positive region and experiences its maximum positive pressure. Finally, the ICP begins to oscillate in a under-damped manner back towards the equilibrium point. An example of this ICP behavior can be seen in figure 6.9.

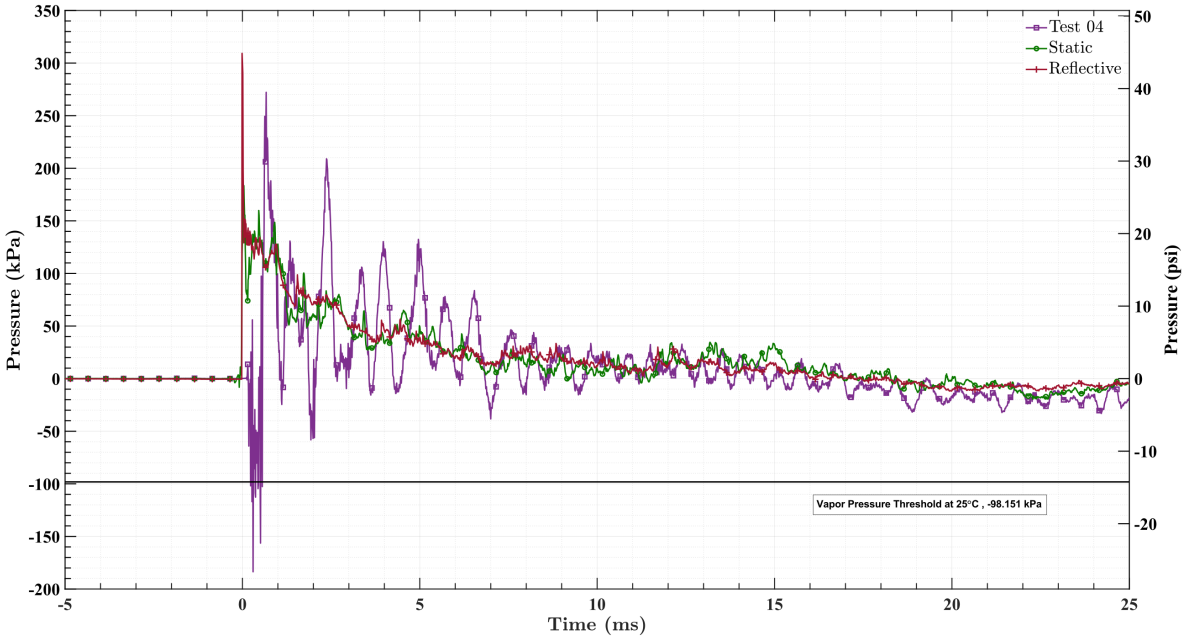


**Figure 6.9.** Evolution of intracranial Pressure for Test #4, (*higher exposure*) overlaid with *reflective* and *static* pressure profiles from the tunnel: maximum ICP 272.2 kPa, minimum ICP -183.61 kPa.

This description for the evolution of ICP can further be seen in figures 6.10 and 6.11. One will notice that figures 6.10 and 6.11 display the same pressure profiles as seen in figure 6.9. The only difference between the three figures is the total displayed time. In order to clarify the previous description for the evolution of the ICP profiles within the test object, the three figures 6.9-6.11 display consecutively shorter and shorter time periods. Figure 6.9 demonstrates the full behavior of the ICP profile for a period of 25 ms. Figure 6.10 highlights the quick shift from the initial negative phase to the positive oscillations that returns to atmospheric pressure within 10 ms. Lastly, figure 6.11 emphasizes the initial delay that lasts 0.12 ms, as well as the initial negative pressure response in the ICP of the test object.

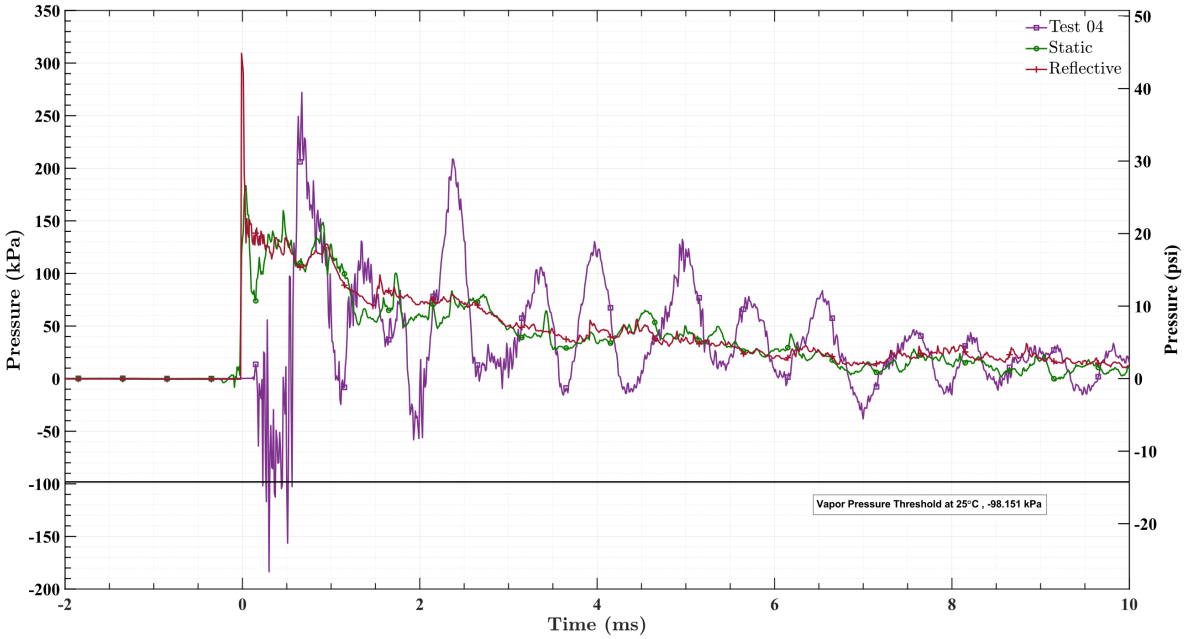


**Figure 6.10.** Abbreviated view, $0 \rightarrow 10\,ms$, of ICP for Test #4, (*higher exposure*) overlaid with *reflective* and *static* pressure profiles from the tunnel.

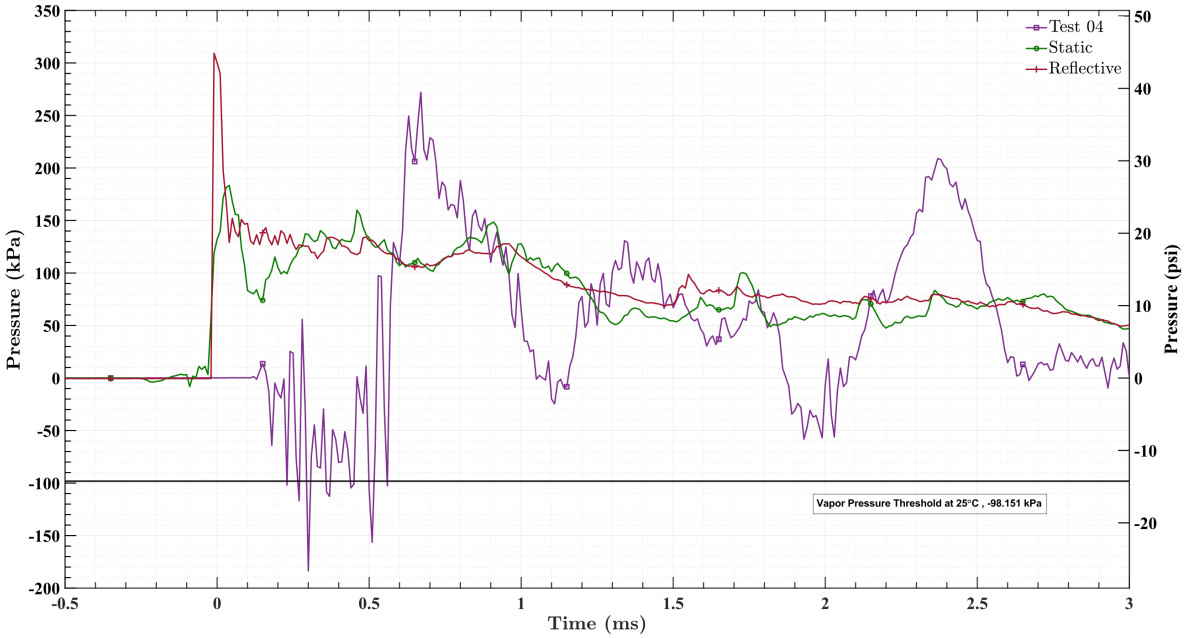


**Figure 6.11.** Abbreviated view, $0 \rightarrow 3\,ms$, of ICP for Test #4, (*higher exposure*) overlaid with *reflective* and *static* pressure profiles from the tunnel.

It is important to note that the data presented in figures 6.9-6.11 are all the raw signals obtained from the pressure transducers; no filtering of the data from the ABC experiments has been performed up to this point. This aspect is highlighted to emphasize the good agreement between the *static* and *reflective* pressure profiles seen in the figures. This is further emphasized in all of the pressure profiles presented in Appendix E. The raw pressure profiles immediately demonstrate the reliability of the pressure transducers as well as the repeatability of the experiments themselves; the repeatability of the ABC experiments can be directly seen in figures E.4 and E.5.

In addition to the excellent agreement of the *reflective* pressure within the ABC tunnel between experiments there is considerable agreement between the ICP profiles for each of the ABC experiments. Figure 6.12 demonstrates the nearly identical ICP profile for the three *higher exposure* ABC experiments. Examination of figure 6.12 establishes how each of the ICP profiles follow the same temporal domain and how each oscillation extrema reach the same overall pressure magnitudes. The performance of all the pressure transducers (*static*, *reflective*, and ICP) provides substantial evidence to the overall precision that the ABC is capable of achieving.

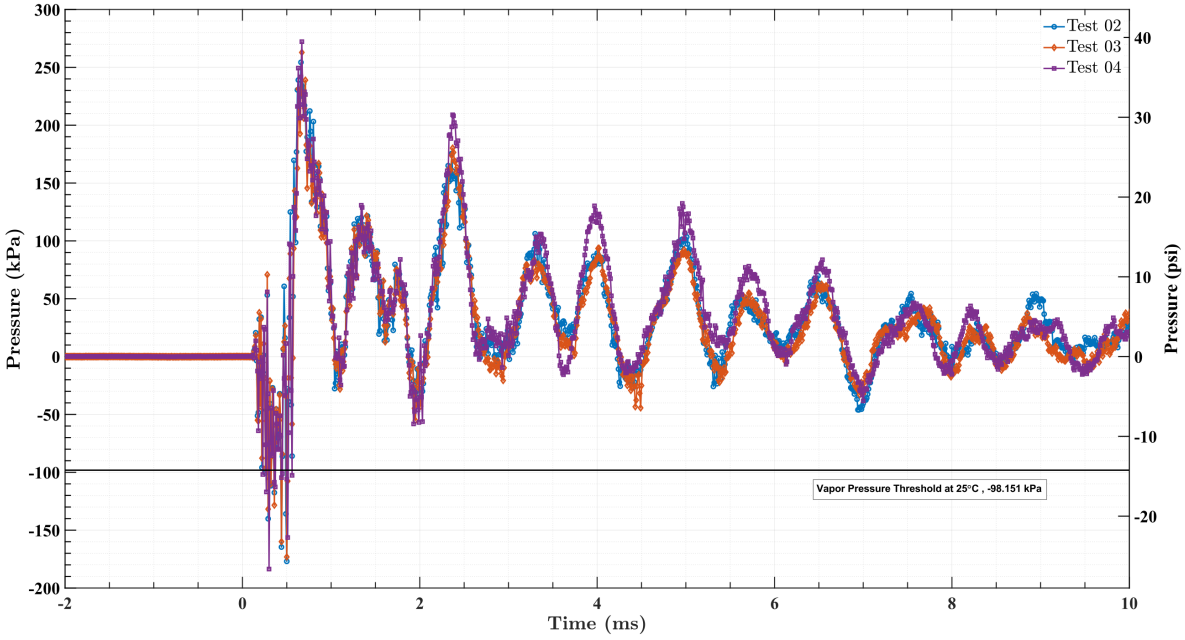


**Figure 6.12.** Intracranial pressure profiles for all of the *higher exposure* ABC Experiments. Time-span of $0 \rightarrow 10\,ms$.

The ICP data illuminates several intriguing observations present in the ABC experiments. The first immediate observation has been previously pointed out – the pressure profiles are nearly identical between consecutive tests. The next observation expands on the similarity between pressure profiles but is specifically centered around the initial response of the test object. The initial ICP response of the test object can be seen in figure 6.13. Figure 6.13 illustrates the first millisecond post interaction with the blast wave. Now, much like the drop tower experiments, the ICP drops below the theoretical vapor threshold for water at 25°C ($-98.15 kPa$) for all of the *higher exposure* experiments. However, unlike the drop tower experiments none of the ABC experiments presented the formation of cavitation within the captured high-speed images.

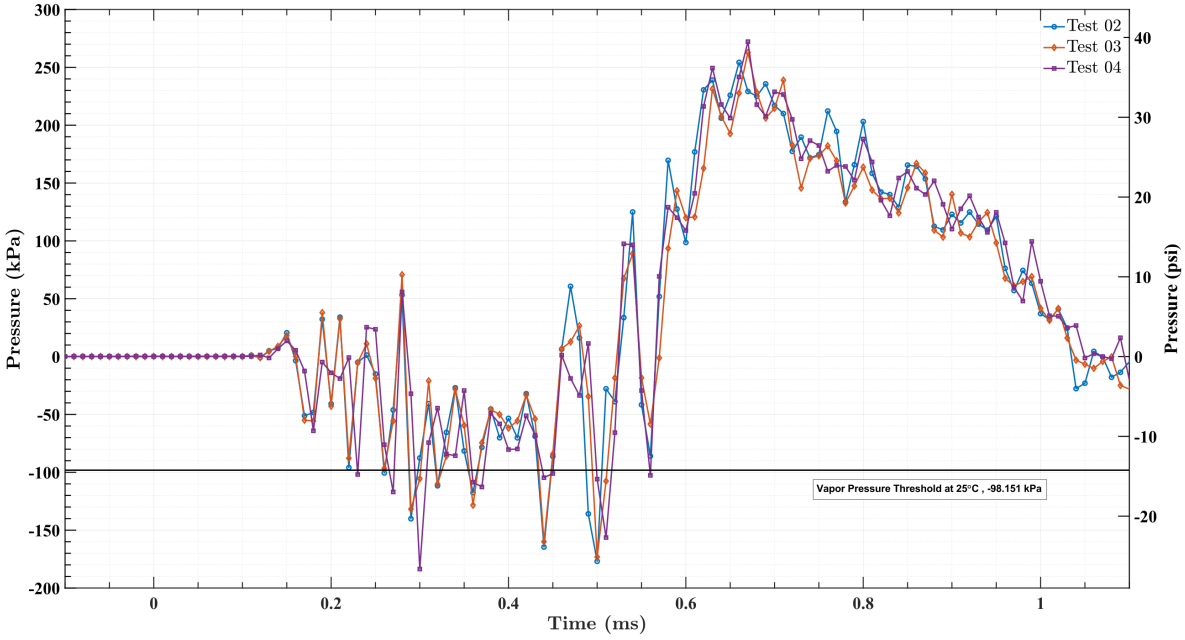


**Figure 6.13.** Intracranial pressure profiles for all of the *higher exposure* ABC Experiments. Time-span of $0 \rightarrow 1\,ms$.

The entirety of high-speed images for each of the ABC experiments have been closely examined to ensure that cavitation was, in fact, not present in any of the experiments. Special care, specifically at the captured images corresponding to the time where the pressure fell below the theoretical vapor threshold, was taken during the evaluation of the high-speed images. Unfortunately, cavitation was not observed in the ABC experiments as it was in the drop tower experiments. With this being said, it

is important to indicate that just because there was no video evidence of the presence of cavitation it does not, with absolute certainty, rule out the specific phenomena from existing within the test object. There is supporting evidence within the ICP profiles that cavitation may have existed within the test object. First, there are multiple data points where the pressure reaches or exceeds the vapor pressure threshold. Secondly, the high-frequency oscillations, from $0.15 \rightarrow 0.45\,ms$, are characteristic of bubble dynamics, which agree with data that has been previously reported [45]. Without video evidence, the presence of cavitation is ultimately unknown. A simple explanation for the *"unseen"* cavitation can be clarified by the limitations within the data acquisition systems; the high-speed camera acquired images at 25kHz and the ICP transducer at 100kHz. These acquiring rates (25kHz and 100kHz) correspond to data points taken every $40\,\mu s$ and $10\,\mu s$, respectively. While these are fast acquisition rates, they may still be insufficient to resolve formation and collapse of extremely small cavitation bubbles. Further work is necessary to quantify the presence of cavitation after exposure to a blast wave within human head phantoms that have complex geometries such as the one used throughout this research.

The ICP profiles presented in figure 6.13 also provide conflicting evidence in regard to cavitation. The overall agreement between the individual ICP profiles suggests that the pressure experienced within the test object itself is related to the overall system, specifically, with how the test object responds to the distributive loading created by the propagating shock wave. If cavitation would be present, there is an expectation that there would be variations within the pressure profiles; this is evident due to the creation / collapse of unique cavitation bubbles as seen in comparing the ICP profiles from the drop tower experiments presented in Appendix C. There are slight variations within the ICP profiles seen in figures 6.12 and 6.13, but these are small perturbations that can easily fall within the signal-to-noise ratio present within the pressure transducer itself. There is high probability that the high-frequency oscillations present in the initial response, $0.15 \rightarrow 0.45\,ms$, is due to an internal mode within the head / neck assembly. Comparing the ICP profiles to their respective high-speed videos for this time-period shows that there is practically no global movement in the test object. Since there is no global movement within the head / neck assembly, this suggests that the

presence of the high-frequencies oscillations are localized to within the skull itself. Additionally, the near identical agreement between the three ICP profiles seen in figure 6.13 further suggests that the high-frequency oscillations within the time-period, $0.15 \rightarrow 0.45\,ms$, are due to a systemic response of the test object and not because of an outside force acting on the test object. If the oscillations are isolated to the 3D printed skull itself, and not due to a combination of skull oscillations and wave propagation with the intracranial contents, this provides direct evidence to support the skull-flexure mechanism.

Now, similar to the lack of visual evidence of cavitation, there is a lack of visual observations capable of directly proving the presence of skull oscillations. The data acquisition instruments utilized (pressure transducer and high-speed camera) for the ABC experiments are incapable of determining the nature of any vibrations located within the skull. To quantify the vibrations within the skull would require the use of strain gauges. As depicted in §5.2, no strain gauges were implemented during the ABC experiments. The incorporation of strain gauges and the presence of skull oscillations will be discussed again later.

### 6.2.2 Displacement of the Test Object

The sequences of high-speed images were used to determine the displacement of the test object for each of the ABC experiments. A MATLAB script (MathWorks® Natick, MA) was created around a segmentation algorithm initially developed by Kellner [64] utilizing basic digital image processing techniques to track six individual areas of the test object based on seeding points; five of the areas were embedded in the gelatin and the sixth was the pressure transducer embedded in the contrecoup region of the skull. The exact locations of the six areas that were tracked can be seen in figure 6.14. The areas within the gelatin were small, embedded *scale-bars* positioned to be at the mid-plane of the gelatin in the same manner as the embedded tracer particles. Figure 6.14 additionally shows the full field-of-view (FOV) captured for the entirely of the ABC experiments, where the blast wave propagated from left-to-right as seen in the figure.

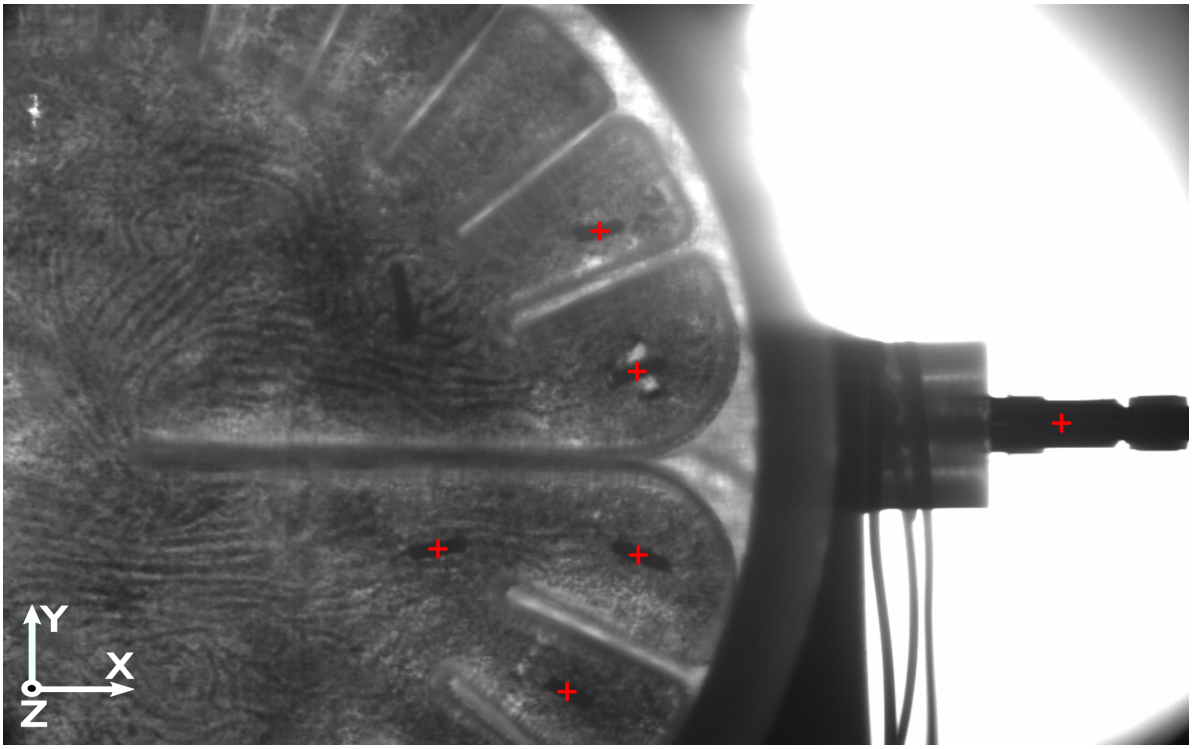


**Figure 6.14.** The red crosses (✚) mark the locations of the individual areas tracked to determine the kinematics of the test object for the ABC experiments.

Before detailed explanation of the test object's motion is discussed, it is important to clarify the general nomenclature and anatomical significance of the test object's response to the blast loading. First, positive $x$ and $y$ displacements refer to quadrant one of the Cartesian coordinate system (i.e., to the right is positive $x$ and upwards is positive $y$). Next, there are four key phases to the test object's response to blast loading: pre-loading, initial loading to the maximum initial displacement, the maximum rebound, and finally returning to the initial position. An example of these four key phases is demonstrated in figure 6.15. Additionally, figure 6.16 further breaks down these individual phases and how they are segmented into non-dimensional time vector descriptors.

These four phases are highlighted to demonstrate both the mechanical and anatomical significance relating to the overall response of the test object. The first phase (i.e., the reference state), corresponds to pre-loading of the test object and is bounded by time periods $t_{0\_} \rightarrow t_0$. Next, there is the initial displacement phase; this phase encompasses the initial blast loading and the subsequent displacement of the test object. This initial displacement phase is terminated at the point of maximum initial displacement, which is $t_1 = 58\,ms$ in figures 6.15 and 6.16.

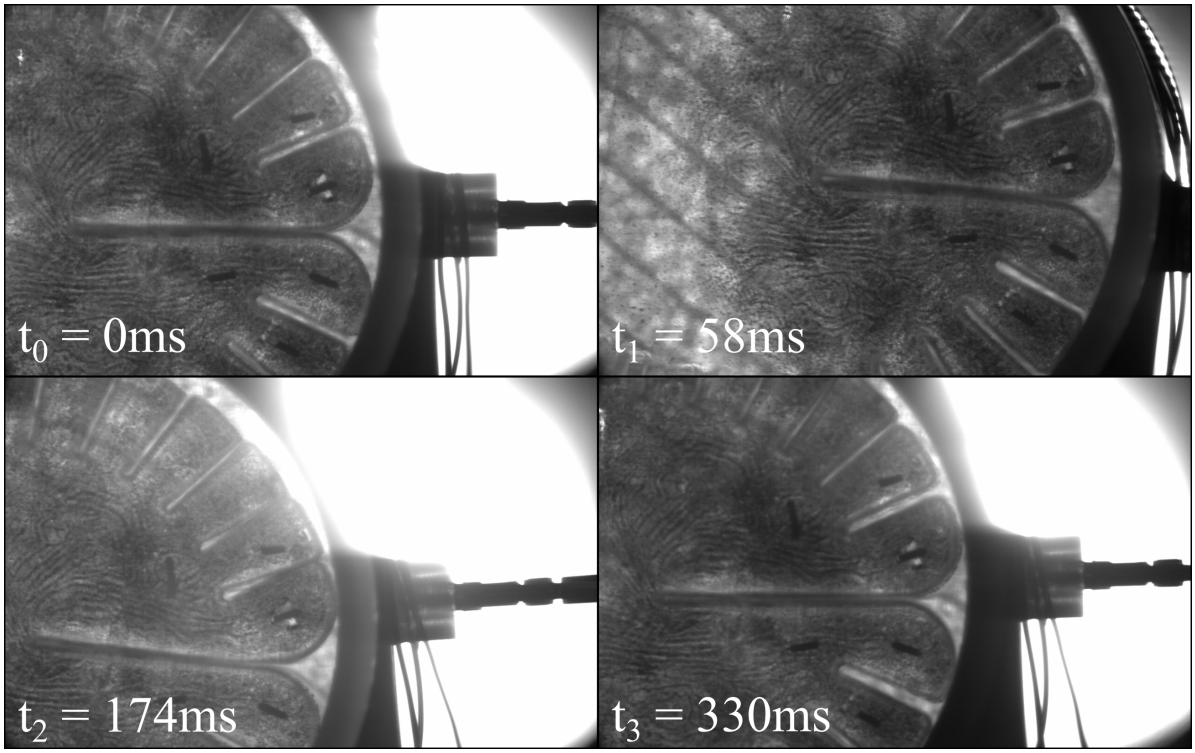


**Figure 6.15.** Compiled frames of the test object's response from blast loading at key displacements for Test #4 (*higher exposure*). $t_0$: pre-loading, $t_1$: maximum initial displacement, $t_2$: maximum displacement of rebound phase, $t_3$: return to initial position

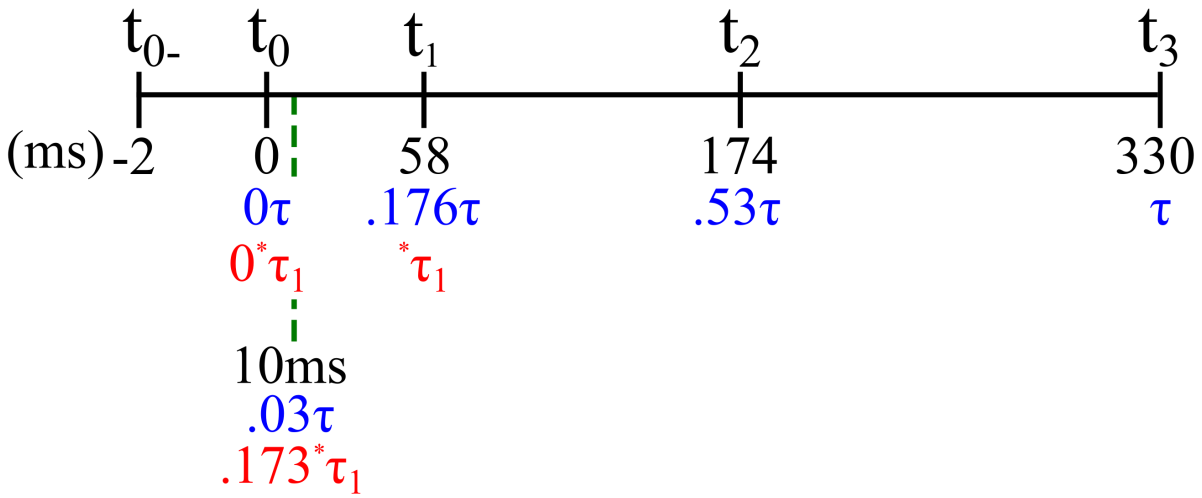


**Figure 6.16.** Non-dimensional time vector descriptors used to define key displacement events for the test object's response to blast-loading. $t_0$: moment right before blast loading, $t_1$: maximum initial displacement, $t_2$: maximum displacement of rebound phase, $t_3$: return to initial position

The third anatomical phase corresponds to the test object rebounding from the maximum initial displacement back towards its initial position. The test object ultimately overshoots its original position and establishes a secondary maximum displacement in the opposite direction as the initial displacement. The initial displacement phase coupled with the rebound phase is complementary to the kinematics of a *"whiplash"* injury that is common in motor vehicle collisions – this similarity will be discussed again later. This phase lasts for approximately $90\,ms$ and is bounded by time periods $t_1 \rightarrow t_2$. The last key phase relates to the time-frame in which the test object returns to its initial position. Important to note here is that each test has slight differences in the exact timing of each phases, especially in comparing when the test object returns to its initial position. The time periods displayed in figures 6.15 and 6.16 are the idealized time stamps for each of these key anatomical phases. Each test is in good agreement with these general time periods as all of them differ by only fractions of a millisecond from the displayed time-stamps.

To further expand on each of these key phases in the test object's response to blast loading, the time segments associated with each phase has been non-dimensionalized by the full time required for the test object to return to its initial position. Additionally, the first phase (maximum initial displacement) has a second non-dimensional time vector descriptor established to aid the reader in understanding the full description of the test object's kinematic response. To clarify, figure 6.16 displays five aspects relating to the key time-periods of the test object's response. First, the general time-period terms, $t_{0\_} \rightarrow t_3$, as seen on the top of the figure are for the ease of the reader. Immediately beneath these general terms are the corresponding physical times (in milliseconds) for each time period. Underneath the physical time-stamps is the corresponding portion of the first non-dimensional term, $\tau$, and is colored blue. The term $\tau$ has been established as the time required for the test object to return to its initial position after the onset of motion for the test object (i.e., $\tau = 330\,ms$). Thus, each time period can be referred to by the physical time stamp or by the percentage of the total time required for the test object to return to its initial position. Similarly, the time period, $t_0 \rightarrow t_1$, has been further classified by its own non-dimensional time vector descriptor, ${}^*\tau$, and is colored red. The reason for the second non-dimensional descriptor, ${}^*\tau$, resides in the

period of time in which the test object's response falls within the translational acceleration regime of motion. As seen from the callout with the green dashed line in figure 6.16, the period of time associated with translational acceleration of the test object corresponds to 10 $ms$ or 3% of the total time the test object is moving or approximately 17% of the initial displacement of the test object. The data presented for the remainder of this section will be limited to the first 10 ms as it isolates the translational response of the test object.

As explained previously, there were five individual points depicted in figure 6.14, which optically tracked within the gelatin to obtain displacement data. Preliminary analysis of each point demonstrated that these regions responded uniformly to the blast loading. Since the individual regions of gelatin behaved uniformly across a large spatial domain, it was concluded that the kinematics of the gelatin were within the linear regime. Therefore, the bulk kinematics of the gelatin was averaged from the displacement data from the five individual regions. The sixth region tracked was the pressure transducer, which was mechanically mounted to the test object and thus allows for the rigid-body motion of the entire test object to be determined. Additionally, there was some dispersion within the calculated displacement data because of the thresholding technique employed to track the individual regions across the sequences of high-speed images. Hence, there was some digital noise present. To mitigate the effects of this noise, a fourth-order Legendre polynomial was fitted to the displacement data. The subsequent velocity and acceleration for the test object was calculated from the derivation/s of the displacement function.

A representation of the test object's displacement, velocity, and acceleration during its response to blast loading can be seen in figures 6.17- 6.19, respectively. Each of the figures displays the $x$ component, $y$ component, and the resulting magnitude. The individual components (mainly $x$ and $y$) illustrate unique temporal differences in the test object's response. To remind the reader, the test object was mounted onto the Hybrid-III $50^{th}$ Male neck (H3N), which was designed to mimic the response of the human spine in an upright automotive seated posture. The natural response of the neck allows vertical movement; the vertical movement of the neck is often dwarfed by either the Cervical extension (backwards bending) or the Cervical rotation (turning head side-to-side),

nonetheless it is an important component to overall response and can be clearly seen in figure 6.17. A final figure, 6.20, displays each of the kinematic component's magnitudes on a single plot for direct comparison.

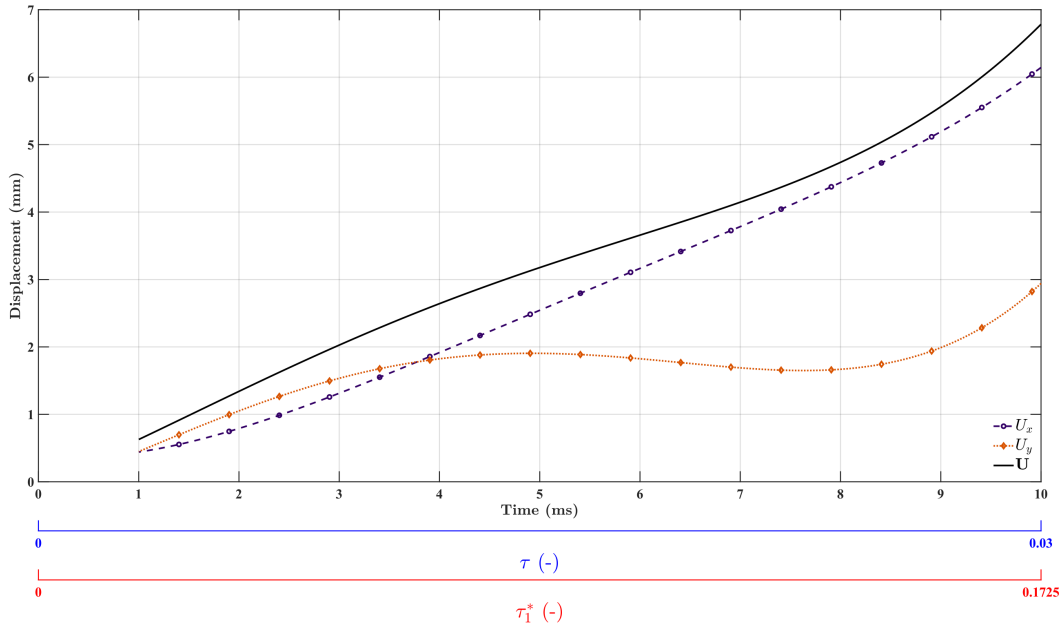


**Figure 6.17.** Representative displacement of the gelatin brain phantom responding to blast loading.

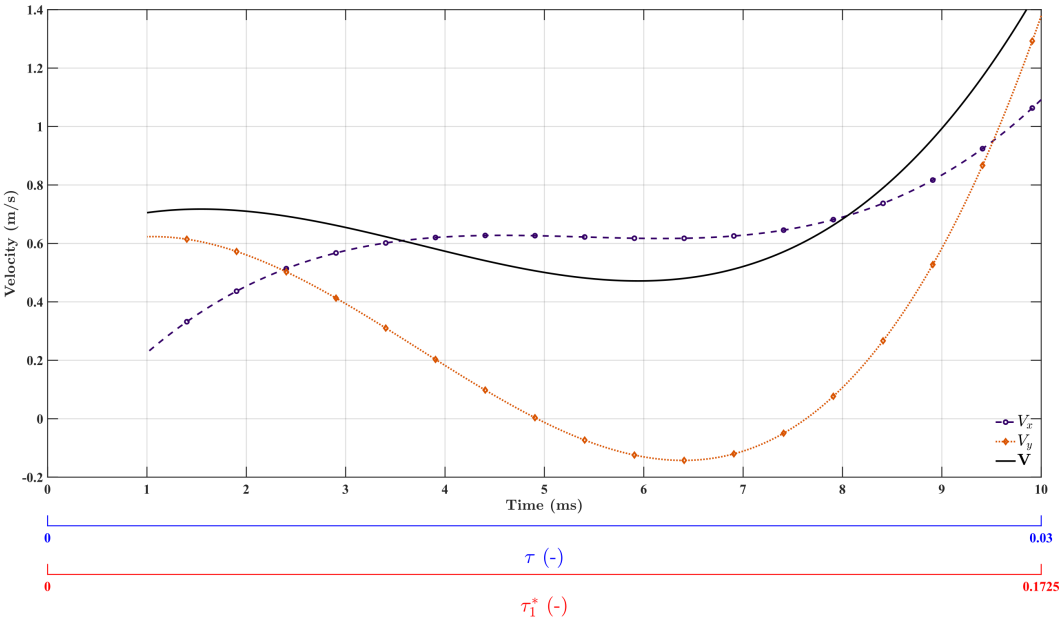


**Figure 6.18.** Representative velocity of the gelatin brain phantom responding to blast loading.

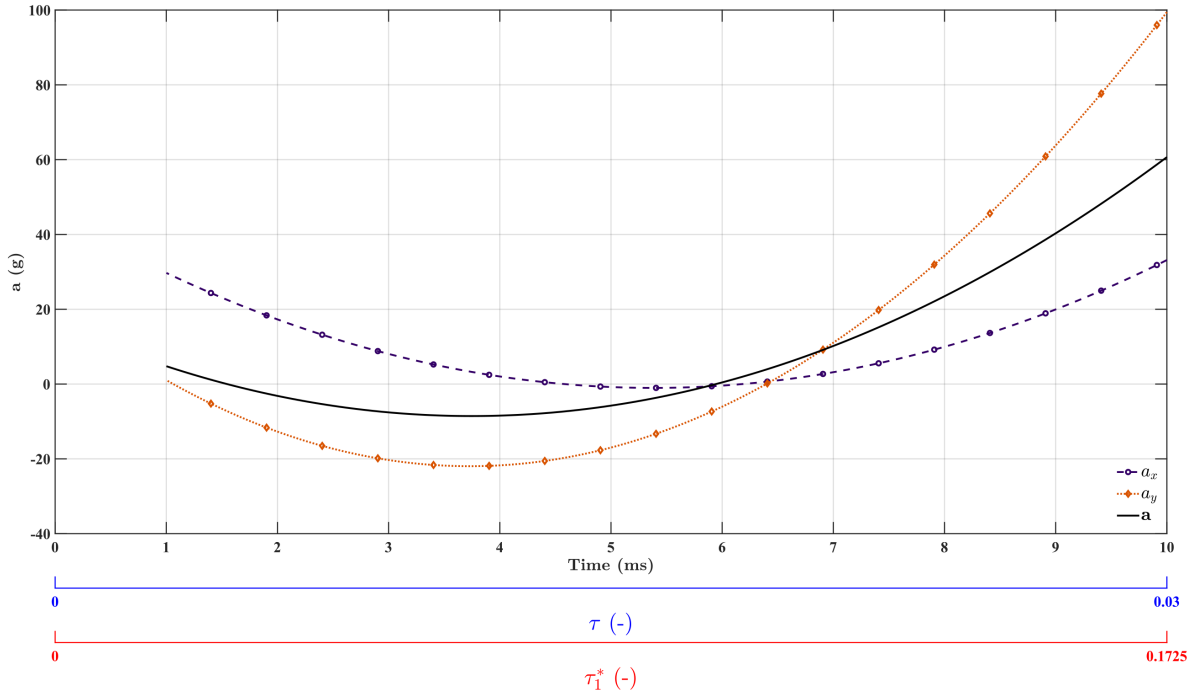


**Figure 6.19.** Representative acceleration of the gelatin brain phantom responding to blast loading.

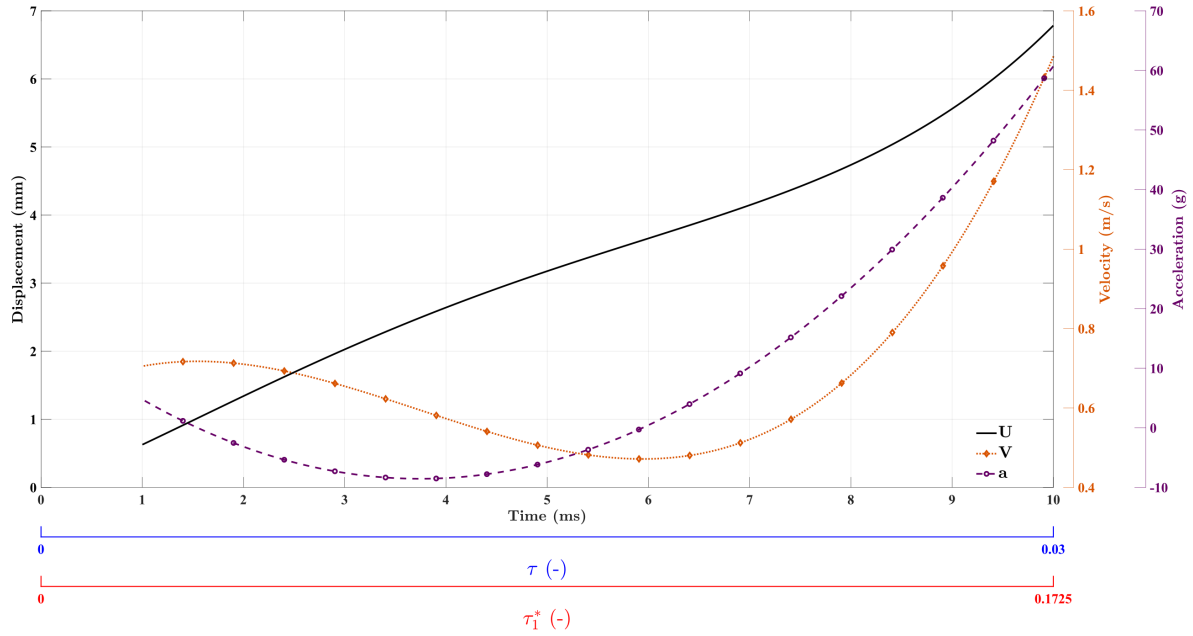


**Figure 6.20.** Representative kinematics of the gelatin brain phantom responding to blast loading. Kinematic components are in terms of their respective magnitudes.

An aspect regarding figures 6.17- 6.20 to be highlighted is the time in which the data starts to be displayed, specifically $1\,ms$. The test object is initially at rest prior to blast loading (i.e., $U = 0$, $V = 0$, and $a = 0$). However, the propagation of the shock wave through the air created high distorted images within the image stack. These specific image frames introduced erroneous results based on the image processing techniques employed to extract the displacement information. For this reason, the high distorted images were not included. The *"starting"* point of the usable images corresponded to $t = 1\,ms$. Therefore, to provide high quality and accurate results, the data presented is for $t \geq 1\,ms$.

The general displacement behavior of the test object was quite similar for each of the ABC experiments. There was positive displacement in both the $x$ and $y$ directions. The displacement in the *x-direction* exceeds that of the *y-direction*; this behavior is as expected due to the limitation of vertical movement that is natural for the H3N. Additionally, there are two unique periods of time where the gelatin brain phantom experienced vertical displacement, $t = 1 \rightarrow 5\,ms$ and $t = 8 \rightarrow 10\,ms$, as seen in figure 6.17. The displacement in the *x-direction* is more uniform in nature than the *y-direction* and is indicative in each of the individual component graphs: straight slope in figure 6.17, constant velocity in figure 6.18, and no acceleration in figure 6.19 from $t = 4 \rightarrow 7\,ms$.

The last aspect regarding the response of the test object for the ABC experiments is the similarity between the motion of the gelatin phantom and the rigid-body motion of the entire test object. The comparison between the bulk gelatin displacement and that of the entire test object is illustrated in figure 6.21. Figure 6.21 shows that the overall displacement magnitudes between the gelatin and the entire test object is nearly identical. The similarity between the bulk gelatin displacement and that of the entire test object is not surprising. As stated previously, the period of interest discussed herein falls within the translational acceleration regime. There was no anticipation of significant differential movement between the gelatin and the entire test object during translational motion. Previously reported data have demonstrated that differential movement between the skull and the brain is a primary factor of rotational / angular acceleration, not translational data [8, 81]. The data presented herein only further support this observation.

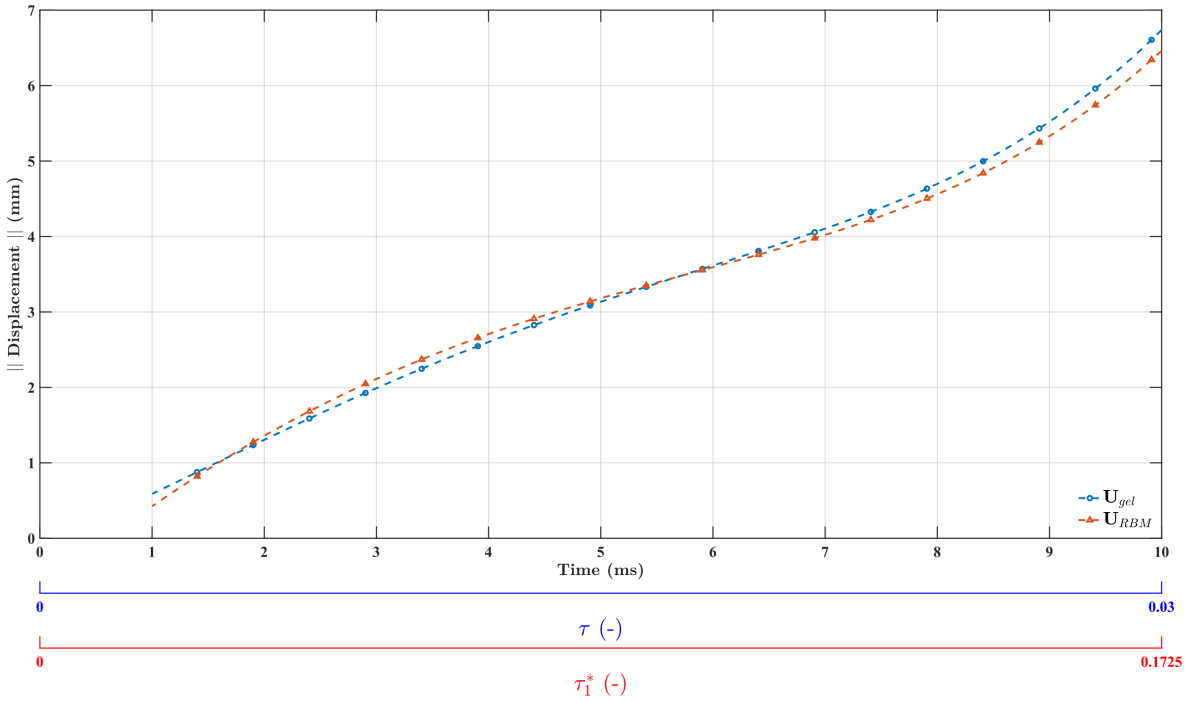


**Figure 6.21.** Representative comparison between the rigid-body motion of the entire Test Object and that of the gelatin brain phantom. Displacements are in terms of their magnitudes.

The rotational / angular acceleration regime was intentionally avoided during the analysis of the test object's displacement. The investigation into the response from blast loading focused on isolating the potential injury mechanisms associated with *primary blast injury*. As explained in §2.1, primary blast injury is classified as injury that is the direct effect of blast wave interaction with the head. Any rotational / angular acceleration would not be classified as a primary injury. Rather, its classification would be a *tertiary injury*, which is an injury resulting in an individual being displaced by the force exerted by the blast. The distinction between *primary* and *tertiary* is paramount to the overall understanding of the presented results. There are some researchers who do include head rotation as a primary injury if the rotation is the result of only the primary blast; however, this is not the widely accepted standard. This research distinctively separates rotation from primary blast loading. Although from an anatomical point-of-view, it is also important to understand that the test object's response (and that of a human head) are not limited to the translational acceleration regime. As clearly illustrated by figures 6.15 and 6.16, the full response encompasses angular displacement in both flexion (forwards) and extension (backwards) directions. By isolating the

test object's response to the translational phase the investigation into the potential injury causing mechanisms associated with primary injury could be performed.

Additionally, unlike the rotational / angular acceleration phase, the translational phase from the ABC experiments can be directly compared to those of the drop tower experiments. With this being said, the comparison of data between the two sets of experiments is still restrictive in nature; the mounting of the test object was different between the two experiments. The physical mounting of the test object influenced its overall displacement response (i.e., fixed versus transient boundary conditions) to the different loading modes. Insights into the behavioral response of the test object can still be gathered from the intracranial pressure data, specifically the differences in the evolution of ICP based on either blunt or blast-loading.

Now, there are general similarities between the ICP response of the test object from the two sets of experiments: an initial negative pressure phase, followed by a large positive pressure shift, and completed by under-damped pressure oscillations back toward atmospheric pressure. However, the initial response of the ICP is unique between the blunt and blast-loading as illustrated in comparing figures 6.5 and 6.13. Furthermore, the positive phase pressure oscillations display particular characteristics depending on the loading mode. The oscillations within the ICP response from the blast loading are more uniform and predictable compared to the oscillations within ICP from the blunt loading. The difference between the ICP response between the two loading modes could be the influence of the restrictive, rigid mounting present in the drop tower experiments. The difference between the ICP profiles of the two experimental methods will be discussed further in §7.

# CHAPTER 7

# CONCLUSION, PERSPECTIVES, & SCIENTIFIC CONTRIBUTIONS

The work presented in this dissertation highlights some key aspects regarding the mechanical response of a human-head surrogate model to both blunt and blast-loading conditions. The absence of prior work in the domain of gyrated human-head phantoms led the author to the conception, fabrication, and implementation of a realistic head phantom used to investigate the potential injury causing mechanism/s associated with TBI / bTBI.

The first and second chapters provide a comprehensive review of the relevant aspects required to understand the complexity of TBI / bTBI research and the multidisciplinary approaches currently being employed to expand the general knowledge of the field. Chapter 1 breaks down the global significance relating to TBI / bTBI and then provides basic information on the important anatomical components as well as common injuries relating to this field of study. Additionally, chapter 1 highlights key aspects regarding the parameters involved in the biomechanical loading modes (contact, inertial, and blast over-pressure) present during injury events. Lastly, chapter 1 provides an introductory explanation into the characteristics of an open-field blast wave and the important parameters associated with blast injuries. The second chapter provides insight into the current research being conducted to further understand TBI / bTBI. The hypothesized injury mechanisms are discussed followed by the extensive research performed into the material properties of brain tissue itself. Next, the importance of computational models as well as their overall limiting capabilities are reviewed. The reader is then introduced to the variety of experimental techniques used to investigate / replicate the parameters associated with blast loading that were first introduced in chapter 1. Finally, the idea of *"scaling laws"* and their limitations regarding predictive capabilities are discussed.

The next two chapters highlight the creation of the biofidelic gyrated brain phantom and the experimental apparatuses used to investigate the mechanical response of said phantom under different loading conditions. Chapter 3 breaks down all of the components relating to the phantom itself; the

conception and computer aided design of the phantom is first described. Then key aspects regarding 3D printing and how it was used is discussed. Next, the material used as the brain tissue simulant itself, a gelatin called polyacrylamide, is reviewed along with its beneficial characteristics. The third chapter is concluded with a descriptive *step-by-step* procedure into the full fabrication of the gelatin brain phantom as well as the overall test object.

The fourth chapter discusses the fabrication and incorporation of the two experimental apparatuses used throughout this research: a drop tower and a blast chamber. Each apparatus was custom-built to investigate the potential damage causing mechanisms associated with TBI / bTBI. Each apparatus was carefully designed with the ability to implement a noninvasive data acquisition system (e.g., high-speed imaging) to monitor the response of the test object to variety of loading conditions. The specific loading conditions for both the drop tower and the blast chamber are reviewed in chapter 5. The fifth chapter also discusses key features regarding the mounting and implementation of the test object in each apparatus. Finally, the results of the experiments conducted with each experimental apparatus are discussed in chapter 6. Additionally, key observations regarding both blunt and blast-loading are also discussed in chapter 6.

The methods used to replicate the human head as well as the experiments conducted in order to investigate the mechanical response of the head phantom are not without their limitations. The first limitation associated with the conducted research relates to the thoracic surge mechanism. As detailed in §2.1.4, the thoracic surge mechanism is unique compared to the other debated mechanisms (direct cranial transmission, skull flexure, and skull orifices) associated with bTBI as it is the only one not directly involved with loading of the head. Rather, it suggests that damage to the intracranial contents is the result of volumetric vascular surge originating from the thorax / abdomen. The thoracic surge mechanism was not investigated in any portion throughout this research. Thus, the findings presented previously can not provide supporting or opposing evidence regarding the validity of the potential damage associated with the thoracic surge mechanism. Now, for the same reason that makes the thoracic surge mechanism unique, was also the reason it was chosen not to be investigated with this conducted research – i.e., does not involve loading directly to the head.

The human head phantom employed throughout this research has provided significant means to studying multiple potential damage causing mechanisms simultaneously. The benefit of being able to investigating multiple mechanism compensated for the inability to study the thoracic surge mechanism within this research.

To expand on the topic of mechanisms, the current test object is also limited in its ability to draw conclusions relating to the skull-orifice mechanism. The primary reason for this is due to the simplistic geometry of the outer-portion of the 3D printed skull; specifics on the geometry can be found in §3.2. Without the direct incorporation of the important air-filled cavities (e.g., nasal, auditory, sphenoid / frontal sinuses, and orbits) relating to the skull-orifice mechanism direct conclusions cannot be formulated from this conducted research. With this being said, the current test object does provide useful data that can be used to compare any future work conducted to investigate the skull-orifice mechanism.

The next set of limitations are related to the overall anatomical accuracy of the human-head phantom itself. The first to be discussed regards the simplistic nature of the head phantom's geometry. The concept of the phantom has been described in detailed in §3. The resulting 2D extruded ellipsoid cylinder grossly underestimates the complexity associated with a real human brain. Specifically, the complex features associated with cranial anatomy were not incorporated into the brain phantom: curved calvarium, sub-cortical structure, ventricles, falx cerebri, tentorium cerebelli, petrous or sphenoid ridges, etc. The lack of incorporating these features limits the interpretations that can be made connecting this study's findings with that of clinical data involving real human heads. With this being said, the current incorporated features (dominant length scales of the sulci, gyri, gray matter thickness, and overall brain dimensions) allow for mechanistic insights to be gathered resulting from loading events. Additionally, the generalized geometry utilized allowed for the investigation of key phenomena present during loading scenarios. The balance between incorporating anatomical features and the necessary simplicity required to investigate potential damage causing mechanisms was paramount during the conception of the gyrated brain phantom. The presented human-head phantom utilized throughout this research is not perfect; however, it was still uniquely capable of

providing insights into the mechanical response of the head following loading.

The next aspect pertains to the 3D printed skull and has already been addressed in §3.2.2.1. Due to the overall importance of the anatomy's role in TBI / bTBI, this particular topic is being reiterated. The use of a 3D printed material for the test object's skull inherently lacks anatomical significance. With this in mind, the 3D printed skull's geometry used throughout this research was created to replicate the anatomy of the flat bones that comprise the neurocranium. This was achieved by mimicking how the trabecula bone is sandwiched between two layers of cortical bone in the use of the 3D printing infill parameter; this layered structure is evident when comparing figures 3.10 and 3.11. Again, the use of a 3D printed skull does not perfectly replicate that of a human's; however, the layered structure incorporated within its design has more anatomic representation than the use of a single material skull as seen with other human head surrogates.

To continue with the anatomical accuracy related limitations, the tissue simulant chosen for the human-head phantoms also has characteristic constraints. Polyacrylamide gelatin was selected as the material of choice to act as the brain tissue simulant for a variety of its beneficial attributes: low-energy requirements, quick fabrication time, easily tunable material properties, and its high level of optical transparency. These intrinsic properties are all around favorable, especially from stand-point of utilizing high-speed imaging as a data acquisition technique. However, polyacrylamide is a homogenous material. Being homogenous is not inherently disadvantageous, but rather it is not anatomically representative of the human brain. The human brain has been well established to be highly anisotropic due to the sub-cortical structures, connective tissue, white matter tracts, and cerebral vasculature. Furthermore, brain tissue itself has been established to be very soft, nonlinear, nearly incompressible, viscoelastic, strain-rate sensitive, anisotropic, and regionally independent. The difference in the material properties between polyacrylamide gelatin and brain tissue ultimately limits the prediction capabilities regarding potential injury patterns associated with the biomechanical loading conditions presented in this research. Nevertheless, the use of polyacrylamide as a brain tissue simulant has provided considerable insights to the mechanical response of the brain resulting from a loading event. Additionally, blunt-force impact and blast over-

pressure are classified as dynamic loading events; the millisecond loading associated with blunt-force impact and the sub-millisecond loading presented during blast loading interacts indiscriminately whether a material is isotropic or anisotropic. Now, the anisotropy of tissues could alter long-term mechanical response from such loading modes; however, the results previously discussed are all within 15 ms of the loading event. Further work is necessary to quantify the difference between any anisotropic nature of biological tissues and that of the polyacrylamide gelatin used for the brain phantom under such ultra-fast time regimes. Under the current time domain presented for the mechanical response of the system, it is reasonable to assume that there would be a degree of similarity between isotropic and anisotropic materials. Thus, making polyacrylamide gelatin a suitable candidate for a tissue simulant under the current application of loading events.

Another limiting aspect regarding the use of polyacrylamide gelatin as a tissue simulant, or any inorganic gelatin for that matter, is seen in the inability to model physiological changes associated with TBI events; epidural hematomas, coup and contrecoup contusions, subarachnoid hemorrhages, cerebral contusion, vasculature damage, etc. While tissue simulants and whole organ phantoms are advantageous in regards to removing biological variations seen throughout animal studies, they do restrict nearly all of the post-injury assays commonly preformed in order to understand biological response to extreme loading events (e.g., histological assays, blood work, etc.). With this being said, the investigation of physiological changes fell outside the scope of this research; however, such topics should be addressed in any future head phantom designs.

Similarly, there is a limitation regarding the physical quantities captured in the results from this research; pressure and displacement data do not have a direct correlation to biological outcomes. Again, understanding the resulting physiological response was not the direct intention of this work. The intention of this work was intended to investigate the response of the head resulting from mechanical loading. Nevertheless, this work was also intended to advance the knowledge base of TBI injuries in general. Being able to directly associate engineering principles (e.g., pressure, displacement, strain, strain-rate, etc.) to that of biological outcomes could greatly improve the clinicians' diagnostic abilities. Additionally, understanding the relationship between the physical

quantities present during an injury to the symptoms seen clinically could lead to greater predictive capabilities for the potential life-threatening conditions (e.g., epidural hematomas, subarachnoid hemorrhages, contusions, etc.) that are often the result of such extreme loading events. Further work, whether *in-vivo* or *in-vitro*, is necessary to quantify the resulting pathology from the injury insults associated with TBI / bTBI.

In spite of all of the previous limitations discussed, there have been a substantial number of insights into the potential damage causing mechanisms associated with TBI / bTBI that have been gathered resulting from the experiments discussed herein. A primary observation relates to the observed formation of cavitation within the intracranial contents following loading. As discussed in §6.1.1, the intracranial pressure of the test object fell below the theoretical vapor pressure threshold of $-98.15\,kPa$ for water at $25°C$ for all of the blunt loading experiments. As a result cavitation was observed at both the coup and contrecoup locations. It is important to highlight that the observed cavitation was the result of purely translational movement and not a combination of translational, rotational, and angular. Additionally, the cavitation was observed in the bulk fluid, at the gelatin / CSF interface, on the surface of the skull, within the depths of the sulci, and finally a single experiment produced cavitation generating within the gelatin substrate itself.

The observation of cavitation forming within the brain tissue simulant is the first of its kind, to the best of the author's knowledge. Now, this observation was isolated to a single region of a single blunt loading experiment; and thus, further work is required to characterize if the conception of cavitation within substrates are more wide-spread. Nonetheless, the potential for cavitation to form within brain tissue is significant. An additional aspect regarding the observed cavitation was the presence of high-frequency longitudinal waves propagating along the surface of the gelatin resulting from the collapse of the cavitation bubbles themselves. These high-frequency *"ripples"* coupled with the known damage causing effects of collapsing cavitation bubbles could significantly contribute to the damage mechanisms associated with diffuse axonal injury.

In addition to the observed cavitation, there is supporting evidence for the skull flexure theory. As first presented in §6.1.2, there is oscillatory behavior superimposed on the total downward

displacement data. The presence as well as the behavior if the specific oscillations suggest they are the result of internal wave propagation within the 3D printed skull. An argument for skull flexure is also presented in §6.2.1. The behavior of the intracranial pressure profiles resulting from blast-loading (specifically during the initial negative pressure phase) suggests that the complex high-frequency oscillations are due to the response of the entire test object. Now, it is important to note, that there was no direct correlation observed between the time-periods of potential skull flexure and any potential damage causing phenomena. The potential skull flexures within both the blunt and blast-loading results are highlighted to emphasize an experimental observation of the phenomena being present as a resulting of biomechanical loading.

Now, one of the key attributes of the researched presented in this dissertation is the use of the specific geometry used for the biofidelic brain phantom. As detailed in §3, the specific gyrated geometry was based on a MRI scan of healthy 35-year-old-male. It should be stated that this was not the first brain phantom to ever be used to investigate TBI / bTBI; rather it is only one of many [3, 39, 56, 83, 145]. However, none of these aforementioned brain phantoms have incorporated as many anatomical features as the one presented throughout this research. Our phantom was developed to include the dominant length scales of the sulci, gyri, gray matter thickness, and overall brain dimensions, which arguably makes it one of the most, if not the most, complicated brain phantom currently being used to study the effects of TBI /bTBI. The phantom was not without its own limitations, but the behavioral response observed in both the blunt and blast-loading experiments can be attributed to the unique geometry of the phantom.

Another meaningful contribution resulting from the work presented here happens not to be related to TBI /bTBI at all. Rather, its significance lies in a specific characteristic of the Advanced Blast Chamber – the logarithmic spiral geometry used in the driver section. The logarithmic spiral geometry was initially introduced as a method to focus incoming shock-waves to a single point. Conversely, this work has shown that the logarithmic spiral geometry is capable of producing a reversible process (i.e., both focusing a shock-wave to a line single point and producing a flat shock wave from said line / single point). Details on this reversible process can be found in, §4.2.3, with

the full characterization of the geometry presented by Mejía-Alvarez et al. [85]. The description and subsequent operational success of the Advanced Blast Chamber can aid future researchers wishing to embark on blast-chamber studies.

The last contributing aspect of this research to be discussed is relating to the overall experimental results obtained from both the drop tower and the Advanced Blast Chamber. The number of experimental studies relating to bTBI are quite few in number compared to its counterpart of TBI. As discussed in §2.4, the number of studies using any method (e.g., shock-tube, blast tube, or open-field testing) to investigate bTBI are quite limited. The results presented herein add to these limited number of experimental studies. Furthermore, the results from both the blunt and blast-loading can be directly used to validate the numerous finite element models currently being employed by different researchers. Aspects regarding the use and implementation of finite element models can be found in §2.3, but the key limitation is that every model has to be independently validated against experimental results. Another beneficial aspect of the collected results is how they can be used for future experimental planning. By understanding the mechanical response of the biofidelic test object in both blunt and blast-loading scenarios researchers can utilize these data sets to aid in any *in-vitro* or *in-situ* experiments.

# CHAPTER 8

# FUTURE WORK

There is still much to learn about the mechanics of TBI / bTBI. The presented experiments and their subsequent results are merely an initial step to furthering the collective knowledge associated with TBI / bTBI but specifically bTBI. The substantial aspects relating to the future work of this specific research resides in the overall anatomical accuracy of the test object. The previous chapter highlighted the limitations associated with the specific biofidelic test object utilized in this research. Each of these limitations (e.g., skull orifice investigation, incorporating more specific anatomical features, improving the 3D printed skull design, implementing anisotropy into the gelatin simulant, etc.) can be addressed or modified for any future design of a human head phantom.

The implementation of more sub-cortical anatomical features is of immediate importance. The current test object lacks key intracranial structures that are important to the overall response of the gelatin phantom. Specifically, the falx cerebri, tentorium cerebelli, and the bony petrous ridge would provide internal boundary conditions that could influence the severity of gelatin phantom's response to loading. Incorporating these structures will aid in any future experimental investigations utilizing human head phantoms.

Lastly, an investigation into the specific response of the 3D printed skull to both blunt and blast-loading would help with understanding the specific level of skull oscillations present after loading, which ultimately aid in understanding the skull-flexure theory. The incorporation of strain gauges would provide the easiest means for such an investigation; however, the current manufacturing approach (fusion deposition modelling) used to create the 3D printed skull inhibits the adhesion of strain gauges. Future researchers will need to account for this limitation before pursuing any investigation into the skull flexure theory.

# APPENDICES

# APPENDIX A

## EXPERIMENTAL IMAGES OF DROP TOWER

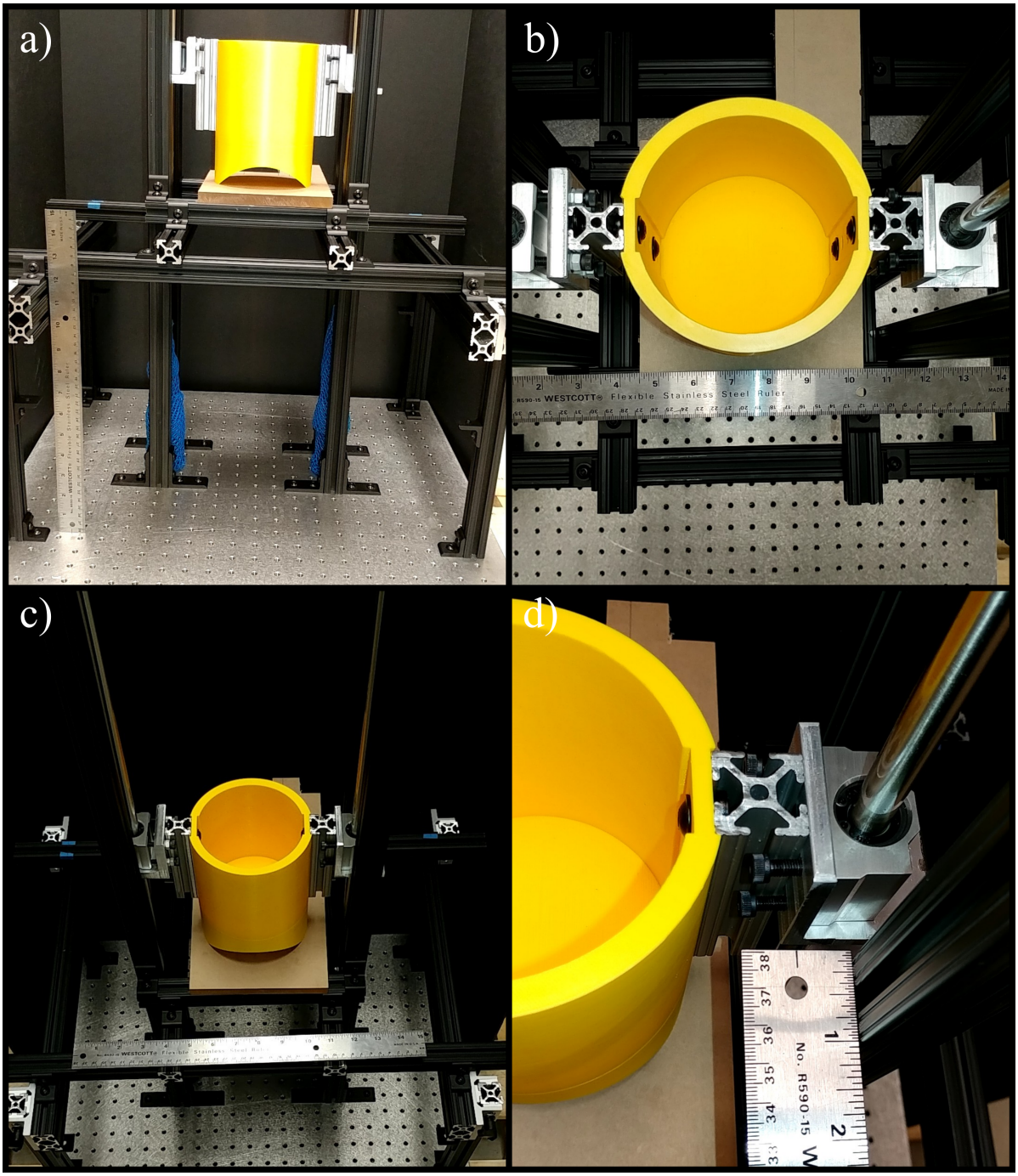


**Figure A.1.** Multiple views of the experimental Drop Tower Apparatus.
a) Front-View, b) Top-View, c) Isometric-Top-View, d) Enlargement of linear bearing mechanism.

## APPENDIX B

## DIMENSIONS OF BIOFIDELIC BRAIN PHANTOM & FULLY ASSEMBLED TEST OBJECT

**Table B.1.** Dimensions for the biofidelic gelatin phantom and the fully assembled 3D test object.

| Parameter | Gelatin Phantom | Test Object |
|---|---|---|
| Mass | 1350 g | 2725 g |
| Vertical Height | 88 mm | 100 mm |
| Transverse Width | 126 mm | 157 mm |
| Anteroposterior Length | 167 mm | 207 mm |
| Skull Thickness | – | 8 mm |
| Gray Matter Thickness | 3.6 mm | – |

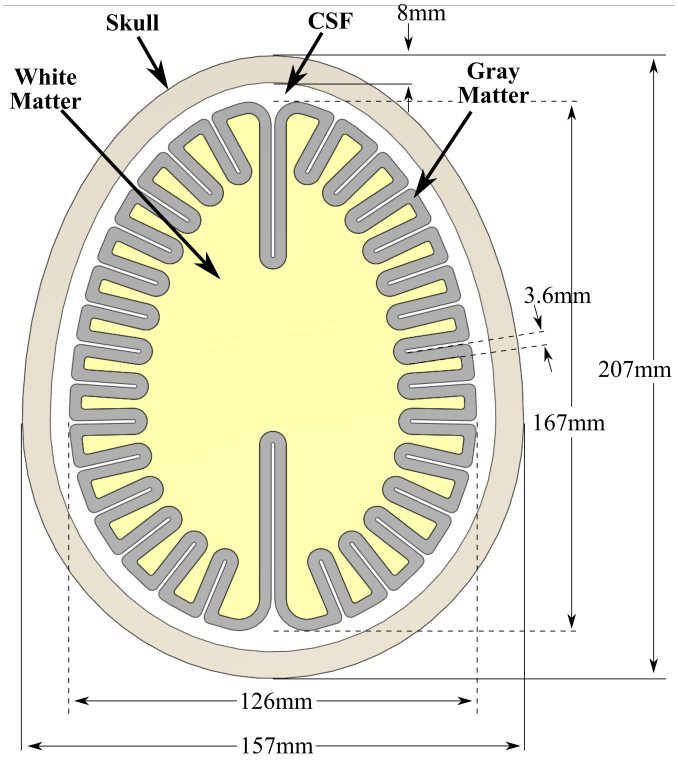


**Figure B.1.** Modification of figure 3.7. Two Dimensional Top Down View of Test Object. Component Coloring: yellow is white matter, gray is gray matter, white is cerebral spinal fluid, and tan is the skull. Gelatin transverse-width: 126mm, gelatin length (anteroposterior): 167mm, gray matter thickness: 3.6mm, skull transverse-width: 157mm, skull length (anteroposterior): 207mm, skull thickness: 8mm.

# APPENDIX C

# INTRACRANIAL PRESSURE PROFILES FOR DROP TOWER EXPERIMENTS

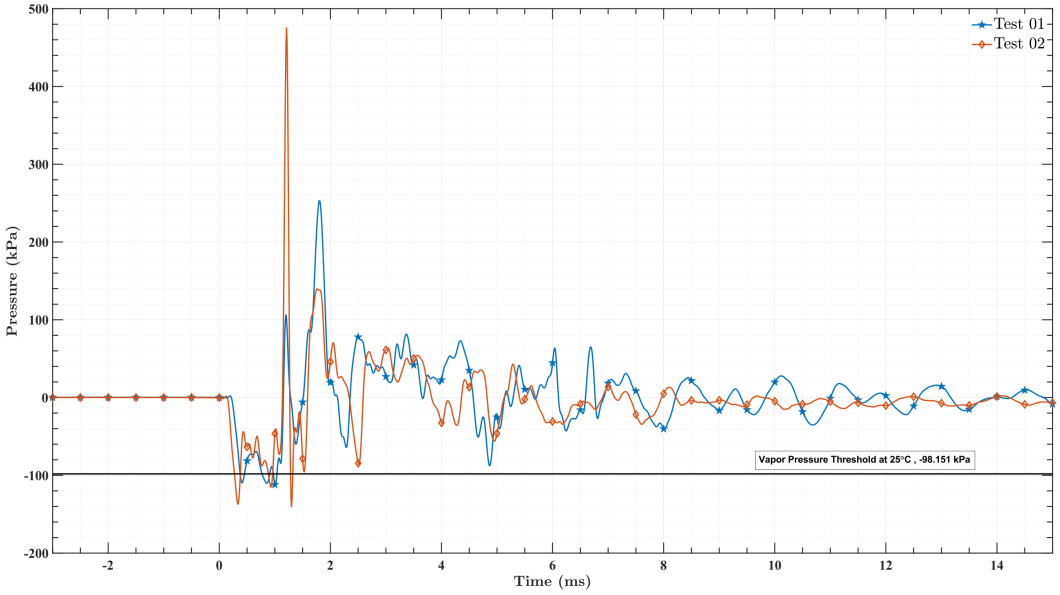


**Figure C.1.** Evolution of Intracranial Pressure for Test #1 and Test #2. 1 kg drop weight. (Reprint of figure 6.1)

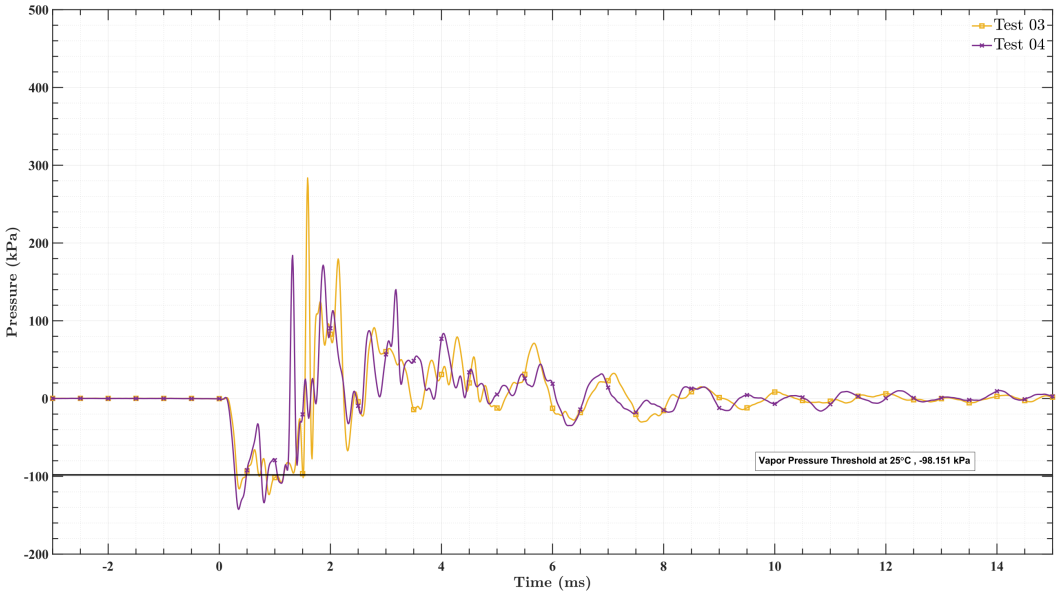


**Figure C.2.** Evolution of Intracranial Pressure for Test #3 and Test #4. 2 kg drop weight.

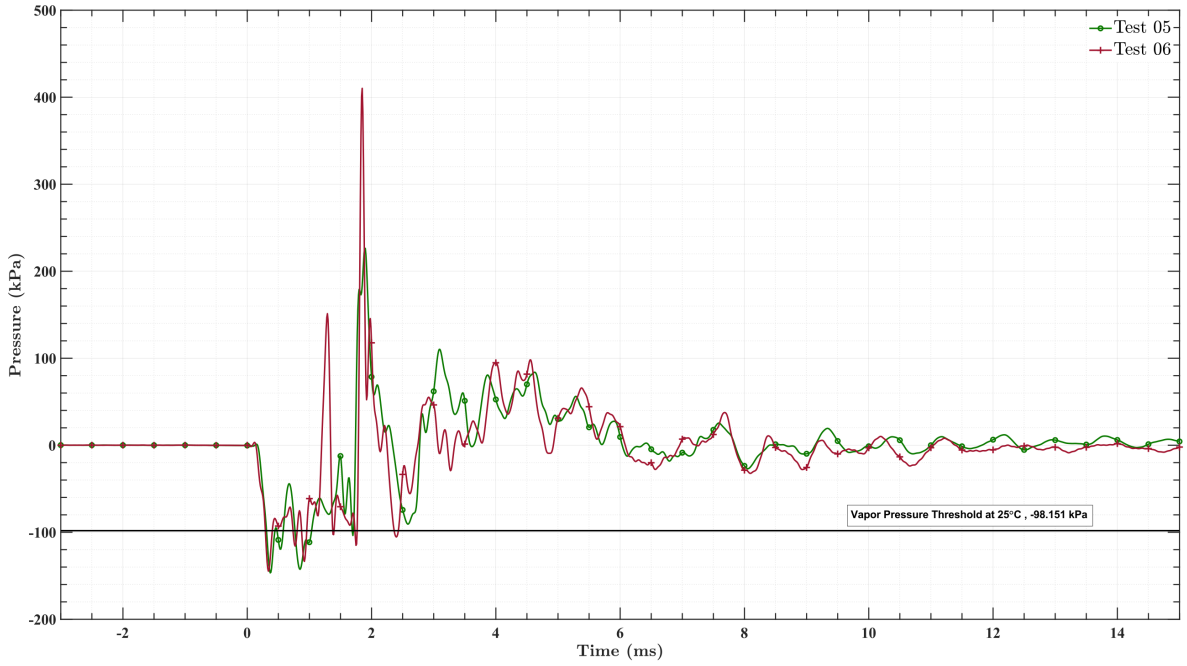


**Figure C.3.** Evolution of Intracranial Pressure for Test #5 and Test #6. 3 kg drop weight.

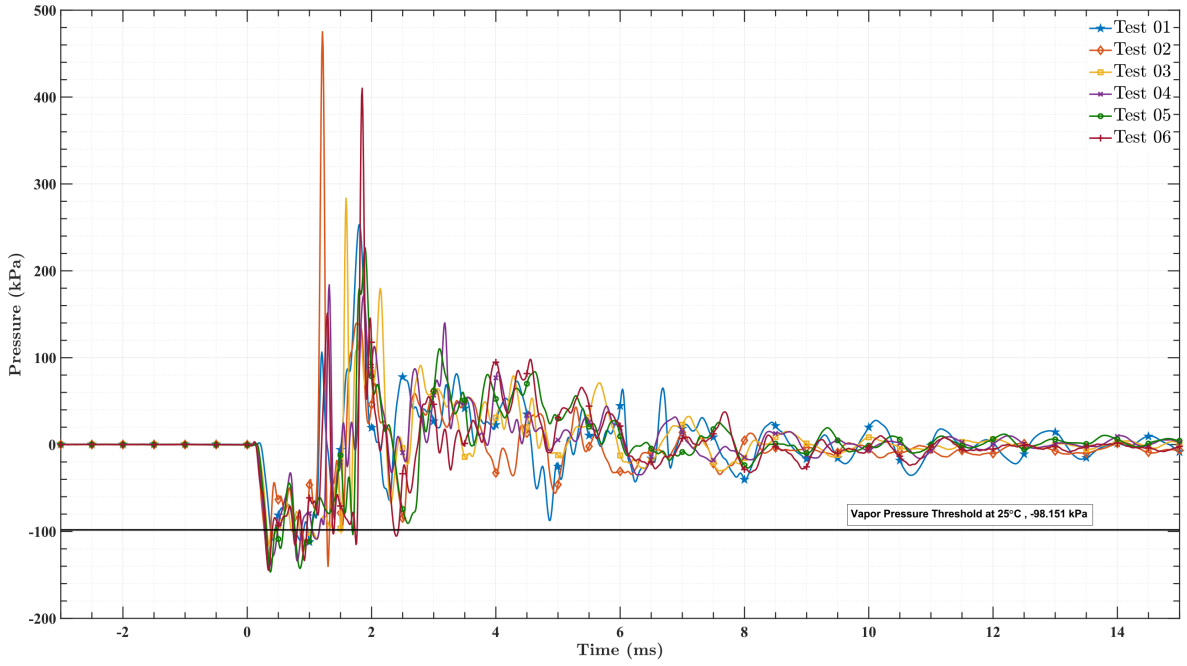


**Figure C.4.** Evolution of Intracranial Pressure for all Drop Tower tests with a data markers. 1 kg: Test #1 and Test #2, 2 kg: Test #3 and Test #4, 3 kg: Test #5 and Test #6.

# APPENDIX D

# DISPLACEMENT PROFILES FOR DROP TOWER EXPERIMENTS

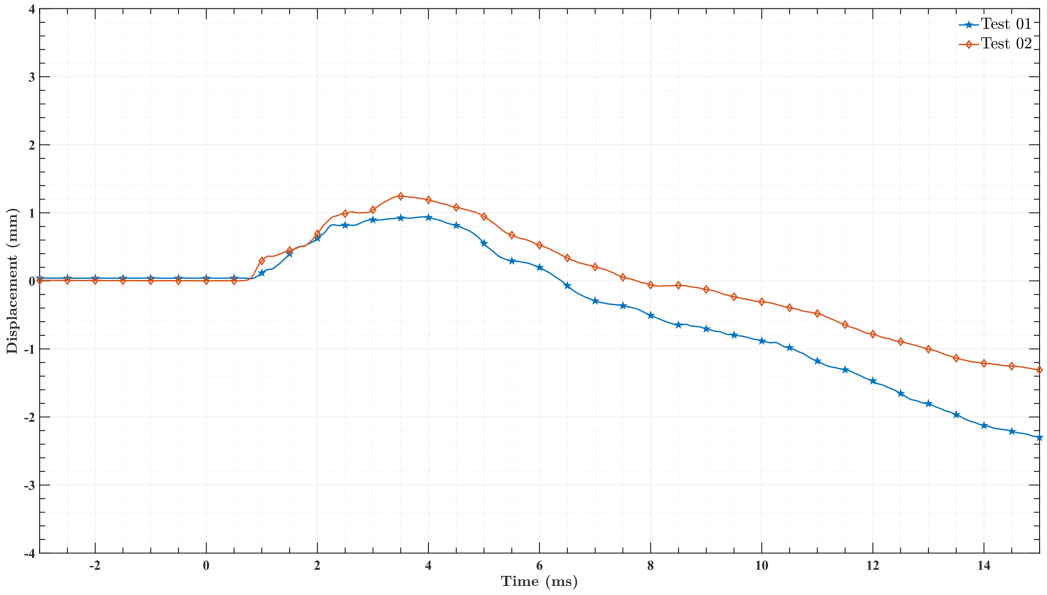


**Figure D.1.** Displacement profile for the Test Object during Test #1 and Test #2. 1 kg drop weight.

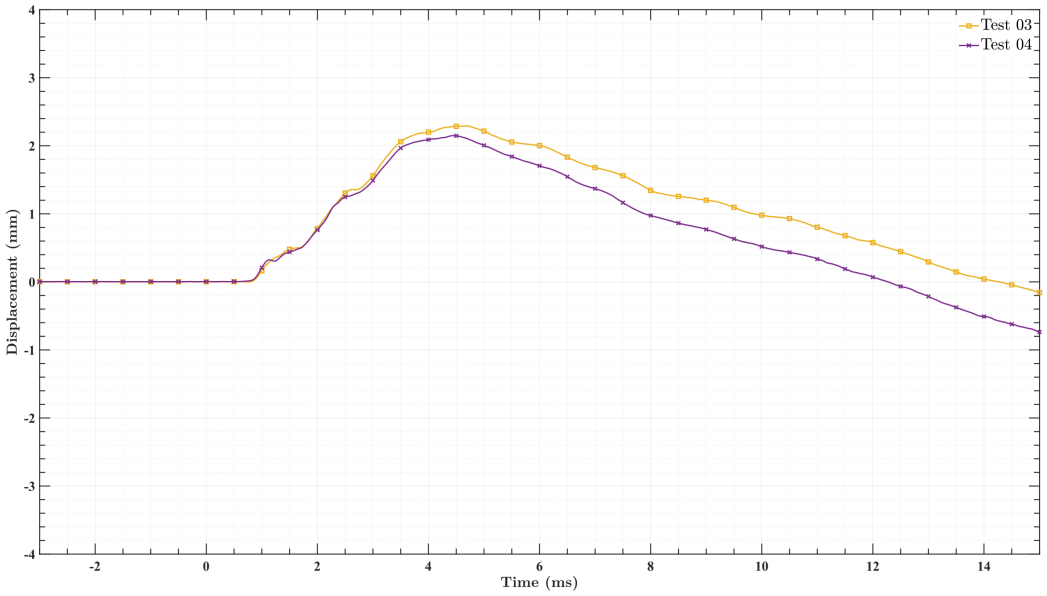


**Figure D.2.** Displacement profile for the Test Object during Test #3 and Test #4. 2 kg drop weight.

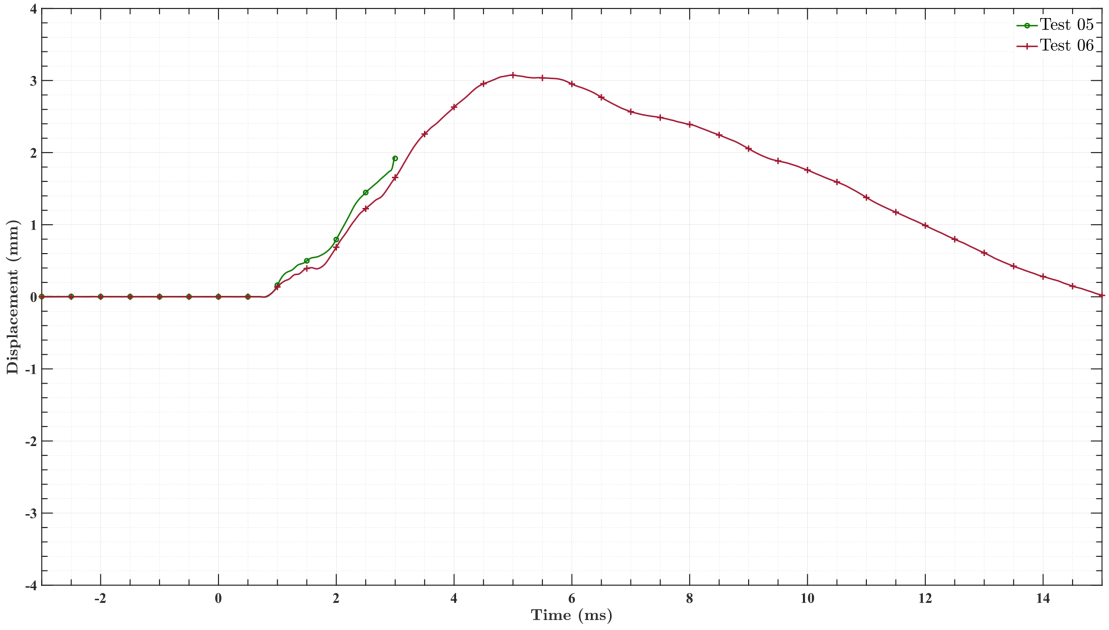


**Figure D.3.** Displacement profile for the Test Object during Test #5 and Test #6. 3 kg drop weight.

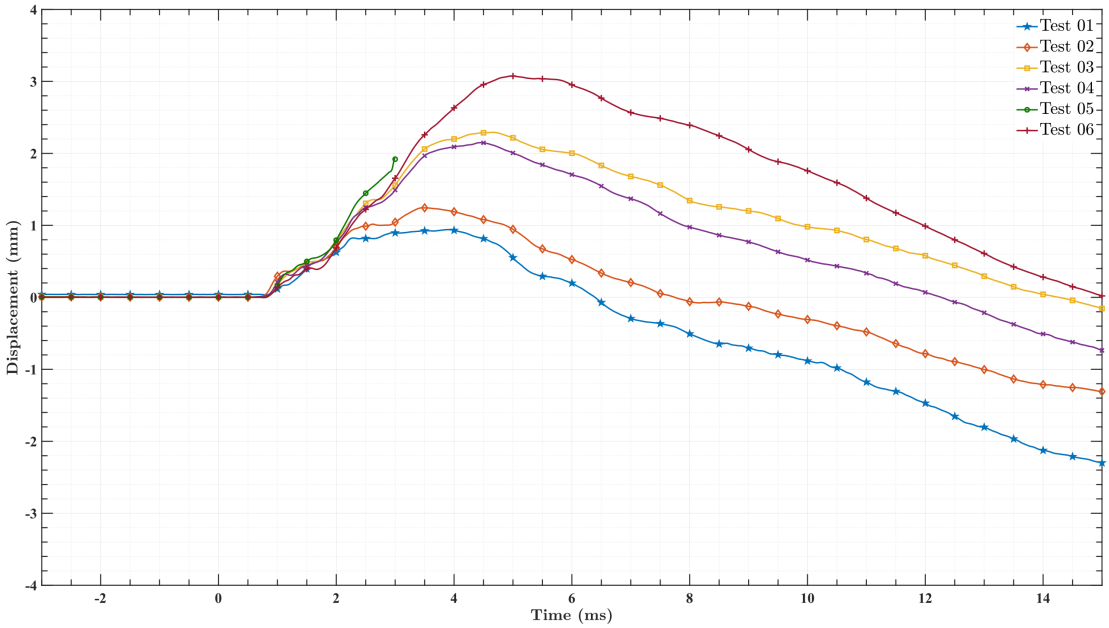


**Figure D.4.** Displacement profiles for the Test Object during all of the Drop Tower Experiments. 1 kg: Test #1 and Test #2, 2 kg: Test #3 and Test #4, 3 kg: Test #5 and Test #6. (Reprint of figure 6.7)

# APPENDIX E

## STATIC AND REFLECTIVE PRESSURE PROFILES FOR THE ABC FOR THE *HIGHER EXPOSURE* EXPERIMENTS

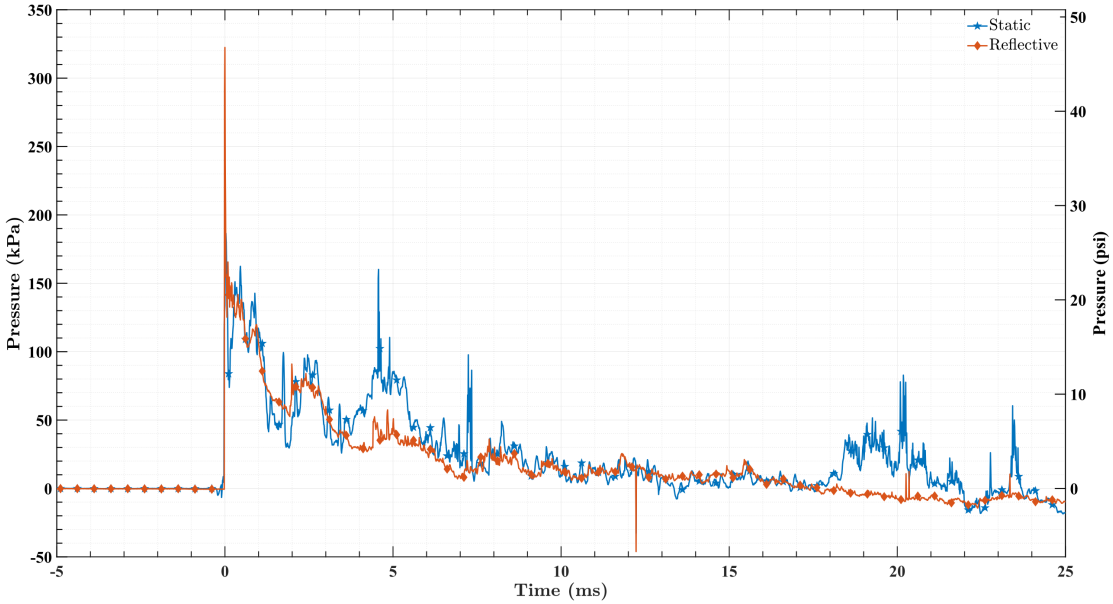


**Figure E.1.** Test # 2: Evolution of static and reflective pressure profiles for the first 25 ms. Maximum reflective pressure 322.42 kPa, maximum static pressure 186.5 kPa.

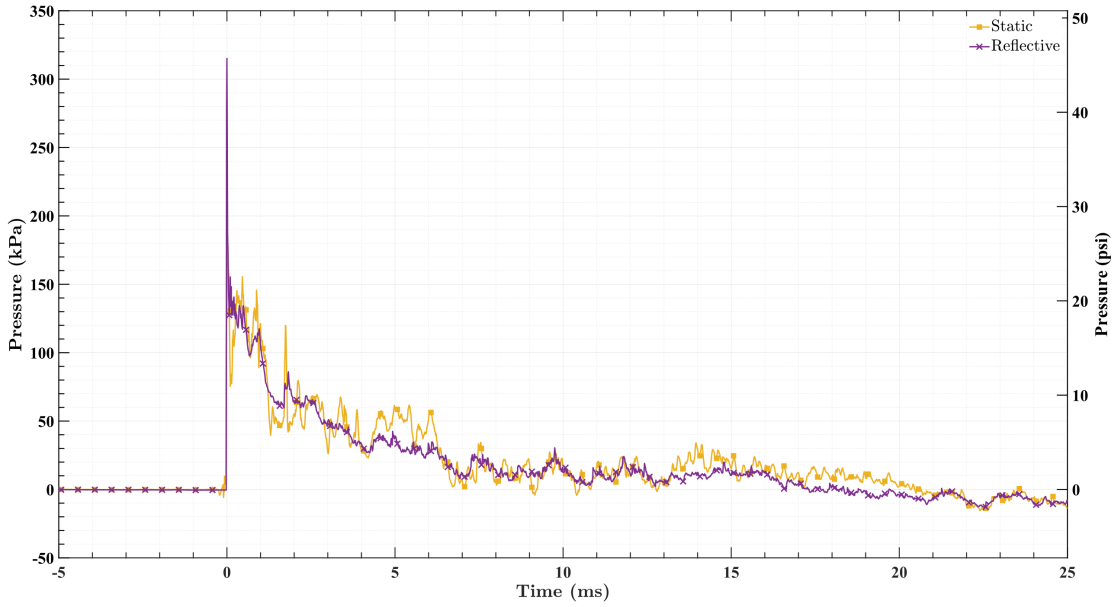


**Figure E.2.** Test # 3: Evolution of static and reflective pressure profiles for the first 25 ms. Maximum reflective pressure 315.12 kPa, maximum static pressure 177.93 kPa.

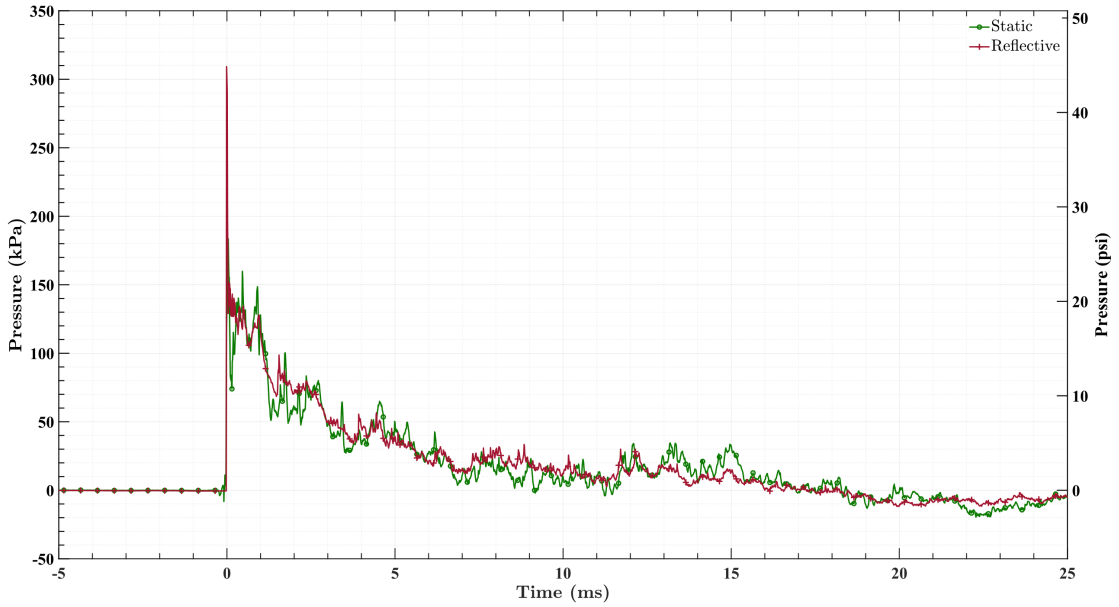


**Figure E.3.** Test # 4: Evolution of static and reflective pressure profiles for the first 25 ms. Maximum reflective pressure 309.24 kPa, maximum static pressure 183.47 kPa. (Reprint of figure 6.8)

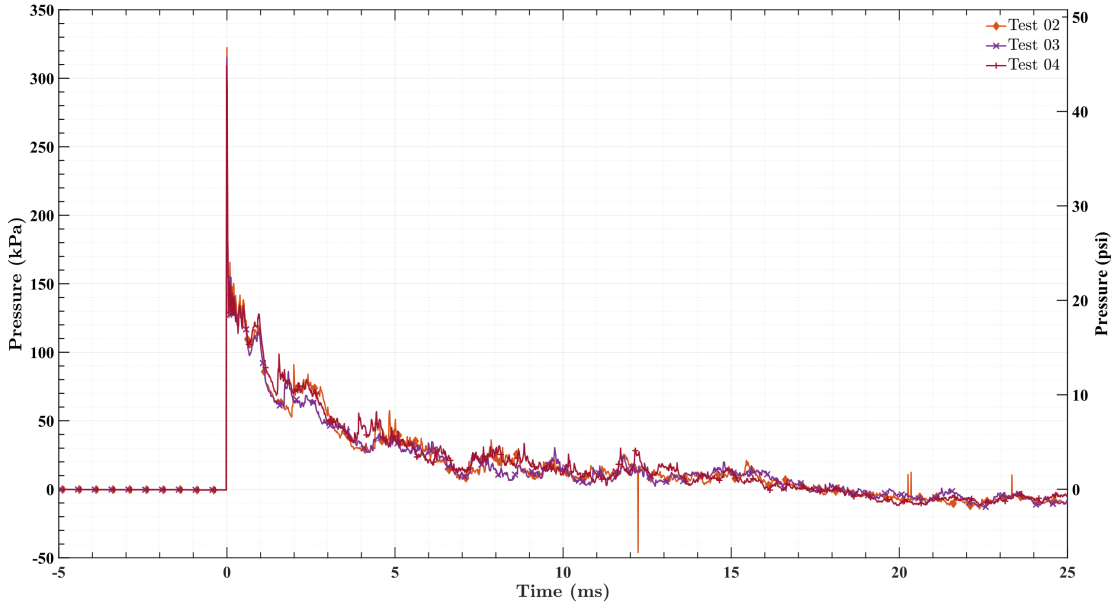


**Figure E.4.** Reflective pressure profiles for all of the ABC experiments performed at the *high exposure* of 172.8 g (0.38 lbs) of PETN.

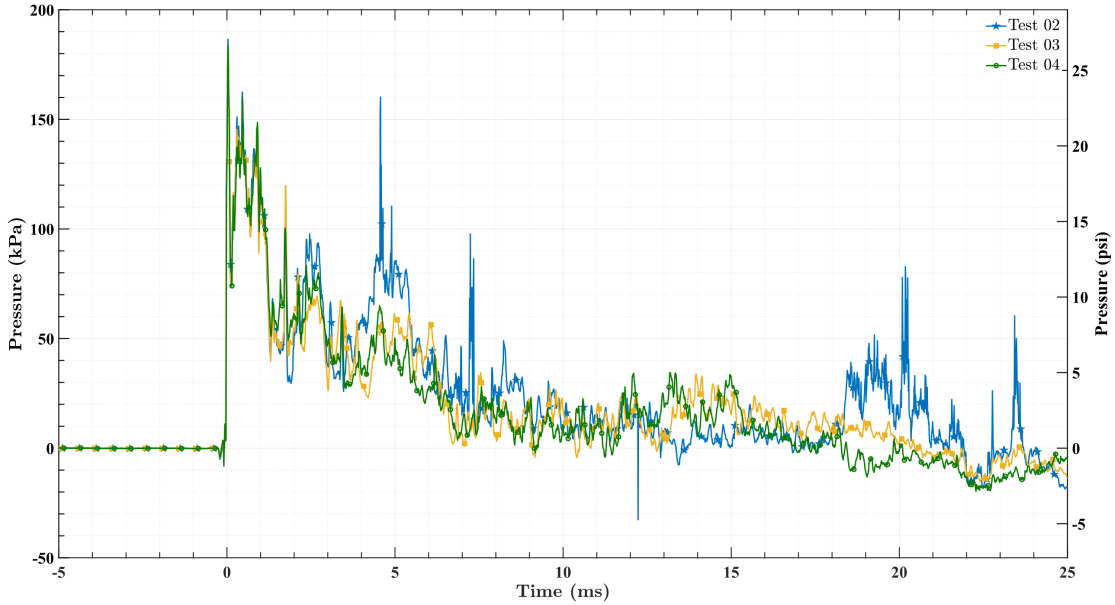


**Figure E.5.** Static pressure profiles for all of the ABC experiments performed at the *high exposure* of 172.8 g (0.38 lbs) of PETN.

**BIBLIOGRAPHY**

# BIBLIOGRAPHY


[1] P. Akula, Y. Hua, and L. Gu. Blast-induced mild traumatic brain injury through ear canal: a finite element study. *Biomedical Engineering Letters*, 5(4):281–288, 2015.

[2] F. Allen. The mechanism of contre-coup and of certain other forms of intracranial injury. *British Medical Journal*, 1(1846):1196, 1896.

[3] M. D. Alley, B. R. Schimizze, and S. F. Son. Experimental modeling of explosive blast-related traumatic brain injuries. *Neuroimage*, 54:S45–S54, 2011.

[4] J. Amos and P. Rincon. Beirut blast was 'historically' powerful, 2020. URL https://www.bbc.com/news/science-environment-54420033#:~:text=The%20blast%20that%20devastated%20large,upper%20limit%20of%201.1%20kilotons. Last accessed 24 February 2021.

[5] J. W. Bales, R. H. Bonow, and R. G. Ellenbogen. 25 - closed head injury. In R. G. Ellenbogen, L. N. Sekhar, N. D. Kitchen, and H. B. da Silva, editors, *Principles of Neurological Surgery (Fourth Edition)*, pages 366–389.e4. Elsevier, Philadelphia, fourth edition, 2018. doi: https://doi.org/10.1016/B978-0-323-43140-8.00025-1. URL https://www.sciencedirect.com/science/article/pii/B9780323431408000251.

[6] S. W. Barnaby. On the formation of cavities in water by screw propellers at high speeds. *Journal of the American Society for Naval Engineers*, 9(4):678–683, 1897.

[7] R. A. Bauman, G. Ling, L. Tong, A. Januszkiewicz, D. Agoston, N. Delanerolle, Y. Kim, D. Ritzel, R. Bell, J. Ecklund, et al. An introductory characterization of a combat-casualty-care relevant swine model of closed head injury resulting from exposure to explosive blast. *Journal of neurotrauma*, 26(6):841–860, 2009.

[8] P. Bayly, P. Massouros, E. Christoforou, A. Sabet, and G. Genin. Magnetic resonance measurement of transient shear wave propagation in a viscoelastic gel cylinder. *Journal of the Mechanics and Physics of Solids*, 56(5):2036–2049, 2008.

[9] BBC. Beirut explosion: What we know so far, 2020. URL https://www.bbc.com/news/world-middle-east-53668493. Last accessed 24 February 2021.

[10] F. P. Beer, E. R. Johnston, and E. R. Eisenberg. *Vector Mechanics for Engineers: Statics*. McGraw-Hill Higher Education, 8th edition, 2007. ISBN 9780072976878.

[11] T. B. Benjamin and A. T. Ellis. The collapse of cavitation bubbles and the pressures thereby produced against solid boundaries. *Philosophical Transactions for the Royal Society of London. Series A, Mathematical and Physical Sciences*, pages 221–240, 1966.

[12] L. E. Bilston, Z. Liu, and N. Phan-Thien. Large strain behaviour of brain tissue in shear: some experimental data and differential constitutive model. *Biorheology*, 38(4):335–345, 2001.

[13] R. Bolander, B. Mathie, C. Bir, D. Ritzel, and P. VandeVord. Skull flexure as a contributing factor in the mechanism of injury in the rat when exposed to a shock wave. *Annals of biomedical engineering*, 39(10):2550, 2011.

[14] I. G. Bowen, E. R. Fletcher, D. R. Richmond, F. G. Hirsch, and C. S. White. Biophysical mechanisms and scaling procedures applicable in assessing responses of the thorax energized by air-blast overpressures or by non-penetrating missiles. technical progress report. Technical report, Lovelace Foundation for Medical Education and Research, Albuquerque, N. Mex., 1966.

[15] C. E. Brennen. *Fundamentals of multiphase flow*. Cambridge university press, 2005.

[16] S. Budday, C. Raybaud, and E. Kuhl. A mechanical model predicts morphological abnormalities in the developing human brain. *Scientific reports*, 4:5644, 2014.

[17] S. Budday, R. Nay, R. de Rooij, P. Steinmann, T. Wyrobek, T. C. Ovaert, and E. Kuhl. Mechanical properties of gray and white matter brain tissue by indentation. *Journal of the mechanical behavior of biomedical materials*, 46:318–330, 2015.

[18] S. Budday, G. Sommer, C. Birkl, C. Langkammer, J. Haybaeck, J. Kohnert, M. Bauer, F. Paulsen, P. Steinmann, E. Kuhl, et al. Mechanical characterization of human brain tissue. *Acta biomaterialia*, 48:319–340, 2017.

[19] S. Budday, T. C. Ovaert, G. A. Holzapfel, P. Steinmann, and E. Kuhl. Fifty shades of brain: a review on the mechanical testing and modeling of brain tissue. *Archives of Computational Methods in Engineering*, pages 1–44, 2019.

[20] S. Canchi, M. Sarntinoranont, Y. Hong, J. J. Flint, G. Subhash, and M. A. King. Simulated blast overpressure induces specific astrocyte injury in an ex vivo brain slice model. *PLoS one*, 12(4):e0175396, 2017.

[21] R. Cao, Z. Huang, T. Varghese, and G. Nabi. Tissue mimicking materials for the detection of prostate cancer using shear wave elastography: A validation study. *Medical physics*, 40(2): 022903, 2013.

[22] CDC. Surveillance report of traumatic brain injury-related emergency department visits, hospitalizations, and deaths—united states, 2014., 2019. URL https://www.cdc.gov/traumaticbraininjury/basics.html. Last accessed 16 September 2020.

[23] H. Celander, C.-J. Clemedson, U. A. Ericsson, and H. I. Hultman. The use of a compressed air operated shock tube for physiological blast research. *Acta Physiologica Scandinavica*, 33 (1):6–13, 1955.

[24] C. D. W. Chandler. Blast-related ear injury in current us military operations: Role of audiology on the interdisciplinary team. *The ASHA Leader*, 11(9):8–29, 2006.

[25] Y. Chen and W. Huang. Non-impact, blast-induced mild tbi and ptsd: concepts and caveats. *Brain injury*, 25(7-8):641–650, 2011.

[26] S. Cheng, E. C. Clarke, and L. E. Bilston. Rheological properties of the tissues of the central nervous system: a review. *Medical engineering & physics*, 30(10):1318–1337, 2008.

[27] C.-H. Choi. Mechanisms and treatment of blast induced hearing loss. *Korean journal of audiology*, 16(3):103, 2012.

[28] E. H. Clayton, G. M. Genin, and P. V. Bayly. Transmission, attenuation and reflection of shear waves in the human brain. *Journal of The Royal Society Interface*, 9(76):2899–2910, 2012.

[29] A. Courtney and M. Courtney. A thoracic mechanism of mild traumatic brain injury due to blast pressure waves. *Nature Precedings*, pages 1–1, 2008.

[30] A. Courtney and M. Courtney. The complexity of biomechanics causing primary blast-induced traumatic brain injury: a review of potential mechanisms. *Frontiers in neurology*, 6:221, 2015.

[31] G. Crile and D. P. Quiring. A record of the body weight and certain organ and gland weights of 3690 animals. *The Ohio Journal of Science*, 1940.

[32] N. C. De Lanerolle, F. Bandak, D. Kang, A. Y. Li, F. Du, P. Swauger, S. Parks, G. Ling, and J. H. Kim. Characteristics of an explosive blast-induced brain injury in an experimental model. *Journal of Neuropathology & Experimental Neurology*, 70(11):1046–1057, 2011.

[33] R. de Rooij and E. Kuhl. Constitutive modeling of brain tissue: current perspectives. *Applied Mechanics Reviews*, 68(1), 2016.

[34] DoD-TBI. Dod worldwide numbers for tbi, 2000-2019. Technical report, Defense and Veterans Brain Injury Center, U.S, 2020. URL https://dvbic.dcoe.mil/dod-worldwide-numbers-tbi. Last accessed 16 September 2020.

[35] G. A. Elder, E. M. Mitsis, S. T. Ahlers, and A. Cristian. Blast-induced mild traumatic brain injury. *Psychiatric Clinics North America*, 33(4):757–781, 2010.

[36] S. L. Eskridge, C. A. Macera, M. R. Galarneau, T. L. Holbrook, S. I. Woodruff, A. J. MacGregor, D. J. Morton, and R. A. Shaffer. Injuries from combat explosions in iraq: injury type, location, and severity. *Injury*, 43(10):1678–1682, 2012.

[37] B. Ferry, A. DeCastro, A. Hays Shapshak, and R. Taylor. Concussion. In *StatPearls*. Treasure Island (FL), 2022. URL https://www.ncbi.nlm.nih.gov/books/NBK537017/.

[38] E. Fievisohn, Z. Bailey, A. Guettler, and P. VandeVord. Primary blast brain injury mechanisms: current knowledge, limitations, and future directions. *Journal of biomechanical engineering*, 140(2), 2018.

[39] A. E. Forte, S. Galvan, F. Manieri, F. R. y Baena, and D. Dini. A composite hydrogel for brain tissue phantoms. *Materials & Design*, 112:227–238, 2016.

[40] A. E. Forte, S. M. Gentleman, and D. Dini. On the characterization of the heterogeneous mechanical response of human brain tissue. *Biomechanics and modeling in mechanobiology*, 16(3):907–920, 2017.

[41] S. Ganpule, A. Alai, E. Plougonven, and N. Chandra. Mechanics of blast loading on the head models in the study of traumatic brain injury using experimental and computational approaches. *Biomechanics and modeling in mechanobiology*, 12(3):511–531, 2013.

[42] S. Ganpule, N. Daphalapurkar, M. P. Cetingul, and K. Ramesh. Effect of bulk modulus on deformation of the brain under rotational accelerations. *Shock waves*, 28(1):127–139, 2018.

[43] A. Gefen and S. S. Margulies. Are in vivo and in situ brain tissues mechanically similar? *Journal of biomechanics*, 37(9):1339–1352, 2004.

[44] A. Georges and J. M Das. Traumatic brain injury. In *StatPearls*. Treasure Island (FL), 2021. URL https://www.ncbi.nlm.nih.gov/books/NBK459300/.

[45] J. Goeller, A. Wardlaw, D. Treichler, J. O'Bruba, and G. Weiss. Investigation of cavitation as a possible damage mechanism in blast-induced traumatic brain injury. *Journal of neurotrauma*, 29(10):1970–1981, 2012.

[46] J. Gordon Betts, K. A. Young, J. A. Wise, E. Johnson, B. Poe, D. H. Kruse, O. Korol, J. E. Johnson, M. Womble, and P. DeSaix. *Anatomy and Physiology*. OpenStax, 2013.

[47] A. G. Gross. A new theory on the dynamics of brain concussion and brain injury. *Journal of neurosurgery*, 15(5):548–561, 1958.

[48] U. Hamhaber, I. Sack, S. Papazoglou, J. Rump, D. Klatt, and J. Braun. Three-dimensional analysis of shear wave propagation observed by in vivo magnetic resonance elastography of the brain. *Acta biomaterialia*, 3(1):127–137, 2007.

[49] K. J. Heltemes, T. L. Holbrook, A. J. MacGregor, and M. R. Galarneau. Blast-related mild traumatic brain injury is associated with a decline in self-rated health amongst us military personnel. *Injury*, 43(12):1990–1995, 2012.

[50] E. Herbert, S. Balibar, and F. Caupin. Cavitation pressure in water. *Physical Review E*, 74(4): 041603, 2006.

[51] Y. Hong, M. Sarntinoranont, G. Subhash, S. Canchi, and M. King. Localized tissue surrogate deformation due to controlled single bubble cavitation. *Experimental Mechanics*, 56(1): 97–109, 2016.

[52] M. Hrapko, J. Van Dommelen, G. Peters, and J. Wismans. Characterisation of the mechanical behaviour of brain tissue in compression and shear. *Biorheology*, 45(6):663–676, 2008.

[53] M. Hrapko, J. Van Dommelen, G. Peters, and J. Wismans. The influence of test conditions on characterization of the mechanical properties of brain tissue. *Journal of Biomechanical Engineering*, 130(3), 2008.

[54] *Harmonized Hybrid III 50th Male User Manual*. Humanetics Innovative Solutions Inc., Plymouth, Michigan 48170 USA, 2017.

[55] H. Ishida, C. Nuntadusit, H. Kimoto, T. Nakagawa, and T. Yamamoto. Cavitation bubble behavior near solid boundaries. In *CAV 2001: Fourth International Symposium on Cavitation*, pages A5–003, Caltech, Pasadena, USA, June 20–23 2001.

[56] A. Iwaskiw, K. Ott, R. Armiger, A. Wickwire, V. Alphonse, L. Voo, C. Carneal, and A. Merkle. The measurement of intracranial pressure and brain displacement due to short-duration dynamic overpressure loading. *Shock Waves*, 28(1):63–83, 2018.

[57] F. Jacob and B. Ted. *A first course in finite elements*. Wiley, 2007.

[58] A. Jean, M. K. Nyein, J. Q. Zheng, D. F. Moore, J. D. Joannopoulos, and R. Radovitzky. An animal-to-human scaling law for blast-induced traumatic brain injury risk assessment. *Proceedings of the National Academy of Sciences*, 111(43):15310–15315, 2014.

[59] X. Jin, F. Zhu, H. Mao, M. Shen, and K. H. Yang. A comprehensive experimental study on material properties of human brain tissue. *Journal of biomechanics*, 46(16):2795–2801, 2013.

[60] John-Hopkins-Medicine. Traumatic brain injury, 2021. URL https://www.hopkinsmedicine.org/health/conditions-and-diseases/traumatic-brain-injury.

[61] John-Hopkins-Medicine. Head injury, 2021. URL https://www.hopkinsmedicine.org/health/conditions-and-diseases/head-injury.

[62] A. Johnson and B. Burns. Hemorrhage. In *StatPearls*. Treasure Island (FL), 2020. URL https://www.ncbi.nlm.nih.gov/books/NBK542273/.

[63] S. Kahali, M. Townsend, M. Mendez Nguyen, J. Kim, E. Alay, M. Skotak, and N. Chandra. The evolution of secondary flow phenomena and their effect on primary shock conditions in shock tubes: Experimentation and numerical model. *PloS one*, 15(1):e0227125, 2020.

[64] D. Kellner. Region growing (2d/3d grayscale), 2011. URL https://www.mathworks.com/matlabcentral/fileexchange/32532-region-growing-2d-3d-grayscale. Last accessed 29 August 2021.

[65] E. Kennard. Cavitation in an elastic liquid. *Physical Review*, 63(5-6):172, 1943.

[66] V. Kenner and W. Goldsmith. Impact on a simple physical model of the head. *Journal of biomechanics*, 6(1):1–11, 1973.

[67] J. Kerwin, S. Vidhate, F. Masoomi, M. Tartis, A. Willis, and R. Mejia-Alvarez. Experimental study of the mechanics of blast-induced traumatic brain injury. *Mechanics of Biological Systems & Micro-and Nanomechanics*, 4:71–74, 2019.

[68] G. F. Kinney and K. J. Graham. *Explosive shocks in air*. Springer Science & Business Media, 1985.

[69] K. M. Labus and C. M. Puttlitz. Viscoelasticity of brain corpus callosum in biaxial tension. *Journal of the Mechanics and Physics of Solids*, 96:591–604, 2016.

[70] A. D. C. Leonardi, C. A. Bir, D. V. Ritzel, and P. J. VandeVord. Intracranial pressure increases during exposure to a shock wave. *Journal of neurotrauma*, 28(1):85–94, 2011.

[71] S. Liou. The hopes brain tutorial, Jun 2010. URL https://hopes.stanford.edu/the-hopes-brain-tutorial-text-version/.

[72] P. Lubock and W. Goldsmith. Experimental cavitation studies in a model head-neck system. *Journal of Biomechanics*, 13(12):1041–1052, 1980.

[73] D. B. MacManus, B. Pierrat, J. G. Murphy, and M. D. Gilchrist. Region and species dependent mechanical properties of adolescent and young adult brain tissue. *Scientific reports*, 7(1): 1–12, 2017.

[74] D. B. MacManus, J. G. Murphy, and M. D. Gilchrist. Mechanical characterisation of brain tissue up to 35% strain at 1, 10, and 100/s using a custom-built micro-indentation apparatus. *Journal of the mechanical behavior of biomedical materials*, 87:256–266, 2018.

[75] A. Madhukar and M. Ostoja-Starzewski. Finite element methods in human head impact simulations: a review. *Annals of biomedical engineering*, 47(9):1832–1854, 2019.

[76] A. Manduca, P. J. Bayly, R. L. Ehman, A. Kolipaka, T. J. Royston, I. Sack, R. Sinkus, and B. E. Van Beers. Mr elastography: Principles, guidelines, and terminology. *Magnetic Resonance in Medicine*, 85(5):2377–2390, 2021.

[77] O. Masataka and K. Ito. *Color Universal Design Handbook*. J*Fly Data Depository for Drosophila researchers, 2006.

[78] Mayo-Clinic. Intracranial hematoma, Jun 2020. URL https://www.mayoclinic.org/diseases-conditions/intracranial-hematoma/symptoms-causes/syc-20356145.

[79] MayoClinicStaff. Concussion, Feb 2020. URL www.mayoclinic.org/diseases-conditions/concussion/symptoms-causes/syc-20355594.

[80] J. McElhaney, R. Stalnaker, M. Estes, and L. Rose. Dynamic mechanical properties of scalp and brain. In *Proc. Of the 6th Annual Rocky Mountain Bioengineering Symposium*, 1969.

[81] D. Meaney, S. Olvey, and T. Gennarelli. Biomechanical basis of traumatic brain injury. *Youmans & Winn Neurological Surgery*, 4:2755–64, 2011.

[82] D. F. Meaney, B. Morrison, and C. Dale Bass. The Mechanics of Traumatic Brain Injury: A Review of What We Know and What We Need to Know for Reducing Its Societal Burden. *Journal of Biomechanical Engineering*, 136(2), 02 2014. ISSN 0148-0731. doi: 10.1115/1.4026364. URL https://doi.org/10.1115/1.4026364. 021008.

[83] J. Mediavilla Varas, M. Philippens, S. Meijer, A. Van Den Berg, P. Sibma, J. Van Bree, and D. De Vries. Physics of ied blast shock tube simulations for mtbi research. *Frontiers in neurology*, 2:58, 2011.

[84] MedlinePlus. Skull fracture: Medlineplus medical encyclopedia, 2019. URL https://medlineplus.gov/ency/article/000060.htm.

[85] R. Mejía-Alvarez, J. Kerwin, S. Vidhate, P. Sandherr, E. Patton, B. Dávila-Montero, A. Yucesoy, and A. Willis. Large cross-section blast chamber: design and experimental characterization. *Measurement Science and Technology*, 32(11):115902, 2021. doi: 10.1088/1361-6501/ac12fc.

[86] Merriam-Webster. *Merriam-Webster medical dictionary*. Merriam Webster, 2021. ISBN 9780877792949. URL https://www.merriam-webster.com/dictionary/contusion.

[87] Merriam-Webster. *Merriam-Webster medical dictionary*. Merriam Webster, 2021. ISBN 9780877792949. URL https://www.merriam-webster.com/dictionary/fracture.

[88] F. Mesfin, N. Gupta, A. Hays Shapshak, and R. Taylor. Diffuse axonal injury. In *StatPearls*. Treasure Island (FL), 2020. URL https://www.ncbi.nlm.nih.gov/books/NBK448102/.

[89] T. Mezger. *The rheology handbook for users of rotational and oscillatory rheometers*. Vincentz, fourth edition, 2014.

[90] S. T. Miller, C. F. Cooper, P. Elsbernd, J. Kerwin, R. Mejia-Alvarez, and A. M. Willis. Localizing clinical patterns of blast traumatic brain injury through computational modeling and simulation. *Frontiers in Neurology*, 12, 2021.

[91] W. C. Moss, M. J. King, and E. G. Blackman. Skull flexure from blast waves: a mechanism for brain injury with implications for helmet design. *Physical review letters*, 103(10):108702, 2009.

[92] W. Murphy, J. Black, and G. W. Hastings. *Handbook of biomaterial properties*. Springer, 2016.

[93] T. P. Naidich, B. N. Delman, E. M. Haacke, S. S. Kollias, H. M. Duvernoy, and A. G. Sorensen. *Duvernoys Atlas of the Human Brain Stem and Cerebellum High-Field MRI: Surface Anatomy, Internal Structure, Vascularization and 3D Sectional Anatomy*. Springer Vienna, 2009.

[94] A. Nakagawa, G. T. Manley, A. D. Gean, K. Ohtani, R. Armonda, A. Tsukamoto, H. Yamamoto, K. Takayama, and T. Tominaga. Mechanisms of primary blast-induced traumatic brain injury: insights from shock-wave research. *Journal of neurotrauma*, 28(6):1101–1119, 2011.

[95] C. E. Needham. *Blast Waves*. Springer, second edition, 2018. ISBN 9783319653815.

[96] C. E. Needham, D. Ritzel, G. T. Rule, S. Wiri, and L. Young. Blast testing issues and tbi: experimental models that lead to wrong conclusions. *Frontiers in neurology*, 6:72, 2015.

[97] W. L. Nowinski. Human brain anatomy in 3d. In K. Miller, editor, *Biomechanics of the Brain: Second Edition*. Springer, 2019.

[98] T. Ogasawara, N. Tsubota, H. Seki, Y. Shigaki, and H. Takahira. Experimental and numerical investigations of the bubble collapse at the center between rigid walls. *J. Phys.: Conf. Ser.*, 656(1):012031–5, Dec. 2015.

[99] Z. Pan, A. Kiyama, Y. Tagawa, D. J. Daily, S. L. Thomson, R. Hurd, and T. T. Truscott. Cavitation onset caused by acceleration. *Proceedings of the National Academy of Sciences*, 114(32):8470–8474, 2017.

[100] M. B. Panzer, K. A. Matthews, A. W. Yu, B. Morrison, D. F. Meaney, and C. R. Bass. A multiscale approach to blast neurotrauma modeling: part i–development of novel test devices for in vivo and in vitro blast injury models. *Frontiers in neurology*, 3:46, 2012.

[101] M. B. Panzer, B. S. Myers, B. P. Capehart, and C. R. Bass. Development of a finite element model for blast brain injury and the effects of csf cavitation. *Annals of biomedical engineering*, 40(7):1530–1544, 2012.

[102] C. A. Parsons and S. S. Cook. Investigations into the causes of corrosion or erosion of propellers. *Journal of the American Society for Naval Engineers*, 31(2):536–541, 1919.

[103] F. Pervin and W. W. Chen. Dynamic mechanical response of bovine gray matter and white matter brain tissues under compression. *Journal of biomechanics*, 42(6):731–735, 2009.

[104] F. Pervin and W. W. Chen. Effect of inter-species, gender, and breeding on the mechanical behavior of brain tissue. *NeuroImage*, 54:S98–S102, 2011.

[105] J. Peterson and P. C. Dechow. Material properties of the human cranial vault and zygoma. *The Anatomical Record Part A: Discoveries in Molecular, Cellular, and Evolutionary Biology: An Official Publication of the American Association of Anatomists*, 274(1):785–797, 2003.

[106] R. Prabhu, M. F. Horstemeyer, M. Tucker, E. Marin, J.-L. Bouvard, J. Sherburn, J. Liao, and L. N. Williams. Coupled experiment/finite element analysis on the mechanical response of porcine brain under high strain rates. *Journal of the mechanical behavior of biomedical materials*, 4(7):1067–1080, 2011.

[107] D. Purves. *Neuroscience*. Oxford University Press, New York, 2018.

[108] K. Rafaels, C. R. "Dale" Bass, R. S. Salzar, M. B. Panzer, W. Woods, S. Feldman, T. Cummings, and B. Capehart. Survival risk assessment for primary blast exposures to the head. *Journal of neurotrauma*, 28(11):2319–2328, 2011.

[109] M. E. Raichle and D. A. Gusnard. Appraising the brain's energy budget. *Proceedings of the National Academy of Sciences*, 99(16):10237–10239, 2002.

[110] B. Rashid, M. Destrade, and M. D. Gilchrist. Mechanical characterization of brain tissue in compression at dynamic strain rates. *Journal of the mechanical behavior of biomedical materials*, 10:23–38, 2012.

[111] B. Rashid, M. Destrade, and M. D. Gilchrist. Temperature effects on brain tissue in compression. *journal of the mechanical behavior of biomedical materials*, 14:113–118, 2012.

[112] B. Rashid, M. Destrade, and M. D. Gilchrist. Mechanical characterization of brain tissue in tension at dynamic strain rates. *Journal of the mechanical behavior of biomedical materials*, 33:43–54, 2014.

[113] L. Rayleigh. Viii. on the pressure developed in a liquid during the collapse of a spherical cavity. *The London, Edinburgh, and Dublin Philosophical Magazine and Journal of Science*, 34(200):94–98, 1917.

[114] B. Redwood, F. Schöffer, and B. Garret. *The 3D printing handbook: technologies, design and applications*. 3D Hubs, 2017.

[115] L. D. Reid Ph.D M.P.H and K. R. Fingar Ph.D M.P.H. Inpatient stays and emergency department visits involving traumatic brain injury, 2017, 2020. URL https://www.hcup-us.ahrq.gov/reports/statbriefs/sb255-Traumatic-Brain-Injury-Hospitalizations-ED-Visits-2017.jsp.

[116] D. R. Richmond, E. G. Damon, I. G. Bowen, E. R. Fletcher, and C. S. White. Air-blast studies with eight species of mammals. Technical report, LOVELACE FOUNDATION FOR MEDICAL EDUCATION AND RESEARCH ALBUQUERQUE NM, 1966.

[117] F. C. Salvado, A. J. Tavares, F. Teixeira-Dias, and J. B. Cardoso. Confined explosions: the effect of compartment geometry. *Journal of Loss Prevention in the Process Industries*, 48: 126–144, 2017.

[118] R. S. Salzar, D. Treichler, A. Wardlaw, G. Weiss, and J. Goeller. Experimental investigation of cavitation as a possible damage mechanism in blast-induced traumatic brain injury in post-mortem human subject heads. *Journal of neurotrauma*, 34(8):1589–1602, 2017.

[119] M. Sarntinoranont, S. J. Lee, Y. Hong, M. A. King, G. Subhash, J. Kwon, and D. F. Moore. High-strain-rate brain injury model using submerged acute rat brain tissue slices. *Journal of neurotrauma*, 29(2):418–429, 2012.

[120] R. N. Saunders, X. G. Tan, S. M. Qidwai, and A. Bagchi. Towards identification of correspondence rules to relate traumatic brain injury in different species. *Annals of biomedical engineering*, 47(9):2005–2018, 2019.

[121] Servier-Medical. Smart servier medical art, Sep 2020. URL https://smart.servier.com/.

[122] L. Simon and E. Newton. Basilar skull fractures. In *StatPearls*. Treasure Island (FL), 2020. URL https://www.ncbi.nlm.nih.gov/books/NBK470175/.

[123] M. Skotak, E. Alay, J. Q. Zheng, V. Halls, and N. Chandra. Effective testing of personal protective equipment in blast loading conditions in shock tube: Comparison of three different testing locations. *PloS one*, 13(6):e0198968, 2018.

[124] P. Sreenivasan and S. Ray. Mechanical testing at high strain rates. In K. J. Buschow, R. W. Cahn, M. C. Flemings, B. Ilschner, E. J. Kramer, S. Mahajan, and P. Veyssière, editors, *Encyclopedia of Materials: Science and Technology*, pages 5269–5271. Elsevier, Oxford, 2001. ISBN 978-0-08-043152-9. doi: https://doi.org/10.1016/B0-08-043152-6/00919-0. URL https://www.sciencedirect.com/science/article/pii/B0080431526009190.

[125] M.-K. Sun, J. Shieh, C.-W. Lo, C.-S. Chen, B.-T. Chen, C.-W. Huang, and W.-S. Chen. Reusable tissue-mimicking hydrogel phantoms for focused ultrasound ablation. *Ultrasonics sonochemistry*, 23:399–405, 2015.

[126] S. Sutar and S. Ganpule. Investigation of wave propagation through head layers with focus on understanding blast wave transmission. *Biomechanics and modeling in mechanobiology*, 19 (3):875–892, 2020.

[127] A. Tangri. Polyacrylamide based hydrogels: Synthesis, characterization and applications. *International Journal of Pharmaceutical, Chemical & Biological Sciences*, 4(4), 2014.

[128] M. Trexler, A. Lennon, A. Wickwire, T. Harrigan, Q. Luong, J. Graham, A. Maisano, J. Roberts, and A. Merkle. Verification and implementation of a modified split hopkinson pressure bar technique for characterizing biological tissue and soft biosimulant materials under dynamic shear loading. *Journal of the mechanical behavior of biomedical materials*, 4 (8):1920–1928, 2011.

[129] P. J. VandeVord, A. D. C. Leonardi, and D. Ritzel. Bridging the gap of standardized animals models for blast neurotrauma: methodology for appropriate experimental testing. In *Injury Models of the Central Nervous System*, pages 101–118. Springer, 2016.

[130] S. Vidhate. *Experimental Systems for Ex-Vivo and In-Vivo Studies of Blast-Induced Traumatic Brain Injury*. PhD thesis, Michigan State University, 2021.

[131] G. Z. Voyiadjis and A. Samadi-Dooki. Hyperelastic modeling of the human brain tissue: effects of no-slip boundary condition and compressibility on the uniaxial deformation. *Journal of the mechanical behavior of biomedical materials*, 83:63–78, 2018.

[132] A. Wardlaw and J. Goeller. Cavitation as a possible traumatic brain injury (tbi) damage mechanism. In *26th Southern Biomedical Engineering Conference SBEC 2010, April 30-May 2, 2010, College Park, Maryland, USA*, pages 34–37. Springer, 2010.

[133] E. D. Weichel, M. H. Colyer, C. Bautista, K. S. Bower, and L. M. French. Traumatic brain injury associated with combat ocular trauma. *The Journal of head trauma rehabilitation*, 24 (1):41–50, 2009.

[134] J. Weickenmeier, R. de Rooij, S. Budday, P. Steinmann, T. Ovaert, and E. Kuhl. Brain stiffness increases with myelin content. *Acta biomaterialia*, 42:265–272, 2016.

[135] J. Weickenmeier, R. de Rooij, S. Budday, T. C. Ovaert, and E. Kuhl. The mechanical importance of myelination in the central nervous system. *Journal of the mechanical behavior of biomedical materials*, 76:119–124, 2017.

[136] J. Weickenmeier, M. Kurt, E. Ozkaya, R. de Rooij, T. Ovaert, R. Ehman, K. B. Pauly, and E. Kuhl. Brain stiffens post mortem. *Journal of the mechanical behavior of biomedical materials*, 84:88–98, 2018.

[137] A. Wermer, J. Kerwin, K. Welsh, R. Mejia-Alvarez, M. Tartis, and A. Willis. Materials characterization of cranial simulants for blast-induced traumatic brain injury. *Military medicine*, 185(Supplement_1):205–213, 2020.

[138] WHO. Lebanon explosion 2020, 2021. URL https://www.who.int/emergencies/funding/appeals/lebanon-explosion-2020. Last accessed 24 February 2021.

[139] S. T. Williams, T. H. Harding, J. K. Statz, and J. S. Martin. Blast wave dynamics at the cornea as a function of eye protection form and fit. *Military medicine*, 182(suppl_1):226–229, 2017.

[140] T. Wu, J. Antona-Makoshi, A. Alshareef, J. S. Giudice, and M. B. Panzer. Investigation of cross-species scaling methods for traumatic brain injury using finite element analysis. *Journal of neurotrauma*, 37(2):410–422, 2020.

[141] T.-H. Yang. Recent applications of polyacrylamide as biomaterials. *Recent Patents on Materials Science*, 1(1):29–40, 2008.

[142] F. R. Young. *Cavitation*. World Scientific, 1999.

[143] A. Yücesoy. The role of morphology and residual stress on blast-induced traumatic brain injury. Master's thesis, Michigan State University, 2019.

[144] K. Zell, J. I. Sperl, M. W. Vogel, R. Niessner, and C. Haisch. Acoustical properties of selected tissue phantom materials for ultrasound imaging. *Physics in Medicine & Biology*, 52(20): N475, 2007.

[145] F. Zhu, C. Wagner, A. D. C. Leonardi, X. Jin, P. VandeVord, C. Chou, K. H. Yang, and A. I. King. Using a gel/plastic surrogate to study the biomechanical response of the head under air shock loading: a combined experimental and numerical investigation. *Biomechanics and modeling in mechanobiology*, 11(3):341–353, 2012.

[146] F. Zhu, C. C. Chou, K. H. Yang, and A. I. King. Some considerations on the threshold and inter-species scaling law for primary blast-induced traumatic brain injury: a semi-analytical approach. *Journal of Mechanics in Medicine and Biology*, 13(04):1350065, 2013.